UNIVERSITY OF CALIFORNIA
RIVERSIDE

Probing Dark Matter Physics With Supermassive Black Holes

A Dissertation submitted in partial satisfaction
of the requirements for the degree of

Doctor of Philosophy

in

Physics

by

Wei-Xiang Feng

September 2023

Dissertation Committee:

Dr. Hai-Bo Yu, Chairperson
Dr. Simeon Bird
Dr. Michael Mulligan

The Dissertation of Wei-Xiang Feng is approved:

Committee Chairperson

University of California, Riverside

Acknowledgments

I am profoundly grateful to my advisor, Hai-Bo Yu, for his invaluable mentorship, which has played a pivotal role in guiding me through the intricacies of particle physics and astrophysics, enabling me to tackle previously unsolved problems. Hai-Bo afforded me the freedom and independence to explore a wide array of topics and pursue my own innovative ideas. I hold a deep respect for the other esteemed committee members: Simeon Bird and Michael Mulligan. I am appreciative of the many insightful discussions about physics I have had with them. Beyond the committee, I am grateful to John Baez, Steve Carlip, Wei-Tou Ni, and Stanley Deser for their inspiring correspondence on fundamental physics, and to Barry Barish, Yanou Cui, Flip Tanedo, and Daneng Yang for our numerous private conversations on physics.

I extend my heartfelt thanks to all my collaborators during my PhD journey, with a special mention to Yi-Ming Zhong, from whom I learned a great deal, especially in sharpening my coding skills. I express my gratitude to the entire team at Academia Sinica, Institute of Physics, with particular appreciation for Che-Yu Chen, Kin-Wang Ng, and Meng-Ru Wu, for their warm hospitality during my visits. Furthermore, I am indebted to Chao-Qiang Geng and Rurng-Sheng Guo for their unwavering support during my time at National Tsing Hua University and National Kaohsiung Normal University.

My heartfelt thanks also go out to all the physics graduate students at Riverside, notably Chia-Feng Chang, Lexi Constantino, Adam Green, Ming-Feng Ho, Pak Kau Lim, Yifan Liu, Yen-Wen Lu, and Mehrdad Phoroutan, with whom I have had many illuminating conversations about physics and shared camaraderie throughout my candidacy.

Additionally, I want to express my gratitude to the individuals I met at various summer schools and workshops during my PhD, including Formosa Summer School 2018, NCTS annual theory meeting 2018, 2019, SoCal BSM 2019, NCTS Dark Physics Workshop 2020, Midwest Relativity Meeting 2021, TASI Lecture 2022, SoCal Strings & Fields 2023, Pollica Workshop 2023, and N3AS Summer School 2023, for engaging discussions and intellectual stimulation.

Last but certainly not least, I wish to convey my heartfelt appreciation to my parents for their unwavering love and support, to my younger brother for his exceptional efforts in managing family affairs during the challenging time of my mother's passing, and to my uncle for his encouragement since my childhood.

Wei-Xiang Feng

University of California, Riverside

September 2023

Publications

1. Wei-Xiang Feng, Hai-Bo Yu, Yi-Ming Zhong, **Seeding Supermassive Black Holes with Self-interacting Dark Matter: A Unified Scenario with Baryons**, Astrophys. J. Lett. **914** (2021) 2, L26, [arXiv:2010.15132 [astro-ph.CO]].

2. Wei-Xiang Feng, Hai-Bo Yu, Yi-Ming Zhong, **Dynamical Instability of Collapsed Dark Matter Halos**, J. Cosmol. Astropart. Phys. **05** (2022) 036, [arXiv:2108.11967 [astro-ph.CO]].

3. Wei-Xiang Feng, **Gravothermal Phase Transition, Black Holes and Space Dimensionality**, Phys. Rev. D **106** (2022) 4, L041501, [arXiv:2207.14317 [gr-qc]].

4. Wei-Xiang Feng, Alessandra Parisi, Chian-Shu Chen, Feng-Li Lin, **Self-interacting Dark Scalar Spikes around Black Holes via Relativistic Bondi Accretion**, J. Cosmol. Astropart. Phys. **08** (2022) 032, [arXiv:2112.05160 [astro-ph.HE]].

5. Wei-Xiang Feng, **On the Dynamical Instability of Monatomic Fluid Spheres in (N+1)-dimensional Spacetime**, Astronomy **2** (2023) 1, 22-46, [arXiv:2111.05341 [gr-qc]].

Dedicated to my beloved mother Jui-Yun

for her altruistic support and measureless love from the Paradise.

ABSTRACT OF THE DISSERTATION

Probing Dark Matter Physics With Supermassive Black Holes

by

Wei-Xiang Feng

Doctor of Philosophy, Graduate Program in Physics
University of California, Riverside, September 2023
Dr. Hai-Bo Yu, Chairperson

We explore the connection between supermassive black hole (SMBH) formation and self-interacting dark matter in the early universe. Observations reveal SMBHs with $\sim 10^9$ $M_\odot$ masses when the universe was only 6% of its current age. Our scenario involves self-interacting dark matter halos undergoing gravothermal instability, forming seed black holes, to account for their existence. In particular, baryonic matter in protogalaxies accelerates halo evolution. We further examine the angular momentum dissipation and conditions for dynamical (general relativistic) instability. We also explore quantum instability in self-gravitating thermal systems, emphasizing quantum degeneracy pressure's role in black hole formation. Additionally, we study spike mass density distribution in a scalar field dark halo, considering self-interaction and relativistic Bondi accretion onto non-spinning black holes. For primordial black holes (PBHs) as dark matter, we compare merger rates of PBH binaries to extremely mass ratio inspirals into SMBHs, which are detectable with gravitational wave technology.

Contents

List of Figures

List of Tables

Chapter 1

Introduction

Understanding the origins of supermassive black holes (SMBHs) represents one of the most profound and enduring challenges in astrophysics and cosmology. These enigmatic cosmic monsters, with masses often exceeding billions of times solar masses, are known to exist as early as when the universe was a mere fraction of its current age. The formation mechanisms of such colossal entities have captivated the imaginations of scientists for decades, prompting investigations into the interplay between gravity, dark matter, and the matter that populates our cosmos.

The foundations of this research are rooted in several key observations and theoretical frameworks. Foremost among these is the revelation that SMBHs, with masses on the order of 10^9 $M_\odot$, existed when the universe had reached a mere 6% of its present age [1]. This astonishing fact poses a profound question:

How did such colossal black holes emerge in the cosmos when the universe was still in its cosmic infancy?

The formation of SMBHs can be quite intricate, with several proposed mechanisms each offering unique advantages and facing distinct challenges; see the flowchart by Martin Rees [2] (Fig. 1). In general, there are two main pathways to their formation. One involves the "mergers" of stellar-mass black holes (formed from dead stars), while the other results from the "direct collapse" of dense gas clouds. The former could potentially explain binary SMBHs but may not fully account for the presence of early universe SMBHs, as it often takes too long to reach supermassive proportions. Consequently, it is challenging to explain the existence of high-redshift ($z \gtrsim 7$) SMBHs. On the other hand, the latter allows for rapid SMBH formation but faces the rarity of suitable conditions, such as the requirement that the temperature must be sufficiently high to prevent the gas cloud from fragmentation, the efficient disposal of angular momentum. Accretion, however, is the most widely accepted mechanism responsible for SMBH growth. Over billions of years, gas and dust gradually accumulate around a central black hole, forming an accretion disk, and are consumed by the black hole, steadily increasing its mass. Additionally, intermediate-mass black holes, larger than stellar-mass ones but smaller than supermassive ones, might serve as seeds for SMBHs. They could form through the collapse of massive stars and evolve into SMBHs through accretion and mergers. In contrast to astrophysical processes, primordial black holes (PBHs) offer an explanation for early universe SMBHs but lack direct evidence and clear formation mechanisms. All these mechanisms collectively contribute to our evolving understanding of the SMBHs at the centers of galaxies. However, we aim to propose a mechanism that can overcome the shortcomings of these models and predict the abundance of SMBHs in the early universe. We outline the dissertation as follows.

In Chapter 2, this dissertation embarks on a journey into the depths of the universe, seeking to unravel the mysteries surrounding the birth of SMBHs. While the existence of these gargantuan black holes is well-established, their origin remains a topic of intense scrutiny and debate. To navigate this complex cosmic terrain, we delve into a scenario that explores the pivotal role of self-interacting dark matter in the formation of SMBHs during the early epochs of the universe. One of the central propositions of this dissertation is the concept of gravothermal instability within self-interacting dark matter halos. Gravothermal instability, a phenomenon within the realm of gravity and thermodynamics, posits that the central regions of these dark matter halos can undergo a collapse process that ultimately gives birth to a seed black hole. This idea forms the core of our exploration into the genesis of SMBHs. Crucially, we recognize that the presence of baryons within protogalaxies can significantly influence the dynamics of dark matter halos. This influence, as we shall elucidate, has the potential to accelerate the gravothermal evolution of these halos, shortening the timescales for the central collapse. The interplay between dark matter and baryonic matter in the early universe is a key focus of our inquiry. Moreover, this research delves into the dissipative aspects of this process, where viscosity induced by self-interactions acts as a catalyst for the dissipation of angular momentum within the central halo. This mechanism is integral to the subsequent formation of SMBHs and is a critical element of our proposed scenario. However, the emergence of SMBHs through this mechanism is not a ubiquitous outcome. It is contingent upon the host halo being situated on the high tails of density fluctuations. In other words, high-redshift SMBHs are expected to be rare occurrences within this framework, offering an explanation for their scarcity in the early universe.

In Chapter 3, the dissertation further delves into the dynamics of this central core within the framework of general relativity. By assuming a truncated Maxwell-Boltzmann distribution to model the dark matter distribution in the central core, the Tolman-Oppenheimer-Volkoff equation is employed to analyze a series of equilibrium configurations. We investigate the conditions under which general relativistic instability is triggered within the collapsed region. This analysis allows us to examine the dynamical instability of the core by considering various factors, including total energy, binding energy, fractional binding energy, and the adiabatic index. The results obtained shed light on the conditions under which these cores collapse into the seed black holes that eventually evolve into SMBHs. This represents a crucial step in the evolution from a dense core to a bona fide black hole. Through a rigorous numerical analysis, we ascertain the specific criteria that must be met for this transition to occur.

The implications of this work are profound. Not only does it offer a plausible mechanism for the formation of SMBHs, but it also provides crucial constraints on various collapse models, particularly those involving dissipative dark matter interactions. These constraints are invaluable for refining our understanding of the early Universe's structure and the role dark matter plays in shaping it. Furthermore, these findings extend beyond the formation of SMBHs. Indeed, they offer a unified explanation for the diverse dark matter distributions observed within galaxies today. By shedding light on the intricate interplay between self-interacting dark matter and the dynamics of the early universe, this research bridges the gap between cosmological observations and theoretical astrophysics. However, the dissertation is not only limited to the classical realm of astrophysics.

In Chapter 4, we extend the investigation into the realm of spacetime dimensionality. We explore the impact of higher dimensions on the dynamical instability, revealing that (3+1)-dimensional spacetime holds a unique position as the "marginal dimensionality." This dimensionality facilitates the stability of the ideal monatomic fluid while avoiding excessive stability. It is also the unique dimensionality allowing stable hydrostatic equilibrium in the presence of a positive cosmological constant—a key feature in understanding the cosmic evolution. In contrast, higher dimensions ($N > 3$) exhibit genuine instability, while (2+1)-dimensional spacetime is deemed "too stable," offering insights into cosmic censorship conjectures and the formation of Bañados-Teitelboim-Zanelli (BTZ) black holes. Here, the role of a negative cosmological constant becomes paramount, leading to the emergence of BTZ black holes and fluid disk equilibrium configurations. This dimensionality analysis has profound implications for our understanding of the cosmos.

In Chapters 5, however, we examine the dynamical instability of self-gravitating thermal systems in the quantum realm. Quantum degeneracy pressure, often considered an obstacle to gravitational collapse, emerges as a pivotal role in triggering general relativistic instability. Additionally, we discuss the formation of massive black holes in the early universe from the collapse of thermalized dark matter clumps. These insights contribute to our understanding of the intricate interplay between quantum effects and gravitation in the cosmos. Intriguingly, the research explores the role of Fermi-degeneracy pressure and Bose-Einstein condensates in the dynamical instability of self-gravitating thermal systems. Our analyses broaden the scope of applicability, highlighting the relevance of these mechanisms in various cosmological scenarios.

In Chapters 6 and 7, we consider two possible probes that could bridge theoretical studies to observation. In Chapter 6, we examine the self-interacting dark scalar spike around a non-spinning black holes by self-consistently solving the relativistic Bondi accretion, in which a quartic self-interaction is considered. The analysis reveals critical insights into the interplay between dark matter and black holes, unveiling a lower bound on the accretion rates and the peculiar density profile within the self-gravitating regime. In Chapter 7, we compare the merger rates of PBH binaries with masses around the solar scale to the extremely mass ratio inspirals (EMRIs) into SMBHs, in which the detectability is accessible given the gravitational wave technology. The study helps differentiate various black hole seeding mechanisms and the potential dark matter candidates, setting up an upper bound on the merger rates through gravitational waves.

All in all, this dissertation embarks on a multifaceted journey through the cosmos, exploring the intricate relationships between SMBHs, self-interacting dark matter, spacetime dimensionality, accretion, and the merger rates. It seeks to unravel the enigma of early universe SMBHs and the role dark matter plays in their formation, while also shedding light on fundamental questions surrounding the nature of spacetime itself. Through investigation with mathematical rigor, this work contributes valuable insights to our evolving understanding of the cosmic tapestry that surrounds us, pushing the boundaries of human knowledge ever further into the cosmic unknown.

Chapter 2

Seeding Supermassive Black Holes with Self-interacting Dark Matter

Astrophysical observations of high-redshift quasars indicate that $\sim 10^9\,\mathrm{M}_\odot$ black holes exist when the Universe is just 800 Myr old after the Big Bang ($z \sim 7$), see [1] for a review. The origin of these supermassive black holes (SMBHs) is still a mystery. In particular, it is extremely puzzling how they could become so massive in such a short time. A popular idea is that there exist heavy seed black holes in the early Universe and they grow massive by accreting baryons. Assuming Eddington accretion, we can relate the black hole mass ($M_{\rm BH}$) and its seed mass ($M_{\rm seed}$) as [3]

$$M_{\rm BH} = M_{\rm seed}\exp(\Delta t/\tau), \tag{2.1}$$

where Δt is the elapse time and $\tau = (450/f_{\rm Edd})[\epsilon/(1-\epsilon)]$ Myr. ϵ is the radiative efficiency assumed to be 0.1 [4], and $f_{\rm Edd}$ is the Eddington ratio, characterizing the accretion efficiency.

Consider J1007+2115, the most massive known quasar with $M_{\rm BH} \approx 1.5 \times 10^9\,{\rm M}_\odot$ at $z > 7.5$ [5]. Taking $f_{\rm Edd} \simeq 1$, we estimate $M_{\rm seed} \sim 10^4\,{\rm M}_\odot$ if it forms at $z \sim 30$, i.e., $\Delta t = 597$ Myr to its observed $z = 7.51$. Such a seed is too massive to be produced from collapsed Pop III stars [1], but it could form through the direct collapse of pristine baryonic gas [6, 7]; see also [8]. The latter scenario predicts $M_{\rm seed} \sim 10^5$–$10^6\,{\rm M}_\odot$. However, observations show there is another population of high-z SMBHs with $f_{\rm Edd}$ much less than 1 [9, 10]. For example, J1205-0000 is observed at $z = 6.7$ with $M_{\rm BH} = 2.2 \times 10^9\,{\rm M}_\odot$ and $f_{\rm Edd} = 0.16$ [9]. The Eddington accretion then implies it grows from a seed with a mass of $2 \times 10^8\,{\rm M}_\odot$ at $z \sim 30$, too heavy to be produced via the direct collapse of gas.

In this chapter, we study the scenario of gravothermal collapse of self-interacting dark matter (SIDM) [11, 12, 13] in explaining the origin of high-z SMBHs. Dark matter self-interactions can transport heat in the halo over cosmological timescales [14, 15, 16, 17]. As a gravothermal system, the SIDM halo has negative heat capacity [18]. The central region could become hot and collapse to a singular state with a finite mass at late stages of the evolution [19, 20]. Thus SIDM has a natural mechanism in triggering gravitational stabilities, a necessary condition to form a black hole. Recent studies also show that SIDM is favored for explaining diverse dark matter distributions over a wide range of galactic systems, see [13] for a review. It is intriguing to explore an SIDM scenario that may explain the origin of the high-z SMBHs and observations of galaxies at $z \sim 0$.

We adopt a typical baryon mass profile for high-z protogalaxies, and show the collapse time can be shortened by a factor of 100, compared to the SIDM-only case. Even for the self-scattering cross section per unit mass $\sigma/m \sim 1\ {\rm cm}^2/{\rm g}$, broadly consistent with the

value used to explain galactic observations [13], the central halo could collapse sufficiently fast to form a seed for $z \gtrsim 7$. Depending on the halo mass, this scenario could explain *both* populations of high-z SMBHs with $f_{\rm Edd} \sim 1$ and 0.1. It also has a built-in mechanism to dissipate angular momentum remanent of the central halo, i.e., viscosity induced by the self-interactions. We will further show when the 3D velocity dispersion of SIDM particles in the collapsed central region reaches $0.57c$, the general relativistic (GR) instability can be triggered. We demonstrate a unified SIDM scenario that could explain observations of galaxies today and high-z SMBHs. In the appendices, we provide additional information.

2.1 Gravothermal evolution

We use a conducting fluid model [19, 21] to study the gravothermal evolution of an SIDM halo, as it yields high resolution for us to closely trace the collapse process. To capture the influence of baryons, we extend the original model with a baryonic component. The evolution of the halo can be described by the following equations

$$\begin{aligned} \frac{\partial M_\chi}{\partial r} &= 4\pi r^2 \rho_\chi, \quad \frac{\partial(\rho_\chi \nu_\chi^2)}{\partial r} = -\frac{G(M_\chi + M_b)\rho_\chi}{r^2}, \\ \frac{\partial L_\chi}{\partial r} &= -4\pi \rho_\chi r^2 \nu_\chi^2 D_t \ln \frac{\nu_\chi^3}{\rho_\chi}, \quad \frac{L_\chi}{4\pi r^2} = -\kappa \frac{\partial(m\nu_\chi^2/k)}{\partial r}, \end{aligned} \tag{2.2}$$

where $M_\chi, \rho_\chi, \nu_\chi$, and L_χ are dark matter mass, density, 1D velocity dispersion, and luminosity profiles, respectively, and they are dynamical variables and evolve with time; M_b is the baryon mass profile in the host galaxy; k is the Boltzmann constant, G is the Newton constant, and D_t denotes the Lagrangian time derivative. Heat conductivity of the dark matter

fluid κ can be expressed as $\kappa = (\kappa_{\rm lmfp}^{-1} + \kappa_{\rm smfp}^{-1})^{-1}$, where $\kappa_{\rm lmfp} \approx 0.27 C \rho_\chi \nu_\chi^3 \sigma k/(Gm^2)$ and $\kappa_{\rm smfp} \approx 2.1 \nu_\chi k/\sigma$ denote conductivity in the long- and short-mean-free-path regimes, respectively, and we set $C \simeq 0.75$ based on calibrations with N-body simulations [22, 23]. In the short-mean-free-path regime, heat conduction can be characterized by the self-interaction mean free path $\lambda = m/\rho_\chi \sigma$ and $Kn = \lambda/H < 1$, where $H = (\nu_\chi^2/4\pi G \rho_\chi)^{1/2}$ is the scale height. In the long-mean-free-path regime, it's characterized by H and $Kn > 1$.

We assume the *initial* halo follows a Navarro-Frenk-White (NFW) profile [24] with r_s and ρ_s as its scale radius and density, respectively. The boundary conditions are $M_\chi = 0$ at $r = 0$, $M_\chi = M_{200}$ and $L_\chi = 0$ at $r = r_{200}$, where M_{200} and r_{200} are the virial halo mass and radius, respectively. We adopt the baryon mass profile $M_b(r) \approx 0.1(4\pi\rho_s r_s^3)(r/r_s)^{0.6}$, based on cosmological hydrodynamical simulations of protogalaxies at $z \sim 17$ [25]; see Appendix A. As an approximation, we assume the baryon mass profile is static and it does not evolve with time. In SIDM, the baryon profile may become more diffuse because of halo core formation [26, 27]. However, if baryon infall occurs early before a large core forms, the distribution can be as compact as the one in the collisionless limit [28, 29]. In addition, since the baryons would further contract as the collapse starts, our approximation could be conservative, see, e.g., [29]. We then recast the fluid equations with dimensionless variables and solve them numerically using the method as in [22, 23]. The fiducial quantities relevant for later discussions are $M_0 = 4\pi\rho_s r_s^3$, $t_0 = 1/\sqrt{4\pi G \rho_s}$ and $(\sigma/m)_0 = 1/(r_s \rho_s)$; hence $M_b(r) = 0.1 M_0 (r/r_s)^{0.6}$. We then map dimensionless outputs from the simulations to physical ones assuming Planck cosmology, i.e., $h = 0.67$, $\Omega_m = 0.315$, and $\Omega_\Lambda = 0.685$ [30].

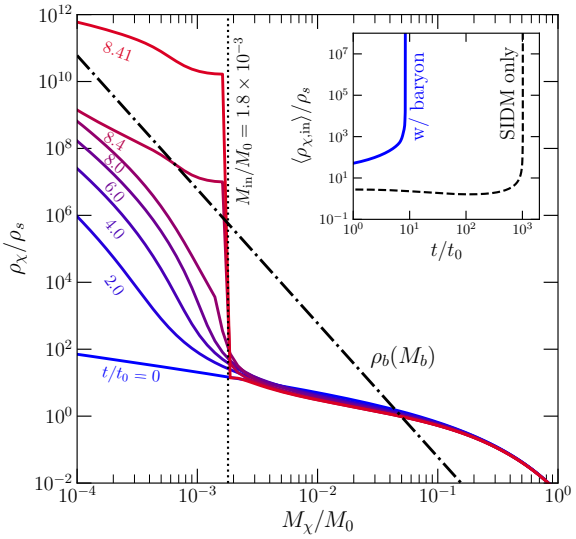

Figure 2.1: Gravothermal evolution of the dark matter density vs. enclosed mass in the presence of the baryonic potential (solid), as well as the fixed baryon profile (dash-dotted). Each dark matter profile is labeled with its corresponding evolution time, and the vertical dotted line indicates the mass of the central halo that would eventually collapse into a seed black hole. The *insert* panel illustrates the evolution of the averaged dark matter density of the central halo with (solid) and without (dashed) including the baryons.

2.2 Roles of baryons

Fig. 2.1 shows the gravothermal evolution of the dark matter density vs. enclosed mass (solid) in the presence of the baryons (dash-dotted), where we fix $(\sigma/m)(r_s\rho_s) = 0.2$. The insert panel illustrates the average inner density vs. evolution time with (solid) and without (dashed) including the baryon mass. The average inner density $\langle\rho_{\chi,{\rm in}}\rangle$ is calculated within the central region where the enclosed mass equals to that of the seed black hole, as we will explain later. With the baryons, the halo does not form a large density core and it quickly evolves into the collapse phase [31, 32]. Its density keeps increasing and eventually becomes super-exponential in the end. The collapse timescale is $t_c = 8.41t_0$, a factor of ~ 100 shorter than the one predicted in the SIDM-only case with the same interaction

strength. We have also considered a Hernquist profile [33] to model the baryon distribution and obtained a similar result if the baryon distribution is compact.

We also see that as the central density increases for $t \gtrsim 8.4t_0$, the enclosed mass for a central region remains almost a constant $M_{\rm in} \approx 1.8 \times 10^{-3} M_0$. This is the region where the halo is in the short-mean-free-path regime. A similar phenomenon also occurs without including the baryons [19]. For the SIDM-only case we consider, the corresponding $M_{\rm in}/M_0$ value is 4.2×10^{-2}, which is larger than the one with the baryons. As the halo evolves further, the density continues increasing and the central halo ($Kn \lesssim 1$) would eventually collapse into a singular state, a seed black hole. We assume the seed mass $M_{\rm seed} = M_{\rm in}$, suggested by numerical studies of collapsed massive stars [34].

2.3 Seeding supermassive black holes

To explain the origin of high-z SMBHs, the initial halo must be sufficiently heavy *and* collapse fast enough. We first check the scaling relations $M_{\rm in} \propto M_0 \propto M_{200}$, and $t_{\rm c} \propto r_s^{-1} \rho_s^{-3/2} \propto M_{200}^{-1/3} c_{200}^{-7/2} (1+z)^{-7/2}$ [23], where $c_{200} = r_{200}/r_s$ is the halo concentration. Apparently, t_c is very sensitive to c_{200}. There is a tight correlation between c_{200} and M_{200} for halos at $z \lesssim 5$, but the c_{200} distribution at higher redshifts is less known. There is a trend that c_{200} gradually becomes independent of M_{200} and its median asymptote to $c_{200} \sim 3$ at $z \sim 5$–10 [35, 36]. We fix $c_{200} = 3$, and leave with two parameters M_{200} and z to vary.

Fig. 2.2 shows benchmarks (red) that could explain the origin of the SMBHs J1205-0000 with the Eddington ratio $f_{\rm Edd} = 0.16$ [9] (upper panel) and J1007+2115 with

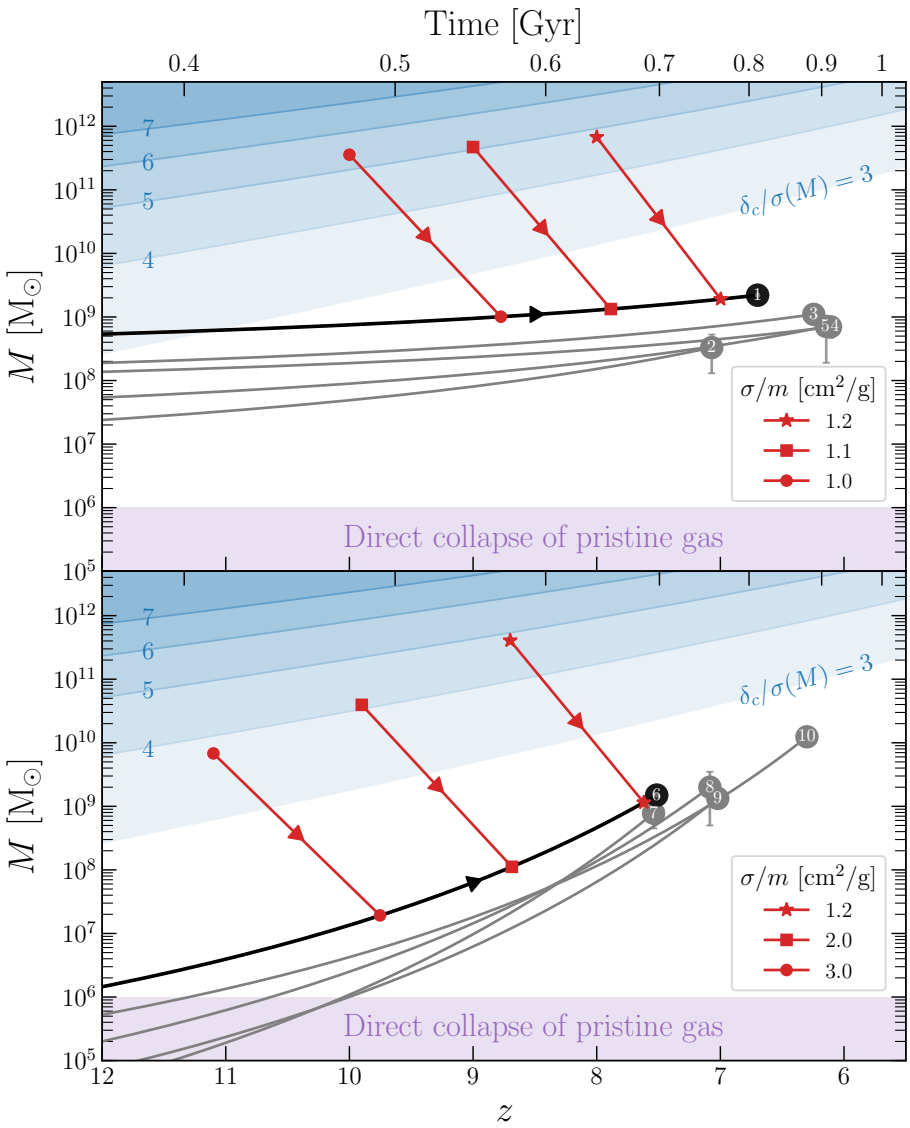

Figure 2.2: SIDM benchmarks (red) that could explain the origin of the SMBHs J1205-0000 (labeled as "1", upper panel) and J1007+2115 ("6", lower panel) with an observed Eddington growth rate of $f_{\rm Edd} = 0.16$ and 1.06, respectively. Other samples can be found in Appendix D. The black curves indicate their Eddington accretion history. For each red arrow, the markers on higher and lower z end denote initial halo and seed masses, respectively, and the horizontal difference between the two ends indicates the timescale of gravothermal collapse. The blue shaded regions indicate the ratio of the critical density fluctuation to the halo mass variance. The magenta bands denote the mass range of the seed produced via the direct collapse of pristine gas. The gray curves are Eddington growth history of other high-z SMBHs with $f_{\rm Edd} \sim 0.1$ (upper) and ~ 1 (lower).

$f_{\rm Edd} = 1.06$ [5] (lower panel). The black curves indicate their Eddington accretion history reconstructed using Eq. 2.1. For reference, the gray ones denote the accretion history of other high-z SMBHs with $f_{\rm Edd} \sim 0.1$ (upper) [9, 10] and those $f_{\rm Edd} \sim 1$ (lower) [5, 37, 38, 39, 40]. We have checked all of them (gray) could also be explained within our scenario. The direct collapse of pristine gas could provide massive enough seeds (magenta) for the SMBHs with $f_{\rm Edd} \sim 1$, but not those with $f_{\rm Edd} \sim 0.1$ [9].

As the redshift of the initial halo increases, the favored halo mass becomes smaller, because the seed black hole has more time to grow. To explain the origin of the SMBHs with $f_{\rm Edd} \sim 1$, the mass is in a range of $M_{200} \sim 10^9$–$10^{11}\,{\rm M}_\odot$ for $z \sim 11$–9. For those with $f_{\rm Edd} \sim 0.1$, M_{200} needs to be relatively higher, $\sim 10^{11}$–$10^{12}\,{\rm M}_\odot$, as their growth rate is much smaller and a heavier seed is required. We have checked that the overall trend holds for halos with $z \gtrsim 11$.

As an example, we take the case with $(M_{200}/{\rm M}_\odot, z) = (6.8 \times 10^{11}, 8)$ that seeds J1205-0000, the most challenging SMBH, to demonstrate our derivation. For the halo, $\rho_s \approx 8.1 \times 10^7\,{\rm M}_\odot/{\rm kpc}^3$ and $r_s \approx 10$ kpc. Hence the fiducial parameters are $t_0 = 15$ Myr, $M_0 = 1.1 \times 10^{12}\,{\rm M}_\odot$ and $(\sigma/m)_0 = 5.8\ {\rm cm}^2/{\rm g}$. The seed mass is $M_{\rm in} = 1.8 \times 10^{-3} M_0 \approx 1.9 \times 10^9\,{\rm M}_\odot$ and the collapse time $t_c = 8.4 t_0 \approx 126$ Myr, and the self-scattering cross section $\sigma/m \approx 1.2\ {\rm cm}^2/{\rm g}$. Since $z = 8$ is equivalent to $t = 642$ Myr after the Big Bang, the seed forms at 766 Myr ($z = 7$). For an SIDM-only halo with the same parameters, we find $t_c \approx 10^3 t_0 \approx 15$ Gyr, too long to form a seed.

To speed up the collapse process in the absence of the baryonic influence, one would need to take much larger σ/m and c_{200} [22], or consider dissipative self-interactions [41,

23, 42]. For comparison, our scenario predicts $\sigma/m \sim 1$ cm^2/g within a minimal elastic SIDM model that has been shown to explain dark matter distributions in the spirals [43], Milky Way satellites [44], and dark-matter-deficient galaxies [45]. It's important to note dwarf galaxies at present that favor a large density core are those with diffuse baryon distributions [46]. Thus their host SIDM halos would still be in the core-expansion phase and a shallow density profile is expected.

2.4 Density fluctuations

For the benchmark cases, the halo mass is in the range of 10^9–$10^{12}\,\mathrm{M}_\odot$ for $z \sim 11$–8. We use the standard Press-Schechter formalism [47] to examine conditions for realizing those halos in the early Universe. The halo mass function scales as $dn(M,z)/dM \propto \exp\left[-\delta_c^2(z)/2\sigma^2(M)\right]$ [48], where $\delta_c(z)$ is the critical density fluctuation at z and $\sigma(M)$ the mass variance. We shaded the regions with various values of $\delta_c(z)/\sigma(M)$ in Fig. 2.2 (blue). As expected, the halo mass increases as the density fluctuation increases and more massive halos form at later times.

The halos for seeding the SMBHs with a sub-Eddington (Eddington) accretion rate correspond to $\delta_c(z)/\sigma(M) \sim 4$–$6$ (3–5). In addition, the baryon concentration of host galaxies needs to be high as well such that the gravothermal collapse could occur fast enough. Thus our scenario predicts that high-z SMBHs should be rare. Indeed, observations show they are extremely rare in the Universe. Quasar surveys indicate that the number density of luminous ($L_{\rm AGN} \gtrsim 10^{46}\,\mathrm{erg/s}$) high-$z$ SMBHs with $M_{\rm BH} \sim 10^9\,\mathrm{M}_\odot$ is $\lesssim 10^{-7}$ Mpc^{-3} [49, 1, 50]. The ratio of their mass to the dynamical (gas+stars) mass is

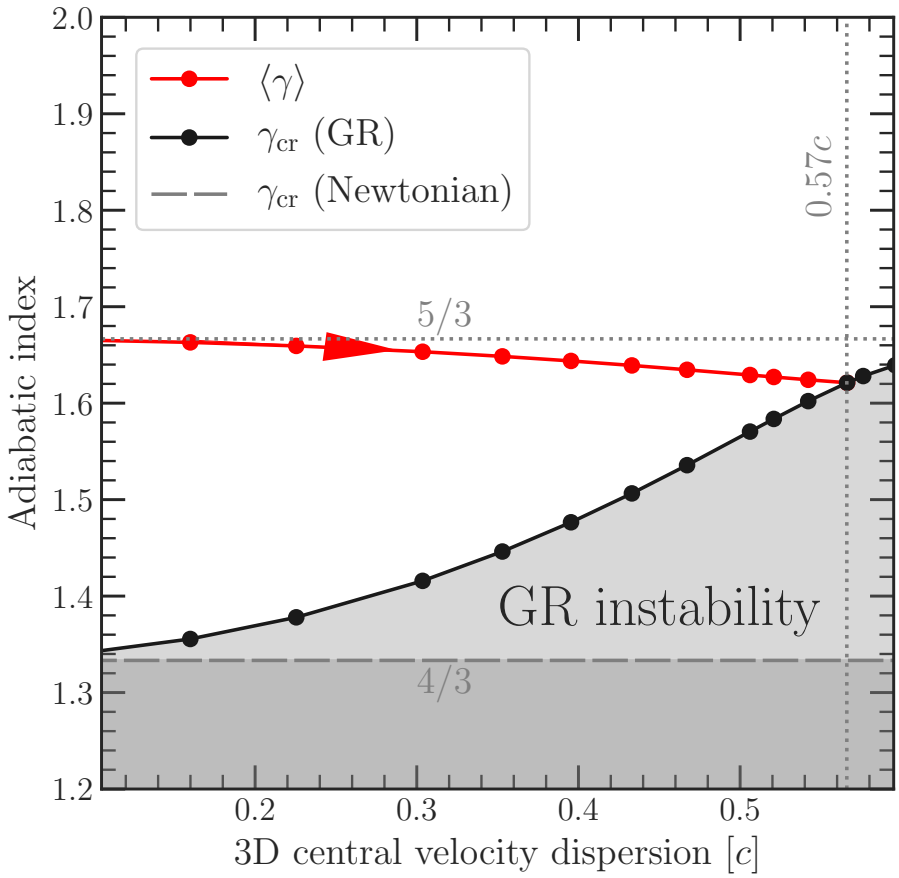

Figure 2.3: The pressure-averaged adiabatic index $\langle\gamma\rangle$ (red) and the critical index $\gamma_{\rm cr}$ (black) vs. the central 3D velocity dispersion for each GR configuration (dot). When $\langle\gamma\rangle < \gamma_{\rm cr}$, the system triggers the GR instability. In the Newtonian limit, $\langle\gamma\rangle = 5/3$ for a monatomic ideal gas, and the instability condition is $\langle\gamma\rangle < 4/3$.

$M_{\rm BH}/M_{\rm b} \sim 1/100$–$1/30$ [50]. Taking $M_{\rm b}/M_{200} \sim 0.2$, we find $M_{\rm BH}/M_{200} \sim (2\text{–}7) \times 10^{-3}$, broadly consistent with our prediction. We also note that baryon infall can occur for a halo heavier than $5 \times 10^3 [(1+z)/10]^{1.5}\,{\rm M}_\odot$ [48], and all of the benchmarks satisfy this condition easily.

2.5 Angular momentum

The angular momentum remnant of the inner halo could counter gravity and even slow down the gravothermal collapse. Besides, there is an upper limit on the specific angular momentum of a black hole, $J_{\rm BH}/M_{\rm BH} \leq (G/c)M_{\rm BH} \approx 1.4\times10^{-4}(M_{\rm BH}/10^7\,{\rm M}_\odot)$ kpc $\cdot$ km/s [51]. Consider the benchmark with $(M_{200}/{\rm M}_\odot, z) = (6.8\times10^{11}, 8)$ again, dark matter particles within the radius $r_{\rm in} = 0.063 r_s \approx 0.63$ kpc of the initial NFW halo would collapse to a seed, where the total enclosed mass is $M_{\rm in}$. We find $J_\chi/M_{\rm in} \approx 8$ kpc $\cdot$ km/s for the halo within $r_{\rm in}$, based on a universal fitting formula [52]. This is a factor of 100 larger than the allowed value for a $10^9\,{\rm M}_\odot$ seed.

Fortunately, dark matter self-interactions that lead to heat conductivity also induce viscosity, which dissipates the angular momentum remnant. In the long-mean-free-path regime, we find it decays as

$$J_\chi^f \approx J_\chi^i \exp\left[-\frac{20}{\sqrt{27\pi}}\int dt\,\frac{\rho_\chi(\sigma/m)\nu_\chi^3 r_{\rm in}}{GM_\chi}\right], \tag{2.3}$$

where J_χ^i and J_χ^f are the initial and final angular momenta of the central halo within $r_{\rm in}$, respectively; see Appendix C for the derivation. For the benchmark, we have $r_{\rm in} = 0.063 r_s$, $M_\chi = M_{\rm in} = 1.8\times10^{-3}M_0$, $\rho_\chi(r_{\rm in}) = 14\rho_s$, $\sigma/m = 0.2/(r_s\rho_s)$ and $\nu_\chi(r_{\rm in}) \approx 0.48\sqrt{4\pi G\rho_s}r_s$. We find the timescale for achieving $J_\chi^f \sim 10^{-2}J_\chi^i$ is $\Delta t \approx 0.2t_0$, much shorter than that of gravothermal collapse $t_c = 8.4t_0$. We have checked that the other five benchmarks in Fig. 2.2 satisfy the dissipation condition. In SIDM, viscosity and conductivity share the same microscopic nature, and both effects are critical for seeding the SMBHs in our scenario.

2.6 Relativistic instability

As the central density increases, the velocity dispersion of the collapsed central region increases as well [19], and it would eventually approach the relativistic limit. To see the fate of the central halo where $Kn \lesssim 1$, we examine conditions for reaching GR instability. Motived by early studies on globular cluster systems [53, 54], we assume that the number density of SIDM particles in the central halo at late stages follow a truncated Maxwell-Boltzmann distribution

$$dn(r) \propto \begin{cases} (e^{-\epsilon/kT} - e^{-\epsilon_c/kT}) d^3p(\epsilon) & (\epsilon \leq \epsilon_c) \\ 0 & (\epsilon > \epsilon_c), \end{cases} \tag{2.4}$$

where T, ϵ, and p are temperature, energy, and momentum; respectively; $\epsilon_{\rm c}$ is the cutoff energy, above which the particle escapes to the boundary. Given the distribution in Eq. 2.4, we use the method in [54] and solve the Tolman-Oppenheimer-Volkoff equation to find density and pressure profiles for the collapsed central region, where we impose the boundary condition $kT = 0.1mc^2$. For each configuration, we follow Chandrasekhar's criterion [55], and calculate the critical adiabatic index $\gamma_{\rm cr}$ and the pressure-averaged adiabatic index $\langle\gamma\rangle$. The sufficient condition for the system to collapse into a black hole is $\langle\gamma\rangle < \gamma_{\rm cr}$. We will discuss technical details in a companion paper [56] (also in Appendix E and Chapter 3).

Fig. 2.3 shows the averaged adiabatic index $\langle\gamma\rangle$ (red) and the critical index $\gamma_{\rm cr}$ (black) vs. 3D velocity dispersion at the center for each configuration denoted as a dot. As the velocity dispersion increases, its averaged index $\langle\gamma\rangle$ gradually decreases from its non-relativistic limit for monatomic ideal gas 5/3 towards the ultra-relativistic limit 4/3.

In contrast, the critical index $\gamma_{\rm cr}$ increases from the Newtonian limit 4/3 [57]. This is because as the pressure starts to dominate the energy density towards the GR limit, it destabilizes the system instead. The relativistic instability occurs when the 3D central velocity dispersion approaches $0.57c$ and $\langle\gamma\rangle = \gamma_{\rm cr} \approx 1.62$, at which the corresponding fractional binding energy is 0.033.

2.7 Conclusions

We have presented a scenario that could explain the origin of high-z SMBHs with Eddington *and* sub-Eddington accretion rates. The presence of baryons in protogalaxies could deepen the gravitational potential and expedite the gravothermal collapse of an SIDM halo. The favored self-scattering cross section is broadly consistent with the one used to explain diverse dark matter distributions of galaxies. In this scenario, dark matter self-interactions induce viscosity that dissipates the angular momentum remnant of the central halo. The initial halo must be on high tails of density fluctuations, which may explain why high-z SMBHs are extremely rare in observations. We also checked that the GR instability condition can be satisfied. The upcoming and future facilities are expected to search for quasars with a wide range of luminosities [50]. The observations would provide a more complete picture of populations of high-z SMBHs and further test our scenario.

Chapter 3

Dynamical Instability of Collapsed Dark Matter Halos

The study of dynamical instability of a self-gravitating system and its collapse to a black hole has a long history [55, 58]. Early work analyzed the evolution of stellar clusters in general relativity and examined conditions for their relativistic instability with linear perturbation theory [59, 60, 61]. The techniques and tools of numerical relativity and N-body simulations were further developed in [62, 63, 64], which can be used to trace full evolution in the nonlinear regime.

Recently, we proposed a scenario to explain the origin of supermassive black holes in the early universe [65]; see also [22, 41, 66]. This is based on the mechanism that a self-interacting dark matter halo can experience gravothermal collapse. Dark matter self-interactions can thermalize the inner halo over cosmological timescales [11, 14, 15, 16, 67, 12, 68, 69]; see [13] for a review. As a self-gravitating system with a finite size, the halo

has negative heat capacity, and the self-interactions transport heat from the central region at late stages of the evolution, resulting in a core with an ultrahigh density [19, 21, 23, 42]. The core can further contact and collapse into a seed black hole [20], which would grow into a supermassive one by accreting baryonic matter. We used a semi-analytical method and derived the condition for triggering dynamical instability of the core. Following Chandrasekhar's criterion [55], i.e., requiring the pressure averaged adiabatic index of the gravothermal system to be less than its critical adiabatic index, we found the instability occurs when the 3D central velocity dispersion of dark matter particles reaches $\sim 0.57c$ at which the adiabatic index is 1.62.

In this chapter, we systematically study the dynamical instability of a collapsed halo. We use a truncated Maxwell-Boltzmann distribution to model the dark matter distribution near the relativistic limit. This is well motivated, as the self-interactions thermalize dark matter particles. In addition, the core is gravitationally bound and particles with a sufficiently high velocity can evaporate and escape from the gravitational pull of the core. We then implement the distribution with the Tolman-Oppenheimer-Volkoff equation [70, 71] and find a series of equilibrium solutions. For each of them, we evaluate its thermal dynamical properties and test its instability. Besides the Chandrasekhar's criterion, we will use the turning-point method [72, 73, 74] to examine instability conditions based on considerations of total energy, binding energy, and fractional binding energy, as illustrated in Fig. 3.1 schematically.

We will compare our numerical results to those from relativistic N-body simulations [63] and show that the agreement is excellent, i.e., they all indicate that the system

can collapse into a black hole when the fractional binding energy reaches 0.035 with a central gravitational redshift of 0.5. Thus the method developed in this work may have broad applications as it is computationally inexpensive. We will further study conditions for the classical Maxwell-Boltzmann distribution to be valid, and discuss their implications for constraining models proposed to explain the origin of supermassive black holes via the gravothermal collapse of dark matter halos. In particular, we show that although the presence of dissipative interactions could help speed up the gravothermal evolution of a halo, they may make it difficult for the core to eventually collapse into a black hole because of energy loss.

The chapter is organized as follows: We present the classical truncated Maxwell-Boltzmann distribution and its Tolman-Oppenheimer-Volkoff equation in Sec. 3.1. We discuss instability conditions and numerical results in Sec. 3.2. We study conditions for the classical distribution to be valid and constraints on dark matter models in Sec. 3.3, discuss connections with the nonrelativistic fluid model in Sec. 3.4, and conclude in Sec. 3.5.

3.1 The truncated Maxwell-Boltzmann model

We treat the high-density central region of a collapsed SIDM halo as a gravitationally bound system. Since dark matter particles with sufficiently high energies will evaporate and move to the outer envelope, it is natural to introduce a distribution function with an energy cutoff to model the system. In this work, we take a truncated Maxwell-Boltzmann distribution, based on Michie-King models [75, 76]. Consider the following general form [77, 54]

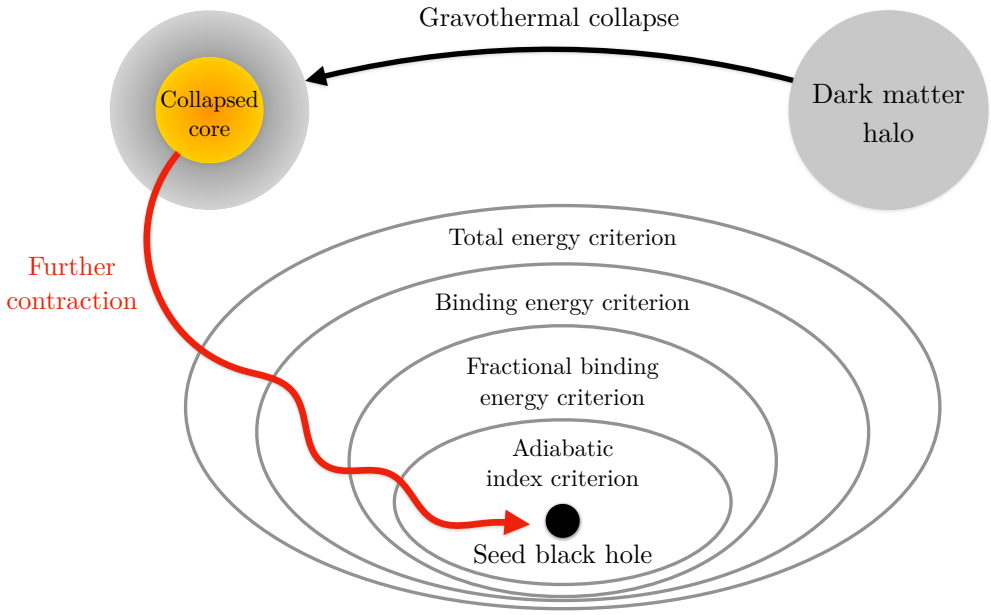

Figure 3.1: Schematic illustration of the formation of a seed black hole via the gravothermal collapse of a self-interacting dark matter halo. At late stages of gravothermal evolution, the halo can be divided into two regimes, i.e., a collapsed central core with an ultrahigh density (orange) and a cuspy outer envelope (gray). As it further contracts, the total mass of the collapsed core remains almost constant. The elliptical circles denote the sequence of dynamical instability conditions when the core collapses into a seed black hole.

$$f(\epsilon \leq \epsilon_c) = \frac{1 - e^{(\epsilon-\epsilon_c)/k_BT}}{e^{(\epsilon-\mu)/k_BT} - \eta}, \quad f(\epsilon > \epsilon_c) = 0, \tag{3.1}$$

where ϵ is the kinetic energy, ϵ_c the cutoff energy, T the temperature and μ the chemical potential. And they are a function of radius. The number factor η is $+1$ and -1 for bosons and fermions, respectively, and k_B is the Boltzmann constant. Note $\epsilon = \sqrt{|\mathbf{p}|^2c^2 + m^2c^4} - mc^2$, where $|\mathbf{p}|$ is the momentum and m the mass of dark matter particles, and we have subtracted the rest mass in defining μ. For a dilute gas of classical particles, $\epsilon - \mu \gg k_BT$, the distribution function reduces to the truncated Maxwell-Boltzmann form

$$f(\epsilon \leq \epsilon_c) = e^{\mu/k_BT}(e^{-\epsilon/k_BT} - e^{-\epsilon_c/k_BT}), \quad f(\epsilon > \epsilon_c) = 0. \tag{3.2}$$

We introduce the following dimensionless variables [78], $w(r) \equiv \epsilon_c(r)/k_BT(r)$, $\alpha(r) \equiv \mu(r)/k_BT(r)$, and $b \equiv k_BT(R)/mc^2$, where R is the boundary radius of the system. Following the Tolman-Klein law [79, 80] for a gravothermal system, we have the relation $w(r) = \alpha(r) - \alpha(R)$. The temperature at a given radius is related to the one at $r = R$ as $T(r) = T(R)/[1 - bw(r)]$. It indicates that the system does not follow an isothermal distribution globally in general relativity, although it can be achieved locally.

Given the distribution function, one can readily derive the equation of state and express the number density n, energy density ρ, thermal energy density u, and pressure p as

$$\begin{aligned} n(r) =& 4\sqrt{2}\pi g m^3 (c^3/h^3) e^{\alpha(R)} I_n(b, w), \\ \rho(r) =& 4\sqrt{2}\pi g m^4 (c^3/h^3) e^{\alpha(R)} I_\rho(b, w), \\ u(r) =& 4\sqrt{2}\pi g m^4 (c^5/h^3) e^{\alpha(R)} I_u(b, w), \\ p(r) =& (8/3)\sqrt{2}\pi g m^4 (c^5/h^3) e^{\alpha(R)} I_p(b, w), \end{aligned} \tag{3.3}$$

respectively, where $g = 2s + 1$ is the spin multiplicity of dark matter particles, h the Planck constant as a normalization factor, and c the speed of light; the $I(b, w)$ functions stand for integrals of [54]

$$\begin{aligned} I_n(b, w) \equiv& \left(\frac{b}{1-bw}\right)^{3/2} \int_0^w (e^{w-x} - 1) \left(1 + \frac{bx/2}{1-bw}\right)^{1/2} \left(1 + \frac{bx}{1-bw}\right) x^{1/2} \mathrm{d}x, \\ I_\rho(b, w) \equiv& \left(\frac{b}{1-bw}\right)^{3/2} \int_0^w (e^{w-x} - 1) \left(1 + \frac{bx/2}{1-bw}\right)^{1/2} \left(1 + \frac{bx}{1-bw}\right)^2 x^{1/2} \mathrm{d}x, \\ I_u(b, w) \equiv& \left(\frac{b}{1-bw}\right)^{5/2} \int_0^w (e^{w-x} - 1) \left(1 + \frac{bx/2}{1-bw}\right)^{1/2} \left(1 + \frac{bx}{1-bw}\right) x^{3/2} \mathrm{d}x, \\ I_p(b, w) \equiv& \left(\frac{b}{1-bw}\right)^{5/2} \int_0^w (e^{w-x} - 1) \left(1 + \frac{bx/2}{1-bw}\right)^{3/2} x^{3/2} \mathrm{d}x. \end{aligned} \tag{3.4}$$

For the model we consider, the Tolman-Oppenheimer-Volkoff equation can be written as

$$\frac{\mathrm{d}M}{\mathrm{d}r} = 4\pi r^2 \rho, \quad \frac{\mathrm{d}w}{\mathrm{d}r} = -\frac{G}{rc^2}\left(\frac{1-bw}{b}\right)\frac{4\pi p r^3 + Mc^2}{rc^2 - 2GM}, \tag{3.5}$$

where G is the Newton constant, $M(r)$ is the enclosed mass at radius r, and $\rho(r)$ the density. We impose the following boundary conditions: $M = 0$ and $w = w(0)$ at $r = 0$; $M = M(R)$ and $w = 0$ at $r = R$. To further simplify the calculation, we introduce a fiducial length scale defined as [54]

$$\zeta = \lambda_{\mathrm{C}}\left(\frac{m_{\mathrm{Pl}}}{m}\right)\left(\frac{8\pi^3}{g e^{\alpha(R)}}\right)^{1/2} \quad \text{with} \quad r = \zeta\hat{r}, \tag{3.6}$$

where $m_{\mathrm{Pl}} = (\hbar c/G)^{1/2}$ is the Planck mass and $\lambda_{\mathrm{C}} = \hbar/mc$ the Compton wavelength of the particle. With the fiducial length, we can express thermal dynamical quantities of the system using their corresponding dimensionless counterpart denoted with a "hat" as $n = (c^2/Gm\zeta^2)\hat{n}$, $\rho = (c^2/G\zeta^2)\hat{\rho}$, $u = (c^4/G\zeta^2)\hat{u}$, $p = (c^4/G\zeta^2)\hat{p}$ and $M = (c^2\zeta/G)\hat{M}$, and uniquely determine their profiles for a given set of b and $w(0)$.

To trigger the onset of dynamical instability, the system needs to be in the relativistic limit. This requirement puts constraints on b and $w(0)$. It is useful to consider the product of b and $w(r)$, the normalized cutoff energy

$$bw(r) = \frac{\epsilon_c(r)/mc^2}{1 + \epsilon_c(r)/mc^2}, \tag{3.7}$$

where we have used the relation $T(r) = \left[1 + \epsilon_c(r)/mc^2\right] T(R)$. In the ultrarelativistic limit

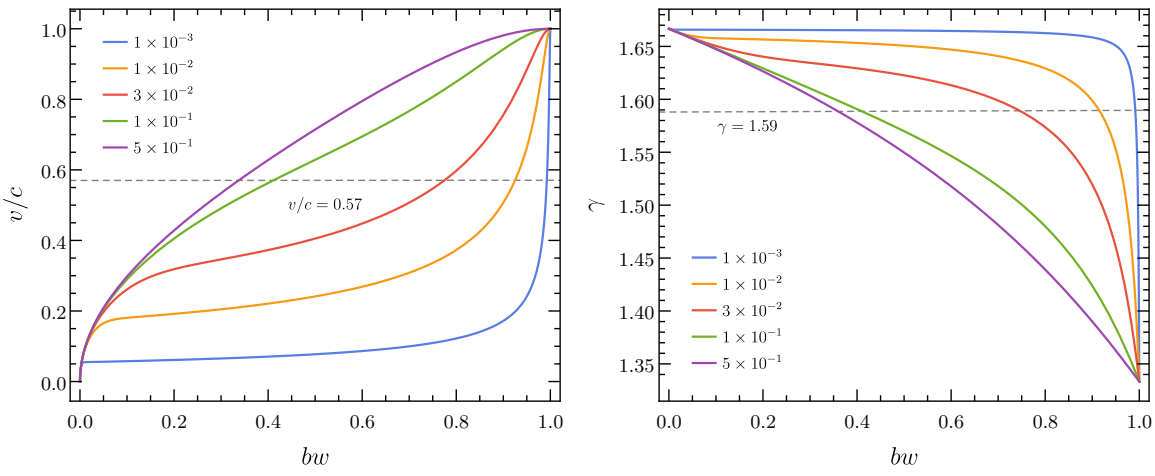

Figure 3.2: 3D velocity dispersion (left) and adiabatic index γ (right) vs. normalized cutoff energy $bw = \epsilon_c/(mc^2 + \epsilon_c)$ for $b = k_BT(R)/mc^2 = (0.5,\ 0.1,\ 0.03,\ 0.01,\ 0.001)$. The dashed horizontal lines denote $v/c = 0.57$ (left) and $\gamma = 1.59$ (right), at which the system approaches the relativistic regime and dynamical instability may occur.

$\epsilon_c \gg mc^2$, $bw \to 1$. In the opposite limit, $bw \to 0$. Since $b = k_BT(R)/mc^2$ determines the temperature at the core boundary, a higher b value indicates a hotter thermal bath. $w(r)$ is related to the cutoff energy as $w(r) = \epsilon_c(r)/k_BT(r)$. For $w \gg 1$, the distribution reduces to the usual Maxwell-Boltzmann form without a truncation, as indicated in equation (3.2).

The 3D velocity dispersion $v(r) \equiv \sqrt{3p/\rho} = c\sqrt{2I_p(b,w)/I_\rho(b,w)}$ also characterizes the relativistic extent of the system. In [65], we showed that when $v(0)$ approaches $0.57c$, dynamical instability can be triggered. In addition, the adiabatic index of the system

$$\gamma(r) = 1 + \frac{p}{u} = 1 + \frac{2}{3}\frac{I_p(b,w)}{I_u(b,w)} \tag{3.8}$$

approaches 4/3 and 5/3 in ultra- and nonrelativistic limits, respectively; see Appendix E.1 for detailed derivation.

To gain insight into instability conditions, we first use Eqs. (3.3) and (3.4), and find the radially independent equation of state without imposing constraints from Eq. (3.5). We choose $b = 0.001,\ 0.01,\ 0.03,\ 0.1$, and 0.5 and evaluate v and γ as a function of bw, as shown in the left and right panels of Fig. 3.2, respectively. We see that it is easier to reach the relativistic limit if b is higher, i.e., a hotter thermal bath. For $b = 0.5$, $bw \sim 0.3$ for achieving $v \sim 0.57c$ at which $\gamma \sim 1.59$. But when b decreases to 10^{-3}, bw needs to be close to 1. For the latter case, both v and γ are hardly changed over the wide range of bw. For low b, the equation of state is stiff, indicating that the system is hard to compress and reach instability. The results shown in Fig. 3.2 provide guidance in choosing boundary conditions as we discuss further in the next section.

3.2 Dynamical instability

The instability of a self-gravitating spherical system sets in when the gravitational energy becomes comparable to its mass energy, $GM^2/R \sim Mc^2$, where M and R are the total mass and characteristic radius, respectively. To be more quantitative, one often considers the compactness of a system calculated as $C = GM/c^2R$ [57]. For a typical neutron star, $M \sim 2\ \mathrm{M}_\odot$ and $R \sim 12$ km, we have $C \sim 0.25$. For a $M \sim 10^9\ \mathrm{M}_\odot$ black hole, $R \sim 2GM/c^2 \sim 3 \times 10^9$ km and $C \sim 0.5$. Its average density is $\sim 6 \times 10^2$ kg/m^3, lower than the water density. As we will discuss later, for a gaseous sphere with $M \sim 10^9\ \mathrm{M}_\odot$, $C \sim 0.04$ when the instability is triggered. Overall, the heavier the system, the easier for it to collapse.

3.2.1 The adiabatic index

A more concrete way to determine the system's instability is by checking its adiabatic index. Chandrasekhar first derived the instability conditions for a spherical system in the context of general relativity [55]. Consider the background metric $\mathrm{d}s^2 = g_{\alpha\beta}\mathrm{d}x^\alpha \mathrm{d}x^\beta = -e^{2\Phi(r)}c^2\mathrm{d}t^2 + e^{2\Lambda(r)}\mathrm{d}r^2 + r^2\mathrm{d}\Omega$, where $\Phi(r)$ and $\Lambda(r)$ satisfy the following conditions

$$e^{2\Phi(r)} = \exp\left(\int_r^\infty \frac{4p(r')r'^3 + M(r')c^2}{r'(r'c^2) - 2GM(r')}\mathrm{d}r'\right),\ e^{2\Lambda(r)} = \left(1 - \frac{2GM(r)}{c^2 r}\right)^{-1}. \tag{3.9}$$

The pulsation equation of a perfect fluid is given by [55]

$$\begin{aligned}\omega^2 e^{2(\Lambda-\Phi)}\left(\rho + \frac{p}{c^2}\right)\xi = \frac{4}{r}\frac{\mathrm{d}p}{\mathrm{d}r}\xi - e^{-(2\Phi+\Lambda)}\frac{\mathrm{d}}{\mathrm{d}r}\left[e^{3\Phi+\Lambda}\frac{\gamma p}{r^2}\frac{\mathrm{d}(r^2 e^{-\Phi}\xi)}{\mathrm{d}r}\right] \\ + \frac{8\pi G}{c^2}e^{2\Lambda}p\left(\rho + \frac{p}{c^2}\right)\xi - \frac{1}{\rho c^2 + p}\left(\frac{\mathrm{d}p}{\mathrm{d}r}\right)^2\xi,\end{aligned} \tag{3.10}$$

where ξ is the Lagrangian displacement and ω is its corresponding oscillation frequency. If $\omega^2 < 0$, the Lagrangian displacement ξ receives unbounded growth and the self-gravitating system becomes unstable. The boundary conditions for Eq. (3.10) are $\xi(0) = 0$ and $p(R) = 0$.

Choosing the Lagrangian displacement $\xi = re^{\Phi}$ that satisfies the boundary conditions, one can show that the system becomes unstable if the pressure-averaged adiabatic index $\langle\gamma\rangle$ is less than the critical adiabatic index γ_{cr}

$$\langle\gamma\rangle \equiv \frac{\int_0^R \gamma e^{3\Phi+\Lambda}p\mathrm{d}^3 r}{\int_0^R e^{3\Phi+\Lambda}p\mathrm{d}^3 r} < \gamma_{\mathrm{cr}}, \tag{3.11}$$

where

$$\gamma_{\rm cr} \equiv \frac{4}{3} + \frac{1}{36}\frac{\int_0^R e^{3\Phi+\Lambda}[16p + (e^{2\Lambda}-1)(\rho c^2+p)](e^{2\Lambda}-1)r^2{\rm d}r}{\int_0^R e^{3\Phi+\Lambda}pr^2{\rm d}r} \tag{3.12}$$
$$+ \frac{4\pi G}{9c^2}\frac{\int_0^R e^{3(\Phi+\Lambda)}[8p + (e^{2\Lambda}+1)(\rho c^2+p)]pr^4{\rm d}r}{\int_0^R e^{3\Phi+\Lambda}pr^2{\rm d}r} + \frac{16\pi^2G^2}{9c^4}\frac{\int_0^R e^{3\Phi+5\Lambda}(\rho c^2+p)p^2r^6{\rm d}r}{\int_0^R e^{3\Phi+\Lambda}pr^2{\rm d}r};$$

see Appendix E.2. The choice of ξ is not unique, but the result is not sensitive to the particular form of ξ as long as the boundary conditions are satisfied [55]. In the limit $\rho \gg p/c^2$ and $\Phi, \Lambda \to 0$, the pulsation equation (3.10) reduces to its Newtonian form and $\gamma_{\rm cr} = 4/3$; see Appendix E.3 for a heuristic derivation in the Newtonian limit. For a monatomic ideal gas, $4/3 < \langle\gamma\rangle < 5/3$ [81, 82, 57]. Thus the instability could hardly occur in the context of Newtonian gravity. On the other hand, in general relativity $\gamma_{\rm cr}$ increases due to relativistic corrections, which are $\mathcal{O}(p/\rho c^2)$. As a result, the spherical system can reach the dynamical instability condition $\langle\gamma\rangle < \gamma_{\rm cr}$ before the particles become ultrarelativistic, i.e., $\langle\gamma\rangle \to 4/3$ as $p \to \rho c^2/3$.

3.2.2 The turning-point method

Aside from the instability condition based on the adiabatic index, we will also use the turning-point method [72, 73, 74] and show the former could be conservative, i.e., dynamical instability could occur before the condition shown in Eq. (3.11) is satisfied. Once the boundary temperature parameter b is fixed, the equation of state only depends on one parameter, i.e., the central energy cutoff $w(0)$. We can define an energy functional S as a function of those two variables,

$$S = S\left[b, w(0)\right]. \tag{3.13}$$

The turning-point ansatz [74] states, for a fixed b value, the marginally stable configuration reaches at

$$\left.\frac{\partial S}{\partial w(0)}\right|_b = 0 \tag{3.14}$$

This tuning point separates the stable and unstable branches along the one parameter sequence of $w(0)$. The turning-point method has been applied to study various stellar systems [83, 84, 85, 86] and gaseous spheres [87, 88]. Our application is similar to those to a rotating relativistic star [85] with its angular momentum being replaced by b in our model.

We consider $S = \{E,\ B,\ \varepsilon\}$, where E, B, ε are total energy, binding energy, fractional binding energy, respectively. The total energy $E = Mc^2$ is associated with the Schwarzschild mass M of the sphere, the binding energy $B = E_{\rm rest} - E$, and $E_{\rm rest}$ is the total rest energy calculated as [82]

$$E_{\rm rest} = \int_0^R mn(r)c^2 \left(1 - \frac{2GM(r)}{rc^2}\right)^{-1/2} {\rm d}^3 r. \tag{3.15}$$

The fractional binding energy is $\varepsilon = B/E_{\rm rest}$. It is easy to see that the internal energy of the system $E - E_{\rm rest} = -B$ can be written as the sum of kinetic and potential energies,

$$E - E_{\rm rest} = \int_0^R \left[1 - \frac{2GM(r)}{rc^2}\right]^{-1/2} u(r){\rm d}^3 r + \int_0^R \left[1 - \left(1 - \frac{2GM(r)}{rc^2}\right)^{-1/2}\right] \rho(r)c^2 {\rm d}^3 r, \tag{3.16}$$

respectively, where $u = (\rho - mn)c^2$. We will find the parameter regions that satisfy $\partial S/\partial w(0)|_b = 0$ for $S = E,\ B$ and ε, respectively. The corresponding turning points separate the stable and unstable branches of the sequence, and delineate various extents of instabilities. We again convert E, $E_{\rm rest}$, and B into dimensionless quantities $\hat{E} = (G/c^4\zeta)E = \hat{M}$,

$\hat{E}_{\rm rest} = (G/c^4\zeta)E_{\rm rest}$ and $\hat{B} = (G/c^4\zeta)B$. We will also use the interior redshift

$$Z(r) = e^{-\Phi(r)} - 1 = \left(1 + \frac{\epsilon_c(r)}{mc^2}\right)\left(1 - \frac{2GM(R)}{c^2R}\right)^{-1/2} - 1 \tag{3.17}$$

to indicate the relativistic extent of the system. Either high ϵ_c or high compactness $GM(R)/c^2R$ will lead to high interior redshift, though they are interrelated.

3.2.3 Numerical results

We use the fourth-order Runge-Kutta algorithm [89] to solve the Tolman-Oppenheimer-Volkoff equation (3.5), together with Eq. (3.4), assuming the two input parameters $b = k_BT(R)/mc^2$ and $w(0) = \epsilon_c(0)/k_BT(0)$. The algorithm is robust and well-suited to solve implicit differential equations, especially when they are stiff as in our case. Given the results shown in Fig. 3.2, we choose $b = \{0.1, 0.2, 0.3, 0.5\}$. For each fixed b value, we scan over the central energy cutoff $w(0)$ and find corresponding equilibrium configurations. We then evaluate their thermal quantities and examine their stability conditions. We collect our numerical results in Table G.1, Appendix G, and highlight the main findings in what follows for $b = 0.1$.

Fig. 3.3 (top left) shows pressure-averaged adiabatic index $\langle\gamma\rangle$ (blue) and critical index $\gamma_{\rm cr}$ (orange) vs. 3D velocity dispersion $v(0)$, and gravitational redshift $Z(0)$. As $v(0)$ increases, $\langle\gamma\rangle$ gradually decreases from its value in the nonrelativistic limit 5/3, while the $\gamma_{\rm cr}$ increases from $\sim 4/3$ due to corrections in general relativity. It reaches the critical value 1.62 when $v(0) = 0.566c$ [65], which corresponds to $Z(0) = 0.750$. The results are largely insensitive to a specific value of b. For $b = 0.1$–0.5 we consider, according to the adiabatic

index criterion, dynamical instability occurs when $\langle\gamma\rangle$ reaches 1.62 at $v(0) = (0.566\text{–}0.564)c$, corresponding to $Z(0) = 0.750\text{–}0.622$; see Table G.1.

The "insensitivity" reflects the degeneracy between the boundary temperature b and the central cutoff energy $w(0)$ in determining the equation of state as indicated in Fig. 3.2. In our numerical study, for given b, we scan $w(0)$ to find the configuration that satisfies the instability condition. If a system has a low boundary temperature, the instability can be triggered only if the central cutoff is high enough so that the evaporation effect is suppressed and more particles are retained on the high-energy tail. For example, to satisfy the adiabatic index criterion, $w(0) = 0.662$ for $b = 0.5$, while $w(0) = 4.05$ for $b = 0.1$, as shown in Table G.1.

Fig. 3.3 (top right) shows the fractional binding energy $\varepsilon = (\hat{E}_{\rm rest} - \hat{E})/\hat{E}_{\rm rest}$ (blue) vs. $v(0)$ and $Z(0)$. As $v(0)$ increases, ε first increases and reaches its maximum $\varepsilon_{\rm max} = 0.0352$ at $v(0) = 0.506c$, corresponding to $Z(0) = 0.548$, then decreases. From the turning-point method, $\varepsilon_{\rm max}$ separates the equilibrium configuration into two branches, i.e., stable (solid) and unstable (dashed). The pattern is universal, i.e., $\varepsilon_{\rm max} = 0.0352\text{–}0.0356$ at $Z(0) = 0.548\text{–}0.522$ is the turning point for $b = 0.1\text{–}0.5$. We also find that $\langle\gamma\rangle = 1.63$ at the turning point of the fractional binding energy, which is slightly higher than 1.62 from the adiabatic index criterion.

Earlier studies [59, 60, 61] suggest that a system becomes dynamically unstable when its fractional binding energy reaches maximum. Fully relativistic N-body simulations [63] show that the system can collapse to a black hole when $\varepsilon \approx 0.035$ at $Z(0) \approx 0.5$, in excellent agreement with what we find based on the semi-analytical method. In several

unstable cases found in [63], the oscillation frequency of radial linear perturbations is still positive, i.e., the adiabatic index condition is not satisfied. Thus the criterion $\gamma_{\rm cr} > \langle\gamma\rangle$ is a sufficient, but may not be necessary condition for the dynamical stability.

Fig. 3.3 (bottom left) shows binding energy $\hat{B} = (\hat{E}_{\rm rest} - \hat{E})$ vs. $v(0)$ and $Z(0)$. $\hat{B}$ reaches its maximum $\hat{B}_{\rm max} = 8.49 \times 10^{-4}$ at $v(0) = 0.395c$, corresponding to $Z(0) = 0.297$, then decreases. $\hat{B}_{\rm max}$ separates the configuration into stable (solid) and unstable (dashed) branches. Similarly, Fig. 3.3 (bottom right) shows the total energy $\hat{E}$ vs. $v(0)$ and $Z(0)$. The maximum value of the total energy is $\hat{E}_{\rm max} = 3.47 \times 10^{-2}$ at $v(0) = 0.225c$ and $Z(0) = 0.087$. According to the turning-point method, the system becomes unstable when $\hat{E}_{\rm max}$ or $\hat{B}_{\rm max}$ is reached. However, it is unlikely that the system could collapse into a black hole at this stage. Instead, it would further evolve until the instability condition based on fractional binding energy or adiabatic index is met. Fig. 3.1 summarizes our numerical results schematically and illustrates the sequence of dynamical instability conditions when a self-interacting dark matter halo collapses to a black hole.

To see whether the four collapsing stages denoted in Fig. 3.1 occur chronologically, we need to trace the time evolution of a collapsing system. In Sec. 3.4, we will estimate the dynamical timescale for collapsing into a seed black hole for the configurations satisfying the instability conditions shown in Fig. 3.3. It turns out that the timescale associated with the total energy criterion is a factor of ~ 3 longer than the other three ones, which are comparable. In this work, we search for quasi-equilibrium, static solutions to the Tolman-Oppenheimer-Volkoff equation. It is interesting to see if the system deviates from quasi-equilibrium after passing the total energy criterion, and we will leave it for future work.

In Fig. 6.2, we show radial profiles for normalized cutoff energy bw (top left), cutoff energy ϵ_c/mc^2 (top right), density $\hat{\rho}$ (middle left), 3D velocity dispersion v/c (middle right), temperature k_BT/mc^2 (bottom left), and adiabatic index γ (bottom right), for marginally stable configurations with criteria based on the adiabatic index (dash-dotted orange), fractional binding energy (dotted purple), binding energy (dashed blue) and total energy (solid magenta). We fix the boundary temperature to be $b = k_BT(R)/mc^2 = 0.1$ and adjust the central cutoff function $w(0)$ to find the corresponding marginal configurations. It is clear that ϵ_c/mc^2, so as for $bw(0)$, becomes higher for a stronger instability condition, which is expected. For a given configuration, the cutoff energy drops significantly towards outer regions $\hat{r} \to 1$. The v and $\hat{\rho}$ profiles follow a similar behavior. The temperature becomes higher towards the center due to the gravitational redshift effect. The adiabatic index decreases towards inner regions as the pressure increases and the equation of state becomes softer accordingly. And it is much softer for a stronger instability criterion, in particular, the configuration with $\gamma(0) \approx 1.59$ has $\langle\gamma\rangle = \gamma_{\rm cr} \approx 1.62$.

We have also performed a finer scan of b values for marginally stable configurations under the adiabatic index criterion, and the results are summarized in Table G.2, Appendix G. For $b = 0.09$–5.0, the configurations that satisfy $\langle\gamma\rangle \approx \gamma_{\rm cr} = 1.62$ have a central velocity dispersion of $v(0) = (0.588$–$0.566)c$, compactness of $C \simeq 0.0236$–0.0793, and the central redshift of $Z(0) \simeq 0.889$–0.613. Thus the instability condition exhibits a universal pattern. For $b \gtrsim 1$, pair production of dark matter particles could be relevant, and we will leave it for future work.

3.3 Constraining dark matter models

We have demonstrated the conditions of dynamical instability for a gravothermal system. Our study assumes a classical truncated Maxwell-Boltzmann distribution, which neglects quantum statistics. To examine the validity of this assumption, it is useful to calculate the de Broglie thermal wavelength in relativistic thermodynamics $\lambda_{\rm dB} = \hbar/|\mathbf{p}|$. Setting $\epsilon = [\sqrt{1+(\mathbf{p}c/mc^2)^2}-1]mc^2 = 3k_BT/2$, we have

$$\lambda_{\rm dB} = \lambda_{\rm C}\left[\left(1+\frac{3k_BT}{2mc^2}\right)^2-1\right]^{-1/2}. \tag{3.18}$$

In the nonrelativistic limit $k_BT/mc^2 \ll 1$, this reduces to the familiar expression $\lambda_{\rm dB} = \lambda_{\rm C}\sqrt{mc^2/3k_BT}$, where $\lambda_{\rm C}$ is the Compton wavelength, and typically $\lambda_{\rm dB} \gg \lambda_{\rm C}$. They become compatible, $\lambda_{\rm dB} \sim \lambda_{\rm C}$, when the temperature is comparable to the particle rest mass, i.e., in the relativistic regime. When the ultrahigh density core collapses, we demand the thermal de Broglie wavelength much smaller than the average separation distance, i.e., $n\lambda_{\rm dB}^3 \ll 1$, where n is the number density of dark matter particles. In the relativistic regime $\lambda_{\rm dB} \simeq \lambda_{\rm C}$, so we have $n\lambda_{\rm dB}^3 \sim (M_{\rm seed}/mR^3)\lambda_{\rm C}^3 \ll 1$, where $M_{\rm seed}$ is the mass of seed black holes. Using the compactness relation $C = GM_{\rm seed}/Rc^2$, we can write $n\lambda_{\rm dB}^3 = C^3(m_{\rm Pl}/M_{\rm seed})^2(m_{\rm Pl}/m)^4$, and hence

$$n\lambda_{\rm dB}^3 \approx 0.27\left(\frac{C}{0.04}\right)^3\left(\frac{10^9\ {\rm M}_\odot}{M_{\rm seed}}\right)^2\left(\frac{5\ {\rm keV}}{mc^2}\right)^4 \ll 1. \tag{3.19}$$

Thus for given $M_{\rm seed}$, we can derive a lower limit on the particle mass m.

Consider a benchmark case discussed in [65], where the core of a 6.8×10^{11} $M_\odot$ halo collapses to a seed black hole with $M_{\rm seed} = 1.9\times10^9$ $M_\odot$. Such a seed could further grow into a supermassive black hole with a mass of 2.2×10^9 $M_\odot$ through accreting baryonic matter, to be consistent with observations of the J1205-0000 quasar at redshift 6.7 [9]. J1205-0000 has a low accretion efficiency, and hence a massive $\sim 10^9$ $M_\odot$ seed is needed, assuming an Eddington accretion history. Taking these into account, the particle mass needs to be larger than a few keV such that the classical truncated Maxwell-Boltzmann distribution is valid.

We further check constraints on the boundary temperature $b = k_BT(R)/mc^2$ and the central cutoff energy $w(0) = \epsilon_c(0)/k_BT(0)$. Consider a 10^9 $M_\odot$ core, when the onset of dynamical instability occurs, the boundary radius is $R = GM_{\rm seed}/Cc^2 \approx 10^{-3}$ pc, where we take $C = 0.04$. Setting the characteristic length scale $\zeta = \lambda_{\rm C}(m_{\rm Pl}/m)(8\pi^3/ge^{\alpha(R)})^{1/2}$ to be $R/\hat{R}$ and taking $m = 1$ GeV$/c^2$ and $\hat{R} = 0.37$, see Table G.1 ($b = 0.1$), we find $\alpha(R) \approx -44$ for fermionic dark matter, $g = 2$. The central degeneracy $\alpha(0) = \alpha(R)+w(0)$ must be much less than -1 for classical distribution to be valid, i.e., $-\mu(0)/k_BT(0) \gg 1$; see Eq. (3.2). Thus there is an upper limit on $w(0)$, i.e., $w(0) \ll 43$. As shown in Fig. 6.2 (top left), the instability condition requires $bw(0) \gtrsim 0.3$. For $b \sim 0.1$, we have $w(0) \gtrsim 3$. In this case, the core can collapse to a seed black hole when the system is still in the classical regime where quantum effects are negligible. On the other hand, for $b \sim 0.001$, the required $w(0)$ would be larger than 300. Thus for the core to collapse to a black hole in the classical regime, the boundary temperature needs to be $b \gtrsim 0.1$ at the onset of the instability.

This can be used to test the collapse models based on self-interacting dark matter. In [65], the self-interactions are purely elastic and gravothermal collapse could occur early

enough to explain the origin of supermassive black holes at high redshifts after taking into account the effects of baryons. Recent studies [41, 66] consider dissipative interactions, as they could speed up the onset of gravothermal collapse [23, 42, 90]. However, it is not clear whether dynamical instability can be triggered in this case, as the temperature of the central core may not reach the quasirelativistic limit, i.e., $b \sim 0.1$, due to the energy loss induced by the dissipative interactions. It is possible that the energy release could be confined within the collapsing core as the radiation particle has a mean free path much less than the core radius. A detailed study is needed to further assess those models.

In this study, we have assumed a spherical symmetry. Dark matter self-interactions lead to a spherical shape of the inner halo [14, 91]. They also induce viscosity that can dissipate away net angular momentum of the core inherited from the main halo in a short timescale [65]. Thus our spherical assumption is self-consistent and well justified. It is interesting to see whether our work can be generalized to axisymmetric cases. However, fully relativistic numerical simulations show that a marginally unstable system can collapse into a black hole containing 90% of the total mass even if it rotates at the mass shedding limit (Keplerian speed) [92, 93, 94].

3.4 Connecting to the conducting fluid model

Another direction is to develop a formalism that bridges the relativistic truncated Maxwell-Boltzmann model in this work, the analytical SIDM halo model [12], as well as the nonrelativistic conducting fluid model [19]. The latter has been widely used to study the gravothermal collapse of SIDM halos. The two essential parameters in our model, i.e.,

boundary temperature $b = k_B T(R)/mc^2$ and central energy cutoff $w(0) = \epsilon_c(0)/k_B T(0)$, would be ultimately related to the halo parameters and the self-interacting cross section. To fully establish such relations, one would need simulations with a relativistic fluid model, which is beyond the scope of this work. Here, we highlight a few useful comparisons between our results and those in the relevant literature.

In the nonrelativistic limit $bw(r) \ll 1$, the Tolman-Oppenheimer-Volkoff equation (3.5) for $w(r)$ becomes $\mathrm{d}w/\mathrm{d}r = -GM(r)/(br^2c^2)$. For the truncated model, one can show [54]

$$\frac{\mathrm{d}p}{\mathrm{d}r} = \frac{b}{1-bw}\left(p+\rho c^2\right)\frac{\mathrm{d}w}{\mathrm{d}r} = b\rho c^2\frac{\mathrm{d}w}{\mathrm{d}r}, \tag{3.20}$$

where the last equality assumes the nonrelativistic limit. Thus we obtain the Newtonian hydrostatic equation $\mathrm{d}p/\mathrm{d}r = -GM(r)\rho/r^2$. Ref. [12] uses the hydrostatic equation and proposes an analytical model to describe an SIDM halo when it reaches the maximal gravothermal expansion. It further assumes an isothermal equation of state $p = \rho v^2/3$ over the inner halo, where the 3D velocity dispersion v is a constant, and hence the adiabatic index is fixed to $\gamma = 5/3$. In this case, $k_B T/m = v^2/3$ is a constant, and we have a simple relation of $b = k_B T/mc^2 = (v/c)^2/3$. Using the relation $\epsilon_c(r) = w(r)k_B T$, we find $\mathrm{d}\epsilon_c/\mathrm{d}r = -GM(r)m/r^2$, thus ϵ_c is the escape energy as expected.

When the SIDM halo reaches its maximal expansion, $v \approx V_{\max} = 1.64 r_s\sqrt{G\rho_s}$ [12], where $V_{\max}$ is the maximal circular velocity of the initial halo, r_s and ρ_s are its scale radius and density, respectively. Since $r_s \propto M_{200}^{1/3}/c_{200}$ and $\rho_s \propto c_{200}^3/f_{200}$, where M_{200} is the halo mass, c_{200} is the concentration and $f_{200} = \ln(c_{200}+1) - c_{200}/(c_{200}+1)$, we obtain a scaling relation of $b \propto M_{200}^{2/3} c_{200}/f_{200}$ in the context of the analytical SIDM halo model [12].

For a collapsed halo, v increases with the evolution time and it becomes much larger than $V_{\rm max}$, as we will show an example later. It is interesting to see whether the scaling relation $b \propto M_{200}^{2/3} c_{200}/f_{200}$ still holds in the collapse phase. Qualitatively, if the initial halo has a high mass and concentration, the collapsed inner halo has a large energy reservoir, leading to a high boundary temperature.

We further compare our numerical results with simulations in [65] based on the nonrelativistic conducting fluid model. Consider the J1205-0000 benchmark case again [65], where $\rho_s \approx 8.1\times10^7$ M$_\odot$/kpc^3 and $r_s \approx 10$ kpc for the halo with a mass of 6.8×10^{11} M$_\odot$ and $M_{\rm seed} = 1.9 \times 10^9$ M$_\odot$ [65]. Taking $b = 0.1$, the instability occurs when the compactness reaches $C = 3.9 \times 10^{-2}$, see Table G.1, and we can obtain the boundary radius as $R = GM_{\rm seed}/Cc^2 \approx 2.3 \times 10^{-3}$ pc. The average density within R is $\langle\rho_{\rm seed}\rangle = 3M_{\rm seed}/(4\pi R^3) \approx 3.5\times10^{25}$ M$_\odot$/kpc^3. For comparison, the simulations based on the nonrelativistic fluid model find that the average density of the collapsed halo is $\langle\rho_{\rm in}\rangle \sim 10^{11}\rho_s = 8.1 \times 10^{18}$ M$_\odot$/kpc^3 at the last snapshot shown in Fig. 1 of [65]. We see that $\langle\rho_{\rm seed}\rangle \,/\, \langle\rho_{\rm in}\rangle \sim 4.4 \times 10^6$, a significant difference. Thus the simulated halo needs to evolve further for matching $\langle\rho_{\rm seed}\rangle$, which requires a relativistic version of the conducting fluid model towards the end.

When the instability occurs, the central 3D velocity dispersion reaches the relativistic limit, $v(0)/c = \sqrt{3p/\rho c^2} \approx 0.57$, but on the boundary $v(R)/c \approx 8.8 \times 10^{-3}$ ($b = 0.1$), see Table G.2. Interestingly, $v(R)/c$ is comparable to the velocity dispersion found in the fluid simulations $v/c \approx 10 \times \sqrt{12\pi\rho_s r_s^2/c^2} = 37.4 V_{\rm max}/c \approx 3.8 \times 10^{-2}$, derived from the last snapshot in Fig. 1 of [65] assuming the hydrostatic condition. During the gravothermal collapse the change in the velocity dispersion is much milder than that in the density, as the pressure increases as well and $v \propto \sqrt{p/\rho}$. One may consider exactly mapping the thermal quantities, such as ρ and p, from the truncated Maxwell-Boltzmann model, to those from the fluid model. However, this is challenging because the adiabatic index γ varies dynamically towards the onset of the instability, as illustrated in Figure 3.3, but the original nonrelativistic fluid model assumes a specific value of $\gamma = 5/3$ [19]. To resolve this, we could consider a relativistic fluid model and find a class of solutions by varying γ from $\gamma = 5/3$ to 4/3.

Lastly, we examine timescales for the ultrahigh density core to collapse into a black hole. For the gravothermal collapse of an SIDM halo, $t_{\rm halo} \sim \mathcal{O}(100)/[r_s\rho_s(\sigma/m)\sqrt{4\pi G\rho_s}]$ [19], where σ/m is the self-scattering cross section. The presence of the baryonic potential could shorten the collapse timescale by a factor of ~ 100 [65] and $r_s\rho_s(\sigma/m)$ is typically 0.1–1 [23], we take $t_{\rm halo} \sim 1/\sqrt{4\pi G\rho_s}$ after neglecting $\mathcal{O}(1)$ numerical factors. We estimate the timescale for collapsing into a seed as $t_{\rm seed} \sim 1/\sqrt{4\pi G\,\langle\rho_{\rm seed}\rangle}$. For the J1205-0000 benchmark, $\langle\rho_{\rm seed}\rangle \approx 3.5 \times 10^{25}$ $\mathrm{M}_\odot/\mathrm{kpc}^3$ based on the adiabatic index criterion and $\rho_s \approx 8.1 \times 10^7$ $\mathrm{M}_\odot/\mathrm{kpc}^3$, and hence $t_{\rm seed} \sim \sqrt{\rho_s/\langle\rho_{\rm seed}\rangle} = 1.5 \times 10^{-9} t_{\rm halo} \sim 69$ days, where we take $t_{\rm halo} = 124$ Myr for J1205-0000 [65]. Thus the timescale for collapsing into a seed

black hole is extremely short compared to that of the gravothermal collapse of an SIDM halo.

For the J1205-0000 benchmark, we have further checked that the $t_{\rm seed}$ values associated with the adiabatic index, fractional binding energy, and binding energy criteria are comparable, but a factor of ~ 3 shorter than the one with the total energy criterion. This indicates that the total energy criterion may not be a sufficient condition for collapsing into a black hole. On the other hand, the system may deviate from a hydrostatic equilibrium after the total energy criterion is satisfied, which we will leave for future work. In addition, we have a scaling relation of $\langle\rho_{\rm seed}\rangle \propto M_{\rm seed}/R^3 \propto 1/M_{\rm seed}^2$, where $R = GM_{\rm seed}/Cc^2$ is used. For the SIDM model, $M_{\rm seed} \sim 10^{-3} M_{200}$ [19, 65], and we expect that the compactness C, a dimensionless quantity, is largely independent of specific halo parameters. Thus the collapse time increases with the initial halo mass as $t_{\rm seed} \propto 1/\sqrt{\langle\rho_{\rm seed}\rangle} \propto M_{200}$.

3.5 Conclusions

The origin of supermassive black holes remains unknown and the gravothermal collapse of dark matter halos is a promising mechanism to explain the puzzle. In this chapter, we have investigated a key aspect of this mechanism, i.e., dynamical instability of the ultrahigh density core produced at late stages of gravothermal evolution. We used a truncated Maxwell-Boltzmann distribution to model the dark matter distribution in the core, solved the Tolman-Oppenheimer-Volkoff equation in a self-consistent way, and obtained a series of equilibrium configurations. We examined four instability conditions based on considerations of total energy, binding energy, fractional binding energy, and adiabatic index.

As the core contracts, these conditions would be satisfied in sequential order. The adiabatic index criterion is the strongest among the four. We have also compared our results from the semi-analytical method to those from fully relativistic N-body simulations and found a good agreement. In particular, both show the instability can occur when the fractional binding energy reaches 0.035 with a central gravitational redshift of 0.5.

We further found that to meet the instability condition in the classical regime, the boundary temperature of the core should be at least 10% of the mass of dark matter particles. In addition, the classical Maxwell-Boltzmann distribution is valid only if the particle mass is larger than a few keV for a 10^9 $M_\odot$ seed black hole. We have also shown that the timescale for collapsing into a seed black hole is extremely short compared to that of the gravothermal collapse of an SIDM halo. In the future, we could extend our work to study dynamical instability of a self-gravitating quantum sphere, and whether the presence of a baryonic potential would help trigger the instability. In addition, signatures of the gravothermal collapse could be tested using observations of satellite dwarf galaxies of the Milky Way [44, 95, 96, 97, 98, 99, 100, 101, 102] and substructures of galaxy clusters [32], as the interplay between self- and tidal interactions could seed up the process. It would be interesting to explore formation of seed black holes in those systems.

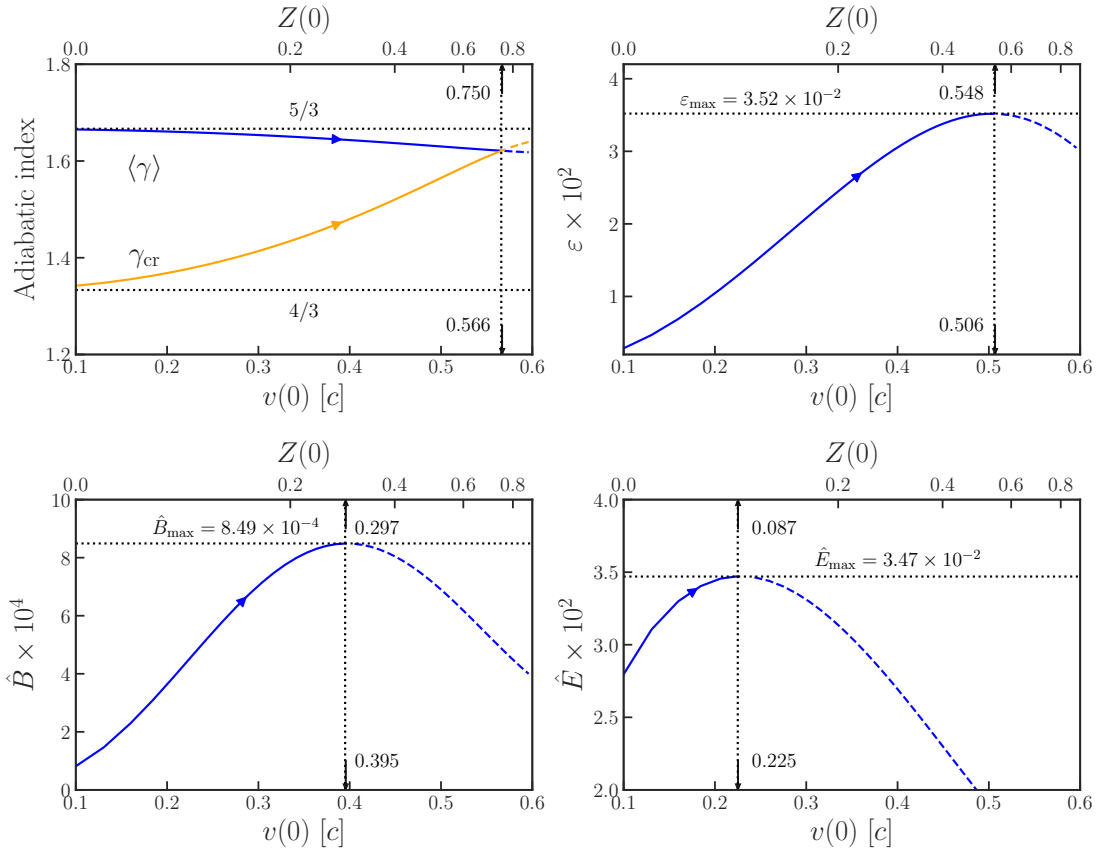

Figure 3.3: Dynamical variables vs. central 3D velocity dispersion $v(0)$ and redshift $Z(0)$ of a gravothermal system near the onset of general relativistic instability. From top left to bottom right panels, the blue curves denote the pressured-averaged adiabatic index $\langle\gamma\rangle$, fractional binding energy ε, binding energy $\hat{B}$, and total energy $\hat{E}$, for stable (solid) and unstable (dashed) configurations, respectively. The vertical line indicates where the instability condition is reached (dotted). In the top left panel, the orange curve denotes the critical adiabatic index $\gamma_{\rm cr}$ (solid), horizontal lines denote $\langle\gamma\rangle = 5/3$ in the Newtonian limit and $4/3$ in the ultrarelativistic limit (dotted). In the other panels, the horizontal line indicates the maximal value of the corresponding dynamical variable (dotted). The boundary temperature is fixed to be $b = k_B T(R)/mc^2 = 0.1$.

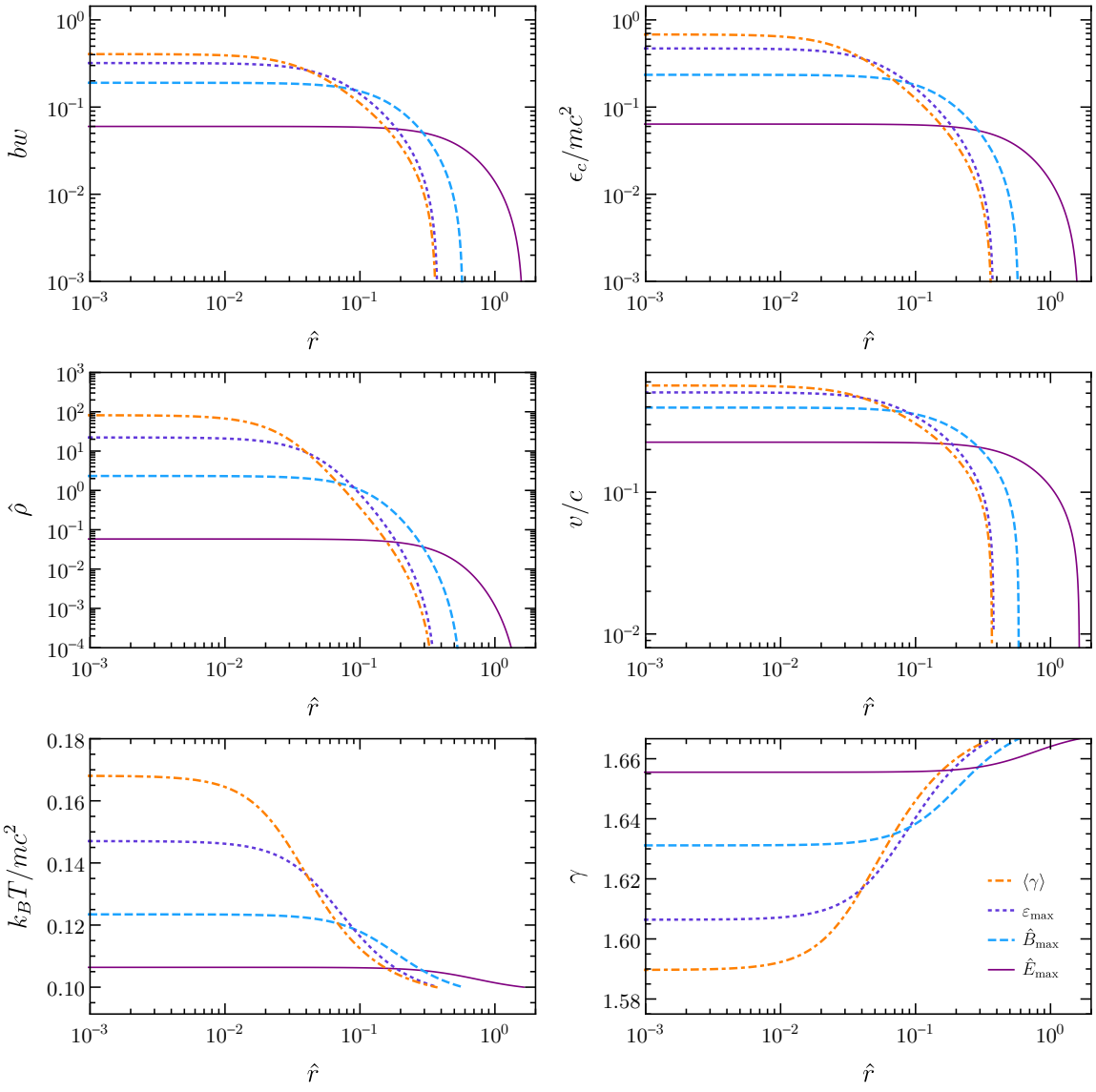

Figure 3.4: Radial profiles of $bw = \epsilon_c(r)/[mc^2 + \epsilon_c(r)]$, cutoff energy ϵ_c/mc^2, density $\hat{\rho}$, 3D velocity dispersion v/c, temperature k_BT/mc^2, and adiabatic index γ, for marginally stable configurations with the criteria based on the adiabatic index (dash-dotted orange), fractional binding energy (dotted purple), binding energy (dashed blue) and total energy (solid magenta). We fix $b = k_BT(R)/mc^2 = 0.1$.

Chapter 4

Gravothermal Phase Transition, Black Holes and Space Dimensionality

Black holes (BHs) are the most profound prediction of Einstein's general relativity (GR), though their existence is questionable in the early days. Oppenheimer and Snyder [103] first demonstrated the dynamical process of forming a BH from dust collapse, and the spacetime singularity is inevitable. However, the idealized collapsing process of spherical symmetry might be unrealistic. Until 1965, Penrose showed [104] mathematically that whenever matter satisfies reasonable energy conditions, a BH is a generic consequence of GR regardless of spherical symmetry. In astrophysics, a BH is the end state of a conventional star running out of fuel. But it could also emerge from the direct collapse of clouds of gas without igniting a nuclear reaction.

In the context of Newtonian gravity (NG), the self-gravitating ideal monatomic fluid is too stable [57]. The pressure always counteracts gravitational attraction and stabilizes the fluid. In GR, the pressure in the fluid is a double-edged sword. Because not only the energy density but also the pressure is sourcing gravity, once the pressure starts to dominate energy density at some point, it will destabilize the fluid. This is why the instability and collapse into BHs from a fluid can happen in the framework of GR. All of the above concern BHs in (3+1)-dimensional spacetime. Of course, there is nothing to hinder theorists from considering BHs in (N+1) dimensions with $N \neq 3$. BHs in higher dimensions have been studied thoroughly in the literature [105, 106, 107]. Although the stability of a fluid sphere and its dimensional constraint has been explored somewhat [108], less investigated is the instability condition of the higher-dimensional BHs coming from collapsing fluids. As we shall see, the ideal fluids in the context of NG are genuinely unstable for $N > 3$, and the GR effect makes the situation worse. However, the presence of cosmological constant λ will modify the situation, in particular, $\lambda < 0$ can stabilize the fluid sphere. We also note that the dynamical instability of stellar equilibrium for $N = 3$ with cosmological constant was studied to some extent in Refs. [109, 110, 111].

In lower dimensions, i.e., $N = 2$, gravity is bizarre. The Bañados-Teitelboim-Zanelli (BTZ) BH solution exists only if a "negative" cosmological constant $\lambda = -1/\ell^2 < 0$ is introduced, where ℓ is the background radius of curvature [112]. This can be understood from the unit of Newton's constant in (N+1) dimensions: $[G_N] = [\mathrm{M}]^{-1}[\mathrm{L}]^N[\mathrm{T}]^{-2}$. For $N = 2$, setting $c = 1$ determines the fundamental "mass scale" in terms of the Newton's constant G_2, but the fundamental "length scale" cannot be settled down. Thus an

independent length scale $\ell = (-\lambda)^{-1/2}$ must be introduced independently. Moreover, the negativeness of λ permits the BH solution [113]. In addition, there is no Newtonian limit in (2+1) dimensions. Gravity has no local degrees of freedom (locally flat), thus no gravitational wave (or graviton) can propagate. This reflects the fact that static particles do not gravitate [114, 115, 116]. In contrast, the collective behavior of thermal particles will gravitate and demand the fluid description under its self-gravity. Crucially, $\lambda < 0$ is also to guarantee the hydrostatic equilibrium (the pressure is monotonically decreasing) [117].

The basic mechanism of hierarchical structure formation (stars, galaxies, halos, etc.) relies on the Jeans instability [118], which determines the largest mass (Jeans mass, also called Bonnor-Ebert mass [119, 120]) of an isothermal gas sphere can still remain in hydrostatic equilibrium. For the gas sphere heavier than this, it will further collapse or fragment into smaller and denser objects [121]. Then it transitions into *gravothermal evolution*. As a gravitationally bound system, it gets hotter and hotter as it releases thermal energy through dissipation [18, 122, 123]. If the mass sphere is sufficiently heavy ($\gtrsim 10^6\ M_\odot$), this process will persist without triggering the thermonuclear sources of energy, while it behaves as a "supermassive star." Nevertheless, the gravothermal evolution will end eventually and probably collapse into a BH once relativistic instability is triggered [56]. It serves as the prototype of supermassive BHs from direct collapse of pristine gas [7, 124, 125, 126, 127] or dark matter halo with self-interaction [20, 19, 22, 128, 65].

As long as heat transport occurs, a self-gravitating monatomic fluid (or supermassive star) will relax and shrink automatically due to the negative specific heat of a gravitationally bound system [19, 65]. During the gravothermal process in the hydrostatic

limit, the thermal evolution timescale of the contraction is much larger its free-fall (dynamical) timescale $t_{\rm ff} \sim 1/\sqrt{G_N \rho}$, where ρ is the (mean) energy density of the fluid [57]. In this scenario, we can idealize the evolution process by a sequence of virialized quasiequilibria characterized by the mass and radius of the fluid sphere. In particular, the particles in the fluid will follow the same distribution function, albeit the dispersion varies during the process until the onset of relativistic instability. Moreover, we assume *no* extra degrees of freedom, e.g., nuclear reaction of our universe in (3+1) dimensions, will be ignited to halt the direct collapse into a BH. We note that the final BH formation near the end of the gravothermal evolution requires dynamically evolving the fluid and the spacetime given initial data [129, 130, 131, 132], which is beyond the scope of this study. Without a cosmological constant in (3+1), it has been shown that unstable static spherical Tolman-Oppenheimer-Volkoff solutions exist on saddle points that, when perturbed from their unstable equilibrium, will tend to either black hole formation or a perturbed stable solution [132]; while with positive cosmological constant, the dynamical evolution of a homogeneous dust would drag the entire spacetime into a "big crunch" singularity if the fluid mass is sufficiently large [129].

The goal of this chapter is to examine the *sufficient* condition that can *naturally* trigger the instability of a self-gravitating monatomic fluid in $(N+1)$ dimensions, in particular, in the presence of cosmological constant. We adopt homogeneous solutions, which are adequate for the purpose. In the end, we will briefly discuss the implications on the dimensionality of spacetime. The geometric unit $G_N = c = 1$ is used, unless noted otherwise.

4.1 Dynamical instability in (N+1) dimensions

The method exploited by Chandrasekhar [55] is to examine the *radial pulsation equation* of a perturbed fluid sphere of mass $\mathcal{M}$ within radius R:

$$\delta\ddot{R} + \omega^2 \delta R = 0 \quad \text{with} \quad \omega^2 \propto \langle\gamma\rangle - \gamma_{\rm cr}, \tag{4.1}$$

where ω is oscillation frequency, the critical adiabatic index $\gamma_{\rm cr}$ depends on the given equilibrium configuration, and $\langle\gamma\rangle$ is the pressured-averaged adiabatic index of the fluid sphere. Thus the stability problem boils down to the Sturm-Liouville eigenvalue problem. The *sufficient* condition for the fluid to become unstable is $\gamma_{\rm cr} > \langle\gamma\rangle$ such that $\omega^2 < 0$, implying the perturbation $\delta R \sim e^{i\omega t}$ would be an exponential growth.

The adiabatic index of a fluid,

$$\gamma = \left(\frac{\partial \ln p}{\partial \ln n}\right)_s, \tag{4.2}$$

is a *stiffness/compressibility* parameter signifying how the fluid pressure p responds to the adiabatic ($\mathrm{d}s = 0$) compression on number density n. In particular, an ideal fluid parametrized by the γ-law form $p = K(mn)^\gamma$ [133], where m is the particle's mass, satisfies the above definition as long as γ and K are not explicit functions of n under adiabatic perturbation. The first law of thermodynamics results in [82, 57, 134] $\gamma = 1 + p/(\rho - mn)$. Given a distribution function $f(\mathbf{x}, \mathbf{p})$ of monatomic particles with phase space measure $\mathrm{d}^N\mathbf{x}\ \mathrm{d}^N\mathbf{p}$, the adiabatic index of the ideal fluid merely depends on its *velocity dispersion*

$v \equiv \sqrt{Np/\rho} < 1$ and the *degrees of freedom* N, specifically

$$\gamma = 1 + \frac{1 + \sqrt{1 - v^2}}{N} \tag{4.3}$$

ranges from $1 + 2/N$ (nonrelativistic $v \to 0$) to $1 + 1/N$ (ultrarelativistic $v \to 1$) [134].

Considering NG in (N+1)-dimensional spacetime, one can derive the *critical adiabatic index* [134]:

$$\gamma_{\mathrm{cr(NG)}} = 2\left(1 - \frac{1}{N}\right). \tag{4.4}$$

In order to have a stable configuration, it is *necessary* that $\langle\gamma\rangle > \gamma_{\mathrm{cr(NG)}}$. For ultrarelativistic (nonrelativistic) ideal fluids, this implies the spatial dimensions must be $N < 3$ ($N < 4$) in order to have a stable sphere. From this viewpoint, the privilege of (3+1) dimensions is manifest because *the fluid sphere is stable but not too stable.* However, in (2+1) dimensions the fluid disk is too stable because $\gamma_{\mathrm{cr(NG)}} = 1 < 1.5\ (2) = \gamma$ as always for an ultrarelativistic (nonrelativistic) fluid. Nevertheless, in the context of GR the pressure effect is crucial to destabilize the fluid disk. Besides, in order for the fluid to have equilibrium configurations and a BTZ solution, a *negative cosmological constant* is required [112].

Thus we have to first examine the equilibrium configurations with cosmological constant $\lambda = \pm 1/\ell^2$ in (N+1) dimensions. For homogeneous solutions, the critical adiabatic index (the exact expression is derived in Ref.[134] and see also Appendix F.1)

$$\begin{aligned}\gamma_{\mathrm{cr(GR)}} &= \frac{\lambda R^2}{(N-2)\mathcal{M}/R^{N-2} - \lambda R^2} \\ &+ \sum_{j,k=0,1,\ldots} f_{jk}^{(N)} \left(\frac{\mathcal{M}}{R^{N-2}}\right)^j \left(\lambda R^2\right)^k,\end{aligned} \tag{4.5}$$

where the post-Newtonian coefficients $f_{jk}^{(N)}$ depend on the density distribution and spatial dimensions N, except $f_{00}^{(N)} = \gamma_{\mathrm{cr(NG)}}$; and the *stabilizer/destabilizer*:

$$\frac{\lambda R^2}{(N-2)\mathcal{M}/R^{N-2} - \lambda R^2} \begin{cases} \text{stabilizer if negative} \\ \\ \text{destabilizer if positive} \end{cases} \tag{4.6}$$

characterizes the relative competition between compactness and background curvature. We note that its appearance is generically from GR as long as λ is switched on, and *cannot* be regarded as post-Newtonian correction.

Qualitatively, the GR instability depends on the pressure effect of the fluid through $p/\rho \propto \mathcal{M}/R^{N-2} \equiv \mathcal{C}_N$, the *compactness parameter* in $(N+1)$ dimensions. On the other hand, the stability of a fluid will also depend on the relative size of the fluid to the radius of curvature of the space, specifically, the curvature parameter λR^2. As was mentioned, in the context of NG, fluid spheres are genuinely subject to dynamical instability for $N > 3$. Even worse, the corrections from GR deteriorate the situation, especially if $\lambda > 0$. However, it is possible to have stable hydrostatic equilibrium if $\lambda < 0$. We also note that for $\lambda = 0$ the post-Newtonian approximation $f_{10}^{(3)} = 19/21$ is exactly the result shown in Ref. [55].

4.2 Gravitationally bound systems

In GR, the *gravitational* mass of a fluid sphere $\mathcal{M}$ is the corresponding Schwarzschild mass ($N \geq 3$) if it were to collapse into a BH. It includes the energy of self-gravity due to the curved spacetime, which is thus not conserved during the gravothermal evolution. By contrast, the rest mass $\mathcal{M}_{\mathrm{rest}}$ of the fluid is conserved (see Appendix F.2 for definition). It

is the mass of total particles in the fluid when they are dispersed to infinity. Therefore, to form a gravitationally bound state the total internal energy must be

$$\mathcal{M} - \mathcal{M}_{\rm rest} < 0. \tag{4.7}$$

Before we are able to examine the dynamical instability reasonably, it is necessary to see if the quasistatic equilibrium is gravitationally bound during the gravothermal evolution. The solutions can be categorized as stable or unstable *only* if they are gravitationally bound. If the *initial* configuration is a unbound state, $\mathcal{M}-\mathcal{M}_{\rm rest} > 0$, dynamical evolution of the fluid and the spacetime is required to determine the final fate (BH or naked singularity) [130], which is again beyond the scope of the chapter.

4.3 Fluid spheres in (3+1) and higher dimensions

Assuming a fluid sphere in $(N+1)$ dimensions is in hydrostatic quasiequilibrium, the fluid (rest) mass $\mathcal{M}_{\rm rest}$ = const during the gravothermal evolution. The radius will contract such that $\mathcal{C}_N$ increases gradually as more and more thermal energy dissipates until reaching the critical compactness as $\langle\gamma\rangle = \gamma_{\rm cr}$. Given $\lambda =$ const, we can tell from the phase diagrams (Figs. 4.1 and 4.2) when the phase transition into BH could be triggered. For $N \geq 3$ the evolution follows $\mathcal{M}_{\rm rest}|\lambda|^{(N-2)/2} =$ const, only those paths passing through the stable bound region will be in the "long-lived" stage of gravothermal evolution.

As we have already noted, a fluid sphere is genuinely unstable for $N \geq 4$, and $\lambda > 0$ just deteriorates the situation. Remarkably, the privileged position of $N = 3$ can be

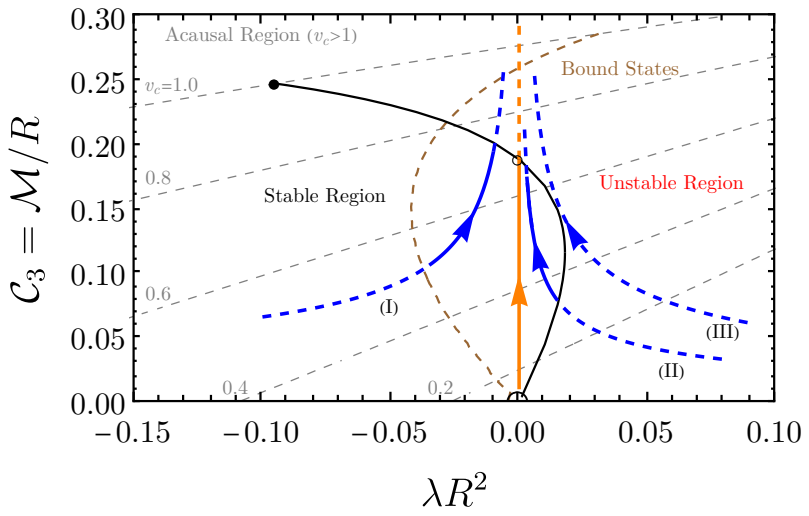

Figure 4.1: $\mathcal{C}_3 - \lambda R^2$ phase diagram of homogeneous fluid spheres in (3+1) dimensions. Bound states are to the right of the brown dashed line. The stable and unstable regions are separated by the marginal stable curve (black solid), and the black dot denotes the end point $(-0.0949, 0.248)$ at the causal limit. As the radius contracts with $\mathcal{M}_{\rm rest} = \text{const}$, the orange path follows $\lambda = 0$, and the circle denotes the critical point $(0, 0.189)$ of instability; the blue paths (I), (II), (III) follow $\mathcal{M}_{\rm rest}\sqrt{|\lambda|} = 0.02(\lambda < 0), 0.01(\lambda > 0)$, $0.02(\lambda > 0)$, respectively.

seen also from the fact that *it is the unique dimensionality that allows stable hydrostatic equilibrium with positive cosmological constant.* From Fig. 4.1, we see that for $\lambda > 0$ stable hydrostatic equilibrium exists only between some upper bound and lower bound of compactness, and the stable region of compactness diminishes as λR^2 increases; for $\lambda < 0$, the stable region enlarges as $\left|\lambda R^2\right|$ increases until the critical compactness $\mathcal{C}_3 = 0.248$ at causal limit $v(0) \equiv v_c = 1$. However, bound states no longer exist well before this critical point. The orange path ($\lambda = 0$) will gravothermally transition from a stable region into an unstable one after passing critical compactness $\mathcal{C}_3 = 0.189$ and the collapse into BH might ensue. The blue path (I), which follows $\mathcal{M}_{\rm rest}\sqrt{|\lambda|} = 0.02(\lambda < 0)$, will be gravothermally transitioning from the stable region into the unstable one after hitting the marginal stable curve if it starts from the region of bound states; while the blue path (II),

which follows $\mathcal{M}_{\rm rest}\sqrt{|\lambda|} = 0.01(\lambda > 0)$, starting from the unstable region could directly collapse into the stable region of gravothermal evolution until exceeding the upper critical compactness; however, if the mass is sufficiently heavy as blue (dashed) path (III) with $\mathcal{M}_{\rm rest}\sqrt{|\lambda|} = 0.02(\lambda > 0)$, there is no long-lived gravothermal evolution of the fluid.

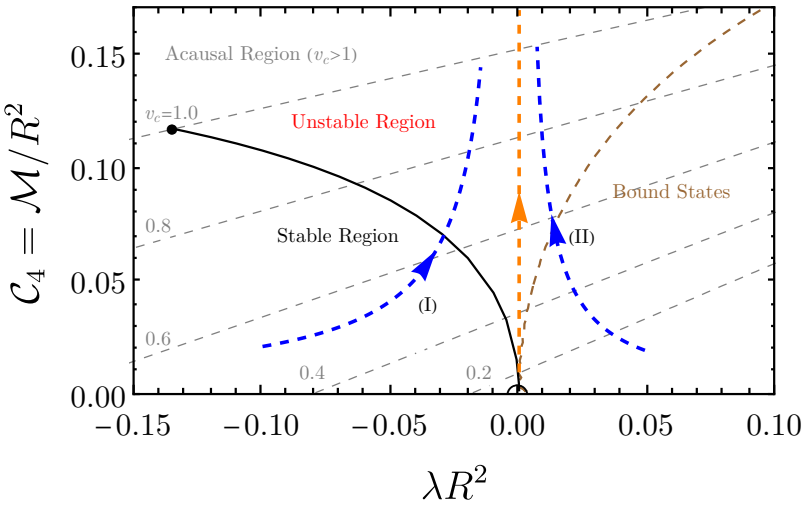

Figure 4.2: $\mathcal{C}_4 - \lambda R^2$ phase diagram of homogeneous fluid spheres in (4+1) dimensions. Bound states are to the right of the brown dashed line. The stable and unstable regions are separated by the marginal stable curve (black solid), and the black dot denotes the end point $(-0.135, 0.118)$ at the causal limit. As the radius contracts with $\mathcal{M}_{\rm rest} = \text{const}$, the orange path follows $\lambda = 0$, which is unbound; the blue paths (I), (II) follow $\mathcal{M}_{\rm rest}|\lambda| = 0.002(\lambda < 0), 0.001(\lambda > 0)$, respectively.

On the other hand, in Fig. 4.2, we see that for $N = 4$ there is no stable hydrostatic equilibrium for $\lambda \geq 0$. A stable region emerges if $\lambda < 0$, and the critical compactness increases as $\left|\lambda R^2\right|$ increases until $\mathcal{C}_4 = 0.118$ at $v_c = 1$. Nevertheless, no bound state exists in the domain of $\lambda \leq 0$. For instance, there is no stable bound state along the orange dashed path ($\lambda = 0$). Although the blue dashed path (I), following $\mathcal{M}_{\rm rest}|\lambda| = 0.002(\lambda < 0)$, could transition from the stable region into an unstable one, it is by no means gravothermal as no static bound state is available along this path. Finally, the blue dashed path (II), which

N	$\mathcal{C}_N$	λR^2	$\langle\gamma\rangle = \gamma_{\rm cr}$
2	0.518001	-0.060912	1.81893
3	0.248179	-0.094853	1.56387
4	0.117505	-0.134605	1.43352
5	0.062846	-0.151149	1.35328
6	0.037099	-0.154395	1.29861
7	0.023595	-0.151406	1.25884

Table 4.1: End points of marginal stable curves for $N = 2, 3, 4, 5, 6$, and 7 with $\lambda < 0$ at causal limit $v_c = 1$.

follows $\mathcal{M}_{\rm rest}|\lambda| = 0.001(\lambda > 0)$, always lies in the unstable region no matter if it starts from a bound or an unbound state. The phase diagrams are similar for $N > 4$ but it becomes less compact on the marginal stable curves as N increases. In Table 4.1, we show the end points ($v_c = 1$) of the marginal stable curves for $N = 2, 3, 4, 5, 6$ and 7.

Remarkably, the region of bound states *never* overlaps with the stable region for $N \geq 4$. Dynamically, if the fluid starts from any point on the dashed paths in Figs. 4.1 and 4.2, BH formation, dispersal of the fluid to infinity, or gravitationally bound and oscillatory states could be the possible outcome depending on the initial velocity perturbation and density [132], which deserves further investigation.

4.4 Fluid disks in (2+1) dimensions

By matching the junction conditions, the mass of the BTZ BH is related to the gravitational mass of the fluid disk by [134]

$$\mathcal{M}_{\rm BTZ} = 2\mathcal{M} - 1, \tag{4.8}$$

thus $\mathcal{M} > 0.5$ is the threshold to have $\mathcal{M}_{\rm BTZ} > 0$, the excited state, if collapse ensues. Dynamical collapse into BTZ BHs and naked singularities has been shown possible from pressureless dust [135]. However, static stars of perfect fluid qualitatively differ in their behavior from static stars of dust [114]; it is curious to see if the GR instability will be triggered in (2+1), especially under the influence of a negative cosmological constant.

Therefore we have to examine the critical adiabatic index for $N = 2$:

$$\gamma_{\rm cr(GR)} = -1 + \sum_{j,k=0,1,...} f^{(2)}_{jk} \mathcal{M}^j \left(\lambda R^2\right)^k \tag{4.9}$$

starts from $-1 + f^{(2)}_{00} = -1 + \gamma_{\rm cr(NG)} = 0$ with "post-Newtonian" corrections, thus *the Einsteinian stars are much stabler than Newtonian stars in (2+1).* We note that for $N = 2$ the "compactness" parameter reduces to $\mathcal{M}$, the gravitational mass of the disk itself. That manifests the reason why there is no Buchdahl-like bound in (2+1) dimensions [117]. Furthermore, this also implies that *a self-gravitating disk cannot gravothermally evolve to a singular state on its own* because the compactness $\mathcal{M}$ always *decreases* with $\mathcal{M}_{\rm rest} = {\rm const}$ due to the gravothermal dissipation. However, it can become unstable by external agents, such as compression by external force while adding mass to keep $\mathcal{M}$ large [134].

To illustrate, we see from Fig. 4.3 that as the negative cosmological constant is switched on, there is no unstable configuration for $\gamma_{\rm cr}$ to cross $\langle\gamma\rangle$ of the fluid disk as the fluid mass grows from $\mathcal{M} = 0$ to 0.5 (the would-be $\mathcal{M}_{\rm BTZ} = -1$ to $\mathcal{M}_{\rm BTZ} = 0$), which means there is no instability for a fluid disk to collapse into a naked singularity from an ideal fluid within causal region $v_c \leq 1$. Therefore, along the solid blue path (I), $\mathcal{M}_{\rm rest} = 0.5$

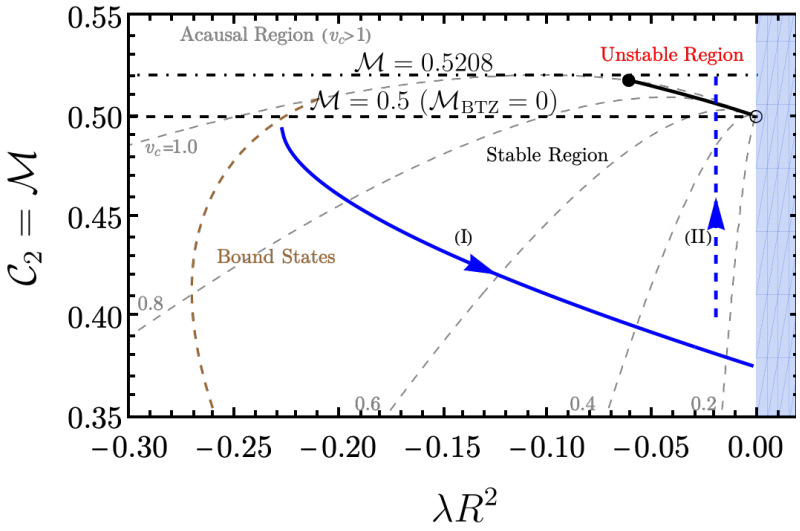

Figure 4.3: $\mathcal{C}_2 - \lambda R^2$ phase diagram of homogeneous fluid disks in (2+1) dimensions. Bound states are to the right of the brown dashed line. The stable and unstable regions are separated by the marginal stable curve (solid black), and the black dot denotes the end point $(-0.0609, 0.518)$ at the causal limit. The shaded region ($\lambda > 0$) is forbidden to have hydrostatic equilibrium. The circle denotes $\mathcal{M} = 0.5$ exactly at $\lambda = 0$, which is independent of central velocity dispersion. The upper bound of fluid mass is $\mathcal{M} = 0.5208$ at the causal limit. The region under $\mathcal{M} = 0.5$ is stable, which means that no homogeneous fluid disk can trigger the instability and collapse into a naked singularity. Path (I) follows $\mathcal{M}_{\rm rest} = 0.5$ under gravothermal evolution; (II) follows $\lambda R^2 = -0.02$ by adding mass. Only path (II) could transition into a BTZ BH under the causal limit.

in Fig. 4.3, the compactness decreases from $\mathcal{M} = 0.495$ to 0.375 during the gravothermal shrinking, it never meets the instability. That is to say, although dissipation or thermal radiation can make the disk shrink naturally given $\lambda = \text{const}$, it never drives the fluid into an unstable state. Nevertheless, in the range $-0.061 \lesssim \lambda R^2 < 0$ a BTZ BH could emerge from a collapsing fluid of $0.5 < \mathcal{M} \lesssim 0.518$ without violating causality. For example, under the background $\lambda = \text{const}$ this can be achieved by "adding more mass" to the fluid disk, while the radius remains fixed, as shown by the dashed blue path (II): $\lambda R^2 = -0.02$ in Fig. 4.3.

4.5 Discussions and implications

In the context of gravothermal evolution, we have examined the dynamical instability of a self-gravitating fluid sphere in $(N+1)$-dimensional spacetime by adopting homogeneous fluid solutions. Although the critical $\mathcal{C}_N$ may vary quantitatively depending on the density distribution, the main conclusion generally holds as it is based on the three assumptions made implicitly [134]: (i) The monatomic fluids obey the first law of thermodynamics, and the pressure is isotropic due to equipartition theorem. (ii) The particles composing the fluid follow the mass-energy dispersion relation. (iii) Gravity is governed by Einstein field equations in $(N+1)$ dimensions.

From the dynamical instability viewpoint, we can reexamine why (3+1) is privileged rather than why it must be (3+1). If BH is the pathway to generate a baby universe [136, 137, 138, 139, 140, 141], the collapsing matter squeezing into a $(N+1)$-dimensional BH near the classical singularity would result in a new-born universe of ar-

bitrary dimensions. If the spacetime dimensionality reshuffling [142] is a random process in the reign of quantum gravity near singularity, it repeats this process again and again until the new-born universe is just (3+1)-dimensional, in which the fluid sphere is stable but not too stable. As a self-gravitating fluid sphere (or a star) in $N \geq 4$ is genuinely subject to dynamical instability, and could transition into a BH automatically without undergoing the stage of long-lived gravothermal evolution. Although a fluid star can be stabilized by introducing a negative cosmological constant, no gravitationally bound state of a monatomic fluid could exist in this region.

Remarkably, (3+1) is the unique dimensionality that allows stable hydrostatic equilibrium with positive cosmological constant. Given the cosmological constant observed [143] (or $\ell \sim 10^{61}\ell_{\rm Pl}$, where $\ell_{\rm Pl}$ is the Planck length), the mass of a virialized stellar object, e.g., dark matter halo, must be $\mathcal{M} \ll 0.02\ell c^2/G_3 \sim 10^{21}\ M_\odot$ (see Fig. 4.1) in order to avoid the dynamical instability and a possible BH formation from its direct collapse. However, a big crunch singularity would form if $\mathcal{M} > (1/3\sqrt{3})\ell c^2/G_3 \sim 10^{22}\ M_\odot$ [129]. On the other hand, (2+1)-dimensional gravity is bizarre. The fluid disk cannot gravothermally evolve into a singular state through dissipation, but a BTZ hole could emerge from a collapsing fluid disk with external agents, while a naked singularity cannot emerge from a fluid disk, which supports the cosmic censorship conjecture [144].

Chapter 5

Dynamical Instability in the Quantum Limit

Black holes (BHs) are the inevitable consequence of gravitational collapse regarding Einstein's general relativity (GR). In conventional astrophysics, a BH of solar-mass scale results from a dying star; while much massive BHs could emerge from the direct collapse of the pristine gas [6, 7, 2] without undergoing the star formation. Given that, various mechanisms to produce massive BHs have been proposed in the literature [2] in order to account for those at central galaxies. However, the origin of high-redshift ($z \gtrsim 6-8$) supermassive black holes (SMBHs) remains a big puzzle [5, 9, 10, 37, 39, 40, 145, 146, 147] (see [1, 148, 149, 150] for a review). By contrast, there are other possibilities, including primordial black holes (PBHs) produced from large density fluctuations near the end of inflation [151, 152, 153, 154, 155]; PBHs generated from the first-order phase transition before the matter-radiation equality [156, 157, 158, 159, 160, 161]; or astrophysical BHs

from turbulence of cold gas flows [162]. Moreover, the idea of BH formation from the collapse of dark matter has been extensively explored. This especially includes those BHs that originate from the collapsed halos of non-cold dark matter, such as self-interacting dark matter [20, 22, 41, 65] or the ultralight dark matter [163]. The idea could also explain those BHs in the mass gap [164].

However, it is necessary to carefully examine the corresponding dynamical instability to form the BH, which, in turn, could bridge the theories of dark matter and the BH populations. The dynamical instability of the self-gravitating system, in the framework of GR, was first studied in the context of supermassive stars [55, 58, 165, 166, 167, 168]. As a gravitationally-bound thermal system, a supermassive star evolves and shrinks due to thermal dissipations until triggering the dynamical instability, and results in the seed BHs. Although the exact conditions rely on the accretion models (see [148, 149] for a review), a star generally tends to collapse into a BH when its gravitational energy is comparable with the mass energy, i.e., $GM^2/R \sim Mc^2$, where R is characteristic radius of the star. One can then roughly examine the instability regarding the compactness parameter $C \equiv GM/c^2R$. Other factors, such as the cosmological constant [109, 110, 111, 169] and space dimensionality [169], also impact the stability.

In Ref. [56] (Chapter 3), we show that the dynamical instability of gravothermal spheres in the classical limit, in which the local distribution function of the gaseous sphere is a truncated Maxwell-Boltzmann (MB) distribution, agrees well with those from the N-body simulations [62, 63, 64]. However, particles in nature, making up the ordinary matter or the dark matter, follow the quantum statistics and have phenomena such as *Pauli*

blocking, *Bose-Einstein condensation (BEC)*, and *particle production/annihilation*. Those phenomena are hard to deal with by N-body simulation.

In this chapter, we apply the truncated quantum distributions and focus on the impact of the quantum pressure and the pair production/annihilation on the dynamical instability on a self-gravitating *quantum* gaseous system. The resulting condition for the dynamical instability is generic and is applicable to systems made of baryonic matter, dark matter, and other exotic particles. As a concrete example, we apply the condition to DM systems that seed BHs from their collapse. First, we derive the equation-of-state (EoS) from the distribution function following the methodology in [56]. Second, by solving the Tolman-Oppenheimer-Volkoff (TOV) equation [70, 71] given that EoS, one can determine if the mass sphere is gravitationally bound or not. Lastly, we examine its stability according to the Chandrasekhar's method [55]. The resulting condition for the dynamical instability is generic and applicable to systems made of baryonic matter, dark matter, and other exotic particles. In Supplemental Material, we provide additional details and numerical results.

5.1 The truncated Fermi-Dirac and Bose-Einstein models

We introduce a truncated quantum distribution function [56, 77] for the ideal-gas sphere,

$$f_\eta(\epsilon) = \begin{cases} \frac{1-e^{(\epsilon-\epsilon_c)/k_BT}}{e^{(\epsilon-\mu)/k_BT}-\eta}, & \epsilon \leq \epsilon_c; \\ 0, & \text{otherwise} \end{cases} \tag{5.1}$$

where ϵ is the kinetic energy, ϵ_c the cutoff energy, T the temperature, and μ is the chemical potential with the particle's rest energy mc^2 subtracted off. They are functions of the radius r. k_B is the Boltzmann constant and c is the speed of light. The number factor η is $+1$

(-1) for bosons (fermions), and the quantum effect kicks in if $e^{(\epsilon-\mu)/k_BT} \lesssim 1$, or $\mu/k_BT \gtrsim 0$ as $\epsilon \geq 0$. The temperature profile is given by [56]

$$T(r) = \left(1 + \epsilon_c(r)/mc^2\right) T(R), \tag{5.2}$$

meaning the system cannot follow an isothermal distribution globally due to the *gravitational redshift* [79].

For convenience, we introduce the dimensionless variables, cutoff function $w(r) \equiv \epsilon_c(r)/k_BT(r)$, degeneracy $\alpha(r) \equiv \mu(r)/k_BT(r)$, and $b \equiv k_BT(R)/mc^2$. The cutoff function is connected to the *degeneracy contrast* to that of the boundary

$$w(r) = \alpha(r) - \alpha(R) \tag{5.3}$$

by Tolman-Klein law [79, 80] for a gravothermal system. Although we consider a specific truncated model in this work, it must be emphasized that Eqs. 5.2 and 5.3 are only based on laws of thermodynamics and GR. They are *generic* and independent of specific forms of the truncation. One can then determine the number density n, energy density ρ, internal energy density u, and pressure p, as functions of b, w and $\alpha(R)$. Thus once the profile $w(r)$ is solved by the TOV equation [56] for a given set of boundary conditions, b, $w(0)$ and $\alpha(R)$, all the thermodynamic profiles are determined.

5.2 Dynamical instability

Qualitatively, to trigger the onset of dynamical instability, the system needs to be in the relativistic limit, which imposes constraints on b and $w(0)$. It is indicative to consider their product, the normalized cutoff energy [56]:

$$bw(r) = \frac{\epsilon_c(r)/mc^2}{1 + \epsilon_c(r)/mc^2}. \tag{5.4}$$

In the ultrarelativistic limit $\epsilon_c \gg mc^2$, $bw \to 1$; in the non-relativistic limit, $bw \to 0$. Since $b = k_B T(R)/mc^2$ determines the temperature at the core boundary, a higher b value indicates a hotter thermal bath. Either high b with small cutoff w or vice versa can drive the core into relativistic regime, i.e., $bw \lesssim 1$. In the former situation, the *evaporation* effect is significant and one needs to take into account the pair production/annihilation effect if $b \lesssim 1$; in the latter of $w \gg 1$ the distribution reduces to the usual form without a truncation, while Pauli blocking kicks in if $\alpha(R) > -w$. To quantitatively determine the instability, however, we resort to the Chandrasekhar's criterion [55], as this method is physically intuitive. Specifically, one can determine the marginally stable configuration $\langle\gamma\rangle = \gamma_{\rm cr}$ [56] for a given set of $\{b, w(0), \alpha(R)\}$.

5.3 Gravitationally bound systems

When a gravitationally bound sphere contracts, it will heat up by converting its gravitational energy. To examine whether the system remains gravitationally bound in

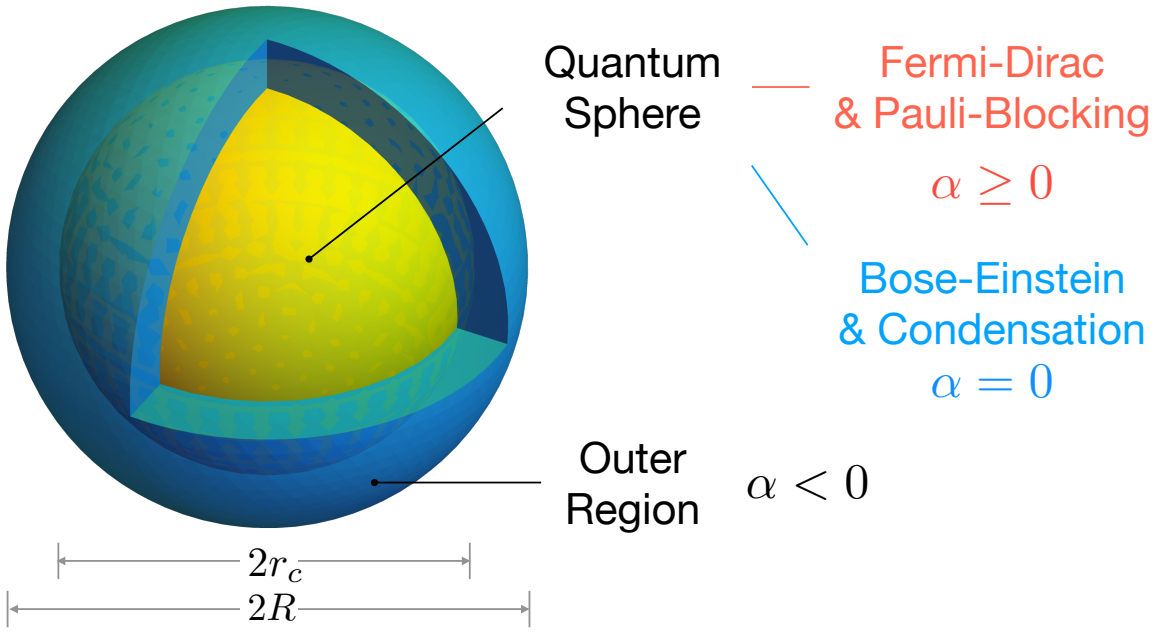

Figure 5.1: Schematic cartoons of quantum spheres for the Fermi-Dirac (FD) or the Bose-Einstein (BE) statistics. The values of α is ≥ 0 $(= 0)$ for the FD (BE) quantum sphere. The quantum sphere is surrounded by the outer region with $\alpha < 0$. The outer radius for the quantum sphere and outer region are r_c and R, respectively.

GR, it is pivotal to differentiate the *gravitational* mass M with the *rest* mass $M_{\rm rest}$ of the sphere [82, 56]. M involves not only the thermal but also the gravitational energy of the particles bound into the sphere. Whereas $M_{\rm rest}$ is the sum of the total rest mass of the particles as if they were dispersed to infinity, thus $M < M_{\rm rest}$ is required for the sphere to be gravitationally bound. In the regime $k_B T \sim mc^2$, the pair production/annihilation of (anti)particles, $\chi\bar{\chi} \leftrightarrow$ radiations, is relevant to make gravitationally bound spheres unbound. Here the radiations could be the Standard Model particles such as photons or neutrinos, or dark radiations such as dark photons, whose rest mass can be ignored and the equation of state $p_{\rm rad}/\rho_{\rm rad} = c^2/3$. For a particle χ with chemical potential μ and degeneracy α, the corresponding quantities for its antiparticle $\bar{\chi}$ are given by $\bar{\mu} = \mu - 2mc^2$ or $\bar{\alpha} = \alpha - 2mc^2/k_B T$. With this replacement for antiparticles, the (net) number density becomes

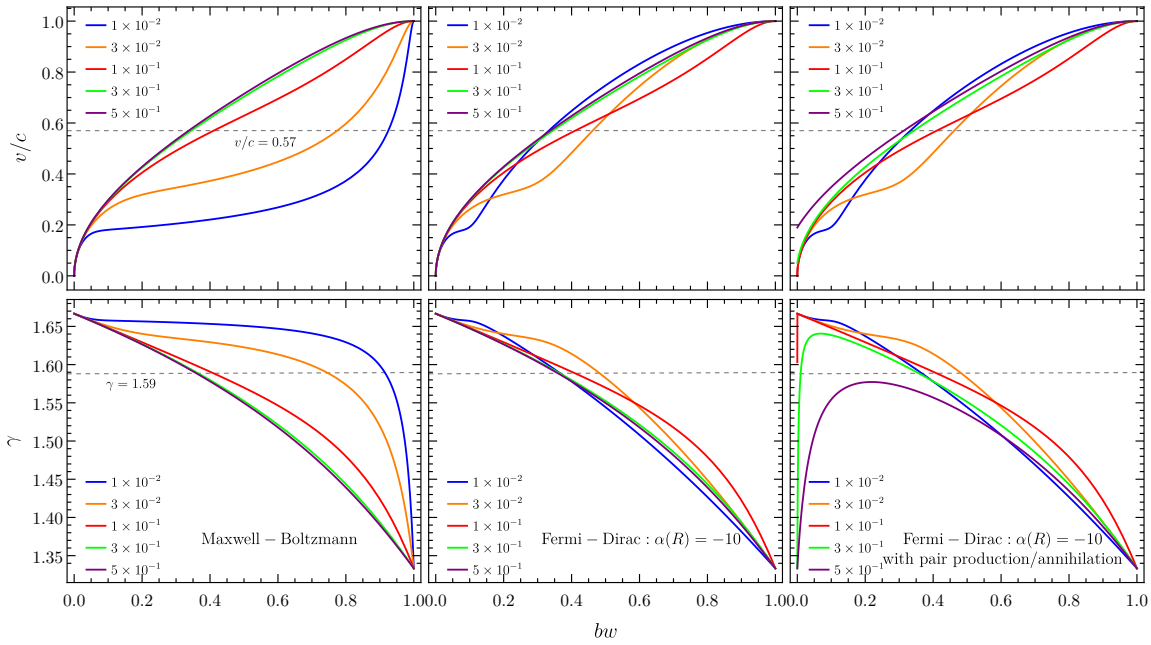

Figure 5.2: EoS for truncated MB and FD distributions with and without pair production/annihilation effect: 3D velocity dispersion $v/c = \sqrt{3p/\rho c^2}$ and adiabatic index γ vs. normalized cutoff energy $bw = \epsilon_c/(mc^2 + \epsilon_c)$ for $b = k_B T(R)/mc^2 = (0.5,\ 0.3,\ 0.1,\ 0.03,\ 0.01)$. For FD model, we take $\alpha(R) = -10$ for illustration. The 3D velocity dispersion (adiabatic index) can increase (decrease) significantly even in low temperature due to the Fermi-degeneracy pressure when $\alpha = w + \alpha(R) > 0$. In high temperature ($b \gtrsim 0.1$) regime, evaporation (lower cutoff w) makes pair production/annihilation effect more significant because the (massless) radiations dominate the EoS.

$n = n_\chi - n_{\bar\chi}$ and the energy density of radiation $\rho_{\rm rad} = 2\rho_{\bar\chi}$. The abundance ratio of antiparticles to particles, $n_{\bar\chi}/n_\chi \simeq e^{-2/b} = e^{-2mc^2/k_B T(R)}$, is Boltzmann suppressed if $b \ll 1$. To examine the stability, however, we have to adopt the effective adiabatic index γ (see Appendix H) for this two-fluid (χ + radiations) model when $b \gtrsim 0.1$. In addition, as the mass of the resultant radiations through pair annihilation is negligible in the sphere, the rest mass $M_{\rm rest}$ decreases as the temperature increases. If the temperature is sufficiently high ($b \gtrsim 0.5$), the sphere becomes *unbound* as $M \gtrsim M_{\rm rest}$.

5.4 Fermi-degeneracy pressure

For Fermi-degeneracy supported mass sphere consisting of M/m fermions with rest mass m, Landau estimated [72, 170] the gravitational energy per fermion $\sim GMm/R$; while the typical separation between fermions is $R/(M/m)^{1/3}$, and thus the relativistic Fermi energy $\sim \hbar c(M/m)^{1/3}/R$. In order for the degeneracy pressure to balance the gravitational attraction, $GMm/R \sim \hbar c(M/m)^{1/3}/R$. Therefore, Landau's estimate gives the maximal mass sphere $M \sim m_{\rm Pl}^3/m^2$, with $m_{\rm Pl} = (\hbar c/G)^{1/2}$ the Planck mass. Thereafter, the folklore say that the quantum degeneracy pressure prevents the gravitational collapse. However, this estimate is in the context of Newtonian gravity and concerns only the *equilibrium condition*, rather than its *stability*.

To see how the quantum pressure plays a role, we have to first examine the degeneracy $\alpha(R)$. The numerical results for a quantum system with $\alpha(R) \lesssim -50$ are almost the same as the truncated MB for a classical system [56], thus we take $\alpha(R) = -50$ as the benchmark for the classical regime. In terms of physical units, however, the border between classical and quantum regimes is determined by $n\lambda_{\rm dB}^3 = g$, where $g = 2s + 1$ is the spin multiplicity and $\lambda_{\rm dB}$ the de Broglie thermal wavelength [56].

For Fermi-Dirac (FD) statistics, we categorize two cases: (i) $\alpha(R) < 0$, but the sphere is partially degenerate $\alpha(r) \geq 0$ for $r \leq r_c < R$, where $\alpha(r_c) = 0$, and (ii) $\alpha(R) \geq 0$, the sphere is completely degenerate $\alpha(r) > 0$ for $r < r_c = R$, see Fig. 5.1 for illustration. Before examining the stable/unstable configurations, we first discuss the stiffness of the EoS by its adiabatic index γ. We take $\alpha(R) = -10$, for example, in Fig. 5.2. At low $b = 10^{-2}$,

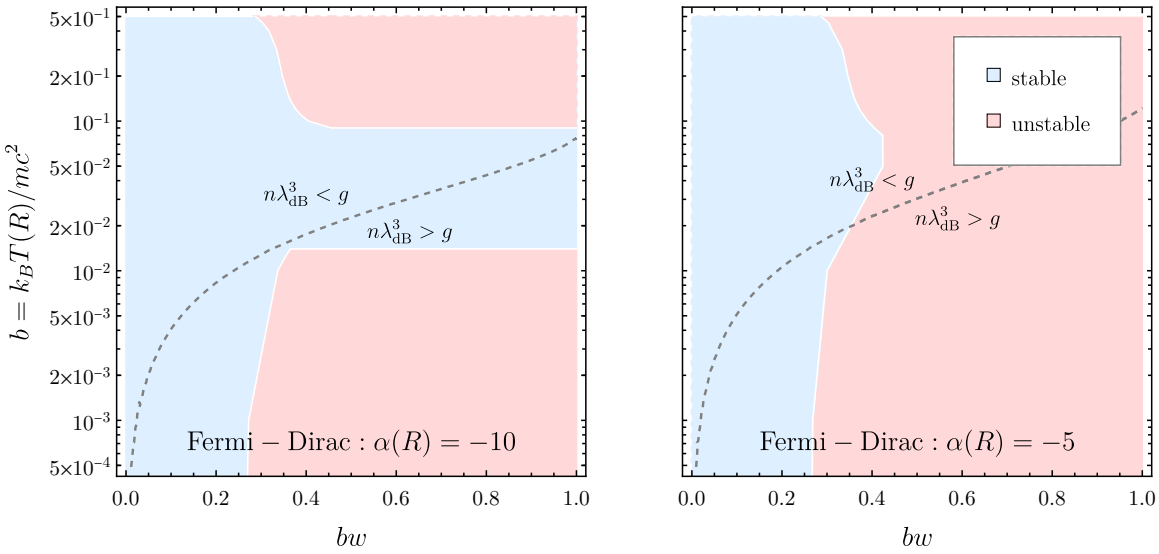

Figure 5.3: Central normalized cutoff energy $bw(0) = \epsilon_c(0)/\left(mc^2 + \epsilon_c(0)\right)$ vs. boundary temperature $b = k_B T(R)/mc^2$. The stable (blue shaded) and unstable (red shaded) for FD statistics. The gray dashed line delineates the border between the classical ($n\lambda_{\rm dB}^3 < g$) and the quantum ($n\lambda_{\rm dB}^3 > g$) regimes.

the EoS gets *softened* (γ decreases) significantly when $w \gtrsim 30$, compared to the MB model, as the particles become relativistically ($bw \gtrsim 0.3$) degenerate ($\alpha = w + \alpha(R) > 0$) by Pauli blocking. Although for $b \gtrsim 0.5$ the radiations from pair annihilations soften the EoS, it can barely remain gravitationally bound due the evaporation effect ($w \lesssim 0.6$). However, for completely degenerate case $\alpha(R) \gtrsim 0$, the threshold decreases down to $b \gtrsim 0.4$ to be gravitationally unbound (see Appendix I). This is because the Pauli blocking takes energy to bind fermions together. Thus slightly lower temperature is sufficient to break them apart.

For partially degenerate spheres, there is no unstable configuration for $10^{-2} \lesssim b \lesssim 0.1$ if $\alpha(R) = -10$, see Fig. 5.3 (left panel). In contrast to the classical spheres, the instability can still happen in the low $b \lesssim 10^{-2}$ is due to the Fermi-degeneracy pressure as $\alpha(r) = w(r) + \alpha(R) > 0$ (degenerate regime) with $bw(0) \simeq 0.3$ (relativistic regime);

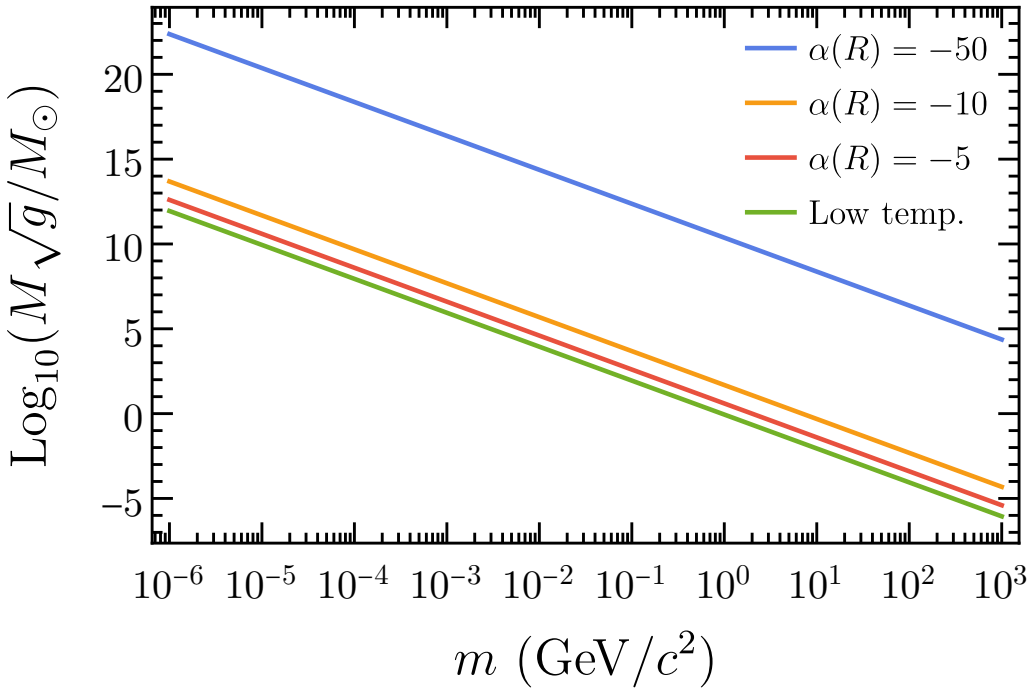

Figure 5.4: Critical mass M, supported by thermal pressure for $\alpha(R) = (-50, -10, -5)$ in high temperature $0.1 \lesssim b \lesssim 0.5$; supported by degeneracy pressure in low temperature $b \lesssim 10^{-2}$, as functions of particle mass m.

while the high $b \gtrsim 0.1$ is due to the highly random thermal pressure as in the classical MB case. *The gap in temperature exists because of the thermal effect interferes the quantum degeneracy, but not sufficiently strong to reach the GR instability.* Interestingly, this gap shrinks as $\alpha(R)$ increases and vanishes for $\alpha(R) \gtrsim -5$, and thus the instability becomes b-independent, see Fig. 5.3 (right panel). Generally for $\alpha(R) < 0$, one can extrapolate the temperature b below which the degeneracy pressure is significant to trigger the instability by observing $b\alpha(R) \gtrsim -0.1$ or $-\mu(R) \lesssim 0.1mc^2$, equivalently.

At the marginally stable point $\langle\gamma\rangle = \gamma_{\rm cr}$, the critical compactness $C \simeq 0.04$–0.08 slightly increases as $\alpha(R)$ increases in high temperature $b \gtrsim 0.1$; whereas $C \simeq 0.04$–0.13 is more compact for $b \lesssim 10^{-2}$ owing to the Fermi-degeneracy pressure. As for the critical

mass, Landau's estimate [170] gives the critical mass $M \sim m_{\rm Pl}^3/m^2$, while the exact values in high and low temperature thermal baths, depending on $\alpha(R)$, can be quite disparate. At the onset of instability, we find that in high temperature $0.1 \lesssim b \lesssim 0.5$, the critical mass,

$$M \gtrsim 0.2\ g^{-1/2} e^{-\alpha(R)/2} m_{\rm Pl}^3/m^2 \tag{5.5}$$

for $\alpha(R) \leq 0$. Therefore *it is easier to have heavier BH seeds in the classical regime*, $\alpha(R) \ll -1$, see Fig. 5.4. For example, taking $\alpha(R) = -50$ with $mc^2 = 1$ GeV gives $M \gtrsim 10^9\ M_\odot$. On the other hand, in low temperature $b \lesssim 10^{-2}$ the critical mass,

$$M \gtrsim 0.54\ g^{-1/2} m_{\rm Pl}^3/m^2 \tag{5.6}$$

universally in the nearly degenerate regime $\alpha(R) \gtrsim -10$, and it still holds for $b \gtrsim 10^{-2}$ when $\alpha(R) \gtrsim -1$ and ≥ 0.

5.5 Bose-Einstein condensation

The concept of BEC forming a self-gravitating bound state, known as a boson star, traces back to Ref. [171, 172, 173, 174, 175]. If there is no self-interaction between the ground state bosons, the supporting pressure, primarily given by Heisenberg's uncertainty principle, leads to a condensate of mass $M \sim m_{\rm Pl}^2/m$, which is much smaller than the Chandrasekhar mass, approximately $M \sim m_{\rm Pl}^3/m^2$. On the other hand, BEC with attractive self-interaction is inherently unstable, even in the absence of gravity [176]. However, it can form a stable

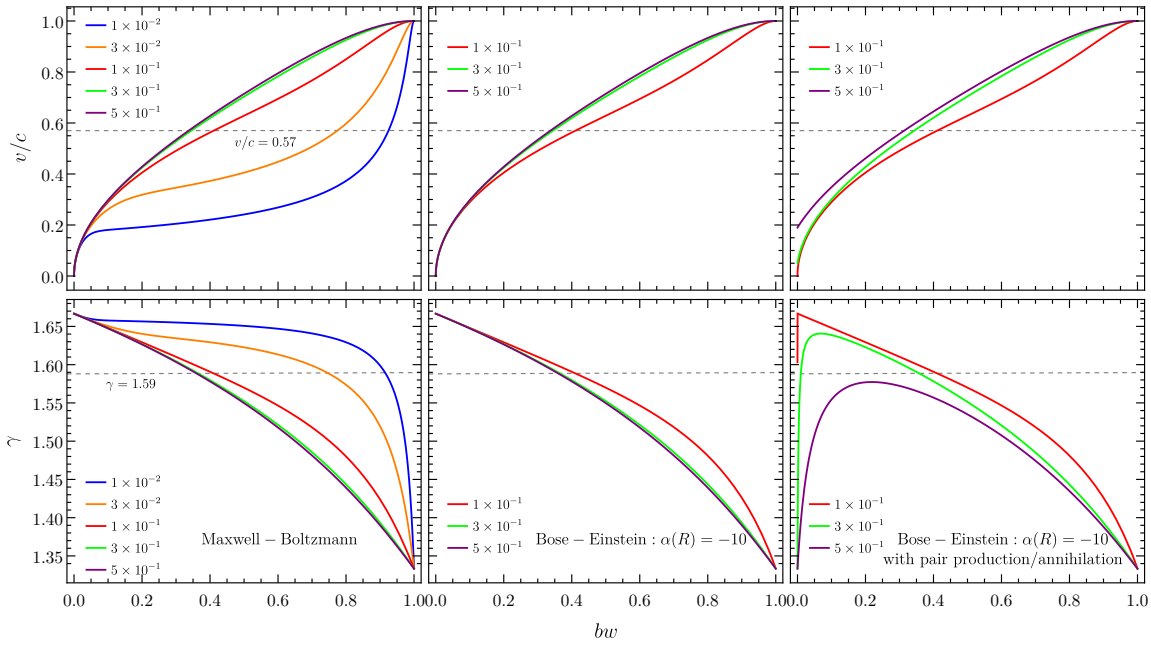

Figure 5.5: EoS for truncated MB and BE distributions with and without pair production/annihilation effect: 3D velocity dispersion $v/c = \sqrt{3p/\rho c^2}$ and adiabatic index γ vs. normalized cutoff energy $bw = \epsilon_c/(mc^2 + \epsilon_c)$ for $b = k_B T(R)/mc^2 = (0.5,\ 0.3,\ 0.1,\ 0.03,\ 0.01)$. For BE model, we take $\alpha(R) = -10$ for illustration. It is required that $\alpha = w + \alpha(R) < 0$ and the behavior is similar to MB if there is no condensate. In high temperature ($b \gtrsim 0.1$) regime, evaporation (lower cutoff w) makes pair production/annihilation effect more significant because the (massless) radiations dominate the EoS.

gravitationally bound sphere, roughly on the order of $m_{\rm Pl}^3/m^2$, even with a small *repulsive* self-interaction [174], which can be comparable to conventional stellar objects. Additionally, the repulsive nature can be realized through particle physics considerations [177], see also the recent studies within the context of cosmology [178, 179, 180] and structure formation [163, 181, 182, 183, 184, 185].

For Bose-Einstein (BE) statistics it must be $\alpha(r) \leq 0$, thus $w(r) = \alpha(r) - \alpha(R) \leq -\alpha(R)$ and $w(r \leq r_c) = w_{\rm max} = -\alpha(R)$ as $\alpha(r \leq r_c) = 0$. Because of the cutoff $w_{\rm max}$, we find $n\lambda_{\rm dB}^3 < g$ for BE statistics, where $g = 2s + 1$ is the spin multiplicity and $\lambda_{\rm dB}$

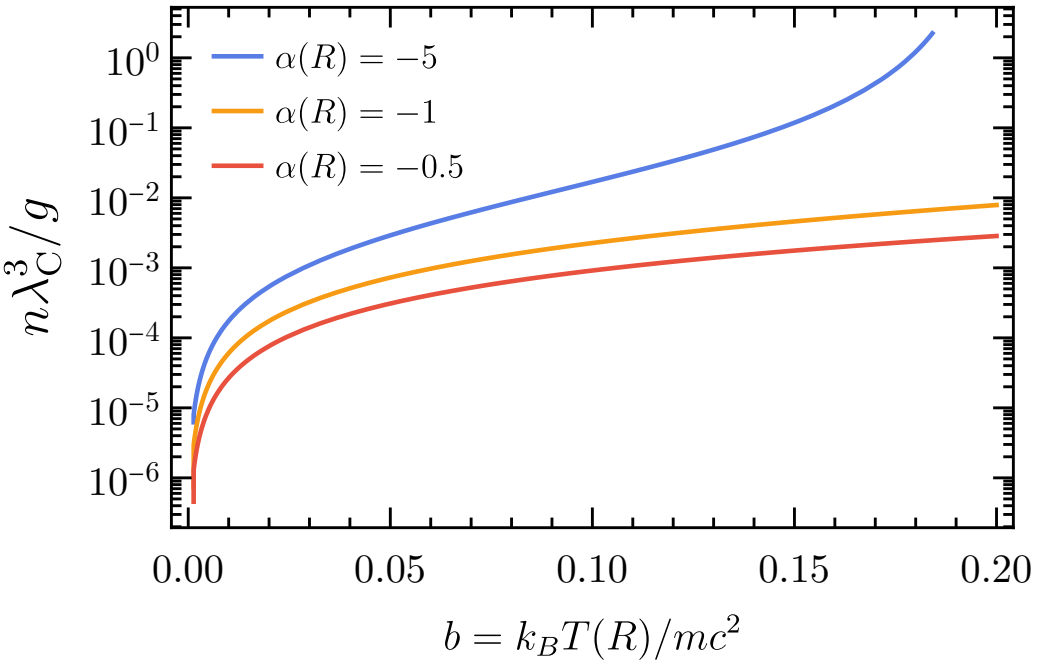

Figure 5.6: Number density $n\lambda_C^3/g$ as functions of critical temperature $b_{\rm bec} = k_B T_{\rm bec}(R)/mc^2$ given the phase space in Eq. 5.1 saturated at $w_{\rm max} = -\alpha(R)$, where $\lambda_C = \hbar/mc$ is the Compton wavelength.

the de Broglie thermal wavelength [56]. And the EoS behaves as the MB case at $b > 0.1$, see Fig. 5.5; whereas it becomes softened due to pair annihilations, similar to the FD case [186]. Thus the system stays classical unless BEC is triggered at $r \leq r_c$ to enter the quantum regime $n\lambda_{\rm dB}^3 \gtrsim g$. We assume $r_c = 0$ (R) if the system consists 0% (100%) BEC, see Fig. 5.1 for illustration.

BEC can happen even in the presence of antibosons [187], and one can determine the critical temperature of the BEC formation $b_{\rm bec}(n(r))$ when the particle occupation number n saturates the phase space in Eq. 5.1 at $w_{\rm max} = -\alpha(R)$. For a given temperature, the BEC formation threshold is lower if $\alpha(R)$ increases, see Fig. 5.6. In addition, according to $bw < 1$ in Eq. 5.4, BEC will form well before reaching the ultrarelativistic limit as

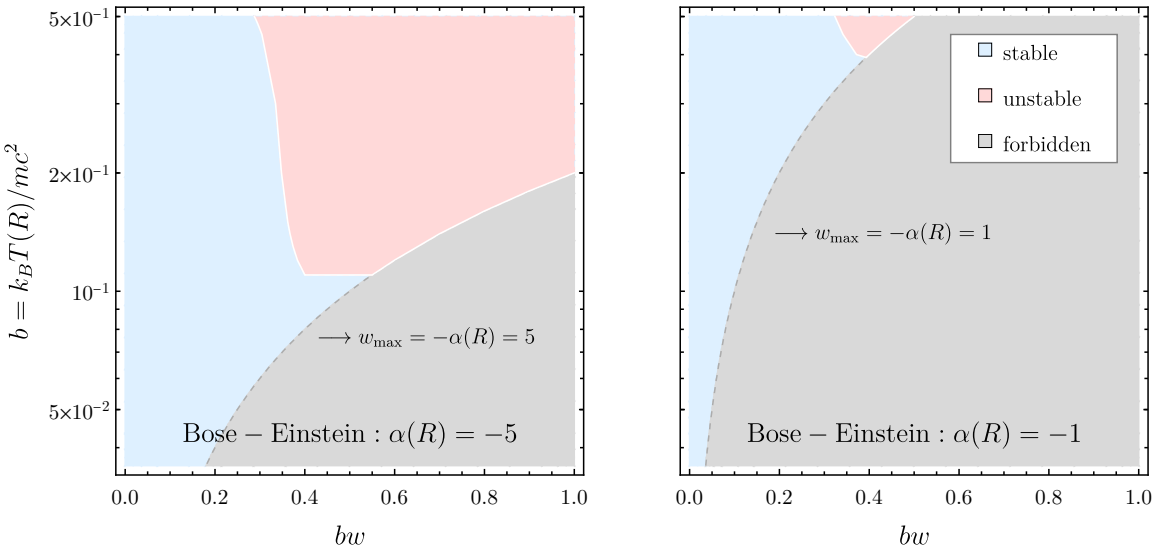

Figure 5.7: Central normalized cutoff energy $bw(0) = \epsilon_c(0)/\left(mc^2 + \epsilon_c(0)\right)$ vs. boundary temperature $b = k_B T(R)/mc^2$. The stable (blue shaded) and unstable (red shaded) for BE statistics. The gray dashed line delineates the available ($w < w_{\max}$) and the forbidden ($w > w_{\max}$) regions (gray shaded).

long as $bw_{\max} = -b\alpha(R) < 1$, which implies $-\mu(R) < mc^2$ is a necessary condition. If BEC happens, we have to deal with a mixture of two fluids, with net number density $n = n_{\rm bec} + n_{\rm thermal}$, one is the *thermal* bosons $n_{\rm thermal}$ and the other is the *non-thermal* condensate $n_{\rm bec}$ residing in the ground state. In the two-fluid formalism, assuming no mutual interaction [188], the total energy density $\rho = \rho_{\rm bec} + \rho_{\rm thermal}$, and the BEC happening at $r \leq r_c$ is governed by

$$\frac{\mathrm{d}p_{\rm bec}}{\mathrm{d}r} = -\left(\rho_{\rm bec}c^2 + p_{\rm bec}\right)\frac{G\left(4\pi p r^3 + M(r)c^2\right)}{rc^2\left(rc^2 - 2GM(r)\right)}, \tag{5.7}$$

where $M(r) = 4\pi\int_0^r r'^2\rho\,\mathrm{d}r'$ and $p = p_{\rm bec} + p_{\rm thermal}$ are the enclosed gravitational mass and pressure, respectively. While the thermal bosons always saturate its phase space given

$\{b, w_{\max}\}$ for $r \leq r_c$ when BEC is present, we only need to solve $w(r)$ for $r_c < r \leq R$. As the BEC deepens the potential well and increases the cutoff energy for the thermal bosons at $r \leq r_c$, we note that Eq. 5.4 is valid only for $r > r_c$. In this case, however, one should derive $\epsilon_c(r \leq r_c)$ through gravitational redshift in temperature [79] regarding $w_{\max} = \epsilon_c/k_B T$.

5.5.1 Thermal bosons

Consider the sphere composed of purely thermal bosons, i.e., $n = n_{\text{thermal}}$ and $r_c = 0$. As there is no Fermi-degeneracy pressure for thermal bosons, *no relativistic instability will occur at low temperature without BEC*. In other words, the instability is determined by the thermal effect as the MB case. However, the threshold of the boundary temperature b to reach instability increases as $\alpha(R)$ approaches zero. We find $b \geq 0.09$ for $\alpha(R) = -10$; $b \geq 0.11$ for $\alpha(R) = -5$; whereas $b \gtrsim 0.4$ is required for $\alpha(R) = -1$ as $w(0) = w_{\max} = 1$ at the central core. The available unstable region shrinks as $\alpha(R)$ increases, see Fig. 5.7. In the regime $k_B T \sim mc^2$, the sphere becomes *unbound* as M (gravitational mass) $\gtrsim$ M_{rest} (rest mass) due to the pair production/annihilation if $b \gtrsim 0.5$; while it increases up to $b \gtrsim 0.7$ in the nearly degenerate limit $\alpha(R) = -0.5$ (see Appendix J). This is in contrast to the Pauli blocking of fermions, bosons tend to party and are easier to be gravitationally bound. Thus slightly higher temperature is required to break them apart.

5.5.2 Pure condensate

We now consider another extreme case, $n_{\text{thermal}} \ll n_{\text{bec}}$, namely the whole sphere is just a condensate, $n = n_{\text{bec}}$ with $\alpha(R) = 0$ and $r_c = R$. As a relativistic extension to Gross-Pitaevskii equation governing nonrelativistic BEC, we consider the condensate of

non-thermal bosons in the ground state to be described by a coherent scalar field φ, obeying Klein-Gordon equation, with quartic and repulsive self-interaction $V_{\rm int}(\varphi) = \frac{\lambda}{4}|\varphi|^4$ ($\lambda > 0$). The constant (*dimensionless*) self-coupling strength λ is related to the s-wave *scattering length* a_s by $\lambda \equiv 8\pi a_s/\lambda_{\rm C}$, where $\lambda_{\rm C} = \hbar/mc$ is the Compton wavelength. As a good mean-field approximation, the self-interaction range should be much smaller than the mean interparticle distance, i.e., $na_s^3 \ll 1$. Macroscopically, this interaction results in the *quantum pressure* of the condensate. In the Thomas-Fermi (*fast oscillation*) limit, $\lambda m_{\rm Pl}^2/m^2 \gg 1$, the effective EoS reads [174, 178, 189],

$$p_{\rm bec} = \frac{1}{3}\rho_\lambda c^2 \left[\sqrt{1+\rho_{\rm bec}/\rho_\lambda} - 1\right]^2, \tag{5.8}$$

where $\rho_\lambda = m/3\lambda\lambda_{\rm C}^3$ is the fiducial density. The corresponding adiabatic index

$$\gamma_{\rm bec} = \frac{4}{3}\left[1 + \frac{1}{2\sqrt{1+\rho_{\rm bec}/\rho_\lambda}}\right] \tag{5.9}$$

and number density

$$n_{\rm bec} = \frac{2}{3}\frac{\rho_\lambda}{m}\left(\sqrt{1+\rho_{\rm bec}/\rho_\lambda} - 1\right)\sqrt{3\left(1+2\sqrt{1+\rho_{\rm bec}/\rho_\lambda}\right)} \tag{5.10}$$

are obtained with the aid of mass-energy conservation $(\partial\rho/\partial n)_s = (\rho + p)/n$ [190]. We note that the EoS reduces to nonrelativistic condensate, $p_{\rm bec} \propto n_{\rm bec}^2$ and $\gamma_{\rm bec} \to 2$ as $\rho_{\rm bec} \ll \rho_\lambda$ [176, 191]; while it becomes radiationlike, $p_{\rm bec} \to \rho_{\rm bec}c^2/3$ and $\gamma_{\rm bec} \to 4/3$ when $\rho_{\rm bec} \gg \rho_\lambda$.

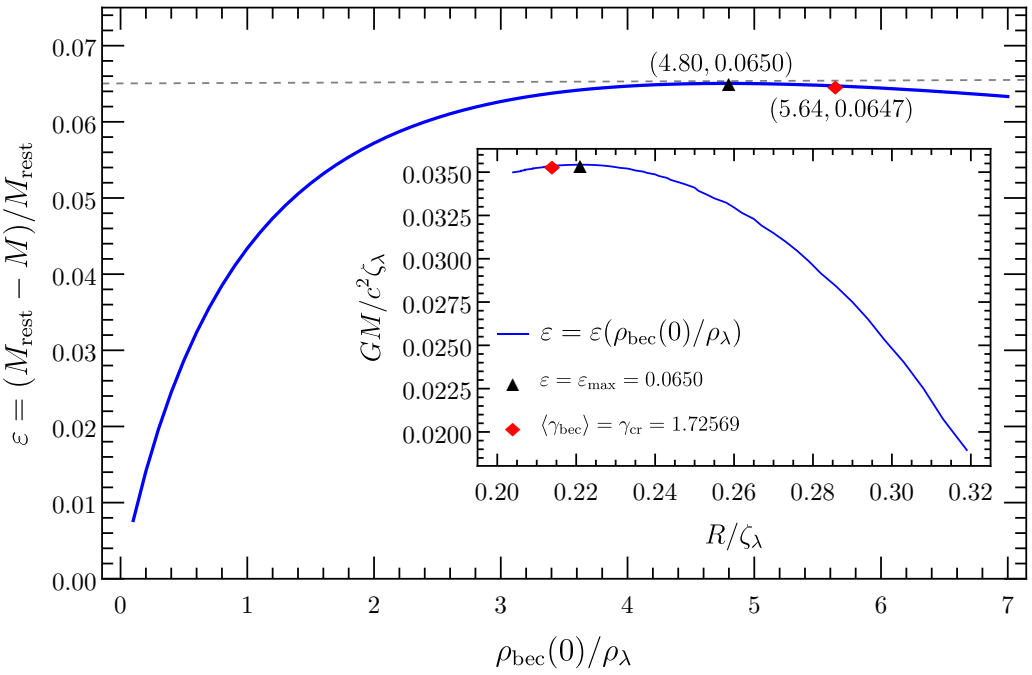

Figure 5.8: Fractional binding energy ε vs. central density $\rho_{\rm bec}(0)$ along a sequence of solutions of completely condensate spheres. The insert panel represents the mass-radius relation of the completely condensate sphere.

As the fiducial length in this scenario depends on λ, i.e., $\zeta_\lambda = \sqrt{c^2/G\rho_\lambda} = \sqrt{3\lambda}\lambda_{\rm C}(m_{\rm Pl}/m)$, the mass scale $\sim c^2\zeta_\lambda/G$ explicitly depends on λ. Compared to the turning-point method [56], Fig. 5.8 shows that the critical values $\rho_{\rm bec}(0) = 5.64\rho_\lambda$ at $\langle\gamma_{\rm bec}\rangle = \gamma_{\rm cr} = 1.72569$, which occurs shortly after the maximum of fractional binding energy $\varepsilon_{\rm max} = 0.065$ at $\rho_{\rm bec}(0) = 4.80\rho_\lambda$. At this marginal point, we find the compactness $C = GM/c^2R = 0.165$ and $M = 0.0353\ c^2\zeta_\lambda/G$, thus the critical mass

$$M \gtrsim 0.061\ \lambda^{1/2} m_{\rm Pl}^3/m^2. \tag{5.11}$$

In the Thomas-Fermi regime, it is required that $M \gtrsim \lambda^{1/2}\left(mc^2/{\rm MeV}\right)^{-2} 10^4\ {\rm M}_\odot \gg$

$\left(mc^2/\mathrm{eV}\right)^{-1} 10^{-12}$ $\mathrm{M}_\odot$. However, bound states cannot form if $\rho_{\mathrm{bec}}(0) \gtrsim 58.2\rho_\lambda$, where $M \gtrsim M_{\mathrm{rest}}$ as the EoS becomes radiationlike ($p_{\mathrm{bec}} \simeq \rho_{\mathrm{bec}}c^2/3$).

In the case of the mixture, when the BEC core, wrapped with thermal bosons, transitions to a radiationlike state and reduces the effective adiabatic index of the entire sphere, especially at sufficiently high central densities, it is expected to trigger the collapse even at low temperatures. However, a detailed analysis of this phenomenon is reserved for future work.

5.6 Applications and discussions

According to our model at low temperature $b \ll 1$, say $\alpha(R) = 0$ and $g = 2$ in Appendix I, marginally stable neutron stars of mass $\simeq 0.7$ $\mathrm{M}_\odot$ with $C \simeq 0.12$ is obtained if the neutrons formed a degenerate cold Fermi gas. This agrees remarkably well with the results of [71], while the discrepancy with observation of $\simeq 2$ $\mathrm{M}_\odot$ with $C \simeq 0.25$ simply means that the ideal-gas assumption is no longer valid in the neutron cores.

Now we consider dark matter clumps as gravothermal systems under the ideal-gas assumption. Dark matter clumps could form even in the radiation dominated era [192, 193, 194, 195]. In order to describe them as gravothermal spheres, the clumps must be well *thermalized*, i.e., its relaxation time $\lesssim$ its dynamical time. Therefore the dark matter clumps are assumed to be in thermal *(quasi)equilibrium* with the homogeneous cosmological background. However, they can become gravitationally bounded only after the temperature drops down to $b \lesssim 0.5$ due to radiations. In addition, $n_\chi - n_{\bar{\chi}} \neq 0$ suitably fits into the scenario of asymmetric dark matter [196, 197, 198, 199, 200, 201].

For fermions to form the observed dark matter halo, the Tremaine-Gunn bound [202, 203] requires the fermion mass $m \gtrsim 0.4$ keV$/c^2$, while it can be relaxed if many distinct species of fermions are allowed [204]. In the degenerate regime $\alpha(R) \gtrsim -1$, the would-be seed BH mass from fermionic dark matter, $M_{\rm seed} \sim 10^5$ M$_\odot \left(mc^2/{\rm MeV}\right)^{-2}$, is independent of the thermal bath (if $b \lesssim 0.5$) at the onset of instability. Specifically, if we take $mc^2 \simeq 0.4$ keV with $\alpha(R) = 0$ and $g = 2$ at $b \ll 1$, $M_{\rm seed} \simeq 3.9 \times 10^{12}$ M$_\odot$, which is much larger than the most massive SMBH we have observed. Incidentally, if $mc^2 \gtrsim$ MeV, the dark clumps of mass $\lesssim 10^4$ M$_\odot$ [205] could have formed after the quantum chromodynamics phase transition $k_BT \sim 200$ MeV and before the neutrino decoupling at $\sim$ MeV. One can then examine whether those dark clumps would evolve into PBHs. On the other hand, our model can be also applied to the *gravothermal core-collapse* of self-interacting dark matter halos [20, 65, 56] after cosmological recombination (redshifts $z < 1100$).

For ultralight bosons as dark matter [206], the boson mass ranges from $\gtrsim 10^{-22}$ eV$/c^2$ to $\lesssim 10$ eV$/c^2$. Therefore we have $M_{\rm seed} \gg 10^{10}$ M$_\odot$ ($m = 10^{-22}$ eV$/c^2$) or $M_{\rm seed} \gg 10^{-13}$ M$_\odot$ ($m = 10$ eV$/c^2$) in Thomas–Fermi regime. However, the boson mass could be even heavier if the condensate results from BCS-BEC crossover [207, 208], in which the boson mass is not fundamental but determined by the fermion pairs. If the BEC were to account for 100% of dark matter, cosmological constraints [178] require that 1.75×10^7 eV/cm$^3 \leq \rho_\lambda c^2 \leq 4.17 \times 10^{15}$ eV/cm^3 [1] and $m \geq 2.4 \times 10^{-21}$ eV$/c^2$. However, it can be even more constrained to $\rho_\lambda c^2 \simeq 3.8 \times 10^{10\text{–}13}$ eV/cm^3 regarding the local structures (galaxies and clusters) [190]. Since the unstable bound condensates could form if $5\rho_\lambda \lesssim \rho_{\rm bec}(0) \lesssim 60\rho_\lambda$ in the

[1] In Ref. [178], it is written as 1.9×10^{-8} eV^{-1}cm$^3 \leq \lambda\lambda_C^3/mc^2 \leq 8 \times 10^{-17}$ eV^{-1}cm^3. The difference in numerics here comes from the factor in defining the self-interacting potential $\lambda|\varphi|^4$.

overdense region, this implies the they could abundantly generate seed BHs roughly before the matter-radiation equality era where the EoS transitions from radiationlike to CDM-like phase [178]. Given the constraints on ρ_λ above, one can obtain $M_{\rm seed} \sim 10^{16\text{–}18}$ $\mathrm{M}_\odot$, although stupendously huge [209], which still lies in the allowed window where PBHs could have an appreciable density [210].

In this chapter, we have examined the dynamical instability of a gravitationally-bound and thermalized sphere in the quantum limit, i.e., the particles in the gaseous sphere follows the FD and BE distributions, where the quantum pressure and pair production/annihilation effects are significant. At high temperature when the pair production/annihilation into radiations (massless particles) is significant, the sphere can be gravitationally bound only if the boundary temperature is less than half of the particle's rest energy, $k_B T(R) \lesssim 0.5\ mc^2$ in the classical limit. However, the threshold temperature decreases (increases) as the degeneracy increases for fermions (bosons).

Furthermore, we emphasize the importance of the quantum pressure, in contrast to the thermal pressure ($k_B T(R) \gtrsim 0.1\ mc^2$) in the classical limit [56], to trigger the collapse. The condition can be applied to various self-gravitating dark matter systems. For fermionic dark matter, the quantum pressure from Pauli blocking in low temperature is pivotal to trigger the instability. While for bosonic dark matter at low temperature ($k_B T(R) < 0.1\ mc^2$), the lack of Fermi-degeneracy pressure prevents it from collapse if there is no BEC. Nevertheless, the repulsive self-interaction in the BEC is expected to trigger the instability, where the details will be presented in the future [186].

Chapter 6

Dark Matter Density Spikes around Supermassive Black Holes

It is well established that dark matter (DM) contributes about one quarter of the total energy of the universe [211]. Many DM models have been proposed, in particular, the introduction of new stable particles. However, the natural properties of DM are still elusive. In the standard ΛCDM cosmology, DM is assumed to be collisionless. Despite the success of ΛCDM on large scales, difficulties remain to explain the sub-galactic scales. The core-cusp and missing satellites problems are the discrepancies between the numerical N-body simulations and astrophysical observations on small scales of structure. The deviations may come from the insufficient implementation of the baryonic processes such as the supernova feedback and photoionization or might be due to the unknown properties of DM. Self-interacting dark matter (SIDM) was first proposed to reconcile these issues with the cross-section per unit mass in the range of 0.45 $\mathrm{cm}^2/\mathrm{g} < \sigma/m < 450\ \mathrm{cm}^2/\mathrm{g}$ (m

denotes the DM mass) [11]. It should be mentioned that some investigations showed that the velocity-independent cross-sections cannot account for the observed ellipticities in clusters [212, 213]. Furthermore, bullet cluster 1E 0657-56 seems to constrain σ/m to be less than 0.7 cm^2/g, and the cross-section of SIDM would be too small to be distinguished from the collisionless DM [214, 215]. While some studies indicate the SIDM with velocity-dependent cross-sections can provide a broader parameter region, $\sigma/m \sim 0.1 - 50\ \mathrm{cm}^2/\mathrm{g}$, to accommodate above puzzles [216, 217, 218, 219]. (see Ref. [13] for a review). The issues of SIDM are still under investigation, in this chapter we adopt the constraint in the range of

$$0.1\ \mathrm{cm}^2/\mathrm{g} < \sigma/m < 1\ \mathrm{cm}^2/\mathrm{g} \tag{6.1}$$

in our study.

It is generally believed that all large galaxies immersed in dark halos host central supermassive black holes (SMBHs). The dynamics of the presence of a central black hole (BH) will alter the surrounding stellar distribution and generate a density cusp within its radius of influence [220, 221, 222, 223, 224, 225, 226, 227, 228, 229, 230]. It was Peebles [231] who first derived a power law for the stellar distribution function based on the scaling argument. He adopted the picture that the stars are bounded in orbits due to the gravitational potential of the central BH and then diffuse into another bound orbit via the star-star gravitational scattering. Bahcall and Wolf obtained the scaling law of steady-state stellar density profile as $n_{\mathrm{star}}(r) \propto r^{-7/4}$ in the cusp region by numerically solving the one-dimensional Fokker-Planck equation for spherical clusters and isotropic velocity distribution [232]. The study is then extended to two-dimensional problems after considering the anisotropy in ve-

locity space and the effect of high eccentricity/low angular momentum orbits (the so-called loss-cone in J-space) considered by Frank and Rees [233] and Lightman and Shapiro [234]. Monte-Carlo simulations as well as numerical integration of two-dimensional Fokker-Planck equation were also performed in Refs [235, 236, 237, 238]. Some recent studies taking into account the nonspherical clusters, relativistic corrections, and extreme mass ratio inspirals, etc. can be referred to [239] for a review. On the other hand, for the galactic nuclei one may address the similar question where the DM distributes in the center region of galaxies, and will be entrained towards the massive BH. The redistribution of DM density profile around the massive BH is usually called the central "spike," that might be observed as a point sources of gamma rays [240] and neutrinos [241] or through the dephasing of the gravitational waveform induced by DM [242, 243] that can be probed with future interferometers. Different investigations have shown the adiabatic growth of spike density to be $\rho(r) \propto r^{-1.5}$ and $\rho(r) \propto r^{-\beta}$ with $2.25 \leq \beta \leq 2.5$ under the assumptions of isothermal DM distribution [244] and singular power-law cusp DM distribution [221, 245], respectively.

In this chapter, we aim to provide a self-consistent study of the spike density formed by Bondi accretion [246, 247] onto a central BH in a typical dark halo dominated by SIDM. The motivation for choosing this setup is as follows. The Bondi accretion is the simplest mechanism to study the accretion near a massive object. Later, one can extend to more realistic accretion dynamics based on the results derived from Bondi accretion. The model of SIDM considered in this chapter is a Standard Model gauge singlet self-interacting scalar field with interaction potential $\frac{1}{4!}\lambda|\phi|^4$. From the perspective of particle physics, this model is one of the simplest SIDM models satisfying the current detections [248]. Due to its

simplicity and elegance, this SIDM model or its simple extension with interaction potential $\frac{1}{n!}\lambda_n|\phi|^n$ have been widely adopted in the context of cosmology [191, 249, 250, 251, 252, 253, 254, 255, 256], or the construction of dark boson stars [174, 171, 172, 257, 258, 259, 260, 261, 262]. Especially, in [174] it is for the first time shown that this model can form compact objects due to nonzero self-interaction. Moreover, an EoS of this model is also extracted in the isotropic limit [174], which can then be adopted for hydrodynamical studies, such as Bondi accretion considered in this chapter. Given the exact form of equation of state (EoS), we are able to solve the relativistic Bondi accretion of the flow of this SIDM analytically, and obtain the spike density profile within the range of self-gravitating regime.

Inspired by the early works [263, 264, 265], there are recent studies on the spike or cusp profiles around a BH by quite different approaches for various DM models [266, 267, 268, 269, 270, 271, 272]. Our work can be seen as an extension along the same line but consider a nontrivial SIDM with a closed form of non-polytropic EoS. This contrasts with the results obtained based on either polytropic EoS or the assumption of velocity-dependent cross-section. The rest of the chapter is organized as follows. In Sec. 6.1 we study the relativistic Bondi accretion of SIDM in DM halo. We then apply the observational constraints in our model parameters and adopt the fluid description for the spike density profile in Sec. 6.2. We conclude in Sec. 6.3. Throughout the chapter, $G = \hbar = c = 1$ is adopted unless otherwise noted.

6.1 Relativistic Bondi accretion of self-interacting dark scalar

The resultant profile of the accreting matter due to the Bondi accretion is supposed to depend on the EoS. The simplest EoS is the polytropic type, $p = K\rho_0^\Gamma$ with ρ_0 indicating the mass density, which, however, may not be the realistic one for nontrivial DM. In this chapter, we will consider a nontrivial but simple DM model which goes beyond the polytropic one. This is just a massive canonical scalar field with quartic self-coupling, which was first proposed in [174] for boson stars, with the following Lagrangian,

$$\mathcal{L} = -\frac{1}{2}g^{\mu\nu}\phi^*_{;\mu}\phi_{;\nu} - V(|\phi|) \tag{6.2}$$

where the scalar potential is given by

$$V(|\phi|) = \frac{1}{2}m^2|\phi|^2 + \frac{\lambda}{4!}|\phi|^4. \tag{6.3}$$

Here m is the mass of DM mass and λ represents the self-coupling strength. This is a simple and viable DM model with discrete symmetry. The resulting cross-section of DM-DM scattering is [273]

$$\sigma = \frac{\lambda^2}{64\pi m^2} \tag{6.4}$$

in the non-relativistic limit. This cross-section should be constrained by Eq. 6.1 to yield profiles of DM halos consistent with the observed ones.

To consider the accretion of the above scalar SIDM by a central massive object such as a BH or a compact star of mass M, which is described by the Schwarzschild metric

$$\mathrm{d}s^2 = -\left(1-\frac{2M}{r}\right)\mathrm{d}t^2 + \left(1-\frac{2M}{r}\right)^{-1}\mathrm{d}r^2 + r^2(\mathrm{d}\theta^2+\sin^2\theta\mathrm{d}\phi^2)\,. \tag{6.5}$$

Instead of directly solving the above Einstein-scalar system in such a background spacetime for the hydrodynamics of the accreting matter, we can consider the regime with $\lambda m_{\rm Pl}^2/m^2 \gg 1$, where $m_{\rm Pl}$ is the Planck mass, for which the scalar field only varies on a relatively large length scale $\lambda m_{\rm Pl}^2/m^3 \gg 1/m$. Therefore, the stationary scalar field configuration in this regime can be approximated by a perfect fluid for the hydrodynamical study with the following EoS [174]

$$\frac{p}{\rho_B} = \frac{4}{9}\left[\left(1+\frac{3\rho}{4\rho_B}\right)^{1/2}-1\right]^2 \quad \text{or} \quad \frac{\rho}{\rho_B} = \frac{3p}{\rho_B} + 4\sqrt{\frac{p}{\rho_B}}, \tag{6.6}$$

where the free parameter ρ_B is given by

$$\rho_B = \frac{3m^4}{2\lambda} = \frac{3.48}{\lambda}\left(\frac{m}{\mathrm{GeV}}\right)^4 \times 10^{20}\ \mathrm{kg\ m^{-3}}. \tag{6.7}$$

The EoS Eq. 6.6 reduces to a condensate fluid $p \propto \rho^2$ [176] in the non-relativistic limit, $p \ll \rho \ll \rho_B$; while $\rho \simeq 3p \gg \rho_B$ as a radiation fluid in the relativistic limit. To study the Bondi accretion for the considered SIDM, we can start with either the non-relativistic formulation or the relativistic one. The corresponding sets of the continuity equation and the Euler equation are given in Appendix K.1 and K.2, respectively. However, as shown in Appendix K.1, the non-relativistic Bondi accretion of the SIDM with EoS Eq. 6.6 gives the

relativistic sound speed near the sonic horizon, so that this formulation is not appropriate for our consideration. Therefore, we will adopt the relativistic formulation to consider the Bondi accretion in the following.

Start with the continuity equation, which can be understood as the expression for the constant accretion rate $\dot{M} \equiv \mathrm{d}M/\mathrm{d}t$, *i.e.*,

$$\dot{M} \equiv 4\pi r^2 \rho_0 u = \text{constant}, \tag{6.8}$$

where u is the negative radial component of 4-velocity of the hydrodynamic flow and ρ_0 represents the rest mass density. The mass-energy conservation [57] yields the relation between the total energy density ρ and ρ_0, *i.e.*,

$$\left(\frac{\partial \rho}{\partial \rho_0}\right)_{\mathrm{ad}} = \frac{\rho + p}{\rho_0}, \tag{6.9}$$

where the subscript "ad" denotes the variation is adiabatic during the accretion process. Based on Eq. 6.6 and Eq. 6.9, one can then derive

$$\frac{\rho_0}{\rho_B} = \frac{8}{9}\left(\sqrt{1+\frac{3\rho}{4\rho_B}}-1\right)\sqrt{3\left(1+2\sqrt{1+\frac{3\rho}{4\rho_B}}\right)} \tag{6.10}$$

and the (adiabatic) sound speed square

$$a^2 \equiv \left(\frac{\partial p}{\partial \rho}\right)_{\mathrm{ad}} = \frac{1}{3}\left(1-\frac{1}{\sqrt{1+3\rho/4\rho_B}}\right) = \frac{\sqrt{p/\rho_B}}{3\sqrt{p/\rho_B}+2}. \tag{6.11}$$

It is obvious that the existence of a sound barrier at $a = 1/\sqrt{3}$ when $\rho, p \gg \rho_B$. Considering

that the sound speed profile $a = a(r)$ is the elementary dynamical quantity characterizing the fluid dynamics, we can invert Eq. 6.10 and Eq. 6.11 to express ρ_0, ρ and p in terms of a. The results are

$$\frac{\rho_0}{\rho_B} = \frac{8a^2}{1-3a^2}\sqrt{\frac{1-a^2}{1-3a^2}}, \quad \frac{\rho}{\rho_B} = \frac{4a^2(2-3a^2)}{(1-3a^2)^2} \quad \text{and} \quad \frac{p}{\rho_B} = \frac{4a^4}{(1-3a^2)^2}\,. \tag{6.12}$$

As for the relativistic Euler equation (see Appendix K.2), we can integrate it with the help of Eq. 6.9 to the relativistic Bernoulli equation [57]

$$\left(\frac{P+\rho}{\rho_0}\right)^2\left(1+u^2-\frac{2M}{r}\right) = \left(\frac{p_\infty+\rho_\infty}{\rho_{0,\infty}}\right)^2, \tag{6.13}$$

or equivalently by Eq. 6.12,

$$\left(\frac{1-a^2}{1-3a^2}\right)^2\left(1+u^2-\frac{2M}{r}\right) = \left(\frac{1-a_\infty^2}{1-3a_\infty^2}\right)^2, \tag{6.14}$$

where the quantity with the subscript ∞ denotes its value at $r=\infty$ at which u vanishes. Given an accretion rate and the sound speed at a particular location, we can first solve $u = u(a,r)$ and then turn the Bernoulli equation Eq. 6.14 to a profile equation for the sound speed. See Appendix K.3 for details. Besides, the relativistic sonic horizon is better to be defined by the radial location r_s where the *local* Mach number [57]

$$\mathcal{M} = \frac{u/a}{\sqrt{1-2M/r+u^2}}, \tag{6.15}$$

takes the unity value, *i.e.*, $\mathcal{M}_s \equiv \mathcal{M}\,|_{r=r_s} = 1$. In Appendix K.4, we sketch how $\mathcal{M}$

characterizes the "local" fluid speed over the sound speed. Note that both $\mathcal{M}_s$ and $\mathcal{M}_h \equiv \mathcal{M}\,|_{r=r_h} = 1/a$ at event horizon $r_h = 2M$ are independent of u. Later on, we will use $\mathcal{M}$ instead of u to characterize the local stream speed of fluid.

The profile equation of sound speed, *i.e.*, Eq. K.16, does not admit analytical solutions, we will instead solve it numerically in the next section to yield the spike profile of the mass density. Despite that, one can determine the sound speed at sonic horizon r_s and the event horizon r_h (if the center object is a BH) without solving the complicated profile equation. At the sonic horizon, the degenerate feature of the relativistic Euler equation yields the relations [57]

$$u_s^2 = \frac{a_s^2}{1+3a_s^2} = \frac{M}{2r_s}\,. \tag{6.16}$$

This reduces the Bernoulli equation Eq. 6.14 which solves the sound speed at sonic horizon, a_s by

$$a_s^2 = \frac{1-3a_\infty^2+\sqrt{1+66a_\infty^2-63a_\infty^4}}{18(1-a_\infty^2)}\,. \tag{6.17}$$

On the other hand, the continuity equation implies $r_h^2\rho_{0h}u_h = r_s^2\rho_{0s}u_s$, which we can solve for the sound speed at the horizon u_h in terms of a_s with the help of Eqs. 6.10 and 6.16. Impose the right-side of Eq. 6.14 at the event horizon, then solve it with the above $u_h = u_h(a_s)$ for the sound speed a_h at $r = r_h$, we obtain

$$a_h^2 = \frac{1}{3} - \frac{1}{3}\left[\frac{3}{16}\left(\frac{1+3a_s^2}{1-3a_s^2}\right)^{3/2}\sqrt{\frac{1-a_s^2}{a_s^2}}\sqrt{\frac{1-3a_\infty^2}{1-a_\infty^2}}+1\right]^{-1}\,, \tag{6.18}$$

where a_s is given by Eq. 6.17. See the top panel of Fig. 6.1 for the numerical profiles of

Eqs. 6.17 and 6.18. Therefore, the physical range of $0 \leq a_\infty^2 < 1/3$ implies

$$\frac{1}{5} \leq a_h^2 < \frac{1}{3}\,, \quad \text{and} \quad \frac{1}{9} \leq a_s^2 < \frac{1}{3}\,. \tag{6.19}$$

Remarkably, no matter what value a_∞ takes, the sound speeds at event and sound horizons are always the order of light speed. This justifies the use of the relativistic formalism. Furthermore, given the boundary condition, *i.e.*, fixing the value of a_s (or a_∞), then the accretion rate $\dot{M}$ is fixed up to the dimensional parameters M and ρ_B. Specifically by Eqs. 6.10, 6.8 and 6.16, one obtains the accretion rate

$$\dot{M} = 8\pi \left(\frac{1+3a_s^2}{1-3a_s^2}\right)^{3/2} \sqrt{\frac{1-a_s^2}{a_s^2}} M^2 \rho_B. \tag{6.20}$$

In an astrophysical system, it is useful to define the Bondi (capture) radius of the accretion range

$$r_{\rm B} \equiv \frac{2M}{a_\infty^2}, \tag{6.21}$$

beyond which the accretion becomes less significant as the particles of the fluid around are no longer gravitationally bound. Consider the two extreme cases: (i) $a_s^2 = 1/9$ ($a_\infty = 0$) $\Rightarrow$ $\dot{M} = 64\pi M^2 \rho_B$, $r_s = 6M$, and $r_{\rm B} \to \infty$; (ii) $a_s^2 \to 1/3$ ($a_\infty \to 1/3$) $\Rightarrow$ $\dot{M} \to \infty$, $r_s = 3M$, and $r_{\rm B} = 6M$. Therefore, one can conclude:

$$64\pi M^2 \rho_B \leq \dot{M} < \infty, \tag{6.22}$$

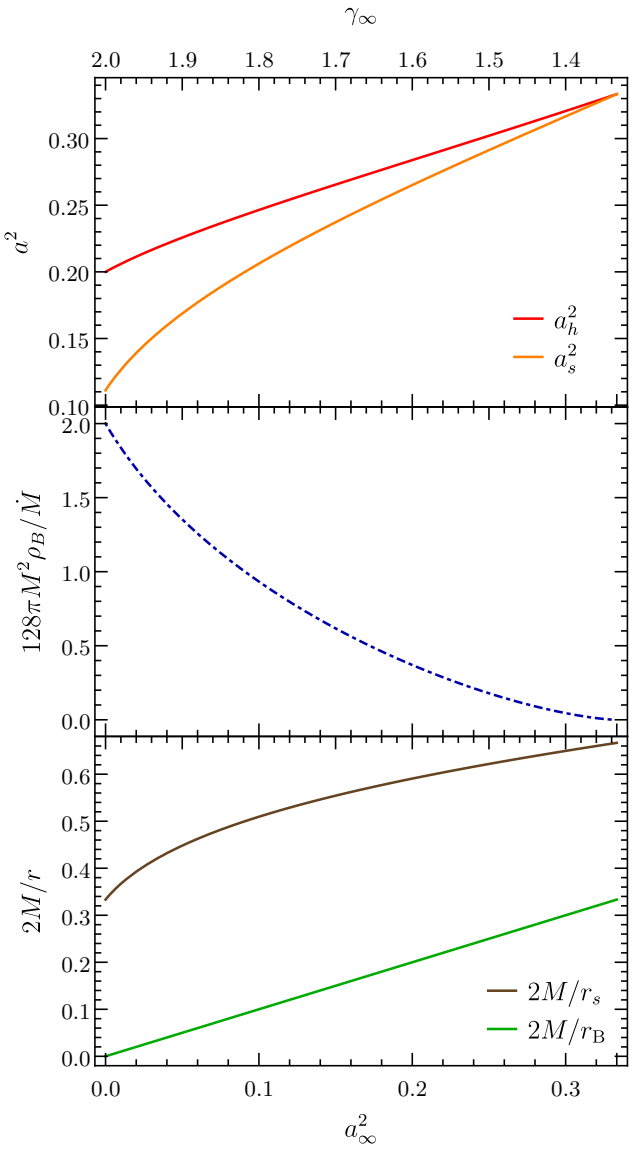

Figure 6.1: Sound speed squares a_h^2, a_s^2 at different radii (top panel), inverse accretion rate $128\pi M^2\rho_B/\dot{M}$ (middle panel) and inverse radii $2M/r_s$ and $2M/r_\mathrm{B}$ (bottom panel), which are the results of Sec. 6.1 given a_∞^2 (or adiabatic index γ_∞) at infinity. We note that as $\gamma_\infty \to 4/3$, the sound speeds in all range approach the sound barrier $a_\infty^2 \to a_s^2 \to a_h^2 \to 1/3$. The accretion rate increases $\dot{M}$ rapidly as the adiabatic index becomes softer, and diverges as $\gamma_\infty \to 4/3$ ($a_\infty^2 \to 1/3$). The sound horizon r_s is bounded between $3M$ and $6M$; while the Bondi radius r_B between $6M$ and ∞. They both decrease as the adiabatic index becomes softer, and vice versa. While the Bondi radius diverges as $\gamma_\infty \to 2$ ($a_\infty^2 \to 0$).

and

$$3M \leq r_s \leq 6M \leq r_{\rm B} < \infty \tag{6.23}$$

depending on the boundary condition. It is interesting to note that the sonic horizon is bound between the smallest circular orbits of massless (photon sphere $3M$) and massive (innermost stable circular orbit $6M$) particles. We see that the accretion rate increases rapidly as the sound speed a_∞ increases, and becomes divergent when approaching the sound barrier, see the middle panel of Fig. 6.1. This contrasts with the result of [269] in considering the relativistic Bondi accretion of the matter with polytropic EoS, for which the accretion rate remains finite as a_∞ increases.

However, there is a trade-off between the accretion rate ($\dot{M}$) and accretion range ($r_{\rm B}$): *The larger the accretion rate, the smaller the accretion range,* see Fig. 6.1 (middle and bottom panels). As long as $r_{\rm B}$ is finite, once the self-interacting bosons are vacuumed up within the region set by r_B, the accretion will stop so that it cannot grow indefinitely. Via integration of Eq. 6.22, we can obtain the accretion time given the initial and final BH mass,

$$\left(\frac{1}{M_i} - \frac{1}{M_f}\right) \geq 64\pi\rho_B \left(t_f - t_i\right). \tag{6.24}$$

Note that the model parameter ρ_B is crucial to the accretion time scale, and it can be determined given ρ_∞/ρ_B from astrophysical observations.

6.2 Spike profile of the dark halo density around a BH

In this section, we would like to apply the results derived in the last section to obtain the accreting spike density profile around the central massive object. This is the ideal case of accreting the DM in the halo by a central massive object such as a BH. We will first obtain the numeric windows for the model parameters of the considered SIDM model from the astrophysical observational constraints. With these numerical values of the model parameters, we then numerically solve the profile equation of the sound speed Eq. K.16, and thus obtain the spike profile of the halo density.

6.2.1 Parameters of SIDM for a typical dark halo

For a virialized system in the fluid description, it is more useful to measure the velocity dispersion square

$$v_{\rm dis}^2 \equiv \frac{3p}{\rho} = 1 - \frac{2}{1+\sqrt{1+3\rho/4\rho_B}} \tag{6.25}$$

rather than the sound speed square Eq. 6.11. However, they are at the same order of magnitude if $\rho_\infty/\rho_B \ll 1$ far away from the Bondi radius. Specifically, one can determine the model parameter

$$\rho_B \simeq \frac{3}{16}\frac{\rho_\infty}{v_{\rm dis,\infty}^2} \tag{6.26}$$

if $v_{\rm dis,\infty}^2 \ll 1$. This is reasonable as the DM halos are generally non-relativistic. In reality, the dispersion of DM itself is not directly measurable, while it is correlated to that of baryonic matter if the whole system is virialized through gravitational interaction [274].

On galactic (cluster) scale, $\rho_\infty \sim 10^{-2}$ (10^{-3}) $\mathrm{M}_\odot$ pc^{-3} and $v_{\mathrm{dis},\infty} \sim 10^2$ (10^3) km s^{-1} [13], for example, we can determine $\rho_B \sim 10^4$ (10) $\mathrm{M}_\odot$ $\mathrm{pc}^{-3} = 6.77 \times 10^{-16}$ (10^{-19}) kg m^{-3}. This implies the parameters in our SIDM model to have the relation by utilizing Eq. 6.7,

$$m \sim 10^{-9}\ (10^{-10})\ \lambda^{1/4}\ \mathrm{GeV}. \tag{6.27}$$

We note that even though the possible ρ_B ranges three orders of magnitude from galaxies to clusters, the mass is still constrained in a narrow window as $m \propto \rho_B^{1/4}$. Moreover, for typical halos considered above, the lower bound of the accretion rate of Eq. 6.22 yields

$$\dot{M}_{\mathrm{min}} = 64\pi M^2 \rho_B \simeq 1.41 \times 10^{-9}\ (10^{-6})\ \mathrm{M}_\odot\ \mathrm{yr}^{-1} \tag{6.28}$$

for BHs of mass $M = 10^6$ (10^9) $\mathrm{M}_\odot$ at the central galactic (cluster) mass halos [275], which is subdominant compared to the Eddington accretion [3] of baryons $\simeq 2 \times 10^{-2}$ (10^1) $\mathrm{M}_\odot$ yr^{-1}.

If the SIDM model could also resolve the small-scale structure problem, the constraint of Eq. 6.1 together with the cross-section in Eq. 6.4 would impose

$$30 \left(\frac{m}{\mathrm{GeV}}\right)^{3/2} < \lambda < 90 \left(\frac{m}{\mathrm{GeV}}\right)^{3/2}, \tag{6.29}$$

where the upper (lower) corresponds to the galactic (cluster) scale [13]. Combining Eqs. 6.27 and 6.29, we have the self-coupling constant to be constrained in the range of

$$10^{-22} \lesssim \lambda \lesssim 10^{-19} \tag{6.30}$$

or expressed in terms of scalar mass

$$10^{-7}\ \mathrm{eV} \lesssim m \lesssim 10^{-5}\ \mathrm{eV}, \tag{6.31}$$

which overlaps the range of axion DM [276, 277]. In addition, the mass window Eq. 6.31 satisfies the Bullet Cluster constraint $2.92 \times 10^{-22}\ \mathrm{eV} < m < 1.10 \times 10^{-3}\ \mathrm{eV}$ [256], and is compatible with $4.17\ \mathrm{eV}^4 < m^4/\lambda < 6.25\ \mathrm{eV}^4$ window[1] determined from the rotation curve of the dwarf spiral galaxy, DDO 154 [255].

On the other hand, the accretion time for $M_f \gg M_i$ from Eq. 6.24 results in

$$t_f - t_i \equiv \Delta t \lesssim \frac{1}{64\pi\rho_B M_i} = 4.8 \times 10^{12} \left(\frac{\rho_\infty}{\rho_B}\right) \left(\frac{10^{-2}\ \mathrm{M}_\odot\ \mathrm{pc}^{-3}}{\rho_\infty}\right) \left(\frac{10^6\ \mathrm{M}_\odot}{M_i}\right)\ \mathrm{Gyr}, \tag{6.32}$$

which is significantly longer than a Hubble time for a galactic halo of $\rho_\infty/\rho_B \simeq 10^{-6}$ with a central BH of initial mass $M_i = 10^6\ \mathrm{M}_\odot$. If this SIDM model dominates the main component of the dark halo, it is expected that the accretion is still persisting even for the most massive BHs in our universe. Therefore, it is reasonable to see how the accretion shapes the DM density spikes around BHs.

6.2.2 Position-dependent adiabatic index

Most EoSs for realistic astrophysical consideration are not polytropic, instead they can be approximated as piecewise polytropic functions. We can extend this approximation

[1]The values shown here are not exactly the same as in [255] because of the different convention defining the Lagrangian $\mathcal{L}$ and the scalar potential $V(|\phi|)$.

by introducing the following position-dependent adiabatic index,

$$\gamma(r) \equiv \left(\frac{\partial \ln p}{\partial \ln \rho_0}\right)_{\rm ad} . \tag{6.33}$$

The introduction of $\gamma(r)$ helps to compare with the usual polytropic results whenever $d\gamma/dr$ is small over some region. Besides, γ is related to sound speed in a simple manner via Eq. 6.9, *i.e.*,

$$a^2(r) \equiv \left(\frac{\partial p}{\partial \rho}\right)_{\rm ad} = \frac{p}{\rho + p}\gamma = 1 - \frac{\gamma(r)}{2}. \tag{6.34}$$

Applying to EoS Eq. 6.6, we have

$$\gamma(r) = \frac{4}{3}\left(1 + \frac{1}{2\sqrt{1 + 3\rho/4\rho_B}}\right) \tag{6.35}$$

which ranges from 2 ($p \ll \rho \ll \rho_B$) to 4/3 ($\rho \simeq 3p \gg \rho_B$)[2]. Note that $\rho \to \rho_0$ when $p \ll \rho \ll \rho_B$ in the non-relativistic limit, thus $p \propto \rho_0^2$ from Eq. 6.6, which implies the adiabatic index $\gamma(r) \simeq 2$ in sharp contrast to the non-relativistic monatomic ideal gas with the corresponding $\gamma = 5/3 < 2$. Since the adiabatic index characterizes the *compressibility* of a fluid, the EoS Eq. 6.6 is *stiffer* due to the *repulsive self-interaction.*

6.2.3 Spike profile

Since the Bondi radius is the range in which the self-gravity effect is relevant for accretion, we shall just consider the spike density profile around the BH within this range.

[2]This lower bound happens when the sound speeds a_∞ (and a_s) reaches the sound barrier $1/\sqrt{3}$. However, as shown in Fig. 6.2 for non-relativistic $a_\infty \simeq 10^{-7}$, the sound speed can only reach its maximum $1/\sqrt{5}$ at the event horizon so that the lower bound of γ is 8/5 instead of 4/3.

Applying the typical velocity dispersion $v_{\rm dis,\infty} \sim a_\infty$ of galactic halos as discussed, the Bondi radius

$$r_{\rm B} = \frac{2M}{a_\infty^2} \simeq 10^7 \times r_h \simeq \left(\frac{M}{10^6\ {\rm M}_\odot}\right)\ {\rm pc}\ . \tag{6.36}$$

To obtain the profiles of the sound speed and mass density, we solve the profile equation Eq. K.16 for the sound speed numerically within the aforementioned range of Bondi radius, and then obtain the density profile accordingly via Eq. K.16. Our results are shown in Fig. 6.2 for the local Mach number $\mathcal{M}$ (top panel) to characterize the local stream speed of the fluid, the position-dependent adiabatic index γ (middle panel) to characterize the sound speed, and the dimensionless spike density profile ρ_0/ρ_B (bottom panel). We see that the local Mach number ranges from unity at the sonic horizon to about 10^{-3} near the Bondi radius with a slowly varying $\log r$ profile.

As discussed, the position-dependent index γ (or equivalently the sound-speed-squared a^2) can help to characterize the piecewise feature of EoS. From the variational behavior shown in Fig. 6.2 this feature is manifest for the EoS we consider, and it can be divided into three regions: (1) the near zone region ranging from the event horizon r_h to the sonic horizon $3r_h$; (2) the middle zone ranging from the sonic horizon about $3r_h$ to $100r_h$; (3) the far zone ranging from $100r_h$ to the Bondi radius. The far zone is a region of almost constant $\gamma \simeq 2$, and can be thought of as the region with EoS $p \propto \rho_0^2$. On the other hand, γ other than the far zone changes more rapidly and ranges from 1.6 at event horizon to about 2 around $100r_h$, so that it cannot be well-approximated by a single polytropic EoS over the near and middle zones.

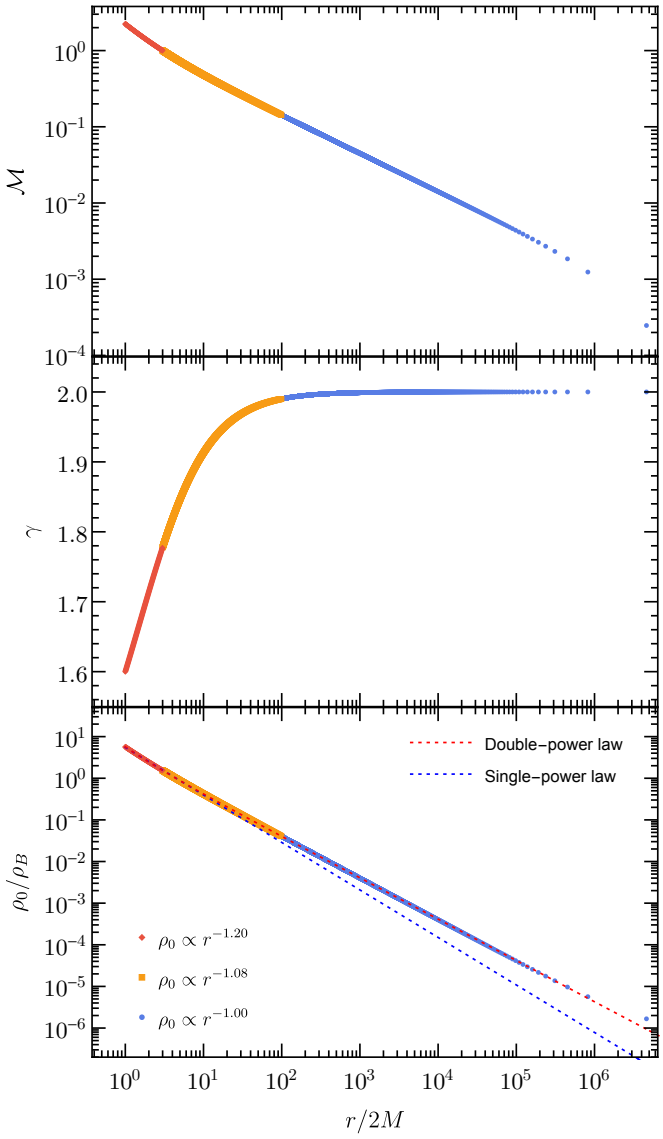

Figure 6.2: Profiles of local Mach number $\mathcal{M}$ (top panel), position-dependent adiabatic index γ (middle panel) and mass density ρ_0 (bottom panel) for accreting SIDM with EoS Eq. 6.6 around a massive BH. The data are the solutions of Eq. K.16 with $a_\infty^2 = 10^{-7}$. The profile of $\mathcal{M}$ characterizes the local fluid speed. The profile of γ characterizes the local behavior of EoS, which remains stiff ($\gamma \approx 2$) in the spike and starts to decrease promptly from $200M$ towards the central BH ($\gamma \to \gamma_h = 8/5$). The profile of ρ_0 shows the spike profile, which can be fitted well by *double-power law* of Eq. 6.37, but not by the single-power law as shown. As shown, we also fit the mass density profile by single-power law for three regions defined in the main text with small relative error: (1) $\rho_0/\rho_B = 5.62(2M/r)^{1.20}$ for near zone (red); (2) $\rho_0/\rho_B = 4.98(2M/r)^{1.08}$ for middle zone (orange); (3) $\rho_0/\rho_B = 4.07(2M/r)^{1.00}$ for far zone (blue).

Guided by the power-law spike $\rho_0(r) \propto r^{-\beta}$ in the literature [232, 234, 278] when considering the stellar density around a SMBH, it is tempting to also fit the mass density profile shown in Fig. 6.2 by the power law. However, the power-law fitting to the *whole* region turns out to be not good. This could be due to the non-polytropic nature of our EoS, *i.e.*, non-constant γ. Instead, *double-power law* gives a better fit of our model,

$$\rho_0(r) = \left[1.82\left(\frac{2M}{r}\right)^{1.81} + 3.84\left(\frac{2M}{r}\right)^{0.99}\right]\rho_B \tag{6.37}$$

with quite small relative error, *i.e.*, 0.558%. The second term $\rho_0(r) \propto r^{-0.99} \approx r^{-1}$ dominates at large radii near the Bondi radius, which can match the Navarro-Frenk-White (NFW) [24] cusp outside the Bondi radius of the BH.

On the other hand, we can fit some particular region over which γ remains constant. In such cases, the result shall take the limiting power-law form obtained in [269] (see (A.8) therein)

$$\rho_0(r) \propto r^{-\frac{1}{\Gamma-1}} \quad \text{with} \quad \Gamma > \frac{5}{3}. \tag{6.38}$$

for the accreted matter with polytropic EoS, *i.e.*, $p \propto \rho_0^\Gamma$. Indeed, if we fit our mass density profile in the far zone, it is consistent with Eq. 6.38 with $\Gamma = \gamma\,\big|_{\text{far zone}} \simeq 2$, *i.e.*, $\rho_0(r) \propto r^{-1}$. Similarly, in the region near the sonic horizon, $\gamma\,\big|_{\text{sonic}} \simeq 16/9$ so that the mass density fit to Eq. 6.38 with $\Gamma = 16/9$, *i.e.*, $\rho_0(r) \propto r^{-1.29}$. Therefore, our results are consistent with the polytropic ones. We have also fit the mass density in the near, middle, and far zones separately, and the results are: (1) $\rho_0(r)/\rho_B = 5.62(r_h/r)^{1.20}$ for near zone (2) $\rho_0(r)/\rho_B = 4.98(r_h/r)^{1.08}$ for middle zone (3) $\rho_0(r)/\rho_B = 4.07(r_h/r)^{1.00}$ for far zone. We

see that in all three cases, the spike profiles are less cuspy than the one from the usual Bondi accretion of non-relativistic monatomic fluid with $\Gamma = 5/3$, for which the spike behaves as $\rho_0(r) \propto r^{-1.5}$ [57]. This is due to the *repulsive* nature of self-interaction of the chosen SIDM model.

In our scenario, the spike profile is formed by accreting the DM, this is different from the Bahcall-Wolf scaling law for the cusp in the number density of stars, *i.e.*, $n_{\rm star}(r) \propto r^{-7/4}$ by considering the accretion of stars into a SMBH at the center of galaxy or cluster. However, we can compare our result with the ones for the accretion of SIDM but different nature of self-interactions. In [266], the SIDM with velocity-dependent cross-section $\sigma \propto v^{-\alpha}$ is considered for the spike profile, and the resultant spike profile is $\rho_0(r) \propto r^{-(\alpha+3)/4}$. Therefore, the Bahcall-Wolf exponent $\beta = 7/4$ can be obtained for $\alpha = 4$, which corresponds to the Coulomb-like self-interaction. This contrasts with the results obtained by our velocity-independent cross-section, for which the steepest spike in the near zone is $\rho_0(r) \propto r^{-1.20}$. Thus, the steepest spike profile from our model is still less cuspy than the Bahcall-Wolf law. Again, this is due to the *repulsive self-interaction* of the chosen SIDM model.

In a broader scenario, the core-expansion phase of SIDM halos can resolve the core-cusp problem of dwarf galaxies [44] if there is no central BH. During the core-collapse phase, a central BH could form directly from DM via gravothermal catastrophe[3] [19, 20, 22, 65]. After that, the cusp could still behave as the NFW, $\rho_0(r) \propto r^{-1}$ with the central BH, and match Eq. 6.37. Some comments of possible extensions are made. The velocity-independent

[3]Although the SIDM we consider here is stiffer ($\gamma = 2$) than the traditional ideal gas ($\gamma = 5/3$) in non-relativistic regime [56], it could still trigger the relativistic instability and collapse into a BH if the core density is sufficiently high such that γ varies from 2 towards 4/3.

cross-section $\sigma/m \sim \lambda^2/m^3$ was used in our calculation, therefore, it predicts a constant cross-section universally over all scales and might not be able to describe dwarf halos and clusters simultaneously. In general, for the interaction mediated via a force-carrier might induce velocity-dependent cross-sections and enhance the cross-section by Sommerfeld effect or resonance scattering [279, 280].

6.3 Conclusions

Inspired by obtaining the spike profile by accreting the DM into a central BH inside the dark halo, in this chapter we consider the relativistic Bondi accretion of a specific type of DM. This DM model is a massive scalar field with quartic self-interaction, which results in the non-polytropic EoS. This model is well motivated from the perspective of particle physics by its simplicity and elegance. Our work can then be viewed as an interesting interplay between astrophysics and particle physics.

By solving the relativistic Bondi accretion problem, we find that the corresponding accretion rate, $\dot{M} \geq 96\pi G^2 M^2 m^4/\lambda\hbar^3$, is bounded from below, and can become divergently large when the initial sound speed approaches the sound barrier. This is quite different from the one for the polytropic type of matter [269]. Assuming this scalar field dominates the main component of DM around the BH, the shape of the density spike is determined by the model parameters of the DM model, *i.e.*, mass and quartic coupling. Thus, the observation of the spike profile will then put a severe constraint on these model parameters. Moreover, due to the repulsive nature of the self-interaction, the spike found in this work is less cuspy than the one predicted by the polytropic type of DM, and also the Bahcall-Wolf power law

of the stellar accretion. Specifically, we find the power law varies from $\rho_0(r) \propto r^{-1.2}$ near the BH to r^{-1} towards the Bondi radius for typical dark halos, which are all independent of the mass of the central BH. Overall, the spike density within the self-gravitating region can be well-fitted by a double-power law of Eq. 6.37. This is the main prediction of our model, which can be scrutinized by the observational spike data.

Our formalism can be easily extended to the SIDM with more generic self-coupling. For example, the SIDM with $V(\phi) = \frac{1}{2}m^2|\phi|^2 + \frac{\lambda_n}{n!}|\phi|^n$ (for $n > 2$) can yield EoS of the form $\rho/\rho_* = \frac{n+2}{n-2}\ p/\rho_* + \frac{1}{2}\left(\frac{2n}{n-2}\ p/\rho_*\right)^{2/n}$, which becomes $p \propto \rho_0^{n/2}$ in the non-relativistic limit [191]. Following the same procedure of this work, one can solve the spike density due to the relativistic Bondi accretion on to a central BH, although the numerical solution could be more complicated. In the long run, one may pin down the SIDM model by the observation data of spike densities. For indirect detection, the self-annihilation of DM can differentiate the small difference in the logarithmic density slope as the annihilation rate depends on the square of the density [221, 230], though the annihilation effect could also soften the spike [229]. In particular, Event Horizon Telescope can serve as a powerful probe of the DM spikes near BHs [228, 230]. However, this deserves further scrutiny for future works.

Chapter 7

Extremely Mass Ratio Inspirals from Supermassive Black Holes

The nature of dark matter represents one of the most enduring and perplexing enigmas in physics. Cosmological measurements have now determined the abundance of dark matter with exquisite precision, and from both observations and numerical simulations, we have gained substantial insights into its distribution within Galactic halos. Yet, the identity of dark matter remains shrouded in mystery. An alternative hypotheses for dark matter, primordial black holes (PBHs) of ~ 30 $M_\odot$, has been explored through their binary merger rate [281, 282], which overlaps $2-53$ Gpc^{-3} yr^{-1} estimated from GW150914 by LIGO. Moreover, the merger rate enhancement inside the dark matter spikes around supermassive black holes (SMBHs) is expected due to the higher dark matter density [283].

However, extreme mass ratio inspirals (EMRIs), which involve binary systems consisting of a compact stellar-mass object orbiting a SMBH, are expected to be among the

primary sources of gravitational waves (GWs) for the upcoming LISA mission [284, 285, 286]. Therefore, in this chapter, we aim to compute the EMRI merger rate resulting from PBHs within dark matter spikes and compare it with the PBH binary merger rate. Although our study only considers redshift $z = 0$, the results can be generally extended to higher redshifts and used to infer the abundance of SMBHs in the early universe.

7.1 Merging via gravitational radiation

First, we review the basics for moving objects to merge through emitting gravitational waves. If the two point masses with initial relative velocity $v_{\rm rel}$ pass away narrowly, where the eccentricity $e \gtrsim 1$, we can assume it is close parabolic orbit and consider the leading term for $e \to 1$. The distance of closest approach of two massive objects of parabolic orbit ($e = 1$),

$$r_{\rm min} = \frac{\ell^2}{2\mu k} = \frac{(\mu v_{\rm rel} b)^2}{2\mu G m_1 m_2} = \frac{b^2 v_{\rm rel}^2}{2G(m_1 + m_2)} \tag{7.1}$$

with $\mu \equiv \frac{m_1 m_2}{m_1 + m_2}$ the reduced mass and b the impact parameter. The quadrupole formalism gives the total energy of the gravitational radiation at Newtonian order

$$\Delta E = \frac{8}{15} \frac{G^{7/2}}{c^5} \frac{(m_1 + m_2)^{1/2} m_1^2 m_2^2}{r_{\rm min}^{7/2}} g(e) \tag{7.2}$$

with $g(e = 1) = 425\pi/32\sqrt{2}$ [287]. The condition for the two masses to pass away is

$$\Delta E = \frac{8}{15} \frac{G^{7/2}}{c^5} \frac{(m_1 + m_2)^{1/2} m_1^2 m_2^2}{r_{\rm min}^{7/2}} g(e) < \frac{1}{2} \mu v_{\rm rel}^2 = \frac{1}{2} \frac{m_1 m_2}{m_1 + m_2} v_{\rm rel}^2. \tag{7.3}$$

Combined with Eq. 7.1 one obtains

$$b > \left(\frac{8}{15}g(e)\right)^{1/7} 2^{9/14}\frac{G}{c^{5/7}}\frac{(m_1+m_2)^{5/7}m_1^{1/7}m_2^{1/7}}{v_{\rm rel}^{9/7}} \equiv b_{\rm merging} \tag{7.4}$$

the minimum (maximum) impact parameter for them to pass away (merge). Therefore, the merging cross section [288, 289]

$$\sigma_{\rm merging} \equiv \pi b_{\rm merging}^2 = 2\pi\left(\frac{85\pi}{6\sqrt{2}}\right)^{2/7}\frac{G^2(m_1+m_2)^{10/7}m_1^{2/7}m_2^{2/7}}{c^{10/7}v_{\rm rel}^{18/7}}. \tag{7.5}$$

If $m_1 = m_2 = m$, we have, in terms of Schwarzschild cross section $\sigma_{\rm Sch} = \left(2Gm/c^2\right)^2$,

$$\sigma_{\rm merging} = \left(\frac{85\pi}{3}\right)^{2/7}\pi\left(\frac{2Gm}{c^2}\right)^2\left(\frac{c}{v_{\rm rel}}\right)^{18/7} \simeq \left(\frac{85\pi}{3}\right)^{2/7}\sigma_{\rm Sch}\left(\frac{c}{v_{\rm rel}}\right)^{18/7},$$

or, in terms of gravitational scattering cross-section[1] $\sigma_{\rm scattering} \simeq \left(2Gm/v_{\rm rel}^2\right)^2$,

$$\sigma_{\rm merging} = \left(\frac{85\pi}{3}\right)^{2/7}\pi\left(\frac{2Gm}{v_{\rm rel}^2}\right)^2\left(\frac{v_{\rm rel}}{c}\right)^{10/7} \simeq \left(\frac{85\pi}{3}\right)^{2/7}\sigma_{\rm scattering}\left(\frac{v_{\rm rel}}{c}\right)^{10/7}.$$

Thus, it is clear that if $v_{\rm rel} \ll c$,

$$\sigma_{\rm Sch} \simeq \left(\frac{v_{\rm rel}}{c}\right)^{18/7}\sigma_{\rm merging} \ll \sigma_{\rm merging} \ll \left(\frac{c}{v_{\rm rel}}\right)^{10/7}\sigma_{\rm merging} \simeq \sigma_{\rm scattering}, \tag{7.6}$$

[1]To be precise, the gravitational (Coulomb-like) scattering cross section [123, 290, 291]

$$\sigma_{\rm scattering} = 2\pi\left(\frac{2Gm}{v_{\rm rel}^2}\right)^2\ln\Lambda,$$

where $\ln\Lambda = \ln\left(b_{\rm max}/b_{\rm min}\right)$ is the Coulomb logarithm, with $b_{\rm max} \sim (4\pi\rho/3m)^{-1/3}$ being the average separation between objects at a mass density $\rho = mn$, and $b_{\rm min} \sim 2Gm/v_{\rm rel}^2$ is the impact parameter for a 90° deflection.

which means that for non-relativistically moving objects to merge through emitting gravitational waves, they can be far from head-on collision; while the merging cross-section must be much smaller than the gravitational scattering cross-section if they were to scatter off.

7.2 Primordial black hole binary mergers

In this section, we review the methodology in Ref. [281] to calculate the merger rate of PBHs inside halos. Given the merging cross-section in the previous section, we can calculate the merger rate of PBHs within each halo. Since these things are just like large dark matter particles, we use the same calculation as for dark matter annihilation

$$\mathcal{R} = 4\pi \int_0^{r_{200}} \frac{1}{2} n^2(r) \langle \sigma_{\rm merging} v \rangle r^2 dr = 4\pi \int_0^{r_{200}} \frac{1}{2} \left(\frac{\rho_{\rm NFW}(r)}{m} \right)^2 \langle \sigma_{\rm merging} v \rangle r^2 dr, \quad (7.7)$$

where

$$\rho_{\rm NFW}(r) = \frac{\rho_s}{(r/r_s)\,(1 + r/r_s)^2} \quad (7.8)$$

is the Navarro-Frenk-White (NFW) profile [24] and $r_{200} = c_{200} r_s$ the virial radius with c_{200} the concentration, m is the mass of the PBH and $v = v_{\rm rel}$ is the relative velocity of two PBHs. We also want the cross-section for two PBHs to form a binary and ultimately collide. The merging cross-section for two PBHs of equal mass is then

$$\sigma_{\rm merging} = 4\pi \left(\frac{85\pi}{3} \right)^{2/7} \frac{G^2 m^2}{c^4} \left(\frac{v}{c} \right)^{-18/7}. \quad (7.9)$$

To approximate v, the relative velocity of two PBHs, we assume their velocity distribution follows the standard halo model assumption of a Maxwell-Boltzmann distribution with a cut-off $v_{\rm cut}$:

$$\mathcal{P}(v, v_{\rm dm}) = F_0 \left[\exp\left(-\frac{v^2}{v_{\rm dm}^2}\right) - \exp\left(-\frac{v_{\rm cut}^2}{v_{\rm dm}^2}\right)\right];\ \mathcal{P}(v, v_{\rm dm}) = 0 \text{ for } v > v_{\rm cut}, \tag{7.10}$$

where $F_0 = F_0(v_{\rm dm})$ is the normalization factor determined by $4\pi \int_0^{v_{\rm cut}} \mathcal{P}(v) v^2 dv = 1$ and the cut-off velocity

$$v_{\rm cut} = \sqrt{\frac{2GM_{200}}{r_{200}}} \tag{7.11}$$

is determined by the escape velocity in a dark halo, and $M_{200} = 4\pi\rho_s r_s^3 f(c_{200})$ with $f(x) = \ln(1+x) - x/(1+x)$ for an NFW profile. Comparison to N-body simulations shows that this assumption works well for the small velocities which will dominate our event rate.

For an NFW halo, the Keplerian velocity has a maximum at $r_{\rm max} = c_{\rm max} r_s = 2.1626 r_s$. Then the velocity dispersion of dark matter can be assumed to be

$$v_{\rm dm} = \sqrt{\frac{GM_{\rm max}}{r_{\rm max}}} \tag{7.12}$$

where $M_{\rm max} = 4\pi\rho_s r_s^3 f(c_{\rm max})$ is the mass within $r_{\rm max}$, given by integrating the NFW profile. Therefore, we have

$$v_{\rm dm} = \sqrt{\frac{4\pi G\rho_s r_s^3 f(c_{\rm max})}{c_{\rm max} r_s}} = \sqrt{\frac{4\pi G\rho_s r_s^3 f(c_{200})}{c_{200} r_s}} \sqrt{\frac{f(c_{\rm max}) c_{200}}{f(c_{200}) c_{\rm max}}} = \frac{v_{\rm cut}}{\sqrt{2}} \sqrt{\frac{f(c_{\rm max}) c_{200}}{f(c_{200}) c_{\rm max}}}. \tag{7.13}$$

Then the total cross-section in each halo can be computed by integrating over the velocity

distribution, i.e.,

$$\langle \sigma_{\rm merging} v \rangle = (4\pi)^2 \left(\frac{85\pi}{3}\right)^{2/7} \frac{G^2 m^2}{c^3} \int_0^{v_{\rm cut}} c^3 \mathcal{P}(v, v_{\rm dm}) \left(\frac{v}{c}\right)^{3/7} {\rm d}\left(\frac{v}{c}\right) \tag{7.14}$$

which can be evaluated in terms of gamma functions. Note that it has units of volume per unit time as $c^3\mathcal{P}$ is dimensionless. Since the cross-section is independent of r, we can do the NFW integral to get the merger rate

$$\mathcal{R} = \frac{4\pi \langle \sigma_{\rm merging} v \rangle}{2} \int_0^{r_{200}} r^2 \left(\frac{\rho_{\rm NFW}}{m}\right)^2 dr = \frac{\langle \sigma_{\rm merging} v \rangle}{m^2} \frac{M_{200}^2}{8\pi r_s^3} \frac{1}{3} \left[1 - \frac{1}{(1+c_{200})^3}\right] \frac{1}{f^2(c_{200})}.$$

$$= \frac{8\pi^2}{3} \left(\frac{85\pi}{3}\right)^{2/7} \frac{G^2 \rho_s M_{200}}{c^3} \left[1 - \frac{1}{(1+c_{200})^3}\right] \frac{1}{f(c_{200})} \int_0^{v_{\rm cut}} c^3 \mathcal{P}(v, v_{\rm dm}) \left(\frac{v}{c}\right)^{3/7} {\rm d}\left(\frac{v}{c}\right). \tag{7.15}$$

The PBH mass drops out, thus the merger rate $\mathcal{R} \propto (G^2\rho_s/c^3) M_{200}$ *only* depends on the properties of halos. For a Milky Way halo, $c_{200} \sim 7$, and this is 10^{-19} s^{-1} or 2×10^{-12} yr^{-1}.

7.3 Extremely mass ratio inspirals

We now consider the EMRI merger rate from PBHs plunging into a central SMBH of mass M in each halo. As accretion of dark matter (assuming all of them are PBHs) around a SMBH develops a density spike within the radius of influence $r_{\rm sp}$ of the SMBH, we only consider the PBHs residing in the spike. The merging rate within the spike

$$\Gamma = \langle n \rangle \langle \sigma_{\rm merging} v \rangle, \tag{7.16}$$

where $\langle n \rangle$ is the averaged number density of the PBHs in the spike. Taking $m_1 = M = 10^{\beta} m = 10^{\beta} m_2$ with $\beta \gtrsim 4$ for EMRIs, the merging cross-section

$$\sigma_{\rm merging} = 2\pi \left(\frac{85\pi}{6\sqrt{2}}\right)^{2/7} \frac{G^2 (m_1 + m_2)^{10/7} m_1^{2/7} m_2^{2/7}}{c^{10/7} v^{18/7}}$$

$$\simeq 2\pi \left(\frac{85\pi}{6\sqrt{2}}\right)^{2/7} 10^{12\beta/7} \frac{G^2 m^2}{c^4} \left(\frac{v}{c}\right)^{-18/7}. \tag{7.17}$$

Note that there is a $10^{12\beta/7}$ enhancement compared to the equal mass merger. To approximate v, the relative velocity of the compact object to the SMBH, we assume their velocity distribution follows a Maxwell-Boltzmann distribution with a cut-off $v_{\rm cut}$:

$$\mathcal{P}(v, v_{\rm sp}) = F_0 \left[\exp\left(-\frac{v^2}{v_{\rm sp}^2}\right) - \exp\left(-\frac{v_{\rm cut}^2}{v_{\rm sp}^2}\right)\right];\ \mathcal{P}(v, v_{\rm sp}) = 0 \text{ for } v > v_{\rm cut}, \tag{7.18}$$

where $F_0 = F_0(v_{\rm sp})$ is the normalization factor and the cut-off velocity

$$v_{\rm cut} = \sqrt{\frac{2G\,(M_{\rm sp} + M)}{r_{\rm sp}}} \tag{7.19}$$

is determined by the escape velocity in the density spike, where $M_{\rm sp}$ is the spike mass. And the velocity dispersion of dark matter in the spike is assumed to be

$$v_{\rm sp} = \sqrt{\frac{G\,(M_{\rm sp} + M)}{r_{\rm sp}}} = \frac{v_{\rm cut}}{\sqrt{2}}. \tag{7.20}$$

Then the total cross-section in each halo can be computed by integrating over the velocity distribution

$$\langle \sigma_{\rm merging} v \rangle = (4\pi)^2 \left(\frac{85\pi}{96}\right)^{2/7} 10^{12\beta/7} \frac{G^2 m^2}{c^3} \int_0^{v_{\rm cut}} c^3 \mathcal{P}(v, v_{\rm sp}) \left(\frac{v}{c}\right)^{3/7} {\rm d}\left(\frac{v}{c}\right). \tag{7.21}$$

Without loss of generality, we could assume a power-law density spike

$$\rho(r) = \rho_{\rm sp} \left(r/r_{\rm sp}\right)^{-\alpha} \tag{7.22}$$

within $r_{\rm sp}$, where $1 \leq \alpha < 3$ depending on the matter properties. For example, stellar objects in bound orbits in the gravitational potential well of the central black hole diffuse from one bound orbit to another via gravitational (Coulomb-like) scattering will follow the Bahcall-Wolf power-law $\alpha = 7/4$ [232, 266], which has generally been assumed for EMRI formation for stellar objects surrounding a SMBH [292]. Then the total mass of the spike

$$M_{\rm sp} = \frac{4\pi \rho_{\rm sp} r_{\rm sp}^3}{3-\alpha} \left[1 - \left(\frac{2GM}{c^2 r_{\rm sp}}\right)^{3-\alpha}\right], \tag{7.23}$$

thus

$$\langle n \rangle = \frac{M_{\rm sp}/m}{4\pi r_{\rm sp}^3/3} = \left(\frac{\rho_{\rm sp}}{m}\right) \left(\frac{3}{3-\alpha}\right) \left[1 - \left(\frac{2GM}{c^2 r_{\rm sp}}\right)^{3-\alpha}\right]. \tag{7.24}$$

Here we set the lower bound of the spike profile at $2GM/c^2$, although a more detailed consideration gives $8GM/c^2$ [221] or $4GM/c^2$ in generally relativistic treatment [293, 294] due to the SMBH capture, the difference is negligible. In practice, we can take the Bondi radius as the radius of influence of the SMBH, $r_{\rm sp} = r_{\rm B} = 2GM/v_{\rm dm}^2$, where $v_{\rm dm}$ is the

velocity dispersion of dark matter far away from the Bondi accretion radius. As before, we can approximate $v_{\rm dm} = \sqrt{GM_{\rm max}/r_{\rm max}}$ in an NFW halo. Therefore,

$$\langle n \rangle = \left(\frac{\rho_{\rm sp}}{m}\right)\left(\frac{3}{3-\alpha}\right)\left[1-\left(\frac{GM_{\rm max}}{c^2 r_{\rm max}}\right)^{3-\alpha}\right] \simeq \left(\frac{\rho_{\rm sp}}{m}\right)\left(\frac{3}{3-\alpha}\right)$$

as $v_{\rm dm} \ll c$. Now the task is to determine $\rho_{\rm sp}$. Observationally, $M_{\rm sp}$ must be smaller than the *uncertainty* in determining the dynamical mass M of the SMBH, thus we can set $M_{\rm sp} = \Delta M$ with $\Delta \lesssim 0.1$, and

$$\Delta M = M_{\rm sp} \simeq \frac{4\pi\rho_{\rm sp} r_{\rm sp}^3}{3-\alpha} = \frac{32\pi\rho_{\rm sp}}{3-\alpha}\left(c_{\rm max} r_s\right)^3 \left[\frac{M}{4\pi\rho_s r_s^3 f(c_{\rm max})}\right]^3$$

so the spike density scale

$$\rho_{\rm sp} = \frac{(3-\alpha)\Delta M}{32\pi}\left(\frac{4\pi\rho_s r_s^2}{M}\right)^3\left(\frac{f(c_{\rm max})}{c_{\rm max}}\right)^3 = \frac{(3-\alpha)\Delta}{8}\rho_s\left(\frac{M_{200}}{M}\right)^2\frac{1}{f^2(c_{200})}\left(\frac{f(c_{\rm max})}{c_{\rm max}}\right)^3.$$

Then we can rewrite

$$\langle n \rangle = \frac{3\Delta}{8}\left(\frac{\rho_s}{m}\right)\left(\frac{M_{200}}{M}\right)^2\frac{1}{f^2(c_{200})}\left(\frac{f(c_{\rm max})}{c_{\rm max}}\right)^3 \tag{7.25}$$

which depends on the properties of NFW profile while the power-law index α drops out. Thus the merger rate

$$\Gamma = \langle n \rangle \langle \sigma_{\rm merging} v \rangle$$

$$= 6\pi^2\left(\frac{85\pi}{96}\right)^{2/7} 10^{12\beta/7}\Delta\frac{G^2\rho_s m}{c^3}\left(\frac{M_{200}}{M}\right)^2\frac{1}{f^2(c_{200})}\left(\frac{f(c_{\rm max})}{c_{\rm max}}\right)^3\int_0^{v_{\rm cut}} c^3\mathcal{P}(v, v_{\rm sp})\left(\frac{v}{c}\right)^{3/7}{\rm d}\left(\frac{v}{c}\right)$$

$$= 6\pi^2 \left(\frac{85\pi}{96}\right)^{2/7} 10^{5\beta/7} \Delta \frac{G^2 \rho_s M}{c^3} \left(\frac{M_{200}}{M}\right)^2 \frac{1}{f^2(c_{200})} \left(\frac{f(c_{\rm max})}{c_{\rm max}}\right)^3 \int_0^{v_{\rm cut}} c^3 \mathcal{P}(v, v_{\rm sp}) \left(\frac{v}{c}\right)^{3/7} {\rm d}\left(\frac{v}{c}\right), \tag{7.26}$$

where we have used $m = 10^{-\beta} M$.

7.3.1 PBH binary mergers in the spike

Similar to the PBH mergers in whole halo discussed in Sec. 7.2, we now focus on the mergers happening in the spike, i.e.,

$$\mathcal{R} = 4\pi \int_{2GM/c^2}^{r_{\rm sp}} \frac{1}{2} n^2(r) \langle \sigma_{\rm merging} v \rangle r^2 dr = 2\pi \frac{\langle \sigma_{\rm merging} v \rangle}{m^2} \rho_{\rm sp}^2 r_{\rm sp}^3 \left(\frac{1}{3-2\alpha}\right) \left[1 - \left(\frac{2GM}{c^2 r_{\rm sp}}\right)^{3-2\alpha}\right]$$

$$= \pi^2 (3-\alpha)^2 \Delta^2 \left(\frac{85\pi}{3}\right)^{2/7} \frac{G^2 \rho_s M}{c^3} \left(\frac{M_{200}}{M}\right)^2 \frac{1}{f^2(c_{200})} \left(\frac{f(c_{\rm max})}{c_{\rm max}}\right)^3 \times$$

$$\left(\frac{1}{3-2\alpha}\right) \left[1 - \left(\frac{4\pi G \rho_s r_s^2}{c^2} \frac{f(c_{\rm max})}{c_{\rm max}}\right)^{3-2\alpha}\right] \times \int_0^{v_{\rm cut}} c^3 \mathcal{P}(v, v_{\rm sp}) \left(\frac{v}{c}\right)^{3/7} {\rm d}\left(\frac{v}{c}\right), \tag{7.27}$$

where we have used

$$r_{\rm sp} = \frac{M}{2\pi \rho_s r_s^2} \left(\frac{c_{\rm max}}{f(c_{\rm max})}\right) \quad \text{and} \quad \rho_{\rm sp} = \frac{(3-\alpha)\Delta}{8} \rho_s \left(\frac{M_{200}}{M}\right)^2 \frac{1}{f^2(c_{200})} \left[\frac{f(c_{\rm max})}{c_{\rm max}}\right]^3$$

as well as

$$\langle \sigma_{\rm merging} v \rangle = (4\pi)^2 \left(\frac{85\pi}{3}\right)^{2/7} \frac{G^2 m^2}{c^3} \int_0^{v_{\rm cut}} c^3 \mathcal{P}(v, v_{\rm sp}) \left(\frac{v}{c}\right)^{3/7} {\rm d}\left(\frac{v}{c}\right).$$

It is indicative to compare the EMRI merger rate Eq. 7.26 to the PBH binary merger rate Eq. 7.27 inside the spike. The inspiral merger rate $\Gamma \sim [10^{5\beta/7}/\Delta(3-\alpha)^2]\mathcal{R}$,

roughly a factor of $[10^{5\beta/7}/\Delta(3-\alpha)^2]$ enhancement compared to the binary merger rate $\mathcal{R}$. In particular, the merger rate is *sensitive* to the ratio $M_{\rm sp}/M = \Delta$ (assuming $\Delta = 0.1$ hereafter), and the inspiral merger rate $\Gamma \propto \Delta$; while the PBH binary merger rate $\mathcal{R} \propto \Delta^2$. Thus if we assume that only a fraction $f_{\rm PBH}$ of the dark matter is PBHs, $\Gamma \propto f_{\rm PBH}$; while $\mathcal{R} \propto f_{\rm PBH}^2$.

7.3.2 Merger rate as function of SMBH mass

The merger rate generally depends on redshift z through the scale density and radius of NFW, given by [24]

$$\rho_s(z) = \frac{200 c_{200}^3 \rho_c(z)}{3 f(c_{200})} \quad \text{and} \quad r_s(z) = \left(\frac{3 M_{200}}{800\pi c_{200}^3 \rho_c(z)} \right)^{1/3}$$

with

$$\rho_c(z) = \frac{3H_0^2}{8\pi G} \left[\Omega_{M,0}(1+z)^3 + \Omega_\Lambda \right],$$

$H_0 = 1.02 \times 10^{-4} h$ Myr^{-1}, $\Omega_{M,0} = 0.315$ and $\Omega_\Lambda = 0.685$ [30]. In addition, we need to relate the halo properties to the harbored SMBH mass. Therefore, we consider the M-σ relation [295, 296]

$$\log\left(M/{\rm M}_\odot\right) = a + b \log\left(\sigma/200 \text{ km s}^{-1}\right)$$

with the parameters $a = 8.12 \pm 0.08$, $b = 4.24 \pm 0.41$ in Refs. [297, 298], and we assume

$$\sigma = v_{\rm dm} = \sqrt{\frac{G M_{\rm max}}{r_{\rm max}}} = \sqrt{\frac{4\pi G \rho_s r_s^2 f(c_{200})}{c_{200}}} \sqrt{\frac{f(c_{\rm max}) c_{200}}{f(c_{200}) c_{\rm max}}}.$$

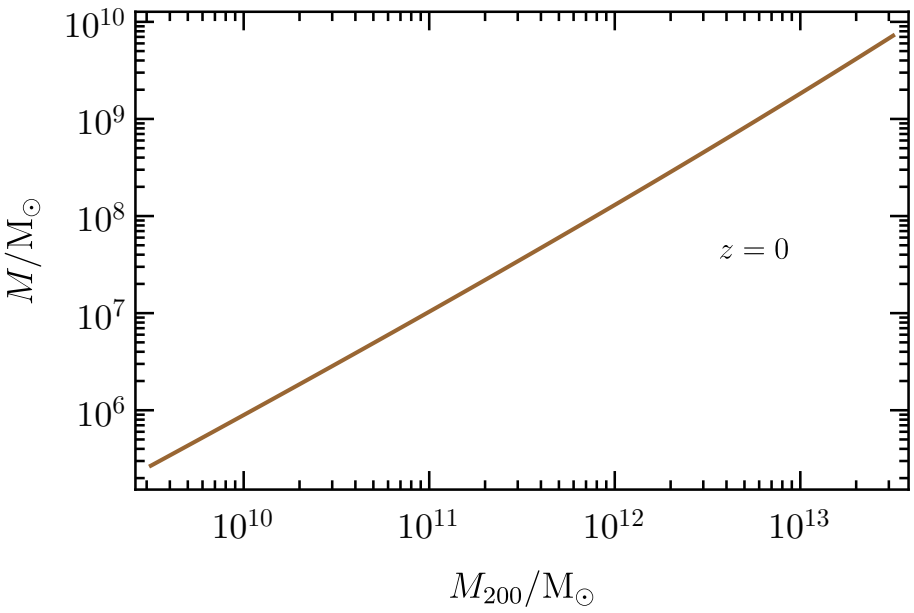

Figure 7.1: SMBH mass vs. halo mass at redshift $z = 0$, according to M-σ relation and concentration mass relation in Prada (2012).

To determine the SMBH mass and merger rate, however, we also need the concentration-mass (c_{200}-M_{200}) relation as a function of redshift [299, 300, 301]. We adopt the empirical (fitted from observations rather than simulations[2]) in Prada (2012) [299, 302]:

$$\log c_{200} = 4.23 - 0.25 \log(M_{200}/\mathrm{M}_\odot) - 0.16 \log\left(\frac{1+z}{1.47}\right).$$

In Fig. 7.1, we plot the SMBH mass as a function of halo mass at redshift $z = 0$; see Fig. 7.2 for the comparison of merger rates. The merger rates of EMRIs and PBH binaries are about the same at $M \sim 10^5 - 10^6$ $\mathrm{M}_\odot$, however, EMRI merger rate increases as the BH mass increases up to 10^{-3} yr^{-1} at $M = 10^{10}$ $\mathrm{M}_\odot$.

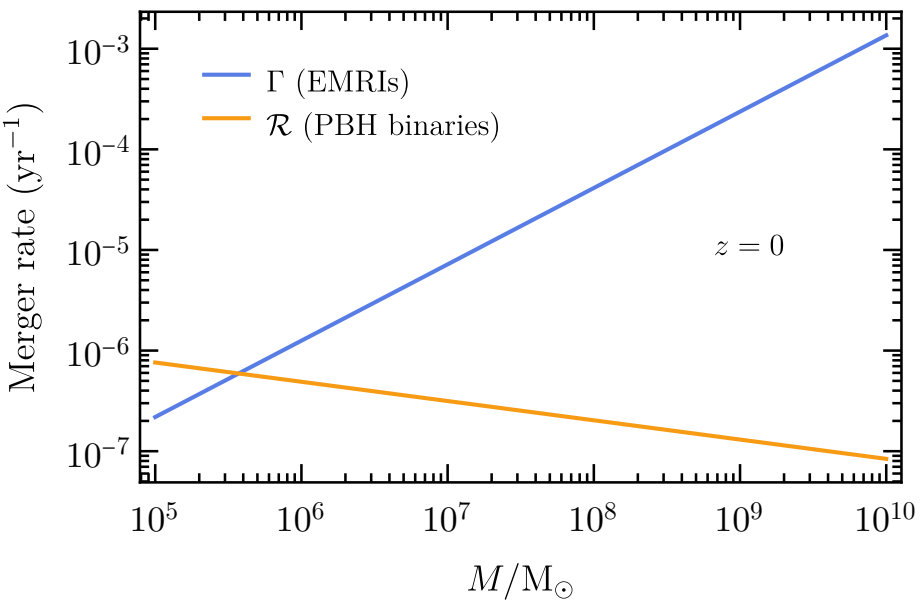

Figure 7.2: Merger rate per halo at redshift $z = 0$, assuming all the matter in the spikes around the central SMBHs is composed of PBHs of mass 30 $\mathrm{M}_\odot$. Here we use $\alpha = 7/4$ for Coulomb-like interaction between PBHs, following the Bahcall-Wolf power-law of the density spike.

7.3.3 Total merger rate

We can determine the total merger rate per unit volume by

$$\mathcal{V}_{\{\mathcal{R},\Gamma\}} = \int \frac{\mathrm{d}n}{\mathrm{d}\log M}(M) \left\{ \begin{array}{c} \mathcal{R}(M) \\ \Gamma(M) \end{array} \right\} \mathrm{d}\log M, \tag{7.28}$$

where $\mathrm{d}n/\mathrm{d}\log M(M)$ is the SMBH mass function. Now, we consider two example SMBH mass functions. First, the estimated SMBH mass function according to kinematic and photometric data based on the empirical relation between the halo velocity dispersion and

[2]See Ref. [301] for a semi-analytic, physically motivated model through fits to the results of numerical simulations.

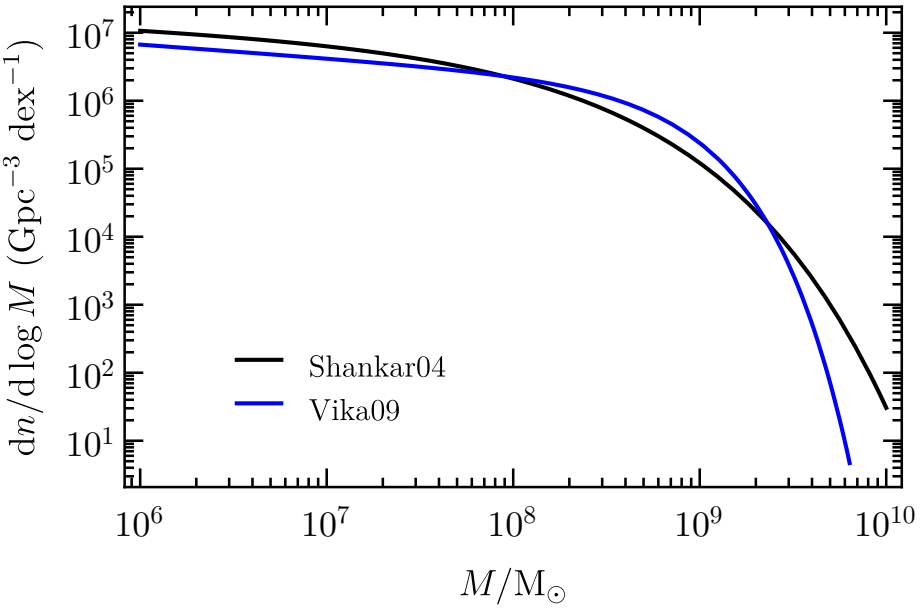

Figure 7.3: Estimated SMBH mass functions according to kinematic and photometric data based on the empirical relation between the halo velocity dispersion and the SMBH mass in Shankar (2004), and based on the assumption that all spheroids contain SMBHs at their center, using 1743 galaxies from the Millennium Galaxy Catalogue in Vika (2009).

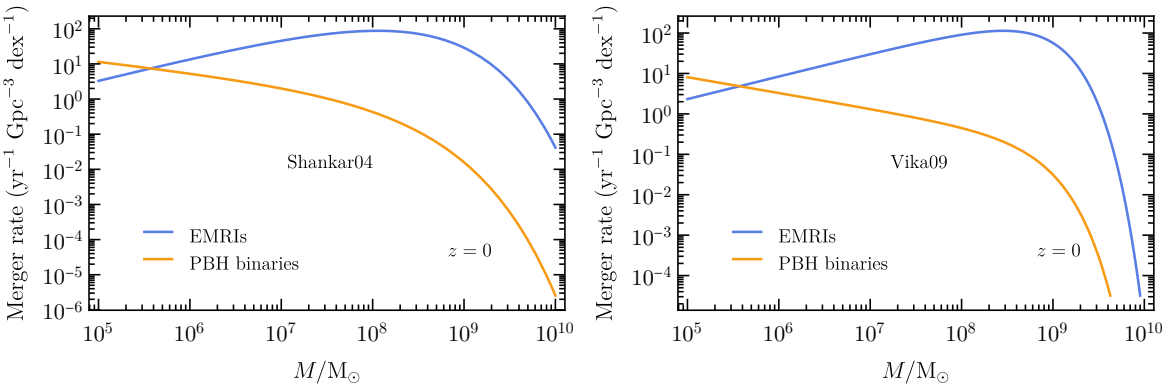

Figure 7.4: The total merger rate per unit volume as a function of SMBH mass, based on the estimated SMBH mass function in *Left*: Shankar (2004); *Right*: Vika (2009).

the SMBH mass in Shankar (2004) [303],

$$\frac{\mathrm{d}n}{\mathrm{d}\log M}(M) = \phi_* \left(\frac{M}{M_*}\right)^{\alpha+1} \exp\left[-\left(\frac{M}{M_*}\right)^{\beta}\right] \tag{7.29}$$

with $\phi_* = 7.7 \times 10^6$ Gpc^{-3}, $M_* = 6.4 \times 10^7$ M$_\odot$, $\alpha = -1.11$ and $\beta = 0.49$. On the other hand, the estimated SMBH mass function based on the assumption that all spheroids contain SMBHs at their center, using 1743 galaxies from the Millennium Galaxy Catalogue in Vika (2009) [304],

$$\frac{\mathrm{d}n}{\mathrm{d}\log M}(M) = \phi_* \left(\frac{M}{M_*}\right)^{\alpha+1} \exp\left[1 - \left(\frac{M}{M_*}\right)\right] \tag{7.30}$$

with $\phi_* = 7.07946 \times 10^5$ Gpc^{-3}, $M_* = 10^{8.71}$ M$_\odot$ and $\alpha = -1.2$. See Fig. 7.3 for comparison of the two mass functions. Multiplied by the mass functions, we see that in Fig. 7.4, the merger rates of EMRIs and PBH binaries are about the same at $M \sim 10^5 - 10^6$ M$_\odot$, however, EMRI rate increases and peaks up to 10^2 yr^{-1} Gpc^{-3} dex^{-1} at $M = 10^8 - 10^9$ M$_\odot$.

After integrating Fig. 7.4 over $\mathrm{d}\log M$, the area under the graphs represents the contribution of different types of SMBH. For PBH mergers, we obtain $\mathcal{V}_\mathcal{R} = 12.68$ yr^{-1} Gpc^{-3} (Shankar(2004)) and 8.508 yr^{-1} Gpc^{-3} (Vika(2009)). Interestingly, the high density enhancement in the spikes makes the merger rate comparable to the mergers inside the whole dark matter halos [281]. For EMRI mergers, we obtain $\mathcal{V}_\Gamma = 177.3$ yr^{-1} Gpc^{-3} (Shankar(2004)) and 188.1 yr^{-1} Gpc^{-3} (Vika(2009)). Therefore, the two mass functions only result in a little different merger rates.

7.4 Discussion

In summary, we have determined the overall merger rate in the spikes at $z = 0$ to be $\mathcal{V}_\mathcal{R} \simeq 10$ yr^{-1} Gpc^{-3} for PBH binaries, and $\mathcal{V}_\Gamma \simeq 180$ yr^{-1} Gpc^{-3} for EMRIs, assuming a PBH dark matter fraction of $f_{\rm PBH} = 1$ (generally, $\mathcal{V}_\mathcal{R} \propto f_{\rm PBH}^2$ while $\mathcal{V}_\Gamma \propto f_{\rm PBH}$).

Since the change in merger rate is negligible from $z = 0$ to $z = 1$, assuming the same SMBH mass functions, we can ignore redshift evolution. Then, the comoving volume is approximately ~ 200 Gpc^3 for $z < 1$, which corresponds to approximately $\sim 3.6 \times 10^4$ EMRI events per year. However, if we assume a relatively high signal-to-noise ratio of 20 is required for EMRI detection [284, 285], we obtain a maximal redshift of 0.05 and a comoving volume of approximately ~ 0.025 Gpc^3, which results in approximately ~ 4.5 events per year. In addition, the merger frequency of these EMRIs ranges from 10^{-2} Hz down to 10^{-6} Hz for SMBH masses ranging from 10^6 $M_\odot$ up to 10^{10} $M_\odot$. Therefore, the EMRI signal falls within the LISA band and is not detectable by a midband experiment [305].

Nevertheless, the methodology developed in this study is general, and EMRIs can also result from conventional stellar objects, not necessarily PBHs. In particular, it can be used to infer the high-redshift SMBH population in various seeding models, such as the one discussed in Chapter 2. However, for mergers at redshift $z > 1$, the effects of frequency redshifting and source evolution will become important. We will leave this aspect for future investigation.

Chapter 8

Summary and Conclusions

In the quest to unravel the enigma of supermassive black hole (SMBH) formation, this dissertation has embarked on a multifaceted exploration that traverses the realms of cosmology, astrophysics, and quantum physics. Our journey began with the recognition that SMBHs, with staggering masses of around 10^9 $M_\odot$, have existed since the universe was but a cosmic toddler at 6% of its present age. This astounding observation served as the impetus for our investigation into the role of self-interacting dark matter in the birth of these celestial giants.

The central tenet of our research rests upon the concept of gravothermal instability within self-interacting dark matter halos. We uncovered a scenario where the presence of baryons in protogalaxies accelerates the gravothermal evolution of these halos, shortening the timescales for central collapse. Viscosity induced by self-interactions emerged as a pivotal factor, aiding in the dissipation of angular momentum and ultimately culminating in the formation of seed black holes. However, the rarity of high-redshift SMBHs in this

scenario underscores the unique conditions required for their genesis. Furthermore, we delved into the conditions for triggering general relativistic instability within the collapsed region, elucidating the precise criteria for the transformation from a dense core to a black hole. These findings not only shed light on the formation of SMBHs but also provide a unified explanation for the diverse dark matter distributions observed in galaxies today.

Our cosmic voyage extended beyond classical astrophysics, venturing into higher dimensions and the quantum realm. In (3+1)-dimensional spacetime, the balance between stability and instability in ideal monatomic fluids became evident, offering insights into the cosmic architecture. Quantum physics, often perceived as an impediment to gravitational collapse, emerged as a catalyst for instability in self-gravitating thermal systems. The dissertation also explored the formation of massive black holes from thermalized dark matter clumps and the role of Fermi-degeneracy pressure and Bose-Einstein condensates. These diverse inquiries have collectively illuminated the intricate tapestry of forces and phenomena that shape the cosmos, bringing us closer to demystifying the genesis of SMBHs and the profound role of self-interacting dark matter in the cosmic drama. Furthermore, we derived the density profile of Bose-Einstein condensate dark matter around SMBHs, assuming relativistic Bondi accretion. Finally, we analyzed the gravitational wave signals originating from dark matter density spikes around SMBHs, considering primordial black holes as an alternative dark matter candidate. As we conclude this odyssey, we are left with a richer and more nuanced understanding of the universe's earliest epochs and the celestial giants that punctuate its history. The mysteries that remain continue to beckon, inspiring future explorations and discoveries in the ever-evolving field of astrophysics and cosmology.

Bibliography

[1] K. Inayoshi, E. Visbal and Z. Haiman, *The Assembly of the First Massive Black Holes*, *Ann. Rev. Astron. Astrophys.* **58** (2020) 27–97, [1911.05791].

[2] M. J. Rees, *Black Hole Models for Active Galactic Nuclei*, *Ann. Rev. Astron. Astrophys.* **22** (1984) 471–506.

[3] E. Salpeter, *Accretion of Interstellar Matter by Massive Objects*, *Astrophys. J.* **140** (1964) 796–800.

[4] N. I. Shakura and R. Sunyaev, *A Theory of the instability of disk accretion on to black holes and the variability of binary X-ray sources, galactic nuclei and quasars*, *Mon. Not. Roy. Astron. Soc.* **175** (1976) 613–632.

[5] J. Yang, F. Wang, X. Fan, J. F. Hennawi, F. B. Davies, M. Yue et al., *Pōniuā'ena: A luminous $z = 7.5$ quasar hosting a 1.5 billion solar mass black hole*, *Astrophys. J. Lett.* **897** (2020) L14, [2006.13452].

[6] V. Bromm and A. Loeb, *Formation of the first supermassive black holes*, *Astrophys. J.* **596** (2003) 34–46, [astro-ph/0212400].

[7] M. C. Begelman, M. Volonteri and M. J. Rees, *Formation of supermassive black holes by direct collapse in pregalactic halos*, *Mon. Not. Roy. Astron. Soc.* **370** (2006) 289–298, [astro-ph/0602363].

[8] K. Freese, C. Ilie, D. Spolyar, M. Valluri and P. Bodenheimer, *Supermassive Dark Stars: Detectable in JWST*, *Astrophys. J.* **716** (2010) 1397–1407, [1002.2233].

[9] M. Onoue, N. Kashikawa, Y. Matsuoka, N. Kato, T. Izumi, T. Nagao et al., *Subaru high-z exploration of low-luminosity quasars (SHELLQs). VI. black hole mass measurements of six quasars at $6.1 \leq z \leq 6.7$*, *Astrophys. J.* **880** (2019) 77, [1904.07278].

[10] Y. Matsuoka, M. Onoue, N. Kashikawa, M. A. Strauss, K. Iwasawa, C.-H. Lee et al., *Discovery of the first low-luminosity quasar at $z > 7$*, *Astrophys. J. Lett.* **872** (2019) L2, [1901.10487].

[11] D. N. Spergel and P. J. Steinhardt, *Observational evidence for selfinteracting cold dark matter*, *Phys. Rev. Lett.* **84** (2000) 3760–3763, [astro-ph/9909386].

[12] M. Kaplinghat, S. Tulin and H.-B. Yu, *Dark Matter Halos as Particle Colliders: Unified Solution to Small-Scale Structure Puzzles from Dwarfs to Clusters*, *Phys. Rev. Lett.* **116** (2016) 041302, [1508.03339].

[13] S. Tulin and H.-B. Yu, *Dark Matter Self-interactions and Small Scale Structure*, *Phys. Rept.* **730** (2018) 1–57, [1705.02358].

[14] R. Dave, D. N. Spergel, P. J. Steinhardt and B. D. Wandelt, *Halo properties in cosmological simulations of selfinteracting cold dark matter*, *Astrophys. J.* **547** (2001) 574–589, [astro-ph/0006218].

[15] K.-J. Ahn and P. R. Shapiro, *Formation and evolution of the self-interacting dark matter halos*, *Mon. Not. Roy. Astron. Soc.* **363** (2005) 1092–1124, [astro-ph/0412169].

[16] M. Rocha, A. H. Peter, J. S. Bullock, M. Kaplinghat, S. Garrison-Kimmel et al., *Cosmological Simulations with Self-Interacting Dark Matter I: Constant Density Cores and Substructure*, *Mon.Not.Roy.Astron.Soc.* **430** (2013) 81–104, [1208.3025].

[17] M. Vogelsberger, J. Zavala and A. Loeb, *Subhaloes in Self-Interacting Galactic Dark Matter Haloes*, *Mon. Not. Roy. Astron. Soc.* **423** (2012) 3740, [1201.5892].

[18] D. Lynden-Bell and R. Wood, *The gravo-thermal catastrophe in isothermal spheres and the onset of red-giant structure for stellar systems*, *Mon. Not. Roy. Astron. Soc.* **138** (1968) 495.

[19] S. Balberg, S. L. Shapiro and S. Inagaki, *Selfinteracting dark matter halos and the gravothermal catastrophe*, *Astrophys. J.* **568** (2002) 475–487, [astro-ph/0110561].

[20] S. Balberg and S. L. Shapiro, *Gravothermal collapse of selfinteracting dark matter halos and the origin of massive black holes*, *Phys.Rev.Lett.* **88** (2002) 101301, [astro-ph/0111176].

[21] J. Koda and P. R. Shapiro, *Gravothermal collapse of isolated self-interacting dark matter haloes: N-body simulation versus the fluid model*, *Mon. Not. Roy. Astron. Soc.* **415** (2011) 1125, [1101.3097].

[22] J. Pollack, D. N. Spergel and P. J. Steinhardt, *Supermassive Black Holes from Ultra-Strongly Self-Interacting Dark Matter*, *Astrophys. J.* **804** (2015) 131, [1501.00017].

[23] R. Essig, S. D. Mcdermott, H.-B. Yu and Y.-M. Zhong, *Constraining Dissipative Dark Matter Self-Interactions*, *Phys. Rev. Lett.* **123** (2019) 121102, [1809.01144].

[24] J. F. Navarro, C. S. Frenk and S. D. White, *The Structure of cold dark matter halos*, *Astrophys. J.* **462** (1996) 563–575, [astro-ph/9508025].

[25] J. H. Wise, M. J. Turk and T. Abel, *Resolving the Formation of Protogalaxies. II. Central Gravitational Collapse*, *Astrophys. J.* **682** (2008) 745, [0710.1678].

[26] M. Vogelsberger, J. Zavala, C. Simpson and A. Jenkins, *Dwarf galaxies in CDM and SIDM with baryons: observational probes of the nature of dark matter*, *Mon. Not. Roy. Astron. Soc.* **444** (2014) 3684–3698, [1405.5216].

[27] A. Cruz, A. Pontzen, M. Volonteri, T. R. Quinn, M. Tremmel, A. M. Brooks et al., *Self-interacting dark matter and the delay of supermassive black hole growth*, *Mon. Not. Roy. Astron. Soc.* **500** (11, 2020) 2177–2187, [2004.08477].

[28] A. Robertson et al., *The diverse density profiles of galaxy clusters with self-interacting dark matter plus baryons*, *Mon. Not. Roy. Astron. Soc.* **476** (2018) L20–L24, [1711.09096].

[29] O. Sameie, M. Boylan-Kolchin, R. Sanderson, D. Vargya, P. F. Hopkins, A. Wetzel et al., *The central densities of Milky Way-mass galaxies in cold and self-interacting dark matter models*, *Mon. Not. Roy. Astron. Soc.* **507** (2021) 720–729, [2102.12480].

[30] Planck collaboration, N. Aghanim et al., *Planck 2018 results. VI. Cosmological parameters*, *Astron. Astrophys.* **641** (2020) A6, [1807.06209].

[31] O. Sameie, P. Creasey, H.-B. Yu, L. V. Sales, M. Vogelsberger and J. Zavala, *The impact of baryonic discs on the shapes and profiles of self-interacting dark matter haloes*, *Mon. Not. Roy. Astron. Soc.* **479** (2018) 359–367, [1801.09682].

[32] D. Yang and H.-B. Yu, *Self-interacting dark matter and small-scale gravitational lenses in galaxy clusters*, *Phys. Rev. D* **104** (2021) 103031, [2102.02375].

[33] L. Hernquist, *An Analytical Model for Spherical Galaxies and Bulges*, *Astrophys. J.* **356** (1990) 359.

[34] M. Saijo, T. W. Baumgarte, S. L. Shapiro and M. Shibata, *Collapse of a rotating supermassive star to a supermassive black hole: Post-Newtonian simulations*, *Astrophys. J.* **569** (2002) 349–361, [astro-ph/0202112].

[35] A. A. Dutton and A. V. Macciò, *Cold dark matter haloes in the Planck era: evolution of structural parameters for Einasto and NFW profiles*, *Mon. Not. Roy. Astron. Soc.* **441** (2014) 3359–3374, [1402.7073].

[36] D. Zhao, Y. Jing, H. Mo and G. Boerner, *Accurate universal models for the mass accretion histories and concentrations of dark matter halos*, *Astrophys. J.* **707** (2009) 354–369, [0811.0828].

[37] E. Banados et al., *An 800-million-solar-mass black hole in a significantly neutral Universe at redshift 7.5*, *Nature* **553** (2018) 473–476, [1712.01860].

[38] D. J. Mortlock et al., *A luminous quasar at a redshift of $z = 7.085$*, *Nature* **474** (2011) 616, [1106.6088].

[39] F. Wang, J. Yang, X. Fan, M. Yue, X.-B. Wu, J.-T. Schindler et al., *The discovery of a luminous broad absorption line quasar at a redshift of 7.02*, *Astrophys. J. Lett.* **869** (2018) L9, [1810.11925].

[40] X.-B. Wu, F. Wang, X. Fan, W. Yi, W. Zuo, F. Bian et al., *An ultraluminous quasar with a twelve-billion-solar-mass black hole at redshift 6.30*, *Nature* **518** (2015) 512–515, [1502.07418].

[41] J. Choquette, J. M. Cline and J. M. Cornell, *Early formation of supermassive black holes via dark matter self-interactions*, *JCAP* **1907** (2019) 036, [1812.05088].

[42] R. Huo, H.-B. Yu and Y.-M. Zhong, *The Structure of Dissipative Dark Matter Halos*, *JCAP* **2006** (2020) 051, [1912.06757].

[43] T. Ren, A. Kwa, M. Kaplinghat and H.-B. Yu, *Reconciling the Diversity and Uniformity of Galactic Rotation Curves with Self-Interacting Dark Matter*, *Phys. Rev. X* **9** (2019) 031020, [1808.05695].

[44] O. Sameie, H.-B. Yu, L. V. Sales, M. Vogelsberger and J. Zavala, *Self-Interacting Dark Matter Subhalos in the Milky Way's Tides*, *Phys. Rev. Lett.* **124** (2020) 141102, [1904.07872].

[45] D. Yang, H.-B. Yu and H. An, *Self-Interacting Dark Matter and the Origin of Ultradiffuse Galaxies NGC1052-DF2 and -DF4*, *Phys. Rev. Lett.* **125** (2020) 111105, [2002.02102].

[46] M. Kaplinghat, T. Ren and H.-B. Yu, *Dark Matter Cores and Cusps in Spiral Galaxies and their Explanations*, *JCAP* **06** (2020) 027, [1911.00544].

[47] W. H. Press and P. Schechter, *Formation of galaxies and clusters of galaxies by selfsimilar gravitational condensation*, *Astrophys. J.* **187** (1974) 425–438.

[48] H. Mo, F. van den Bosch and S. White, *Galaxy Formation and Evolution*. Galaxy Formation and Evolution. Cambridge University Press, 2010.

[49] G. Kulkarni, G. Worseck and J. F. Hennawi, *Evolution of the AGN UV luminosity function from redshift 7.5*, *Mon. Not. Roy. Astron. Soc.* **488** (2019) 1035–1065, [1807.09774].

[50] B. Trakhtenbrot, *What do observations tell us about the highest-redshift supermassive black holes?*, *IAU Symp.* **356** (2019) 261–275, [2002.00972].

[51] R. P. Kerr, *Gravitational field of a spinning mass as an example of algebraically special metrics*, *Phys. Rev. Lett.* **11** (1963) 237–238.

[52] S. Liao, J. Chen and M.-C. Chu, *A universal angular momentum profile for dark matter haloes*, *Astrophys. J.* **844** (2017) 86, [1612.00117].

[53] I. R. King, *The Structure of star clusters. III. Some simple dynamical models*, *Astron. J.* **71** (1966) 64.

[54] M. Merafina and R. Ruffini, *Systems of selfgravitating classical particles with a cutoff in their distribution function*, *Astron. Astrophys.* **221** (1989) 4–19.

[55] S. Chandrasekhar, *Dynamical Instability of Gaseous Masses Approaching the Schwarzschild Limit in General Relativity*, *Phys. Rev. Lett.* **12** (1964) 114–116.

[56] W.-X. Feng, H.-B. Yu and Y.-M. Zhong, *Dynamical instability of collapsed dark matter halos*, *JCAP* **05** (2022) 036, [2108.11967].

[57] S. Shapiro and S. Teukolsky, *Black holes, white dwarfs, and neutron stars: The physics of compact objects*. John Wiley and Sons, New York, 1983.

[58] Y. B. Zel'dovich and M. A. Podurets, *The Evolution of a System of Gravitationally Interacting Point Masses*, *Sov. Astron.* **9** (1966) 742.

[59] J. R. Ipser and K. S. Thorne, *Relativistic, spherically symmetric star clusters. i. stability theory for radial perturbations*, *Astrophys. J.* **154** (1968) 251.

[60] J. R. Ipser, *Relativistic, spherically symmetric star clusters. II. sufficient conditions for stability against radial perturbations*, *Astrophys. J.* **156** (1969) 509.

[61] J. R. Ipser, *Relativistic, spherically symmetric star clusters. III. stability of compact isotropic models*, *Astrophys. J.* **158** (1969) 17.

[62] S. L. Shapiro and S. A. Teukolsky, *Relativistic stellar dynamics on the computer. i - motivation and numerical method*, *Astrophys. J.* **298** (1985) 34.

[63] S. L. Shapiro and S. A. Teukolsky, *Relativistic stellar dynamics on the computer - part two - physical applications*, *Astrophys. J.* **298** (1985) 58.

[64] S. L. Shapiro and S. A. Teukolsky, *Relativistic stellar dynamics on the computer. IV - collapse of a star cluster to a black hole*, *Astrophys. J.* **307** (1986) 575.

[65] W.-X. Feng, H.-B. Yu and Y.-M. Zhong, *Seeding Supermassive Black Holes with Self-interacting Dark Matter: A Unified Scenario with Baryons*, *Astrophys. J. Lett.* **914** (2021) L26, [2010.15132].

[66] H. Xiao, X. Shen, P. F. Hopkins and K. M. Zurek, *SMBH seeds from dissipative dark matter*, *JCAP* **07** (2021) 039, [2103.13407].

[67] M. Vogelsberger, J. Zavala and A. Loeb, *Subhaloes in self-interacting galactic dark matter haloes*, *Mon. Not. Roy. Astron. Soc.* **423** (2012) 3740–3752, [1201.5892].

[68] A. Robertson, R. Massey and V. Eke, *Cosmic particle colliders: simulations of self-interacting dark matter with anisotropic scattering*, *Mon. Not. Roy. Astron. Soc.* **467** (2017) 4719–4730, [1612.03906].

[69] E. O. Nadler, A. Banerjee, S. Adhikari, Y.-Y. Mao and R. H. Wechsler, *Signatures of Velocity-Dependent Dark Matter Self-Interactions in Milky Way-mass Halos*, *Astrophys. J.* **896** (2020) 112, [2001.08754].

[70] R. C. Tolman, *Static solutions of Einstein's field equations for spheres of fluid*, *Phys. Rev.* **55** (1939) 364–373.

[71] J. R. Oppenheimer and G. M. Volkoff, *On massive neutron cores*, *Phys. Rev.* **55** (1939) 374–381.

[72] B. K. Harrison, K. S. Thorne, M. Wakano and J. A. Wheeler, *Gravitation Theory and Gravitational Collapse*. University of Chicago Press, 1965.

[73] Y. B. Zeldovich and I. D. Novikov, *Relativistic astrophysics. Vol.1: Stars and relativity*. University of Chicago Press, 1971.

[74] R. Sorkin, *A criterion for the onset of instability at a turning point*, *Astrophys. J.* **249** (1981) 254.

[75] R. W. Michie, *The dynamics of spherical stellar systems: III. the relative loss of stars WithDifferent mass*, *Mon. Not. Roy. Astron. Soc.* **126** (1963) 331–341.

[76] I. King, *The structure of star clusters. i. an empirical density law*, *Astron. J.* **67** (1962) 471.

[77] R. Ruffini and L. Stella, *On semi-degenerate equilibrium configurations of a collisionless self-gravitating Fermi gas*, *Astron. Astrophys.* **119** (1983) 35–41.

[78] M. Merafina and R. Ruffini, *The relativistic equilibrium configurations of systems of particles with a cutoff in their phase space distribution functions*, *Astron. Astrophys.* **227** (1990) 415–421.

[79] R. C. Tolman and P. Ehrenfest, *Temperature equilibrium in a static gravitational field*, *Phys. Rev.* **36** (1930) 1791–1798.

[80] O. Klein, *On the thermodynamical equilibrium of fluids in gravitational fields*, *Rev. Mod. Phys.* **21** (1949) 531–533.

[81] C. W. Misner, K. S. Thorne and J. A. Wheeler, *Gravitation*. W. H. Freeman, San Francisco, 1973.

[82] S. Weinberg, *Gravitation and Cosmology: Principles and Applications of the General Theory of Relativity*. John Wiley and Sons, New York, 1972.

[83] J. Katz, *On the number of unstable modes of an equilibrium*, *Mon. Not. Roy. Astron. Soc.* **183** (1978) 765–770.

[84] J. M. T. Thompson, *Stability predictions through a succession of folds*, *Philos. Trans. Royal Soc. A* **292** (1979) 1–23.

[85] J. L. Friedman, J. R. Ipser and R. D. Sorkin, *Turning-point method for axisymmetric stability of rotating relativistic stars*, *Astrophys. J.* **325** (1988) 722.

[86] K. Takami, L. Rezzolla and S. Yoshida, *A quasi-radial stability criterion for rotating relativistic stars*, *Mon. Not. Roy. Astron. Soc.* **416** (2011) L1–L5, [1105.3069].

[87] Z. Roupas, *Thermodynamical instabilities of perfect fluid spheres in General Relativity*, *Class. Quant. Grav.* **30** (2013) 115018, [1411.0325].

[88] Z. Roupas and P.-H. Chavanis, *Relativistic Gravitational Phase Transitions and Instabilities of the Fermi Gas*, *Class. Quant. Grav.* **36** (2019) 065001, [1809.07169].

[89] J. Butcher, *Numerical methods for ordinary differential equations in the 20th century*, *J. Comput. Appl. Math.* **125** (2000) 1–29.

[90] X. Shen, P. F. Hopkins, L. Necib, F. Jiang, M. Boylan-Kolchin and A. Wetzel, *Dissipative dark matter on FIRE – I. Structural and kinematic properties of dwarf galaxies*, *Mon. Not. Roy. Astron. Soc.* **506** (2021) 4421–4445, [2102.09580].

[91] A. H. G. Peter, M. Rocha, J. S. Bullock and M. Kaplinghat, *Cosmological Simulations with Self-Interacting Dark Matter II: Halo Shapes vs. Observations*, *Mon. Not. Roy. Astron. Soc.* **430** (2013) 105, [1208.3026].

[92] M. Shibata and S. L. Shapiro, *Collapse of a rotating supermassive star to a supermassive black hole: Fully relativistic simulations*, *Astrophys. J. Lett.* **572** (2002) L39–L44, [astro-ph/0205091].

[93] S. L. Shapiro and M. Shibata, *Collapse of a rotating supermassive star to a supermassive black hole: Analytic determination of the black hole mass and spin*, *Astrophys. J.* **577** (2002) 904–908, [astro-ph/0209251].

[94] S. L. Shapiro, *Collapse of uniformly rotating stars to black holes and the formation of disks*, *Astrophys. J.* **610** (2004) 913–919, [astro-ph/0404338].

[95] H. Nishikawa, K. K. Boddy and M. Kaplinghat, *Accelerated core collapse in tidally stripped self-interacting dark matter halos*, *Phys. Rev. D* **101** (2020) 063009, [1901.00499].

[96] M. Kaplinghat, M. Valli and H.-B. Yu, *Too Big To Fail in Light of Gaia*, *Mon. Not. Roy. Astron. Soc.* **490** (2019) 231–242, [1904.04939].

[97] F. Kahlhoefer, M. Kaplinghat, T. R. Slatyer and C.-L. Wu, *Diversity in density profiles of self-interacting dark matter satellite halos*, *JCAP* **12** (2019) 010, [1904.10539].

[98] C. A. Correa, *Constraining velocity-dependent self-interacting dark matter with the Milky Way's dwarf spheroidal galaxies*, *Mon. Not. Roy. Astron. Soc.* **503** (2021) 920–937, [2007.02958].

[99] H. C. Turner, M. R. Lovell, J. Zavala and M. Vogelsberger, *The onset of gravothermal core collapse in velocity-dependent self-interacting dark matter subhaloes*, *Mon. Not. Roy. Astron. Soc.* **505** (2021) 5327–5339, [2010.02924].

[100] S. Y. Kim and A. H. G. Peter, *The Milky Way satellite velocity function is a sharp probe of small-scale structure problems*, 2106.09050.

[101] O. Slone, F. Jiang, M. Lisanti and M. Kaplinghat, *Orbital evolution of satellite galaxies in self-interacting dark matter models*, *Phys. Rev. D* **107** (2023) 043014, [2108.03243].

[102] Z. C. Zeng, A. H. G. Peter, X. Du, A. Benson, S. Kim, F. Jiang et al., *Core-collapse, evaporation, and tidal effects: the life story of a self-interacting dark matter subhalo*, *Mon. Not. Roy. Astron. Soc.* **513** (2022) 4845–4868, [2110.00259].

[103] J. R. Oppenheimer and H. Snyder, *On Continued gravitational contraction*, *Phys. Rev.* **56** (1939) 455–459.

[104] R. Penrose, *Gravitational collapse and space-time singularities*, *Phys. Rev. Lett.* **14** (1965) 57–59.

[105] R. C. Myers and M. J. Perry, *Black Holes in Higher Dimensional Space-Times*, *Annals Phys.* **172** (1986) 304.

[106] R. Emparan and H. S. Reall, *Black Holes in Higher Dimensions*, *Living Rev. Rel.* **11** (2008) 6, [0801.3471].

[107] G. T. Horowitz, ed., *Black holes in higher dimensions*. Cambridge Univ. Pr., Cambridge, UK, 2012.

[108] F. Rahaman, A. Pradhan, N. Ahmed, S. Ray, B. Saha and M. Rahaman, *Fluid sphere: stability problem and dimensional constraint*, *Int. J. Mod. Phys. D* **24** (2015) 1550049, [1401.1402].

[109] C. G. Boehmer and T. Harko, *Dynamical instability of fluid spheres in the presence of a cosmological constant*, *Phys. Rev. D* **71** (2005) 084026, [gr-qc/0504075].

[110] G. H. Bordbar, S. H. Hendi and B. Eslam Panah, *Neutron stars in Einstein-Λ gravity: the cosmological constant effects*, *Eur. Phys. J. Plus* **131** (2016) 315, [1502.02929].

[111] C. Posada, J. Hladík and Z. Stuchlík, *Dynamical instability of polytropic spheres in spacetimes with a cosmological constant*, *Phys. Rev. D* **102** (2020) 024056, [2005.14072].

[112] M. Banados, C. Teitelboim and J. Zanelli, *The Black hole in three-dimensional space-time*, *Phys. Rev. Lett.* **69** (1992) 1849–1851, [hep-th/9204099].

[113] D. Ida, *No black hole theorem in three-dimensional gravity*, *Phys. Rev. Lett.* **85** (2000) 3758–3760, [gr-qc/0005129].

[114] S. Giddings, J. Abbott and K. Kuchar, *Einstein's theory in a three-dimensional space-time*, *Gen. Rel. Grav.* **16** (1984) 751–775.

[115] S. Deser, R. Jackiw and G. 't Hooft, *Three-Dimensional Einstein Gravity: Dynamics of Flat Space*, *Annals Phys.* **152** (1984) 220.

[116] S. Deser and R. Jackiw, *Three-Dimensional Cosmological Gravity: Dynamics of Constant Curvature*, *Annals Phys.* **153** (1984) 405–416.

[117] N. Cruz and J. Zanelli, *Stellar equilibrium in (2+1)-dimensions*, *Class. Quant. Grav.* **12** (1995) 975–982, [gr-qc/9411032].

[118] J. H. Jeans, *The Stability of a Spherical Nebula*, *Phil. Trans. A. Math. Phys. Eng. Sci.* **199** (1902) 1–53.

[119] W. B. Bonner, *Boyle's Law and gravitational instability*, *Mon. Not. Roy. Astron. Soc.* **116** (1956) 351.

[120] R. Ebert, *Über die Verdichtung von H I-Gebieten. Mit 5 Textabbildungen*, *Z. Astrophys.* **37** (1955) 217.

[121] P.-H. Chavanis, *Gravitational instability of finite isothermal spheres*, *Astron. Astrophys.* **381** (2002) 340, [astro-ph/0103159].

[122] I. Hachisu and D. Sugimoto, *Gravothermal catastrophe and negative specific heat of self-gravitating systems*, *Prog. Theor. Exp. Phys.* **60** (1978) 123–135.

[123] L. Spitzer, *Dynamical evolution of globular clusters*. Princeton University Press, Princeton N.J., 1987.

[124] C. Shang, G. Bryan and Z. Haiman, *Supermassive Black Hole Formation by Direct Collapse: Keeping Protogalactic Gas H_2–Free in Dark Matter Halos with Virial Temperatures T_vir >˜ 10^4 K*, *Mon. Not. Roy. Astron. Soc.* **402** (2010) 1249, [0906.4773].

[125] B. Agarwal, S. Khochfar, J. L. Johnson, E. Neistein, C. D. Vecchia and M. Livio, *Ubiquitous seeding of supermassive black holes by direct collapse*, *Mon. Not. Roy. Astron. Soc.* **425** (2012) 2854–2871.

[126] G. Dunn, J. Bellovary, K. Holley-Bockelmann, C. Christensen and T. Quinn, *Sowing black hole seeds: Direct collapse black hole formation with realistic lyman–werner radiation in cosmological simulations*, *Astrophys. J.* **861** (2018) 39.

[127] J. H. Wise, J. A. Regan, B. W. O'Shea, M. L. Norman, T. P. Downes and H. Xu, *Formation of massive black holes in rapidly growing pre-galactic gas clouds*, *Nature* **566** (2019) 85–88.

[128] S. L. Shapiro, *Star clusters, self-interacting dark matter halos, and black hole cusps: The fluid conduction model and its extension to general relativity*, *Phys. Rev. D* **98** (2018) 023021, [1809.02618].

[129] D. Markovic and S. Shapiro, *Gravitational collapse with a cosmological constant*, *Phys. Rev. D* **61** (2000) 084029, [gr-qc/9912066].

[130] R. Goswami and P. S. Joshi, *Spherical gravitational collapse in N-dimensions*, *Phys. Rev. D* **76** (2007) 084026, [gr-qc/0608136].

[131] C. W. Lai and M. W. Choptuik, *Final fate of subcritical evolutions of boson stars*, 0709.0324.

[132] S. C. Noble and M. W. Choptuik, *Driven neutron star collapse: Type I critical phenomena and the initial black hole mass distribution*, *Phys. Rev. D* **93** (2016) 024015, [1512.02999].

[133] R. F. Tooper, *Adiabatic fluid spheres in general relativity.*, *Astrophys. J.* **142** (1965) 1541.

[134] W.-X. Feng, *On the Dynamical Instability of Monatomic Fluid Spheres in (N + 1)-Dimensional Spacetime*, *Astronomy* **2** (2023) 22–46, [2111.05341].

[135] S. F. Ross and R. B. Mann, *Gravitationally collapsing dust in (2+1)-dimensions*, *Phys. Rev. D* **47** (1993) 3319–3322, [hep-th/9208036].

[136] R. K. Pathria, *The universe as a black hole*, *Nature* **240** (1972) 298–299.

[137] V. P. Frolov, M. A. Markov and V. F. Mukhanov, *Black Holes as Possible Sources of Closed and Semiclosed Worlds*, *Phys. Rev. D* **41** (1990) 383.

[138] V. P. Frolov, M. A. Markov and V. F. Mukhanov, *Through a black hole into a New Universe?*, *Phys. Lett. B* **216** (1989) 272–276.

[139] D. A. Easson and R. H. Brandenberger, *Universe generation from black hole interiors*, *JHEP* **06** (2001) 024, [hep-th/0103019].

[140] N. J. Popławski, *Cosmology with torsion: An alternative to cosmic inflation*, *Phys. Lett. B* **694** (2010) 181–185, [1007.0587].

[141] R. Brandenberger, L. Heisenberg and J. Robnik, *Non-singular black holes with a zero-shear S-brane*, *JHEP* **05** (2021) 090, [2103.02842].

[142] M. Tegmark, *On the dimensionality of space-time*, *Class. Quant. Grav.* **14** (1997) L69–L75, [gr-qc/9702052].

[143] J. Prat, C. Hogan, C. Chang and J. Frieman, *Vacuum energy density measured from cosmological data*, *JCAP* **06** (2022) 015, [2111.08151].

[144] R. Penrose, *Gravitational collapse: The role of general relativity*, *Riv. Nuovo Cim.* **1** (1969) 252–276.

[145] D. J. Mortlock, S. J. Warren, B. P. Venemans, M. Patel, P. C. Hewett, R. G. McMahon et al., *A luminous quasar at a redshift of z = 7.085*, *Nature* **474** (2011) 616–619, [1106.6088].

[146] F. Wang, J. Yang, X. Fan, J. F. Hennawi, A. J. Barth, E. Banados et al., *A luminous quasar at redshift 7.642*, *Astrophys. J. Lett.* (2021) L1, [2101.03179].

[147] R. L. Larson, S. L. Finkelstein, D. D. Kocevski, T. A. Hutchison, J. R. Trump, P. A. Haro et al., *A ceers discovery of an accreting supermassive black hole 570 myr after the big bang: Identifying a progenitor of massive z ¿ 6 quasars*, 2303.08918.

[148] T. E. Woods et al., *Titans of the Early Universe: The Prato Statement on the Origin of the First Supermassive Black Holes*, *Publ. Astron. Soc. Austral.* **36** (2019) e027, [1810.12310].

[149] L. Haemmerlé, L. Mayer, R. S. Klessen, T. Hosokawa, P. Madau and V. Bromm, *Formation of the first stars and black holes*, *Space Sci. Rev.* **216** (2020) 48, [2003.10533].

[150] M. Volonteri, M. Habouzit and M. Colpi, *The origins of massive black holes*, *Nature Rev. Phys.* **3** (2021) 732–743, [2110.10175].

[151] Y. B. Zel'dovich and I. D. Novikov, *The Hypothesis of Cores Retarded during Expansion and the Hot Cosmological Model*, *Soviet Astron. AJ (Engl. Transl.),* **10** (1967) 602.

[152] S. Hawking, *Gravitationally collapsed objects of very low mass*, *Mon. Not. Roy. Astron. Soc.* **152** (1971) 75.

[153] B. J. Carr and S. W. Hawking, *Black holes in the early Universe*, *Mon. Not. Roy. Astron. Soc.* **168** (1974) 399–415.

[154] B. Eggemeier, B. Schwabe, J. C. Niemeyer and R. Easther, *Gravitational collapse in the postinflationary Universe*, *Phys. Rev. D* **105** (2022) 023516, [2110.15109].

[155] L. E. Padilla, J. C. Hidalgo and K. A. Malik, *New mechanism for primordial black hole formation during reheating*, *Phys. Rev. D* **106** (2022) 023519, [2110.14584].

[156] M. J. Baker, M. Breitbach, J. Kopp and L. Mittnacht, *Primordial Black Holes from First-Order Cosmological Phase Transitions*, 2105.07481.

[157] K. Kawana and K.-P. Xie, *Primordial black holes from a cosmic phase transition: The collapse of Fermi-balls*, *Phys. Lett. B* **824** (2022) 136791, [2106.00111].

[158] J. Liu, L. Bian, R.-G. Cai, Z.-K. Guo and S.-J. Wang, *Primordial black hole production during first-order phase transitions*, *Phys. Rev. D* **105** (2022) L021303, [2106.05637].

[159] H. Davoudiasl, P. B. Denton and J. Gehrlein, *Supermassive Black Holes, Ultralight Dark Matter, and Gravitational Waves from a First Order Phase Transition*, *Phys. Rev. Lett.* **128** (2022) 081101, [2109.01678].

[160] T. H. Jung and T. Okui, *Primordial black holes from bubble collisions during a first-order phase transition*, 2110.04271.

[161] H.-J. Li, Y.-Q. Peng, W. Chao and Y.-F. Zhou, *Can supermassive black holes triggered by general QCD axion bubbles?*, 2304.00939.

[162] M. A. Latif, D. J. Whalen, S. Khochfar, N. P. Herrington and T. E. Woods, *Turbulent cold flows gave birth to the first quasars*, *Nature* **607** (2022) 48–51, [2207.05093].

[163] L. E. Padilla, T. Rindler-Daller, P. R. Shapiro, T. Matos and J. A. Vázquez, *Core-halo mass relation in scalar field dark matter models and its consequences for the formation of supermassive black holes*, *Phys. Rev. D* **103** (2021) 063012, [2010.12716].

[164] N. Fernandez, A. Ghalsasi, S. Profumo, N. Smyth and L. Santos-Olmsted, *Dark Black Holes in the Mass Gap*, 2208.08557.

[165] S. Chandrasekhar, *The Dynamical Instability of Gaseous Masses Approaching the Schwarzschild Limit in General Relativity*, *Astrophys. J.* **140** (1964) 417–433.

[166] W. A. Fowler, *Massive Stars, Relativistic Polytropes, and Gravitational Radiation*, *Rev. Mod. Phys.* **36** (1964) 545–555.

[167] J. M. Bardeen, *Stability and dynamics of spherically symmetric masses in general relativity*, Ph.D. thesis, California Institute of Technology, 1965. 10.7907/HQ2N-0J27.

[168] J. R. Ipser, *A binding-energy criterion for the dynamical stability of spherical stellar systems in general relativity*, *Astrophys. J.* **238** (1980) 1101.

[169] W.-X. Feng, *Gravothermal phase transition, black holes and space dimensionality*, *Phys. Rev. D* **106** (2022) L041501, [2207.14317].

[170] L. D. Landau, *On the theory of stars*, *Phys. Z. Sowjetunion* **1** (1932) 285.

[171] D. J. Kaup, *Klein-Gordon Geon*, *Phys. Rev.* **172** (1968) 1331–1342.

[172] R. Ruffini and S. Bonazzola, *Systems of selfgravitating particles in general relativity and the concept of an equation of state*, *Phys. Rev.* **187** (1969) 1767–1783.

[173] E. Takasugi and M. Yoshimura, *Gravitational Stability of Cold Bose Star*, *Z. Phys. C* **26** (1984) 241.

[174] M. Colpi, S. L. Shapiro and I. Wasserman, *Boson Stars: Gravitational Equilibria of Selfinteracting Scalar Fields*, *Phys. Rev. Lett.* **57** (1986) 2485–2488.

[175] M. Gleiser, *Stability of Boson Stars*, *Phys. Rev. D* **38** (1988) 2376.

[176] F. Dalfovo, S. Giorgini, L. P. Pitaevskii and S. Stringari, *Theory of Bose-Einstein condensation in trapped gases*, *Rev. Mod. Phys.* **71** (1999) 463–512, [cond-mat/9806038].

[177] J. Fan, *Ultralight Repulsive Dark Matter and BEC*, *Phys. Dark Univ.* **14** (2016) 84–94, [1603.06580].

[178] B. Li, T. Rindler-Daller and P. R. Shapiro, *Cosmological Constraints on Bose-Einstein-Condensed Scalar Field Dark Matter*, *Phys. Rev. D* **89** (2014) 083536, [1310.6061].

[179] B. Li, P. R. Shapiro and T. Rindler-Daller, *Bose-Einstein-condensed scalar field dark matter and the gravitational wave background from inflation: new cosmological constraints and its detectability by LIGO*, *Phys. Rev. D* **96** (2017) 063505, [1611.07961].

[180] S. T. H. Hartman, H. A. Winther and D. F. Mota, *Constraints on self-interacting Bose-Einstein condensate dark matter using large-scale observables*, *JCAP* **02** (2022) 005, [2108.07496].

[181] J. Chen, X. Du, E. W. Lentz, D. J. E. Marsh and J. C. Niemeyer, *New insights into the formation and growth of boson stars in dark matter halos*, *Phys. Rev. D* **104** (2021) 083022, [2011.01333].

[182] T. Dawoodbhoy, P. R. Shapiro and T. Rindler-Daller, *Core-envelope haloes in scalar field dark matter with repulsive self-interaction: fluid dynamics beyond the de Broglie wavelength*, *Mon. Not. Roy. Astron. Soc.* **506** (2021) 2418–2444, [2104.07043].

[183] P. R. Shapiro, T. Dawoodbhoy and T. Rindler-Daller, *Cosmological structure formation in scalar field dark matter with repulsive self-interaction: the incredible shrinking Jeans mass*, *Mon. Not. Roy. Astron. Soc.* **509** (2021) 145–173, [2106.13244].

[184] H. Foidl and T. Rindler-Daller, *Cosmological structure formation in complex scalar field dark matter versus real ultralight axions: A comparative study using class*, *Phys. Rev. D* **105** (2022) 123534, [2203.09396].

[185] H. Foidl, T. Rindler-Daller and W. W. Zeilinger, *Halo formation and evolution in scalar field dark matter and cold dark matter: New insights from the fluid approach*, *Phys. Rev. D* **108** (2023) 043012, [2305.12982].

[186] W.-X. Feng, H.-B. Yu and Y.-M. Zhong. In Preparation, 2023.

[187] M. Grether, M. de Llano and G. A. B. Jr, *Bose-Einstein Condensation in the Relativistic Ideal Bose Gas*, *Phys. Rev. Lett.* **99** (2007) 200406, [0706.2833].

[188] T. Kodama and M. Yamada, *Theory of superdense stars*, *Progress of Theoretical Physics* **47** (1972) 444–459.

[189] A. Suárez and P.-H. Chavanis, *Hydrodynamic representation of the Klein-Gordon-Einstein equations in the weak field limit: General formalism and perturbations analysis*, *Phys. Rev. D* **92** (2015) 023510, [1503.07437].

[190] W.-X. Feng, A. Parisi, C.-S. Chen and F.-L. Lin, *Self-interacting dark scalar spikes around black holes via relativistic Bondi accretion*, *JCAP* **08** (2022) 032, [2112.05160].

[191] P. J. E. Peebles, *Fluid dark matter*, *Astrophys. J. Lett.* **534** (2000) L127, [astro-ph/0002495].

[192] S. Savastano, L. Amendola, J. Rubio and C. Wetterich, *Primordial dark matter halos from fifth forces*, *Phys. Rev. D* **100** (2019) 083518, [1906.05300].

[193] G. Domènech and M. Sasaki, *Cosmology of strongly interacting fermions in the early universe*, *JCAP* **06** (2021) 030, [2104.05271].

[194] M. M. Flores and A. Kusenko, *Primordial Black Holes from Long-Range Scalar Forces and Scalar Radiative Cooling*, *Phys. Rev. Lett.* **126** (2021) 041101, [2008.12456].

[195] G. Domènech, D. Inman, A. Kusenko and M. Sasaki, *Halo Formation from Yukawa Forces in the Very Early Universe*, 2304.13053.

[196] D. E. Kaplan, M. A. Luty and K. M. Zurek, *Asymmetric Dark Matter*, *Phys. Rev. D* **79** (2009) 115016, [0901.4117].

[197] H. Iminniyaz, M. Drees and X. Chen, *Relic Abundance of Asymmetric Dark Matter*, *JCAP* **07** (2011) 003, [1104.5548].

[198] M. L. Graesser, I. M. Shoemaker and L. Vecchi, *Asymmetric WIMP dark matter*, *JHEP* **10** (2011) 110, [1103.2771].

[199] K. Petraki and R. R. Volkas, *Review of asymmetric dark matter*, *Int. J. Mod. Phys. A* **28** (2013) 1330028, [1305.4939].

[200] K. M. Zurek, *Asymmetric Dark Matter: Theories, Signatures, and Constraints*, *Phys. Rept.* **537** (2014) 91–121, [1308.0338].

[201] S.-Y. Ho, *An asymmetric SIMP dark matter model*, *JHEP* **10** (2022) 182, [2207.13373].

[202] S. Tremaine and J. E. Gunn, *Dynamical Role of Light Neutral Leptons in Cosmology*, *Phys. Rev. Lett.* **42** (1979) 407–410.

[203] A. Boyarsky, O. Ruchayskiy and D. Iakubovskyi, *A Lower bound on the mass of Dark Matter particles*, *JCAP* **03** (2009) 005, [0808.3902].

[204] H. Davoudiasl, P. B. Denton and D. A. McGady, *Ultralight fermionic dark matter*, *Phys. Rev. D* **103** (2021) 055014, [2008.06505].

[205] A. Loeb, *Effective Self-interaction of Dark Matter from Gravitational Scattering*, *Astrophys. J. Lett.* **929** (2022) L24, [2203.11962].

[206] L. Hui, J. P. Ostriker, S. Tremaine and E. Witten, *Ultralight scalars as cosmological dark matter*, *Phys. Rev. D* **95** (2017) 043541, [1610.08297].

[207] M. Randeria and E. Taylor, *BCS-BEC Crossover and the Unitary Fermi Gas*, *Ann. Rev. Condensed Matter Phys.* **5** (2014) 209–232, [1306.5785].

[208] R. Garani, M. H. G. Tytgat and J. Vandecasteele, *Condensed dark matter with a Yukawa interaction*, *Phys. Rev. D* **106** (2022) 116003, [2207.06928].

[209] B. Carr, F. Kuhnel and L. Visinelli, *Constraints on Stupendously Large Black Holes*, *Mon. Not. Roy. Astron. Soc.* **501** (2021) 2029–2043, [2008.08077].

[210] B. Carr and F. Kuhnel, *Primordial black holes as dark matter candidates*, *SciPost Phys. Lect. Notes* **48** (2022) 1, [2110.02821].

[211] G. Bertone, D. Hooper and J. Silk, *Particle dark matter: Evidence, candidates and constraints*, *Phys. Rept.* **405** (2005) 279–390, [hep-ph/0404175].

[212] N. Yoshida, V. Springel, S. D. M. White and G. Tormen, *Weakly self-interacting dark matter and the structure of dark halos*, *Astrophys. J. Lett.* **544** (2000) L87–L90, [astro-ph/0006134].

[213] J. Miralda-Escude, *A test of the collisional dark matter hypothesis from cluster lensing*, *Astrophys. J.* **564** (2002) 60, [astro-ph/0002050].

[214] S. W. Randall, M. Markevitch, D. Clowe, A. H. Gonzalez and M. Bradac, *Constraints on the Self-Interaction Cross-Section of Dark Matter from Numerical Simulations of the Merging Galaxy Cluster 1E 0657-56*, *Astrophys. J.* **679** (2008) 1173–1180, [0704.0261].

[215] J. Zavala, M. Vogelsberger and M. G. Walker, *Constraining Self-Interacting Dark Matter with the Milky Way's dwarf spheroidals*, *Mon. Not. Roy. Astron. Soc.* **431** (2013) L20–L24, [1211.6426].

[216] J. L. Feng, M. Kaplinghat and H.-B. Yu, *Halo Shape and Relic Density Exclusions of Sommerfeld-Enhanced Dark Matter Explanations of Cosmic Ray Excesses*, *Phys. Rev. Lett.* **104** (2010) 151301, [0911.0422].

[217] L. G. van den Aarssen, T. Bringmann and C. Pfrommer, *Is dark matter with long-range interactions a solution to all small-scale problems of \Lambda CDM cosmology?*, *Phys. Rev. Lett.* **109** (2012) 231301, [1205.5809].

[218] S. Tulin, H.-B. Yu and K. M. Zurek, *Resonant Dark Forces and Small Scale Structure*, *Phys. Rev. Lett.* **110** (2013) 111301, [1210.0900].

[219] S. Tulin, H.-B. Yu and K. M. Zurek, *Beyond Collisionless Dark Matter: Particle Physics Dynamics for Dark Matter Halo Structure*, *Phys. Rev. D* **87** (2013) 115007, [1302.3898].

[220] V. S. Berezinsky, A. V. Gurevich and K. P. Zybin, *Distribution of dark matter in the galaxy and the lower limits for the masses of supersymmetric particles*, *Phys. Lett. B* **294** (1992) 221–228.

[221] P. Gondolo and J. Silk, *Dark matter annihilation at the galactic center*, *Phys. Rev. Lett.* **83** (1999) 1719–1722, [astro-ph/9906391].

[222] M. Kaplinghat, L. Knox and M. S. Turner, *Annihilating the cold dark matter cusp crisis*, *Phys. Rev. Lett.* **85** (2000) 3335, [astro-ph/0005210].

[223] D. Merritt, M. Milosavljevic, L. Verde and R. Jimenez, *Dark matter spikes and annihilation radiation from the galactic center*, *Phys. Rev. Lett.* **88** (2002) 191301, [astro-ph/0201376].

[224] D. Merritt, *Evolution of the dark matter distribution at the galactic center*, *Phys. Rev. Lett.* **92** (2004) 201304, [astro-ph/0311594].

[225] O. Y. Gnedin and J. R. Primack, *Dark Matter Profile in the Galactic Center*, *Phys. Rev. Lett.* **93** (2004) 061302, [astro-ph/0308385].

[226] M. Gorchtein, S. Profumo and L. Ubaldi, *Probing Dark Matter with AGN Jets*, *Phys. Rev. D* **82** (2010) 083514, [1008.2230].

[227] T. Lacroix, C. Bœhm and J. Silk, *Ruling out thermal dark matter with a black hole induced spiky profile in the M87 galaxy*, *Phys. Rev. D* **92** (2015) 043510, [1505.00785].

[228] T. Lacroix, M. Karami, A. E. Broderick, J. Silk and C. Boehm, *Unique probe of dark matter in the core of M87 with the Event Horizon Telescope*, *Phys. Rev. D* **96** (2017) 063008, [1611.01961].

[229] S. L. Shapiro and J. Shelton, *Weak annihilation cusp inside the dark matter spike about a black hole*, *Phys. Rev. D* **93** (2016) 123510, [1606.01248].

[230] G. Alvarez and H.-B. Yu, *Density spikes near black holes in self-interacting dark matter halos and indirect detection constraints*, *Phys. Rev. D* **104** (2021) 043013, [2012.15050].

[231] P. J. E. Peebles, *Star Distribution Near a Collapsed Object*, *Astrophys. J.* **178** (1972) 371–376.

[232] J. N. Bahcall and R. A. Wolf, *Star distribution around a massive black hole in a globular cluster*, *Astrophys. J.* **209** (1976) 214–232.

[233] J. Frank and M. J. Rees, *Effects of massive central black holes on dense stellar systems*, *Mon. Not. Roy. Astron. Soc.* **176** (1976) 633.

[234] A. P. Lightman and S. L. Shapiro, *The distribution and consumption rate of stars around a massive, collapsed object*, *Astrophys. J.* **211** (1977) 244–262.

[235] S. L. Shapiro and A. B. Marchant, *Star clusters containing massive, central black holes: Monte Carlo simulations in two-dimensional phase space.*, *Astrophys. J.* **225** (1978) 603–624.

[236] A. B. Marchant and S. L. Shapiro, *Star clusters containing massive, central black holes. II. Self-consistent potentials.*, *Astrophys. J.* **234** (1979) 317–328.

[237] A. B. Marchant and S. L. Shapiro, *Star clusters containing massive, central black holes. III - Evolution calculations*, *Astrophys. J.* **239** (1980) 685–704.

[238] H. Cohn and R. M. Kulsrud, *The stellar distribution around a black hole: numerical integration of the Fokker-Planck equation.*, *Astrophys. J.* **226** (1978) 1087–1108.

[239] P. Amaro-Seoane, *Relativistic dynamics and extreme mass ratio inspirals*, *Living Rev. Rel.* **21** (2018) 4, [1205.5240].

[240] G. Bertone, A. R. Zentner and J. Silk, *A new signature of dark matter annihilations: gamma-rays from intermediate-mass black holes*, *Phys. Rev. D* **72** (2005) 103517, [astro-ph/0509565].

[241] G. Bertone, *Prospects for detecting dark matter with neutrino telescopes in intermediate mass black holes scenarios*, *Phys. Rev. D* **73** (2006) 103519, [astro-ph/0603148].

[242] B. J. Kavanagh, D. A. Nichols, G. Bertone and D. Gaggero, *Detecting dark matter around black holes with gravitational waves: Effects of dark-matter dynamics on the gravitational waveform*, *Phys. Rev. D* **102** (2020) 083006, [2002.12811].

[243] A. Coogan, G. Bertone, D. Gaggero, B. J. Kavanagh and D. A. Nichols, *Measuring the dark matter environments of black hole binaries with gravitational waves*, 2108.04154.

[244] J. R. Ipser and P. Sikivie, *Estimates of the Density of Dark Matter Near the Center of the Galaxy*, *Phys. Rev. D* **35** (1987) 3695.

[245] G. D. Quinlan, L. Hernquist and S. Sigurdsson, *Models of Galaxies with Central Black Holes: Adiabatic Growth in Spherical Galaxies*, *Astrophys. J.* **440** (1995) 554–564, [astro-ph/9407005].

[246] H. Bondi and F. Hoyle, *On the mechanism of accretion by stars*, *Mon. Not. Roy. Astron. Soc.* **104** (1944) 273.

[247] H. Bondi, *On spherically symmetrical accretion*, *Mon. Not. Roy. Astron. Soc.* **112** (1952) 195.

[248] J. McDonald, *Gauge singlet scalars as cold dark matter*, *Phys. Rev. D* **50** (1994) 3637–3649, [hep-ph/0702143].

[249] L. H. Ford, *Gravitational Particle Creation and Inflation*, *Phys. Rev. D* **35** (1987) 2955.

[250] P. J. E. Peebles and A. Vilenkin, *Noninteracting dark matter*, *Phys. Rev. D* **60** (1999) 103506, [astro-ph/9904396].

[251] J. Goodman, *Repulsive dark matter*, *New Astron.* **5** (2000) 103, [astro-ph/0003018].

[252] L. A. Boyle, R. R. Caldwell and M. Kamionkowski, *Spintessence! New models for dark matter and dark energy*, *Phys. Lett. B* **545** (2002) 17–22, [astro-ph/0105318].

[253] A. Arbey, J. Lesgourgues and P. Salati, *Cosmological constraints on quintessential halos*, *Phys. Rev. D* **65** (2002) 083514, [astro-ph/0112324].

[254] A. Riotto and I. Tkachev, *What if dark matter is bosonic and selfinteracting?*, *Phys. Lett. B* **484** (2000) 177–182, [astro-ph/0003388].

[255] A. Arbey, J. Lesgourgues and P. Salati, *Galactic halos of fluid dark matter*, *Phys. Rev. D* **68** (2003) 023511, [astro-ph/0301533].

[256] P.-H. Chavanis, *Jeans mass-radius relation of self-gravitating Bose-Einstein condensates and typical parameters of the dark matter particle*, *Phys. Rev. D* **103** (2021) 123551, [2011.01038].

[257] P. Jetzer, *Boson stars*, *Phys. Rept.* **220** (1992) 163–227.

[258] A. R. Liddle and M. S. Madsen, *The Structure and formation of boson stars*, *Int. J. Mod. Phys. D* **1** (1992) 101–144.

[259] S. L. Liebling and C. Palenzuela, *Dynamical Boson Stars*, *Living Rev. Rel.* **15** (2012) 6, [1202.5809].

[260] K. Zhang and F.-L. Lin, *Constraint on hybrid stars with gravitational wave events*, *Universe* **6** (2020) 231, [2011.05104].

[261] K. Zhang, G.-Z. Huang, J.-S. Tsao and F.-L. Lin, *GW170817 and GW190425 as hybrid stars of dark and nuclear matter*, *Eur. Phys. J. C* **82** (2022) 366, [2002.10961].

[262] C. Vásquez Flores, A. Parisi, C.-S. Chen and G. Lugones, *Fundamental oscillation modes of self-interacting bosonic dark stars*, *JCAP* **06** (2019) 051, [1901.07157].

[263] J. Silk and M. J. Rees, *Quasars and galaxy formation*, *Astron. Astrophys.* **331** (1998) L1–14, [astro-ph/9801013].

[264] J. P. Ostriker, *Collisional dark matter and the origin of massive black holes*, *Phys. Rev. Lett.* **84** (2000) 5258–5260, [astro-ph/9912548].

[265] A. King, *Black holes, galaxy formation, and the M_BH - sigma relation*, *Astrophys. J. Lett.* **596** (2003) L27–L30, [astro-ph/0308342].

[266] S. L. Shapiro and V. Paschalidis, *Self-interacting dark matter cusps around massive black holes*, *Phys. Rev. D* **89** (2014) 023506, [1402.0005].

[267] K. Park and M. Ricotti, *Accretion onto Intermediate Mass Black Holes Regulated by Radiative Feedback I. Parametric Study for Spherically Symmetric Accretion*, *Astrophys. J.* **739** (2011) 2, [1006.1302].

[268] K. Park and M. Ricotti, *Accretion onto Black Holes from Large Scales Regulated by Radiative Feedback. II. Growth Rate and Duty Cycle*, *Astrophys. J.* **747** (2012) 9, [1110.4634].

[269] C. B. Richards, T. W. Baumgarte and S. L. Shapiro, *Relativistic Bondi accretion for stiff equations of state*, *Mon. Not. Roy. Astron. Soc.* **502** (2021) 3003–3011, [2101.08797].

[270] C. B. Richards, T. W. Baumgarte and S. L. Shapiro, *Accretion onto a small black hole at the center of a neutron star*, *Phys. Rev. D* **103** (2021) 104009, [2102.09574].

[271] S. C. Schnauck, T. W. Baumgarte and S. L. Shapiro, *Accretion onto black holes inside neutron stars with piecewise-polytropic equations of state: Analytic and numerical treatments*, *Phys. Rev. D* **104** (2021) 123021, [2110.08285].

[272] T. W. Baumgarte and S. L. Shapiro, *Neutron Stars Harboring a Primordial Black Hole: Maximum Survival Time*, *Phys. Rev. D* **103** (2021) L081303, [2101.12220].

[273] J. Eby, C. Kouvaris, N. G. Nielsen and L. C. R. Wijewardhana, *Boson Stars from Self-Interacting Dark Matter*, *JHEP* **02** (2016) 028, [1511.04474].

[274] H. J. Zahid, J. Sohn and M. J. Geller, *Stellar velocity dispersion: Linking quiescent galaxies to their dark matter halos*, *Astrophys. J.* **859** (may, 2018) 96.

[275] D. Batcheldor, A. Marconi, D. Merritt and D. J. Axon, *How Special are Brightest Cluster Galaxies? The Impact of Near-Infrared Luminosities on Scaling Relations for BCGs*, *Astrophys. J. Lett.* **663** (2007) L85, [astro-ph/0610264].

[276] G. G. Raffelt, *Astrophysical axion bounds*, *Lect. Notes Phys.* **741** (2008) 51–71, [hep-ph/0611350].

[277] V. B. . Klaer and G. D. Moore, *The dark-matter axion mass*, *JCAP* **11** (2017) 049, [1708.07521].

[278] S. L. Shapiro and A. P. Lightman, *The distribution of stars around a massive black hole*, *Nature* **262** (1976) 743–745.

[279] M. Cirelli, M. Kadastik, M. Raidal and A. Strumia, *Model-independent implications of the e+-, anti-proton cosmic ray spectra on properties of Dark Matter*, *Nucl. Phys. B* **813** (2009) 1–21, [0809.2409].

[280] N. Arkani-Hamed, D. P. Finkbeiner, T. R. Slatyer and N. Weiner, *A Theory of Dark Matter*, *Phys. Rev. D* **79** (2009) 015014, [0810.0713].

[281] S. Bird, I. Cholis, J. B. Muñoz, Y. Ali-Haïmoud, M. Kamionkowski, E. D. Kovetz et al., *Did LIGO detect dark matter?*, *Phys. Rev. Lett.* **116** (2016) 201301, [1603.00464].

[282] M. Raidal, V. Vaskonen and H. Veermäe, *Gravitational Waves from Primordial Black Hole Mergers*, *JCAP* **09** (2017) 037, [1707.01480].

[283] H. Nishikawa, E. D. Kovetz, M. Kamionkowski and J. Silk, *Primordial-black-hole mergers in dark-matter spikes*, *Phys. Rev. D* **99** (2019) 043533, [1708.08449].

[284] J. R. Gair, L. Barack, T. Creighton, C. Cutler, S. L. Larson, E. S. Phinney et al., *Event rate estimates for LISA extreme mass ratio capture sources*, *Class. Quant. Grav.* **21** (2004) S1595–S1606, [gr-qc/0405137].

[285] M. Bonetti and A. Sesana, *Gravitational wave background from extreme mass ratio inspirals*, *Phys. Rev. D* **102** (2020) 103023, [2007.14403].

[286] G.-L. Li, Y. Tang and Y.-L. Wu, *Probing Dark Matter Spikes via Gravitational Waves of Extreme Mass Ratio Inspirals*, *Sci. China Phys. Mech. Astron.* **65** (2022) 100412, [2112.14041].

[287] M. Turner, *Gravitational radiation from point-masses in unbound orbits - newtonian results*, *Astrophys. J.* **216** (sep, 1977) 610.

[288] G. D. Quinlan and S. L. Shapiro, *Dynamical evolution of dense clusters of compact stars*, *Astrophys. J.* **343** (1989) 725.

[289] H. Mouri and Y. Taniguchi, *Runaway merging of black holes: analytical constraint on the timescale*, *Astrophys. J. Lett.* **566** (2002) L17–L20, [astro-ph/0201102].

[290] L. Spitzer, *Physics of Fully Ionized Gases*. Interscience Publishers, New York, 1956.

[291] J. Binney and S. Tremaine, *Galactic dynamics*. Princeton University Press, 1987.

[292] S. Babak, J. Gair, A. Sesana, E. Barausse, C. F. Sopuerta, C. P. L. Berry et al., *Science with the space-based interferometer LISA. V: Extreme mass-ratio inspirals*, *Phys. Rev. D* **95** (2017) 103012, [1703.09722].

[293] L. Sadeghian, F. Ferrer and C. M. Will, *Dark matter distributions around massive black holes: A general relativistic analysis*, *Phys. Rev. D* **88** (2013) 063522, [1305.2619].

[294] F. Ferrer, A. M. da Rosa and C. M. Will, *Dark matter spikes in the vicinity of Kerr black holes*, *Phys. Rev. D* **96** (2017) 083014, [1707.06302].

[295] L. Ferrarese and D. Merritt, *A Fundamental relation between supermassive black holes and their host galaxies*, *Astrophys. J. Lett.* **539** (2000) L9, [astro-ph/0006053].

[296] K. Gebhardt et al., *A Relationship between nuclear black hole mass and galaxy velocity dispersion*, *Astrophys. J. Lett.* **539** (2000) L13, [astro-ph/0006289].

[297] K. Gultekin, D. O. Richstone, K. Gebhardt, T. R. Lauer, S. Tremaine, M. C. Aller et al., *The m-sigma and m-l relations in galactic bulges and determinations of their intrinsic scatter*, *Astrophys.J.* **698** (2009) 198–221, [0903.4897].

[298] J. Kormendy and L. C. Ho, *Coevolution (Or Not) of Supermassive Black Holes and Host Galaxies*, *Ann. Rev. Astron. Astrophys.* **51** (2013) 511–653, [1304.7762].

[299] F. Prada, A. A. Klypin, A. J. Cuesta, J. E. Betancort-Rijo and J. Primack, *Halo concentrations in the standard lcdm cosmology*, *Mon. Not. Roy. Astron. Soc.* **423** (2011) 3018–3030, [1104.5130].

[300] A. D. Ludlow, J. F. Navarro, R. E. Angulo, M. Boylan-Kolchin, V. Springel, C. Frenk et al., *The mass–concentration–redshift relation of cold dark matter haloes*, *Mon. Not. Roy. Astron. Soc.* **441** (2014) 378–388, [1312.0945].

[301] C. A. Correa, J. S. B. Wyithe, J. Schaye and A. R. Duffy, *The accretion history of dark matter haloes – III. A physical model for the concentration–mass relation*, *Mon. Not. Roy. Astron. Soc.* **452** (2015) 1217–1232, [1502.00391].

[302] N. Loudas, V. Pavlidou, C. Casadio and K. Tassis, *Discriminating power of milli-lensing observations for dark matter models*, *Astron. Astrophys.* **668** (2022) A166, [2209.13393].

[303] F. Shankar, P. Salucci, G. L. Granato, G. De Zotti and L. Danese, *Super-massive black hole demography: The Match between the local and accreted mass functions*, *Mon. Not. Roy. Astron. Soc.* **354** (2004) 1020–1030, [astro-ph/0405585].

[304] M. Vika, S. P. Driver, A. W. Graham and J. Liske, *The millennium galaxy catalogue: The m_{bh}–$l_{spheroid}$ derived supermassive black hole mass function*, *Mon. Not. Roy. Astron. Soc.* **400** (2009) 1451–1460, [0908.2102].

[305] B. C. Barish, S. Bird and Y. Cui, *Impact of a midband gravitational wave experiment on detectability of cosmological stochastic gravitational wave backgrounds*, *Phys. Rev. D* **103** (2021) 123541, [2012.07874].

[306] G. Guennebaud, B. Jacob et al., "Eigen v3." http://eigen.tuxfamily.org, 2010.

[307] G. Alberti, *Statistical Mechanics of Self-Gravitating Systems in General Relativity JURY*, Ph.D. thesis, Physique Statistique des Systèmes Complexes (LPT), France, 2017.

Appendix A

The Gas Density Profile

To model the gas distribution of protogalaxies, we adopt simulation results in [25] (simulation B). Their simulated gas and dark matter distributions are fitted with a single power law of $\rho_b \sim r^{-2.4}$ and the NFW profile, respectively. We find the following ansatz works well for the gas.

$$\rho_b(r) = \rho_{b,s} \left(\frac{r}{r_s} \right)^{-2.4}, \tag{A.1}$$

where $\rho_{b,s}$ is the scale density of the gas and r_s is the scale radius of the simulated halo. The corresponding mass profile is

$$M_b(r) = 1.67 \times \frac{\rho_{b,s}}{\rho_s} (4\pi \rho_s r_s^3) \left(\frac{r}{r_s} \right)^{0.6} \tag{A.2}$$

We use simulation data shown in Fig. 4 (right, panel b) in [25] to fix the model parameters, $r_s = 73\,\mathrm{pc}$, $\rho_s = 2.6\,\mathrm{M}_\odot/\mathrm{pc}^3$, and $\rho_{b,s} = 0.19\,\mathrm{M}_\odot/\mathrm{pc}^3$; see Fig. A.1 for comparison. Since $1.67 \times \rho_{b,s}/\rho_s \approx 0.1$, we take $M_b(r) = 0.1 M_0 (r/r_s)^{0.6}$ for the static baryon distribution in

our semi-analytical simulations, shown as the dash-dotted line in the left panel of Fig. B.1. Note that the results from [25] have high enough resolutions for setting initial conditions in our simulations, where we trace the collapse process with the conducting fluid model.

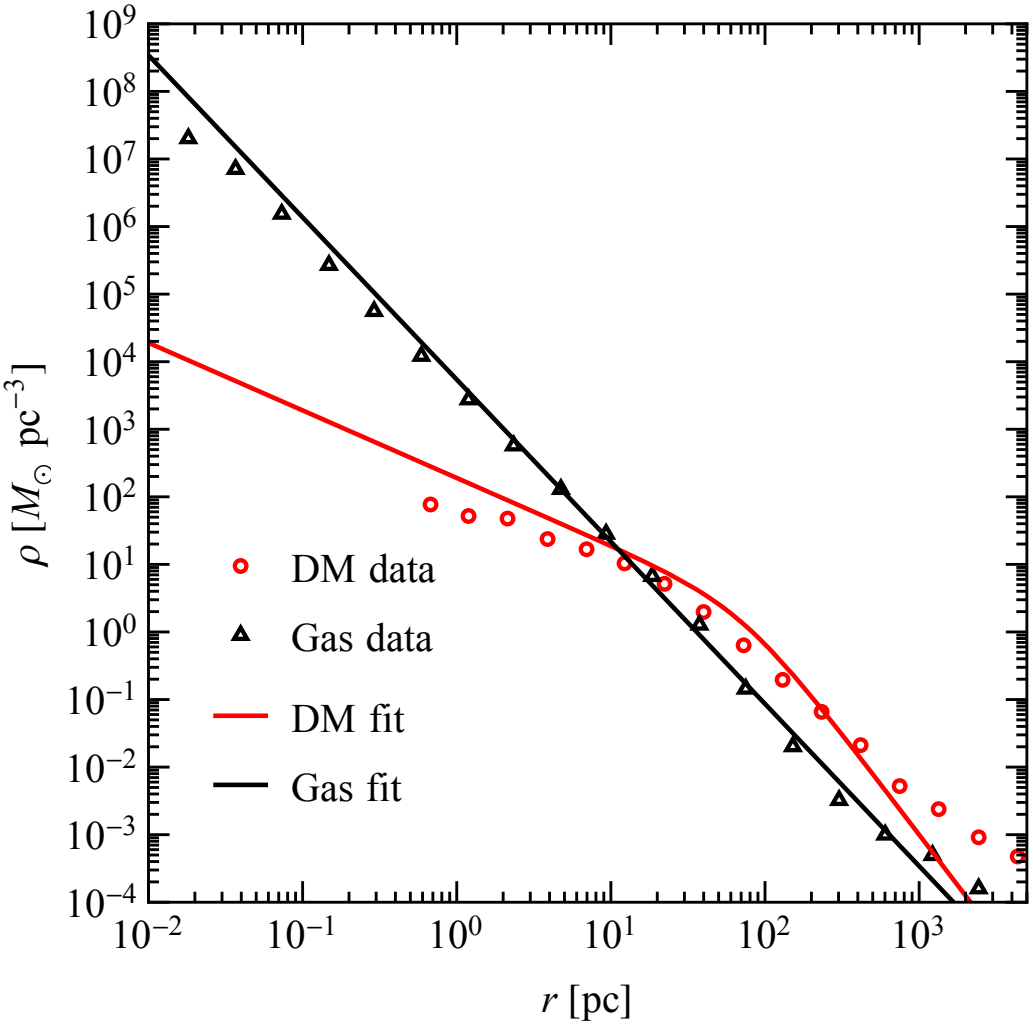

Figure A.1: Dark matter (red) and gas (black) density profiles after fitting to the simulated ones.

Appendix B

Numerical Procedure of Gravothermal Evolution

The procedure of our semi-analytical simulations is largely based on the treatment given in [22, 23]. We first translate a relevant physical quantity x to a dimensionless one $\hat{x}$ as $\hat{x} = x/x_0$, where x_0 is its corresponding fiducial value built from the halo parameters ρ_s and r_s, as shown in Table B.1.

$M_0 = 4\pi\rho_s r_s^3$	$(\sigma/m)_0 = (r_s\rho_s)^{-1}$
$\nu_0 = (4\pi G\rho_s)^{1/2} r_s$	$L_0 = (4\pi)^{5/2} G^{3/2} \rho_s^{5/2} r_s^5$
$t_0 = (4\pi G\rho_s)^{-1/2}$	

Table B.1: Fiducial quantities used in our numerical simulations.

The self-gravitating halo is segmented to $N = 182$ evenly log-spaced concentric shells in radius $\{\hat{r}_1, \hat{r}_2, \cdots, \hat{r}_N\}$ with $\hat{r}_1 = 10^{-4}$ and $\hat{r}_N = 100$. The halo is assumed to be in a quasi-hydrostatic equilibrium and each shell is assumed to be in its local thermal

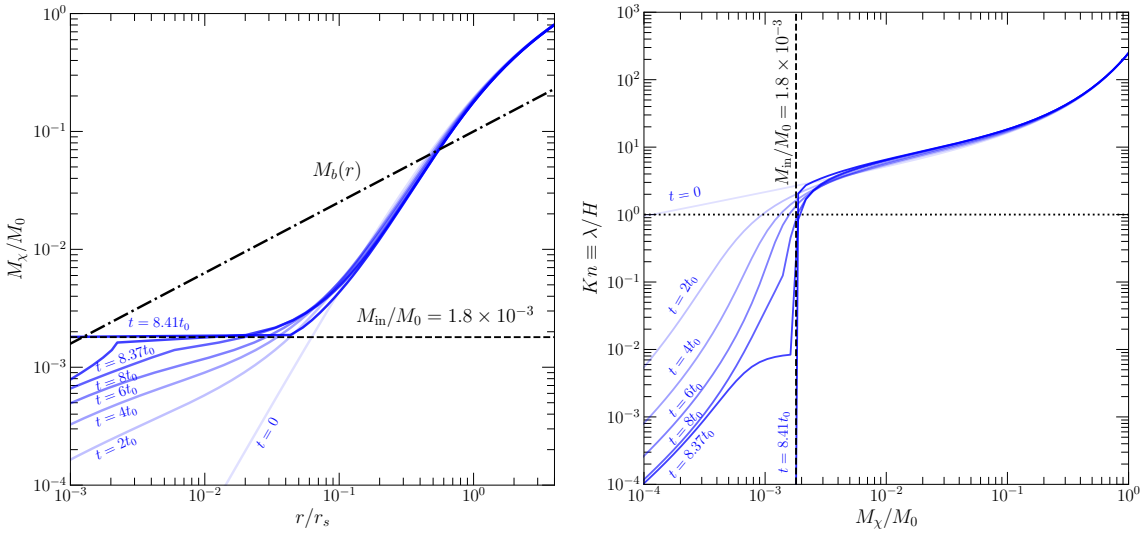

Figure B.1: Left: Evolution of dark matter mass profiles (solid) with $(\sigma/m)r_s\rho_s = 0.2$, together with the fixed baryon mass profile (dash-dotted). Each dark matter profile is labeled with its corresponding evolution time. The dashed line indicates the mass of the central halo with $Kn < 1$. Right: Corresponding Kn value vs. enclosed mass. The dotted horizontal line indicates $Kn = 1$, the boundary between short- and long-mean-free-path regimes, where $Kn < 1$ and > 1, respectively.

equilibrium. The values of extensive quantities ($\hat{M}_i$, $\hat{L}_i$) and intensive quantities ($\hat{\rho}_i$, $\hat{\nu}_i$) are taken as the value at $\hat{r}_i$ and the average between values at $\hat{r}_i$ and $\hat{r}_{i-1}$, respectively. We fix the baryon mass profile $\hat{M}_{b,i}$ as

$$\hat{M}_{b,i} = \hat{M}_b(\hat{r}_i) = 0.1 \times \hat{r}_i^{0.6}. \tag{B.1}$$

Consequently, we only use *one* set of Lagrangian zone radius for the halo through the simulations and dynamically update the enclosed baryon mass according to Eq. (B.1). The workflow is as follows:

1. Compute the initial 1D velocity dispersion profile $\hat{\nu}_{\chi,i}$ based on the input $\hat{r}_i$, $\hat{\rho}_{\chi,i}$, and

$\hat{\rho}_{b,i}$ under the hydrostatic equilibrium condition,

$$\frac{\partial(\hat{\rho}_\chi \hat{\nu}_\chi^2)}{\partial \hat{r}} = -\frac{(\hat{M}_\chi + \hat{M}_b)\hat{\rho}_\chi}{\hat{r}^2}. \tag{B.2}$$

2. Compute the luminosity profile $\hat{L}_{\chi,i}$ based on $\hat{r}_i$, $\hat{\rho}_{\chi,i}$, $\hat{\nu}_{\chi,i}$ and $\hat{\sigma}$ according to Eq. (2) of the main text.

3. Allow a small passage of time $\Delta\hat{t}$ and compute the specific energy change $\Delta\hat{u}_{\chi,i}$, $\hat{u}_{\chi,i} \equiv 3\hat{\nu}_{\chi,i}^2/2$, due to heat conduction,

$$\frac{\Delta\hat{u}_{\chi,i}}{\Delta\hat{t}} = -\left(\frac{\partial \hat{L}_\chi}{\partial \hat{M}_\chi}\right)_i, \tag{B.3}$$

where the dark matter density is fixed. We then update $\hat{u}_{\chi,i}$ with $\hat{u}_{\chi,i} + \Delta\hat{u}_{\chi,i}$. The time step $\Delta\hat{t}$ is sufficiently small, i.e., $|\Delta\hat{u}_{\chi,i}/\hat{u}_{\chi,i}| < 10^{-4}$. such that the linear approximations used in step 4 below are valid.

4. Upon updating $\hat{u}_{\chi,i}$, the i-th dark matter halo shell is no longer virialized. To return to hydrostatic equilibrium, we perturb $\hat{r}_i$, $\hat{\rho}_{\chi,i}$, and $\hat{\nu}_{\chi,i}$, while keeping the mass $\hat{M}_{\chi,i}$ and specific entropy $\hat{s}_{\chi,i} = \ln\left(\hat{\nu}_{\chi,i}^3/\hat{\rho}_{\chi,i}\right)$ of the shell fixed. We treat mass conservation, specific entropy conservation, kinetic energy conservation, and hydrostatic equilibrium relations, shown in the main text, at the linear order and solve them for all shells simultaneously. For the hydrostatic equilibrium relation, we take the sum of $\hat{M}_{\chi,i}$ and $\hat{M}_{b,i} = \hat{M}_b(\hat{r}_i)$ to compute the gravitational potential. For numerical accuracy, we iteratively perform the perturbation 10 times until hydrostatic equilibrium is established everywhere.

5. Re-establishing hydrostatic equilibrium gives new values for $\hat{r}_i$, $\hat{\rho}_{\chi,i}$, and $\hat{\nu}_{\chi,i}$. We return to step 1 and update the luminosity $\hat{L}_i$.

6. Track the Knudsen number $Kn \equiv \lambda/H$ for the innermost shell. The evolution is terminated when Kn drops below 10^{-4}.

The above procedure is coded in `C++` with the `eigen 3.2` library for linear algebra [306].

In Fig. B.1, we show evolution of dark matter mass profile (left panel) and the corresponding Kn value vs. enclosed mass (right panel). These results are complementary to those presented in Fig. 1 of the main text.

Appendix C

Angular Momentum Dissipation

Dark matter self-interactions provide an important avenue to transport angular momentum. To estimate this effect, we keep track of the collapsing central halo with a mass of $M_{\rm in}$, in a Lagrangian zone manner, i.e., the number of particles in each shell is conserved. In SIDM, the mass distribution of the central halo is spherically symmetric [14, 91]. We further assume it is a rigid body through the evolution, and its angular momentum is given by

$$J_{\chi,\rm in} = \frac{2}{5} M_{\rm in} r_{\rm in}^2 \omega \simeq \text{const.}, \tag{C.1}$$

where ω is the rotational frequency of the inner region, $r_{\rm in}$ is its boundary that changes with time. This leads to

$$\frac{d}{dt}\left(r_{\rm in}\omega\right) = \frac{d}{dt}\left(\frac{5J_{\chi,\rm in}}{2M_{\rm in}r_{\rm in}}\right) \simeq -\frac{5J_{\chi,\rm in}}{2M_{\rm in}r_{\rm in}^2}\left(\frac{dr_{\rm in}}{dt}\right). \tag{C.2}$$

The bulk velocity is $v_\phi = r_{\rm in}\omega \sin\theta$ along ϕ-direction of the rotational axis. θ is the polar angle. The bulk velocity increases (decreases) $dv_\phi/dt > 0$ (< 0) as the boundary of the inner region shrinks (expands) $dr_{\rm in}/dt < 0$ (> 0). An increasing in v_ϕ will drag the ambient regions just outside the boundary and exert a shear pressure on the boundary bulk surface,

$$\frac{1}{A_{\rm in}}\frac{d}{dt}\left(N_{r_{\rm in}} m v_\phi\right)_\pm = \mp \eta_{r_{\rm in}} \frac{dv_\phi}{dr_{\rm in}} \tag{C.3}$$

where m is the dark matter particle mass, $A_{\rm in} = 4\pi r_{\rm in}^2$ is the surface area of the inner region, $\eta_{r_{\rm in}} \equiv \eta(r_{\rm in})$ is the viscosity of the SIDM fluid, and $N_{r_{\rm in}}$ is number of particles, on the bulk surface. The subscript $+/-$ indicates if the quantity increases/decreases. Given the Lagrangian zone setup, $N_{r_{\rm in}}$ is a constant through the evolution, and from Eq. (C.3) we can show

$$\left(\frac{dr_{\rm in}}{dt}\right)_\mp = \mp \frac{4\pi r_{\rm in}^2 \eta_{r_{\rm in}}}{N_{r_{\rm in}} m} \tag{C.4}$$

The bulk momentum can be transported out through the shear pressure due to viscosity. Combining Eq. (C.2) and Eq. (C.4), we obtain the rate of momentum transport to the surroundings

$$\frac{d}{dt}\left(r_{\rm in}\omega\right)_\pm = \pm \frac{10\pi \eta_{r_{\rm in}} J_{\chi,{\rm in}}}{M_{\rm in} N_{r_{\rm in}} m}.$$

As the total angular momentum is conserved, the *loss* of the angular momentum of the inner region (shrinking case) is given by

$$\begin{aligned}\frac{dJ_{\chi,\mathrm{in}}}{dt} &\simeq -N_{r_{\mathrm{in}}} m \int \frac{d\Omega}{4\pi}[r_{\mathrm{in}}\sin\theta \times \frac{d}{dt}\left(r_{\mathrm{in}}\omega\sin\theta\right)] \\ &= -\int \frac{\sin^3\theta d\theta d\phi}{4\pi} r_{\mathrm{in}} \frac{d}{dt}\left(N_{r_{\mathrm{in}}} m r_{\mathrm{in}}\omega\right)_+ \\ &= -\frac{20\pi}{3}\frac{J_{\chi,\mathrm{in}}}{M_{\mathrm{in}}}\eta_{r_{\mathrm{in}}} r_{\mathrm{in}}. \end{aligned} \tag{C.5}$$

We have

$$J_{\chi,\mathrm{in}}(t; M_{\mathrm{in}}) = J^i_{\chi,\mathrm{in}} \exp\left(-\frac{20\pi}{3}\int_{t_i}^{t} \frac{\eta_{r_{\mathrm{in}}} r_{\mathrm{in}}(t')}{M_{\mathrm{in}}} dt'\right), \tag{C.6}$$

where $J^i_{\chi,\mathrm{in}}$ is the initial angular momentum of the inner region. As for conductivity [19], the viscosity for both long-mean-free-path and short-mean-free-path regimes can be combined into a single expression,

$$\begin{aligned}\eta &= \frac{1}{3} m n \bar{v} \left(\frac{1}{\lambda} + \frac{\nu t_r}{H^2}\right)^{-1} \\ &= \frac{1}{3}\alpha(\sigma/m)\bar{v}\left[\alpha(\sigma/m)^2 + \frac{4\pi G}{\rho\nu^2}\right]^{-1}, \end{aligned} \tag{C.7}$$

where we have used the gravitational scale height $H = \sqrt{\nu^2/4\pi G\rho}$, the mean free path $\lambda = 1/n\sigma$ and the relaxation time $t_r = 1/(\alpha n \nu \sigma)$ with number density n, cross section σ, and $\alpha = (16/\pi)^{1/2} \approx 2.26$ for hard spheres.

We evaluate η at the boundary r_{in} and take $\bar{v} \simeq \sqrt{3}\nu$, and obtain

$$J_{\chi,\mathrm{in}} = J^i_{\chi,\mathrm{in}} \exp\left[-\frac{20}{\sqrt{27\pi}}\int_{t_{\mathrm{init}}}^{t} \frac{\rho_{r_{\mathrm{in}}}(t')(\sigma/m)\nu_{r_{\mathrm{in}}}(t')^3 r_{\mathrm{in}}(t')}{G M_{\mathrm{in}}} dt'\right] \tag{C.8}$$

in the long-mean-free-path limit, and

$$J_{\chi,\mathrm{in}} = J^{i}_{\chi,\mathrm{in}} \exp\left[-\frac{20\pi}{3\sqrt{3}} \int_{t_{\mathrm{init}}}^{t} \frac{\nu_{r_{\mathrm{in}}}(t') r_{\mathrm{in}}(t')}{M_{\mathrm{in}}(\sigma/m)} dt'\right] \tag{C.9}$$

in the short-mean-free-path limit, where we have used the density $\rho_{r_{\mathrm{in}}} \equiv \rho(r_{\mathrm{in}}) = mn(r_{\mathrm{in}})$ and $\nu_{r_{\mathrm{in}}} \equiv \nu(r_{\mathrm{in}})$ the 1D velocity dispersion at the boundary. In our scenario, the characteristic timescale to dissipate the angular momentum is $0.2t_0$, during which the central halo is largely in the long-mean-free-path regime, see the right panel of Fig. B.1.

Appendix D

The Sample of High-z SMBHs

Label	Name	$M_{\rm BH}$ [$10^9 {\rm M}_\odot$]	z	$f_{\rm Edd}$	Ref.
1	J1205−0000	$2.2^{+0.2}_{-0.6}$	$6.699^{+0.007}_{-0.001}$	$0.16^{+0.04}_{-0.02}$	[9]
2	J1243+0100	$0.33^{+0.2}_{-0.2}$	$7.07^{+0.01}_{-0.01}$	$0.34^{+0.02}_{-0.02}$	[10]
3	J2239+0207	$1.1^{+0.3}_{-0.2}$	$6.245^{+0.008}_{-0.007}$	$0.17^{+0.04}_{-0.05}$	[9]
4	J2216−0016	$0.7^{+0.14}_{-0.23}$	$6.109^{+0.007}_{-0.008}$	$0.15^{+0.05}_{-0.03}$	[9]
5	J1208−0200	$0.71^{+0.24}_{-0.52}$	$6.144^{+0.008}_{-0.010}$	$0.24^{+0.18}_{-0.08}$	[9]
6	J1007+2115	$1.5^{+0.2}_{-0.2}$	$7.5149^{+0.0004}_{-0.0004}$	$1.06^{+0.2}_{-0.2}$	[5]
7	J1342+0928	$0.78^{+0.33}_{-0.19}$	$7.5413^{+0.0007}_{-0.0007}$	$1.5^{+0.5}_{-0.4}$	[37]
8	J1120+0641	$2.0^{+1.5}_{-0.7}$	$7.085^{+0.003}_{-0.003}$	$1.2^{+0.6}_{-0.5}$	[38]
9	J0038−1527	$1.33^{+0.25}_{-0.25}$	$7.021^{+0.005}_{-0.005}$	$1.25^{+0.19}_{-0.19}$	[39]
10	J0100+2802	$12.4^{+1.9}_{-1.9}$	$6.30^{+0.01}_{-0.01}$	$0.99^{+0.22}_{-0.22}$	[40]

Table D.1: The sample of high-z SMBHs shown in Fig. 2.2 of the main text.

In Table D.1, we list high-z SMBHs shown in Fig. 2.2 of the main text, in the order of their labeling number in the figure. The Eddington ratio is calculated as $f_{\rm Edd} = L_{\rm bol}/L_{\rm Edd}$, where $L_{\rm bol}$ is the observed bolometric luminosity and $L_{\rm Edd} = 1.3 \times 10^{38} (M_{\rm BH}/{\rm M}_\odot)$ erg/s is the Eddington luminosity.

Appendix E

The Adiabatic Index

We consider a perfect fluid with energy density $\rho(r)c^2$ and pressure $p(r)$ in a Schwarzschild metric [55]

$$ds^2 = -e^{2\Phi(r)}c^2\mathrm{d}t^2 + e^{2\Lambda(r)}dr^2 + r^2(\mathrm{d}\theta^2 + \sin^2\theta\ \mathrm{d}\phi^2),$$

where $e^{2\Phi} = \exp\left[2\int_r^\infty (dp/dr')/(p+\rho c^2)\mathrm{d}r'\right]$ and $e^{2\Lambda} = [1 - 2GM(r)/rc^2]^{-1}$. The critical adiabatic index is

$$\begin{aligned}\gamma_{\mathrm{cr}} \equiv & \frac{4}{3} + \frac{\int e^{3\Phi+\Lambda}[16p + (e^{2\Lambda}-1)(\rho+p)](e^{2\Lambda}-1)r^2\mathrm{d}r}{36\int e^{3\Phi+\Lambda}pr^2\mathrm{d}r} \\ & + \frac{4\pi G\int e^{3(\Phi+\Lambda)}[8p + (e^{2\Lambda}+1)(\rho c^2+p)]pr^4\mathrm{d}r}{9c^4\int e^{3\Phi+\Lambda}pr^2\mathrm{d}r} \\ & + \frac{16\pi^2G^2\int e^{3\Phi+5\Lambda}(\rho c^2+p)p^2r^6\mathrm{d}r}{9c^8\int e^{3\Phi+\Lambda}pr^2\mathrm{d}r} \end{aligned} \tag{E.1}$$

and the pressure-averaged adiabatic index is $\langle\gamma\rangle \equiv \int e^{3\Phi+\Lambda}\gamma(r)pr^2\mathrm{d}r/(\int e^{3\Phi+\Lambda}pr^2\mathrm{d}r)$.

E.1 Adiabatic index for an ideal fluid

The adiabatic index of a fluid is defined as $\gamma \equiv (\partial \ln p/\partial \ln n)_s$ locally in spacetime. The solution for an ideal fluid is often parametrized as $p = K(mn)^\gamma$, where K and γ are not explicit functions of n in an adiabatic process. We show the derivation of the adiabatic index of an ideal fluid. For an adiabatic process, the first law of thermodynamics tells $\mathrm{d}U = -p\,\mathrm{d}V$, where U is the total internal energy and V is the volume. Suppose N is the total number of particles, u is the internal energy density and n is the number density, $U = Nu/n$ and $V = N/n$. Since N is a constant, we have

$$\mathrm{d}\left(\frac{u}{n}\right) = -p\,\mathrm{d}\left(\frac{1}{n}\right) = Km^\gamma n^{\gamma-2}\mathrm{d}n, \tag{E.2}$$

where the ansatz $p = K(mn)^\gamma$ is used for the last equality. For ideal gas, K and γ are independent of n. Integrating both sides of Eq. (E.2) gives $u = Km^\gamma(\gamma-1)^{-1}n^\gamma = (\gamma-1)^{-1}p$. Since $u = (\rho - mn)c^2$, there is a general relation between ρ and p, i.e., $(\rho - mn)c^2 = p(\gamma-1)^{-1}$ [133, 82, 57]. Thus we have $\gamma = 1 + p/u$, which can be further expressed in terms of b and w,

$$\gamma(b,w) = 1 + \frac{p}{u} = 1 + \frac{2}{3}\frac{I_p(b,w)}{I_u(b,w)}, \tag{E.3}$$

where I_p and I_u are given in Eq. (3.4). In the nonrelativistic limit $bw \to 0$ ($I_p \simeq I_u$), $\gamma \to 5/3$; in the ultrarelativistic limit $bw \to 1$ ($I_p \simeq I_u/2$), $\gamma \to 4/3$.

E.2 Chandrasekhar's instability condition

The pulsation equation (3.10) is derived by perturbing the equilibrium solution to the Einstein equation with a Lagrangian displacement ξ [55]. Here we take a series of steps and convert it into an integral form. Multiplying its both sides by a factor of $r^2 e^{\Phi+\Lambda}\xi$ and integrating it over r, we get ($G = c = 1$)

$$\omega^2 \int_0^R e^{3\Lambda-\Phi}(\rho+p)r^2\xi^2 \mathrm{d}r = -\int_0^R (r^2 e^{-\Phi}\xi)\left[e^{3\Phi+\Lambda}\frac{\gamma p}{r^2}(r^2 e^{-\Phi}\xi)'\right]' \mathrm{d}r + 4\int_0^R e^{\Phi+\Lambda} r\frac{\mathrm{d}p}{\mathrm{d}r}\xi^2 \mathrm{d}r - \int_0^R e^{\Phi+\Lambda}\left(\frac{\mathrm{d}p}{\mathrm{d}r}\right)^2 \frac{r^2\xi^2}{\rho+p}\mathrm{d}r + 8\pi\int_0^R e^{3\Lambda+\Phi}p(\rho+p)r^2\xi^2\mathrm{d}r, \quad \text{(E.4)}$$

where "$'$" denotes "$\mathrm{d}/\mathrm{d}r$" for simplicity. Taking the first term on the right hand side of Eq. (E.4), and integrating it by parts, we have

$$-\int_0^R (r^2 e^{-\Phi}\xi)\left[e^{3\Phi+\Lambda}\frac{\gamma p}{r^2}(r^2 e^{-\Phi}\xi)'\right]' \mathrm{d}r = \int_0^R e^{3\Phi+\Lambda}\frac{\gamma p}{r^2}\left[(r^2 e^{-\Phi}\xi)'\right]^2 \mathrm{d}r - \xi e^{2\Phi+\Lambda}\gamma p(r^2 e^{-\Phi}\xi)'\big|_0^R, \quad \text{(E.5)}$$

where the total derivative term vanishes after imposing the boundary condition $\xi(0) = 0$ and $p(R) = 0$. Integrating the second term by parts gives rise to

$$\begin{aligned} 4\int_0^R e^{\Phi+\Lambda} r\frac{\mathrm{d}p}{\mathrm{d}r}\xi^2\mathrm{d}r &= -4\int_0^R e^{\Phi+\Lambda}[\xi^2 + 2r\xi\xi' + r\xi^2(\Phi'+\Lambda')]p\mathrm{d}r \\ &= -4\int_0^R e^{\Phi+\Lambda}(\xi^2 + 2r\xi\xi')p\mathrm{d}r - 16\pi\int_0^R e^{3\Lambda+\Phi}p(\rho+p)r^2\xi^2\mathrm{d}r, \quad \text{(E.6)} \end{aligned}$$

where we have used $2e^{-2\Lambda}(\Phi'+\Lambda')/r = 8\pi(\rho+p)$ from the Einstein equation.

For the third term on the right hand side of Eq. (E.4), we substitute $\mathrm{d}p/\mathrm{d}r$ with

$$\frac{\mathrm{d}p}{\mathrm{d}r} = -(\rho+p)\left[\frac{M+4\pi pr^3}{r(r-2M)}\right] = -(\rho+p)\left[\frac{1}{2r}(e^{2\Lambda}-1)+4\pi pre^{2\Lambda}\right] \tag{E.7}$$

and find

$$\begin{aligned}-\int_0^R e^{\Phi+\Lambda}\left(\frac{\mathrm{d}p}{\mathrm{d}r}\right)^2\frac{r^2\xi^2}{\rho+p}\mathrm{d}r = \\ -\int_0^R e^{\Phi+\Lambda}(\rho+p)\left[\frac{1}{4}(e^{2\Lambda}-1)^2+4\pi pr^2(e^{2\Lambda}-1)e^{2\Lambda}+16\pi^2p^2r^4e^{4\Lambda}\right]\xi^2\mathrm{d}r.\end{aligned} \tag{E.8}$$

We take $\xi(r) = re^{\Phi}$ as the trial function, which satisfies the boundary condition $\xi(0) = 0$. From the Einstein equation, we have $2\Phi' e^{-2\Lambda}/r - (1-e^{-2\Lambda})/r^2 = 8\pi p$, thus

$$\xi^2 + 2r\xi\xi' = r^2e^{2\Phi} + 2r^2(1+r\Phi')e^{2\Phi} = \left[3r^2+8\pi pr^4e^{2\Lambda}+r^2(e^{2\Lambda}-1)\right]e^{2\Phi}. \tag{E.9}$$

Putting all the relevant terms together, we have

$$\begin{aligned}&\omega^2\int_0^R e^{3\Lambda+\Phi}(\rho+p)r^4\mathrm{d}r = 9\int_0^R e^{3\Phi+\Lambda}\gamma pr^2\mathrm{d}r \\ &-4\int_0^R e^{3\Phi+\Lambda}[3r^2+8\pi pr^4e^{2\Lambda}+r^2(e^{2\Lambda}-1)]p\mathrm{d}r - 8\pi\int_0^R e^{3(\Phi+\Lambda)}p(\rho+p)r^4\mathrm{d}r \\ &-\int_0^R e^{3\Phi+\Lambda}\left[\frac{r^2}{4}(e^{2\Lambda}-1)^2+4\pi pr^4(e^{2\Lambda}-1)e^{2\Lambda}+16\pi^2p^2r^6e^{4\Lambda}\right](\rho+p)\mathrm{d}r \\ =&\int_0^R e^{3\Phi+\Lambda}(9\gamma-12)pr^2\mathrm{d}r - \frac{1}{4}\int_0^R e^{3\Phi+\Lambda}[16p+(e^{2\Lambda}-1)(\rho+p)](e^{2\Lambda}-1)r^2\mathrm{d}r \\ &-4\pi\int_0^R e^{3(\Phi+\Lambda)}[8p+(e^{2\Lambda}+1)(\rho+p)]pr^4\mathrm{d}r - 16\pi^2\int_0^R e^{3\Phi+5\Lambda}(\rho+p)p^2r^6\mathrm{d}r.\end{aligned} \tag{E.10}$$

We determine the critical stability condition by setting the right hand side of Eq. (E.10) to

0 and rewrite it as $\langle\gamma\rangle - \gamma_{\rm cr} = 0$, where

$$\langle\gamma\rangle \equiv \frac{\int_0^R e^{3\Phi+\Lambda}\gamma p r^2 {\rm d}r}{\int_0^R e^{3\Phi+\Lambda} p r^2 {\rm d}r} \tag{E.11}$$

is the pressure-averaged adiabatic index of the system, and

$$\begin{aligned}\gamma_{\rm cr} \equiv & \frac{4}{3} + \frac{1}{36}\frac{\int_0^R e^{3\Phi+\Lambda}[16p + (e^{2\Lambda}-1)(\rho+p)](e^{2\Lambda}-1) r^2 {\rm d}r}{\int_0^R e^{3\Phi+\Lambda} p r^2 {\rm d}r} \\ & + \frac{4\pi}{9}\frac{\int_0^R e^{3(\Phi+\Lambda)}[8p + (e^{2\Lambda}+1)(\rho+p)] p r^4 {\rm d}r}{\int_0^R e^{3\Phi+\Lambda} p r^2 {\rm d}r} + \frac{16\pi^2}{9}\frac{\int_0^R e^{3\Phi+5\Lambda}(\rho+p) p^2 r^6 {\rm d}r}{\int_0^R e^{3\Phi+\Lambda} p r^2 {\rm d}r}\end{aligned} \tag{E.12}$$

is the critical adiabatic index. A similar derivation can also be found in [307].

E.3 Critical adiabatic index in the Newtonian limit: a heuristic derivation

For the illustration purpose, we follow [81] and show a heuristic derivation of the instability condition in the Newtonian limit. The idea is to obtain the pulsation equation of a Newtonian star of mass M and radius R with spherical symmetry, $\delta\ddot{R} + (k/M)\delta R = 0$ and determine the effective "spring constant" k of the star. A tachyonic instability will develop if $k/M < 0$.

Consider a particle on the surface, it is pulled by an inward gravitational force $\bar{f}_g = GM/R^2 \approx G\bar{\rho}^2 R$ and an outward force due to pressure $\bar{f}_p \approx \bar{p}/R$, with the boundary condition $p(r = R) = 0$. The system is in equilibrium when $\bar{f}_g - \bar{f}_p = 0$. Let's perturb the system radius $R \to R + \delta R$ while keep its total mass M fixed. This leads to perturbations

in the density and pressure $\delta\bar{\rho} = -3\bar{\rho}\delta R/R$ and $\delta\bar{p} = -3\bar{\gamma}\bar{p}\delta R/R$, respectively, where have used $\bar{\gamma} \approx (\partial \ln \bar{p}/\partial \ln \bar{\rho})_s$ and $\bar{\rho} = m\bar{n}$. The resulting changes in the force are $\delta\bar{f}_p = -(3\bar{\gamma}+1)\,\bar{f}_p\delta R/R$ and $\delta\bar{f}_g = -5\bar{f}_g\delta R/R$. The acceleration related to the net force is $\delta\ddot{R} = (\bar{\delta}f_p - \bar{\delta}f_g)/\bar{\rho} = -3\,(\bar{\gamma} - 4/3)\,G\bar{\rho}\delta R$. We can identify $3\,(\bar{\gamma} - 4/3)\,G\bar{\rho}$ as k/M. The spherical system will undergo an exponential growth or decay under small radical perturbation if $\bar{\gamma} - 4/3 < 0$.

Appendix F

$(N+1)$-dimensional spacetime

F.1 Critical adiabatic index

In $(N+1)$ dimensions, $\mathrm{d}s^2 = -e^{2\Phi(t,r)}\mathrm{d}t^2 + e^{2\Lambda(t,r)}\mathrm{d}r^2 + r^2\mathrm{d}\Omega^2_{N-1}$ one can show that [134]

$$\begin{aligned}\gamma_{\mathrm{cr(GR)}} =& 2\left(1-\frac{1}{N}\right) + \frac{\int e^{3\Phi+\Lambda}[8(N-1)p + (N-2)(e^{2\Lambda}-1)(\rho+p)](N-2)(e^{2\Lambda}-1)r^{N-1}\mathrm{d}r}{4N^2\int e^{3\Phi+\Lambda}pr^{N-1}\mathrm{d}r} \\ &+ \frac{\kappa_N\int e^{3(\Phi+\Lambda)}\left\{[4(N-1)p + (N-2)(e^{2\Lambda}+1)(\rho+p)](p+p_\lambda) - 2(N-1)p_\lambda(\rho+p)\right\}r^{N+1}\mathrm{d}r}{N^2(N-1)\int e^{3\Phi+\Lambda}pr^{N-1}\mathrm{d}r} \\ &+ \frac{\kappa_N^2\int e^{3\Phi+5\Lambda}(\rho+p)(p+p_\lambda)^2r^{N+3}\mathrm{d}r}{N^2(N-1)^2\int e^{3\Phi+\Lambda}pr^{N-1}\mathrm{d}r},\end{aligned} \tag{F.1}$$

where $\kappa_N = (N-1)\omega_N$ is the (Einstein's) gravitational constant in N-dimensional space $(G_N = c = 1)$ with

$$\omega_N = \frac{2\pi^{N/2}}{\Gamma(N/2)} \tag{F.2}$$

being the area of the unit sphere in N-dimensional space; and

$$\langle\gamma\rangle \equiv \frac{\int e^{3\Phi+\Lambda}\gamma p r^{N-1}\mathrm{d}r}{\int e^{3\Phi+\Lambda} p r^{N-1}\mathrm{d}r} \tag{F.3}$$

the "effective" (pressure-averaged) adiabatic index of the fluid sphere.

F.2 Gravitational and rest masses of fluid sphere

Due to the radiation of internal (thermal) energy during gravothermal evolution, the *gravitational mass* of the fluid sphere

$$\mathcal{M} \equiv \omega_N \int \rho(r) r^{N-1} dr \tag{F.4}$$

is *not conserved*; whereas the *rest mass* of the sphere

$$\mathcal{M}_{\rm rest} \equiv \omega_N \int m n(r) e^{\Lambda(r)} r^{N-1} dr \tag{F.5}$$

is *conserved*, where the rest mass density $mn(r) = \rho(r)\sqrt{1-v^2(r)}$ with N-dimensional velocity dispersion $v = \sqrt{Np/\rho}$. The total internal energy, including the gravitational potential, must be $\mathcal{M} - \mathcal{M}_{\rm rest} < 0$ for a gravitationally bound system.

F.3 Homogeneous solution

The profile of the pressure of an homogeneous density ($\rho = \text{const.}$) fluid sphere of radius R is given by

$$\frac{p(r)}{\rho} = \frac{[N\rho - 2(\rho + \rho_\lambda)]\left[e^{-\Lambda(r)} - e^{-\Lambda(R)}\right]}{N\rho\, e^{-\Lambda(R)} - [N\rho - 2(\rho + \rho_\lambda)]e^{-\Lambda(r)}}, \tag{F.6}$$

and the metric potential

$$e^{\Phi(r)} = \frac{N\rho\, e^{-\Lambda(R)} - [N\rho - 2(\rho + \rho_\lambda)]e^{-\Lambda(r)}}{2(\rho + \rho_\lambda)}, \tag{F.7}$$

where

$$e^{-\Lambda(r)} = \sqrt{1 - \frac{2\kappa_N(\rho + \rho_\lambda)}{N(N-1)}r^2}. \tag{F.8}$$

If the mass of the fluid sphere is $\mathcal{M}$, we can express the fluid density

$$\rho = \frac{N(N-1)\mathcal{M}}{\kappa_N R^N} \tag{F.9}$$

and the cosmological constant

$$\rho_\lambda = \frac{N(N-1)}{2\kappa_N}\lambda = -p_\lambda, \tag{F.10}$$

where $\lambda = \pm 1/\ell^2$, the "+/−" sign corresponds to the positive/negative cosmological constant (scalar curvature). Incidentally, demanding $p(0) < \infty$ and $e^{\Phi(0)} > 0$ leads to the

Buchdahl bound in $(N+1)$-dimension with cosmological constant λ:

$$\frac{N-1}{N^2}\left(1-\sqrt{1-\frac{N^2 a}{(N-1)^2}}\right)<\mathcal{C}_N<\frac{N-1}{N^2}\left(1+\sqrt{1-\frac{N^2 a}{(N-1)^2}}\right), \tag{F.11}$$

where the compactness $\mathcal{C}_N = \mathcal{M}/R^{N-2}$ and the curvature parameter $a = \lambda R^2$. Furthermore, the solution can be parametrized in terms of $\mathcal{C}_N$ and a:

$$\frac{p(x)}{\rho}=\frac{\left[(N-2)\,\mathcal{C}_N-a\right]\left[\sqrt{1-(2\mathcal{C}_N+a)\,x^2}-\sqrt{1-(2\mathcal{C}_N+a)}\right]}{N\mathcal{C}_N\sqrt{1-(2\mathcal{C}_N+a)}-\left[(N-2)\,\mathcal{C}_N-a\right]\sqrt{1-(2\mathcal{C}_N+a)\,x^2}}\equiv y\left(\mathcal{C}_N,a;x\right) \tag{F.12}$$

and

$$e^{\Phi(x)}=\frac{N\mathcal{C}_N\sqrt{1-(2\mathcal{C}_N+a)}-\left[(N-2)\,\mathcal{C}_N-a\right]\sqrt{1-(2\mathcal{C}_N+a)\,x^2}}{2\mathcal{C}_N+a}, \tag{F.13}$$

where $x = r/R$ is the normalized radius, and we have used

$$e^{-\Lambda(x)}=\sqrt{1-(2\mathcal{C}_N+a)\,x^2}. \tag{F.14}$$

The parametrization makes sense only when $\rho \neq 0$ or $\mathcal{C}_N \neq 0$. With all of the above, the rest mass compactness Eq. F.5 turns out to be:

$$\mathcal{C}_{\mathrm{rest},N}\equiv\frac{\mathcal{M}_{\mathrm{rest}}}{R^{N-2}}=N\mathcal{C}_N\int_0^1\sqrt{1-Ny}\;e^{\Lambda}x^{N-1}dx. \tag{F.15}$$

Moreover, the critical adiabatic index for homogeneous sphere can be expressed as:

$$\gamma_{\rm cr(GR)} \equiv 2\left(1-\frac{1}{N}\right)+\frac{\int_0^1 e^{3\Phi+\Lambda}[8(N-1)y+(N-2)(e^{2\Lambda}-1)(1+y)](N-2)(e^{2\Lambda}-1)x^{N-1}{\rm d}x}{4N^2\int_0^1 e^{3\Phi+\Lambda}yx^{N-1}{\rm d}x}$$
$$+\frac{\mathcal{C}_N\int_0^1 e^{3(\Phi+\Lambda)}\left\{[4(N-1)y+(N-2)(e^{2\Lambda}+1)(1+y)](y-a/2\mathcal{C}_N)+(N-1)(a/\mathcal{C}_N)(1+y)\right\}x^{N+1}{\rm d}x}{N\int_0^1 e^{3\Phi+\Lambda}yx^{N-1}{\rm d}x}$$
$$+\frac{\mathcal{C}_N^2\int_0^1 e^{3\Phi+5\Lambda}(1+y)(y-a/2\mathcal{C}_N)^2x^{N+3}{\rm d}x}{\int_0^1 e^{3\Phi+\Lambda}yx^{N-1}{\rm d}x}. \tag{F.16}$$

In the "post-Newtonian" approximations ($\mathcal{C}_N \ll 1$ and $a \ll 1$), we have

$$\gamma_{\rm cr(GR)} = \frac{a}{(N-2)\,\mathcal{C}_N - a} + \sum_{j,k=0,1,...} f_{jk}^{(N)}\mathcal{C}_N^j a^k, \tag{F.17}$$

where $f_{00}^{(N)} = \gamma_{\rm cr(NG)} = 2\,(1-1/N)$, and the *stabilizer/destabilizer* characterizing the *competition* between the compactness and the background curvature (cosmological constant) can be expanded as

$$\frac{a}{(N-2)\,\mathcal{C}_N - a} = \begin{cases} \sum_{n=1}^{\infty}\left(a/\left(N-2\right)\mathcal{C}_N\right)^n & \text{if } |a| < (N-2)\,\mathcal{C}_N \\ -1-\sum_{n=1}^{\infty}\left[(N-2)\,\mathcal{C}_N/a\right]^n & \text{if } |a| > (N-2)\,\mathcal{C}_N. \end{cases} \tag{F.18}$$

Appendix G

Numerical Results of the Truncated Maxwell-Boltzmann Distribution

In this Appendix, we tabulate the numerical results of the truncated Maxwell-Boltzmann (MB) models. In Table G.1, we show properties of equilibrium configurations for boundary temperature parameter as $b = k_B T(R)/mc^2 = 0.1,\ 0.2,\ 0.3$, and 0.5 and scan over the central energy cutoff $w(0) = \epsilon_c(0)/k_B T(0)$ for each b. In Table G.2, we show marginally stable configurations that satisfy the adiabatic index criterion $\langle\gamma\rangle = \gamma_{\rm cr}$, given different values of the boundary temperature $b = k_B T(R)/mc^2$. Generally, the velocity dispersion on the core boundary $v(R)/c$ is not equivalent to $b = k_B T(R)/mc^2$.

Table G.1: Properties of equilibrium configurations scanned over the central energy cutoff $w(0) = \epsilon_c(0)/k_BT(0)$ for $b = k_BT(R)/mc^2 = 0.1,\ 0.2,\ 0.3$, and 0.5. From the 2nd to 14th columns, we show their total energy $\hat{E} = \hat{M}$, total rest energy $\hat{E}_{\rm rest}$, binding energy $\hat{B}$, fractional binding energy ε, system radius $\hat{R}$, compactness $C = GM(R)/c^2R = \hat{M}/\hat{R}$, central interior redshift $Z(0)$, central energy cut off $\epsilon_c(0)$, central energy density $\hat{\rho}(0)$, central pressure $\hat{p}(0)$, central velocity dispersion $v(0)$, pressure averaged adiabatic index $\langle\gamma\rangle$, and critical adiabatic index $\gamma_{\rm cr}$, respectively. For each case, we underscore marginally stable configurations following instability criteria based on total energy, binding energy, fractional binding energy, and adiabatic index by underscoring $w(0)$ and the corresponding critical values.

$$b = k_BT(R)/mc^2 = 0.1$$

$w(0)$	$\hat{E}=\hat{M}$	$\hat{E}_{\rm rest}$	$\hat{B}$	ε	$\hat{R}$	$C=M/R$	$Z(0)$	$\epsilon_c(0)/mc^2$	$\hat{\rho}(0)$	$\hat{p}(0)$	$v(0)/c$	$\langle\gamma\rangle$	$\gamma_{\rm cr}$
0.1	2.72704×10^{-2}	2.72720×10^{-2}	6.54443×10^{-5}	2.39961×10^{-3}	6.82000×10^{0}	3.98936×10^{-3}	1.41544×10^{-2}	1.01010×10^{-2}	4.99923×10^{-4}	1.42585×10^{-6}	9.24965×10^{-2}	1.66545	1.34070
0.3	2.29993×10^{-2}	2.32285×10^{-2}	2.29264×10^{-4}	6.89961×10^{-3}	2.89200×10^{0}	1.41053×10^{-2}	4.29931×10^{-2}	3.09277×10^{-2}	8.69198×10^{-3}	7.40805×10^{-5}	1.59902×10^{-1}	1.66301	1.35554
0.6	3.47240×10^{-2}	3.51790×10^{-2}	4.54900×10^{-4}	1.29311×10^{-2}	1.63800×10^{0}	2.11990×10^{-2}	8.71214×10^{-2}	6.38296×10^{-2}	5.82063×10^{-2}	9.86165×10^{-4}	2.25450×10^{-1}	1.65936	1.37799
1.1	3.29600×10^{-2}	3.36735×10^{-2}	7.13463×10^{-4}	2.11877×10^{-2}	9.64001×10^{-1}	3.41909×10^{-2}	1.64064×10^{-1}	1.22591×10^{-1}	3.55962×10^{-1}	1.09378×10^{-3}	3.03616×10^{-1}	1.65331	1.41580
1.5	3.02662×10^{-2}	3.10835×10^{-2}	8.17290×10^{-4}	2.62934×10^{-2}	7.25001×10^{-1}	4.17464×10^{-2}	2.28846×10^{-1}	1.76464×10^{-1}	9.92442×10^{-1}	4.12090×10^{-3}	3.52943×10^{-1}	1.64851	1.44620
1.9	2.72897×10^{-2}	2.81385×10^{-2}	8.48824×10^{-4}	3.01659×10^{-2}	5.81001×10^{-1}	4.69701×10^{-2}	2.96903×10^{-1}	2.34552×10^{-1}	1.53859×10^{0}	1.21454×10^{-2}	3.95398×10^{-1}	1.64377	1.47651
2.3	2.44394×10^{-2}	2.51671×10^{-2}	8.27673×10^{-4}	3.28872×10^{-2}	4.88001×10^{-1}	4.98757×10^{-2}	3.68726×10^{-1}	2.98693×10^{-1}	2.05282×10^{0}	3.09617×10^{-2}	4.33059×10^{-1}	1.63912	1.50646
2.7	2.15635×10^{-2}	2.23348×10^{-2}	7.71245×10^{-4}	3.45311×10^{-2}	4.25001×10^{-1}	5.07375×10^{-2}	4.44974×10^{-1}	3.69819×10^{-1}	2.98713×10^{0}	7.19304×10^{-2}	4.67177×10^{-1}	1.63459	1.53571
3.2	1.84498×10^{-2}	1.91224×10^{-2}	6.72630×10^{-4}	3.51754×10^{-2}	3.78001×10^{-1}	4.88888×10^{-2}	5.47883×10^{-1}	4.70526×10^{-1}	4.22039×10^{0}	1.89599×10^{-1}	5.06132×10^{-1}	1.62910	1.57054
3.4	1.73316×10^{-2}	1.79606×10^{-2}	6.28996×10^{-4}	3.50209×10^{-2}	3.68001×10^{-1}	4.70966×10^{-2}	5.91899×10^{-1}	5.15125×10^{-1}	4.93421×10^{0}	2.74353×10^{-1}	5.20825×10^{-1}	1.62714	1.58366
3.7	1.58026×10^{-2}	1.63652×10^{-2}	5.62545×10^{-4}	3.43745×10^{-2}	3.61001×10^{-1}	4.57745×10^{-2}	6.61822×10^{-1}	5.87271×10^{-1}	5.84814×10^{0}	4.17035×10^{-1}	5.42423×10^{-1}	1.62423	1.60212
4.05159	1.42556×10^{-2}	1.47424×10^{-2}	4.86859×10^{-4}	3.30243×10^{-2}	3.68001×10^{-1}	3.87378×10^{-2}	7.50107×10^{-1}	6.81035×10^{-1}	8.17923×10^{0}	8.74006×10^{0}	5.66189×10^{-1}	1.62117	1.62117
4.2	1.36891×10^{-2}	1.41457×10^{-2}	4.56567×10^{-4}	3.22761×10^{-2}	3.78001×10^{-1}	3.62145×10^{-2}	7.90144×10^{-1}	7.24120×10^{-1}	1.02219×10^{1}	1.13099×10^{1}	5.76136×10^{-1}	1.62002	1.62010
4.5	1.27271×10^{-2}	1.31271×10^{-2}	4.00052×10^{-4}	3.04753×10^{-2}	4.13001×10^{-1}	3.08160×10^{-2}	8.76941×10^{-1}	8.18182×10^{-1}	1.60208×10^{1}	1.89661×10^{1}	5.95948×10^{-1}	1.61808	1.62033

$$b = k_BT(R)/mc^2 = 0.2$$

$w(0)$	$\hat{E}=\hat{M}$	$\hat{E}_{\rm rest}$	$\hat{B}$	ε	$\hat{R}$	$C=M/R$	$Z(0)$	$\epsilon_c(0)/mc^2$	$\hat{\rho}(0)$	$\hat{p}(0)$	$v(0)/c$	$\langle\gamma\rangle$	$\gamma_{\rm cr}$
0.05	3.87808×10^{-2}	3.88743×10^{-2}	9.34786×10^{-5}	2.40464×10^{-3}	9.67200×10^{0}	4.00960×10^{-3}	1.47753×10^{-2}	1.01010×10^{-2}	2.46406×10^{-4}	7.04972×10^{-6}	9.26448×10^{-2}	1.66545	1.34072
0.15	4.77866×10^{-2}	4.81207×10^{-2}	3.34059×10^{-4}	6.94210×10^{-3}	4.12300×10^{0}	1.15903×10^{-2}	4.39959×10^{-2}	3.09278×10^{-2}	4.11840×10^{-3}	3.57900×10^{-5}	1.60689×10^{-1}	1.66299	1.35569
0.4	5.18443×10^{-2}	5.27274×10^{-2}	8.83084×10^{-4}	1.67481×10^{-2}	1.84400×10^{0}	2.81151×10^{-2}	1.18857×10^{-1}	8.69556×10^{-2}	5.93008×10^{-2}	1.37078×10^{-3}	2.63338×10^{-1}	1.65680	1.39423
0.65	4.97497×10^{-2}	5.09868×10^{-2}	1.23612×10^{-3}	2.44400×10^{-2}	1.20100×10^{0}	4.14160×10^{-2}	2.00179×10^{-1}	1.49422×10^{-1}	2.47787×10^{-1}	9.37848×10^{-3}	3.30967×10^{-1}	1.65052	1.43435
0.85	4.67140×10^{-2}	4.81152×10^{-2}	1.40117×10^{-3}	2.91212×10^{-2}	9.36001×10^{-1}	4.99081×10^{-2}	2.69793×10^{-1}	2.04808×10^{-1}	5.80946×10^{-1}	2.89401×10^{-2}	3.86583×10^{-1}	1.64544	1.46752
1.05	4.32590×10^{-2}	4.47129×10^{-2}	1.45394×10^{-3}	3.25173×10^{-2}	7.65001×10^{-1}	5.65476×10^{-2}	3.44027×10^{-1}	2.65807×10^{-1}	1.19109×10^{0}	7.38902×10^{-2}	4.31138×10^{-1}	1.64034	1.50157
1.2	4.05844×10^{-2}	4.20228×10^{-2}	1.43838×10^{-3}	3.42264×10^{-2}	6.73001×10^{-1}	6.03036×10^{-2}	4.03116×10^{-1}	3.15789×10^{-1}	1.59873×10^{0}	1.37323×10^{-1}	4.62161×10^{-1}	1.63649	1.52760
1.35	3.79259×10^{-2}	3.93103×10^{-2}	1.38436×10^{-3}	3.52163×10^{-2}	6.00001×10^{-1}	6.32097×10^{-2}	4.65490×10^{-1}	3.69827×10^{-1}	2.01906×10^{0}	2.43204×10^{-1}	4.91598×10^{-1}	1.63264	1.55399
1.5	3.53324×10^{-2}	3.66322×10^{-2}	1.29981×10^{-3}	3.54828×10^{-2}	5.43001×10^{-1}	6.59687×10^{-2}	5.31533×10^{-1}	4.28522×10^{-1}	2.56112×10^{0}	3.98834×10^{-1}	5.19707×10^{-1}	1.62879	1.58064
1.65	3.28360×10^{-2}	3.40576×10^{-2}	1.19160×10^{-3}	3.50187×10^{-2}	4.98001×10^{-1}	6.59355×10^{-2}	6.01703×10^{-1}	4.92480×10^{-1}	3.20135×10^{0}	6.90365×10^{0}	5.48340×10^{-1}	1.62497	1.60740
1.7	3.20294×10^{-2}	3.31908×10^{-2}	1.15138×10^{-3}	3.47093×10^{-2}	4.86001×10^{-1}	6.59040×10^{-2}	6.26103×10^{-1}	5.15151×10^{-1}	3.47346×10^{0}	8.10392×10^{-1}	5.55683×10^{-1}	1.62370	1.61631
1.73635	3.14517×10^{-2}	3.25728×10^{-2}	1.12106×10^{-3}	3.44172×10^{-2}	4.77001×10^{-1}	6.59364×10^{-2}	6.44181×10^{-1}	5.31996×10^{-1}	3.81593×10^{0}	8.65548×10^{0}	9.11403×10^{-1}	5.62044×10^{-1}	1.62278	1.62278
1.85	2.96954×10^{-2}	3.07167×10^{-2}	1.02133×10^{-3}	3.32499×10^{-2}	4.53001×10^{-1}	6.55526×10^{-2}	7.02657×10^{-1}	5.87236×10^{-1}	4.59255×10^{0}	1.15907×10^{1}	1.30712×10^{0}	5.81653×10^{-1}	1.61994	1.64293
2.0	2.75004×10^{-2}	2.83817×10^{-2}	8.81323×10^{-4}	3.10525×10^{-2}	4.29001×10^{-1}	6.41034×10^{-2}	7.84825×10^{-1}	6.86595×10^{-1}	1.60159×10^{1}	2.07718×10^{1}	1.66295×10^{0}	6.06946×10^{-1}	1.61625	1.66912

$$b = k_BT(R)/mc^2 = 0.3$$

$w(0)$	$\hat{E}=\hat{M}$	$\hat{E}_{\rm rest}$	$\hat{B}$	ε	$\hat{R}$	$C=M/R$	$Z(0)$	$\epsilon_c(0)/mc^2$	$\hat{\rho}(0)$	$\hat{p}(0)$	$v(0)/c$	$\langle\gamma\rangle$	$\gamma_{\rm cr}$
0.033	4.75157×10^{-2}	4.76291×10^{-2}	1.13485×10^{-4}	2.38268×10^{-3}	1.19480×10^{1}	3.97687×10^{-3}	1.40394×10^{-2}	9.99899×10^{-3}	1.30375×10^{-4}	4.51884×10^{-6}	9.22282×10^{-2}	1.66546	1.34065
0.133	4.14737×10^{-2}	4.26070×10^{-2}	5.63280×10^{-4}	9.07989×10^{-3}	4.03500×10^{0}	1.52351×10^{-2}	5.77953×10^{-2}	4.15580×10^{-2}	5.77271×10^{-3}	6.64531×10^{-5}	1.85835×10^{-1}	1.66176	1.36328
0.267	6.48158×10^{-2}	6.59264×10^{-2}	1.11061×10^{-3}	1.68462×10^{-2}	2.27100×10^{0}	2.85406×10^{-2}	1.19486×10^{-1}	8.70740×10^{-2}	3.81380×10^{-2}	8.90310×10^{-4}	2.64638×10^{-1}	1.65674	1.39468
0.467	6.22397×10^{-2}	6.38962×10^{-2}	1.65647×10^{-3}	2.59345×10^{-2}	1.38700×10^{0}	4.48736×10^{-2}	2.18873×10^{-1}	1.62921×10^{-1}	1.94114×10^{-1}	8.05085×10^{-3}	3.52738×10^{-1}	1.64910	1.44387
0.633	5.78329×10^{-2}	5.96955×10^{-2}	1.86259×10^{-3}	3.12016×10^{-2}	1.04400×10^{0}	5.53854×10^{-2}	3.09024×10^{-1}	2.34409×10^{-1}	5.08491×10^{-1}	2.89754×10^{-2}	4.13460×10^{-1}	1.64265	1.48675
0.733	5.48232×10^{-2}	5.67169×10^{-2}	1.89374×10^{-3}	3.33894×10^{-2}	9.07001×10^{-1}	6.04445×10^{-2}	3.67187×10^{-1}	2.81887×10^{-1}	8.33940×10^{-1}	5.54914×10^{-2}	4.46793×10^{-1}	1.63871	1.51344
0.9	5.27484×10^{-2}	5.46295×10^{-2}	1.88110×10^{-3}	3.44338×10^{-2}	8.33001×10^{-1}	6.33234×10^{-2}	4.07950×10^{-1}	3.15788×10^{-1}	1.13380×10^{0}	8.28133×10^{-2}	4.68104×10^{-1}	1.63606	1.53165
0.867	5.06592×10^{-2}	5.25040×10^{-2}	1.84479×10^{-3}	3.51361×10^{-2}	7.70001×10^{-1}	6.57911×10^{-2}	4.50296×10^{-1}	3.51529×10^{-1}	1.51812×10^{0}	1.20871×10^{-1}	4.88730×10^{-1}	1.63340	1.55012
0.967	4.75566×10^{-2}	4.93089×10^{-2}	1.75236×10^{-3}	3.55384×10^{-2}	6.92001×10^{-1}	6.87233×10^{-2}	5.16649×10^{-1}	4.08626×10^{-1}	2.29463×10^{0}	2.05574×10^{-1}	5.18428×10^{-1}	1.62942	1.57809
1.033	4.55399×10^{-2}	4.72098×10^{-2}	1.66994×10^{-3}	3.53727×10^{-2}	6.49001×10^{-1}	7.01692×10^{-2}	5.62702×10^{-1}	4.49016×10^{-1}	2.97846×10^{0}	2.86744×10^{-1}	5.37417×10^{-1}	1.62678	1.59677
1.067	4.45149×10^{-2}	4.61367×10^{-2}	1.62176×10^{-3}	3.51513×10^{-2}	6.30001×10^{-1}	7.06585×10^{-2}	5.87183×10^{-1}	4.70792×10^{-1}	3.39686×10^{0}	3.38884×10^{-1}	5.47032×10^{-1}	1.62543	1.60645
1.14526	4.27849×10^{-2}	4.43162×10^{-2}	1.53130×10^{-3}	3.45539×10^{-2}	5.99001×10^{-1}	7.14271×10^{-2}	6.30406×10^{-1}	5.09562×10^{-1}	4.23693×10^{0}	4.88981×10^{-1}	5.62366×10^{-1}	1.62311	1.62311
1.167	4.15683×10^{-2}	4.30293×10^{-2}	1.46104×10^{-3}	3.39546×10^{-2}	5.80001×10^{-1}	7.16693×10^{-2}	6.62419×10^{-1}	5.38688×10^{-1}	4.95951×10^{0}	5.45061×10^{-1}	5.74723×10^{-1}	1.62145	1.63597
1.267	3.87411×10^{-2}	4.00187×10^{-2}	1.27798×10^{-3}	3.19270×10^{-2}	5.40001×10^{-1}	7.17426×10^{-2}	7.42982×10^{-1}	6.13138×10^{-1}	7.13493×10^{0}	8.60887×10^{-1}	6.01643×10^{-1}	1.61750	1.66373

$$b = k_BT(R)/mc^2 = 0.5$$

$w(0)$	$\hat{E}=\hat{M}$	$\hat{E}_{\rm rest}$	$\hat{B}$	ε	$\hat{R}$	$C=M/R$	$Z(0)$	$\epsilon_c(0)/mc^2$	$\hat{\rho}(0)$	$\hat{p}(0)$	$v(0)/c$	$\langle\gamma\rangle$	$\gamma_{\rm cr}$
0.02	6.16063×10^{-2}	6.17550×10^{-2}	1.48683×10^{-4}	2.40763×10^{-3}	1.53190×10^{1}	4.02156×10^{-3}	1.41877×10^{-2}	1.01010×10^{-2}	9.77183×10^{-5}	2.80107×10^{-6}	9.27331×10^{-2}	1.66544	1.34073
0.1	8.22934×10^{-2}	8.32134×10^{-2}	9.31015×10^{-4}	1.11883×10^{-2}	4.35600×10^{0}	1.88894×10^{-2}	7.30960×10^{-2}	5.26315×10^{-2}	2.19265×10^{-2}	8.99255×10^{-4}	2.08730×10^{-1}	1.66049	1.37116
0.18	8.51525×10^{-2}	8.67687×10^{-2}	1.61614×10^{-3}	1.86259×10^{-2}	2.66900×10^{0}	3.19043×10^{-2}	1.35727×10^{-1}	9.89006×10^{-2}	3.06823×10^{-2}	8.12905×10^{-4}	2.81927×10^{-1}	1.65545	1.40298
0.28	8.26354×10^{-2}	8.48251×10^{-2}	2.20966×10^{-3}	2.60437×10^{-2}	1.86700×10^{0}	4.57196×10^{-2}	2.19883×10^{-1}	1.62758×10^{-1}	1.30023×10^{-1}	4.41298×10^{-3}	3.54643×10^{-1}	1.64901	1.44473
0.36	7.85954×10^{-2}	8.10666×10^{-2}	2.47127×10^{-3}	3.04845×10^{-2}	1.43200×10^{0}	5.48850×10^{-2}	2.92500×10^{-1}	2.19510×10^{-1}	2.38590×10^{-1}	1.30406×10^{-2}	4.04932×10^{-1}	1.64376	1.47970
0.44	7.38054×10^{-2}	7.63684×10^{-2}	2.56300×10^{-3}	3.35610×10^{-2}	1.18200×10^{0}	6.24411×10^{-2}	3.70462×10^{-1}	2.82048×10^{-1}	4.59406×10^{-1}	3.11249×10^{-2}	4.50833×10^{-1}	1.63843	1.51604
0.48	7.12704×10^{-2}	7.38231×10^{-2}	2.55277×10^{-3}	3.45795×10^{-2}	1.08600×10^{0}	6.56264×10^{-2}	4.11664×10^{-1}	3.13763×10^{-1}	6.18568×10^{-1}	4.60437×10^{-2}	4.72555×10^{-1}	1.63574	1.53470
0.54	6.73963×10^{-2}	6.98728×10^{-2}	2.47644×10^{-3}	3.54421×10^{-2}	9.67001×10^{-1}	6.96962×10^{-2}	4.76532×10^{-1}	3.69836×10^{-1}	9.40223×10^{-1}	7.95828×10^{-2}	5.03912×10^{-1}	1.63168	1.56326
0.58	6.48933×10^{-2}	6.71929×10^{-2}	2.38964×10^{-3}	3.55639×10^{-2}	9.02001×10^{-1}	7.18439×10^{-2}	5.21991×10^{-1}	4.08438×10^{-1}	1.22560×10^{0}	1.12170×10^{-1}	5.24119×10^{-1}	1.62896	1.58265
0.6	6.35111×10^{-2}	6.58478×10^{-2}	2.33667×10^{-3}	3.54860×10^{-2}	8.72001×10^{-1}	7.28337×10^{-2}	5.45434×10^{-1}	4.28534×10^{-1}	1.39327×10^{0}	1.32452×10^{-1}	5.34038×10^{-1}	1.62759	1.59243
0.64	6.09453×10^{-2}	6.31589×10^{-2}	2.21356×10^{-3}	3.50475×10^{-2}	8.19001×10^{-1}	7.44142×10^{-2}	5.93835×10^{-1}	4.70546×10^{-1}	1.79139×10^{0}	1.82965×10^{-1}	5.53541×10^{-1}	1.62486	1.61217
0.662445	5.95204×10^{-2}	6.16658×10^{-2}	2.13537×10^{-3}	3.46337×10^{-2}	7.93001×10^{-1}	7.50572×10^{-2}	6.21927×10^{-1}	4.93258×10^{-1}	2.05035×10^{0}	2.18273×10^{-1}	5.64303×10^{-1}	1.62331	1.62331
0.72	5.59314×10^{-2}	5.78406×10^{-2}	1.90924×10^{-3}	3.30086×10^{-2}	7.33001×10^{-1}	7.63046×10^{-2}	6.97282×10^{-1}	5.62469×10^{-1}	2.90495×10^{0}	3.38632×10^{-1}	5.91365×10^{-1}	1.61940	1.65214
0.76	5.35030×10^{-2}	5.52369×10^{-2}	1.73389×10^{-3}	3.13901×10^{-2}	6.98001×10^{-1}	7.66518×10^{-2}	7.52709×10^{-1}	6.12854×10^{-1}	3.67288×10^{0}	4.55200×10^{-1}	6.09759×10^{-1}	1.61668	1.67225

Table G.2: Properties of marginally stable configurations that satisfy the adiabatic index criterion $\langle\gamma\rangle = \gamma_{\rm cr}$, given different values of the boundary temperature $b = k_BT(R)/mc^2$.

b	$w(0)$	$\hat{E}=\hat{M}$	$\hat{R}$	$C=M/R$	$Z(0)$	$\epsilon_c(0)/mc^2$	$\hat{\rho}(0)$	$\hat{p}(0)$	$v(0)/c$	$v(R)/c$	$\langle\gamma\rangle=\gamma_{\rm cr}$
5.0	6.48150×10^{-2}	2.06015×10^{-1}	2.59700×10^{0}	7.93280×10^{-2}	6.12906×10^{-1}	4.79448×10^{-1}	1.60344×10^{-1}	1.71013×10^{-2}	5.65655×10^{-1}	3.36500×10^{-3}	1.62358
3.0	1.08185×10^{-1}	1.58573×10^{-1}	2.00000×10^{0}	7.90492×10^{-2}	6.13491×10^{-1}	4.80491×10^{-1}	2.71859×10^{-1}	2.89847×10^{-2}	5.65552×10^{-1}	5.01069×10^{-3}	1.62356
2.0	1.62585×10^{-1}	1.28444×10^{-1}	1.63300×10^{0}	7.86552×10^{-2}	6.14252×10^{-1}	4.81854×10^{-1}	4.16754×10^{-1}	4.44142×10^{-2}	5.65434×10^{-1}	8.39347×10^{-4}	1.62354
1.0	3.27070×10^{-1}	8.86277×10^{-2}	1.14300×10^{0}	7.75395×10^{-2}	6.16612×10^{-1}	4.86021×10^{-1}	8.91191×10^{-1}	9.48500×10^{-2}	5.65059×10^{-1}	5.65015×10^{-3}	1.62347
0.5	6.62445×10^{-1}	5.95204×10^{-2}	7.93001×10^{-1}	7.50572×10^{-2}	6.21927×10^{-1}	4.95258×10^{-1}	2.05635×10^{0}	2.18273×10^{-1}	5.64303×10^{-1}	3.66372×10^{-3}	1.62333
0.3	1.12526×10^{0}	4.27849×10^{-2}	5.99001×10^{-1}	7.14271×10^{-2}	6.30406×10^{-1}	5.09562×10^{-1}	4.23693×10^{0}	4.88081×10^{-1}	5.63266×10^{-1}	9.11920×10^{-3}	1.62311
0.2	1.73635×10^{0}	3.14517×10^{-2}	4.77001×10^{-1}	6.59364×10^{-2}	6.44181×10^{-1}	5.31996×10^{-1}	8.65548×10^{0}	9.11403×10^{-1}	5.62044×10^{-1}	7.05363×10^{-3}	1.62278
0.15	2.39865×10^{0}	2.41230×10^{-2}	4.07001×10^{-1}	5.92702×10^{-2}	6.63548×10^{-1}	5.61946×10^{-1}	1.68117×10^{1}	1.76500×10^{0}	5.61211×10^{-1}	9.52828×10^{-3}	1.62239
0.14	2.60081×10^{0}	2.24259×10^{-2}	3.93001×10^{-1}	5.70632×10^{-2}	6.70637×10^{-1}	5.72538×10^{-1}	2.03949×10^{1}	2.14055×10^{0}	5.61128×10^{-1}	1.01614×10^{-2}	1.62225
0.13	2.84350×10^{0}	2.06203×10^{-2}	3.80001×10^{-1}	5.42638×10^{-2}	6.80073×10^{-1}	5.86379×10^{-1}	2.56589×10^{1}	2.69362×10^{0}	5.61190×10^{-1}	8.83738×10^{-3}	1.62209
0.12	3.14240×10^{0}	1.86835×10^{-2}	3.69001×10^{-1}	5.06326×10^{-2}	6.93337×10^{-1}	6.05343×10^{-1}	3.40099×10^{1}	3.57521×10^{0}	5.61577×10^{-1}	5.28167×10^{-3}	1.62188
0.11	3.52490×10^{0}	1.65825×10^{-2}	3.62001×10^{-1}	4.58080×10^{-2}	7.13594×10^{-1}	6.33260×10^{-1}	4.88977×10^{1}	5.16148×10^{0}	5.62734×10^{-1}	6.38807×10^{-3}	1.62159
0.1	4.05150×10^{0}	1.42556×10^{-2}	3.68001×10^{-1}	3.87378×10^{-2}	7.50107×10^{-1}	6.81035×10^{-1}	8.17923×10^{1}	8.74006×10^{0}	5.66189×10^{-1}	8.76561×10^{-3}	1.62117
0.09	5.08620×10^{0}	1.13990×10^{-2}	4.83001×10^{-1}	2.36004×10^{-2}	8.89250×10^{-1}	8.44163×10^{-1}	2.57654×10^{2}	2.96813×10^{1}	5.87872×10^{-1}	5.72277×10^{-3}	1.62023

Appendix H

Truncated Quantum Distributions

Given the distribution function of the particles with a cutoff $w = \epsilon_c/k_BT$,

$$f(x \leq w) = \frac{1 - e^{x-w}}{e^{x-\alpha} - \eta} = \frac{e^{\alpha(R)}(e^{w-x} - 1)}{1 - \eta e^{\alpha(R)+w-x}}, \tag{H.1}$$

where $x = \epsilon/k_BT$ and the number factor η is $+1$ (-1) for bosons (fermions).

H.1 Equation-of-state with pair production/annihilation

In the regime $k_BT \sim mc^2$, the pair production of quantum particles ($\chi\bar{\chi} \leftrightarrow$ radiations) is relevant. The chemical potential of the antiparticles is $\bar{\mu} = \mu - 2mc^2$ or $\bar{\alpha} = \alpha - 2mc^2/k_BT$. Therefore,

$$\bar{\alpha}(R) = \alpha(R) - \frac{2mc^2}{k_BT(R)} = \alpha(R) - \frac{2}{b} \tag{H.2}$$

and thus the distribution function of the antiparticles is

$$\bar{f}(x \leq w) = \frac{1 - e^{x-w}}{e^{x-\bar{\alpha}} - \eta} = \frac{e^{\bar{\alpha}(R)}(e^{w-x} - 1)}{1 - \eta e^{\bar{\alpha}(R)+w-x}} = \frac{e^{\alpha(R)}(e^{w-x} - 1)}{e^{2/b} - \eta e^{\alpha(R)+w-x}}. \tag{H.3}$$

Then the (net) number density becomes

$$n(r) = n_{\chi} - n_{\bar{\chi}} = 4\sqrt{2}\pi g m^3 (c^3/h^3) e^{\alpha(R)} \left(\frac{b}{1-bw}\right)^{3/2} \times$$

$$\int_0^w \left[\frac{\sinh(1/b)\, e^{-\alpha(R)-w+x}\,(e^{w-x} - 1)}{\cosh(1/b - \alpha(R) - w + x) - \eta \cosh(1/b)}\right] \left(1 + \frac{bx/2}{1-bw}\right)^{1/2} \left(1 + \frac{bx}{1-bw}\right) x^{1/2} \mathrm{d}x. \tag{H.4}$$

Clearly, the ratio of antiparticles to particles, $n_{\bar{\chi}}/n_{\chi} \simeq e^{-2/b} = e^{-2mc^2/k_B T(R)}$, is Boltzmann suppressed if $b = k_B T(R)/mc^2 \ll 1$.

The energy density, with radiation energy $u_{\mathrm{rad}} = 2\rho_{\bar{\chi}}$,

$$\rho(r) = \rho_{\chi} - \rho_{\bar{\chi}} + u_{\mathrm{rad}} = \rho_{\chi} + \rho_{\bar{\chi}} = 4\sqrt{2}\pi g m^4 (c^3/h^3) e^{\alpha(R)} \left(\frac{b}{1-bw}\right)^{3/2} \times$$

$$\int_0^w \left[\frac{\left(\cosh(1/b)\, e^{-\alpha(R)-w+x} - \eta e^{-1/b}\right)(e^{w-x} - 1)}{\cosh(1/b - \alpha(R) - w + x) - \eta \cosh(1/b)}\right] \left(1 + \frac{bx/2}{1-bw}\right)^{1/2} \left(1 + \frac{bx}{1-bw}\right)^{2} x^{1/2} \mathrm{d}x. \tag{H.5}$$

While the internal energy,

$$u(r) = u_{\chi} - u_{\bar{\chi}} + u_{\mathrm{rad}} = u_{\chi} - u_{\bar{\chi}} + 2\rho_{\bar{\chi}} = u_{\chi} - u_{\bar{\chi}} + 2\left(u_{\bar{\chi}} + n_{\bar{\chi}} mc^2\right) = u_{\chi} + u_{\bar{\chi}} + 2n_{\bar{\chi}} mc^2,$$

where $2n_{\bar{\chi}} mc^2$ is the energy *threshold* of pair production.

The pressure, with radiation pressure $p_{\rm rad} = \frac{1}{3}u_{\rm rad} = \frac{2}{3}\rho_{\bar{\chi}}$,

$$p(r) = p_\chi - p_{\bar{\chi}} + p_{\rm rad} = p_\chi - p_{\bar{\chi}} + \frac{2}{3}\rho_{\bar{\chi}} = \frac{8\sqrt{2}\pi}{3} g m^4 (c^5/h^3) e^{\alpha(R)} \left(\frac{b}{1-bw}\right)^{5/2} \times$$

$$\int_0^w \left[\frac{\sinh(1/b)\, e^{-\alpha(R)-w+x}\left(e^{w-x}-1\right)}{\cosh(1/b-\alpha(R)-w+x) - \eta\cosh(1/b)}\right] \left(1+\frac{bx/2}{1-bw}\right)^{3/2} x^{3/2}{\rm d}x$$
$$+ \frac{8\sqrt{2}\pi}{3} g m^4 (c^5/h^3) e^{\alpha(R)} \left(\frac{b}{1-bw}\right)^{3/2} \times$$
$$\int_0^w \frac{\left(e^{w-x}-1\right)}{e^{2/b} - \eta e^{\alpha(R)+w-x}} \left(1+\frac{bx/2}{1-bw}\right)^{1/2} \left(1+\frac{bx}{1-bw}\right)^{2} x^{1/2}{\rm d}x. \tag{H.6}$$

Similar to internal energy, pressure can also be written as $p_\chi + p_{\bar{\chi}}+$ pressure *threshold* of pair production, via

$$p(r) = p_\chi - p_{\bar{\chi}} + \frac{2}{3}\rho_{\bar{\chi}} = p_\chi - p_{\bar{\chi}} + \frac{2}{3}\left(u_{\bar{\chi}} + n_{\bar{\chi}}mc^2\right) = p_\chi - p_{\bar{\chi}} + \frac{2}{3}\left[\frac{p_{\bar{\chi}}}{\gamma_{\bar{\chi}}-1} + n_{\bar{\chi}}mc^2\right]$$

$$= p_\chi + p_{\bar{\chi}} - \frac{2}{3}\left[\frac{3\gamma_{\bar{\chi}}-4}{\gamma_{\bar{\chi}}-1}\right] p_{\bar{\chi}} + \frac{2}{3} n_{\bar{\chi}} mc^2 = p_\chi + p_{\bar{\chi}} + \frac{2}{3}\left[n_{\bar{\chi}}mc^2 - \frac{3\gamma_{\bar{\chi}}-4}{\gamma_{\bar{\chi}}-1} p_{\bar{\chi}}\right]$$

$$= p_\chi + p_{\bar{\chi}} + \frac{2}{3}\left[n_{\bar{\chi}}mc^2 - (3\gamma_{\bar{\chi}}-4)\, u_{\bar{\chi}}\right] = p_\chi + p_{\bar{\chi}} + 2\left[(\gamma_{\bar{\chi}}-1)\, n_{\bar{\chi}}mc^2 - \left(\gamma_{\bar{\chi}} - \frac{4}{3}\right)\rho_{\bar{\chi}}c^2\right].$$

For the antiparticles, if they are: ultrarelativistic, $\gamma_{\bar{\chi}} \to 4/3$, $3p_{\bar{\chi}} \simeq \rho_{\bar{\chi}}c^2 \gg n_{\bar{\chi}}mc^2 \Rightarrow p \simeq p_\chi + p_{\bar{\chi}}$; nonrelativistic, $\gamma_{\bar{\chi}} \to 5/3$, $p_{\bar{\chi}} \ll n_{\bar{\chi}}mc^2 \simeq \rho_{\bar{\chi}}c^2 \Rightarrow p \simeq p_\chi + \frac{2}{3}n_{\bar{\chi}}mc^2$.

H.2 Effective adiabatic index of multi-component fluids

If there are multi-component fluids without mutual interactions in hydrostatic equilibrium in a spherically symmetric spacetime, ${\rm d}s^2 = -e^{2\Phi(r)}c^2{\rm d}t^2 + e^{2\Lambda(r)}{\rm d}r^2 + r^2({\rm d}\theta^2 +$

$\sin^2\theta\ \mathrm{d}\phi^2$), the pressure-averaged adiabatic index is given by

$$\langle\gamma\rangle \equiv \frac{\int e^{3\Phi+\Lambda}\sum_i \gamma_i p_i r^2 \mathrm{d}r}{\int e^{3\Phi+\Lambda}\sum_i p_i r^2 \mathrm{d}r}, \tag{H.7}$$

where $\gamma_i \equiv (\partial \ln p_i/\partial \ln n_i)_s$ for the i-th fluid, and for ideal fluids, $\gamma_i = 1 + p_i/u_i$. The above definition follows closely from the Chandrasekhar's derivation, which means the effective adiabatic index

$$\gamma \equiv \frac{\sum_i \gamma_i p_i}{\sum_i p_i} = \frac{\sum_i n_i\,(\partial p_i/\partial n_i)_s}{\sum_i p_i}. \tag{H.8}$$

For ideal fluids with pair production/annihilation and condensate, the effective adiabatic index

$$\gamma = \frac{\gamma_\chi(p_\chi - p_{\bar\chi}) + \gamma_{\rm rad}p_{\rm rad} + \gamma_{\rm bec}p_{\rm bec}}{(p_\chi - p_{\bar\chi}) + p_{\rm rad} + p_{\rm bec}} = \frac{\left(1 + \frac{p_\chi - p_{\bar\chi}}{u_\chi - u_{\bar\chi}}\right)(p_\chi - p_{\bar\chi}) + \frac{8}{9}\rho_{\bar\chi} + \gamma_{\rm bec}p_{\rm bec}}{(p_\chi - p_{\bar\chi}) + \frac{2}{3}\rho_{\bar\chi} + p_{\rm bec}}, \tag{H.9}$$

where we have used $p_{\rm rad} = \frac{1}{3}u_{\rm rad} = \frac{2}{3}\rho_{\bar\chi}$.

H.3 Characteristic scales

The characteristic size of the self-gravitating thermal system can be determined using the fiducial length of the numerical implementation,

$$\zeta \equiv \lambda_{\rm C}\left(\frac{m_{\rm Pl}}{m}\right)\left(\frac{8\pi^3}{g e^{\alpha(R)}}\right)^{1/2} \quad \text{with} \quad r \equiv \zeta\hat{r}, \tag{H.10}$$

where $g = 2s + 1$ is the spin degeneracy of particles, $m_{\rm Pl} = (\hbar c/G)^{1/2}$ the Planck mass, $\lambda_{\rm C} = \hbar/mc$ the Compton wavelength of the particle, and $\hat{r}$ the dimensionless radius. Using

ζ, we can translate the dimensionful quantities of the system using their corresponding dimensionless counterpart denoted with a "hat," i.e., $n = (c^2/Gm\zeta^2)\hat{n}$, $\rho = (c^2/G\zeta^2)\hat{\rho}$, $u = (c^4/G\zeta^2)\hat{u}$, $p = (c^4/G\zeta^2)\hat{p}$ and $M = (c^2\zeta/G)\hat{M}$.

According to Eq. H.10, the gravitational mass of the bound sphere

$$\begin{aligned} M &= \frac{m_{\rm Pl}^3}{m^2}\left(\frac{8\pi^3}{ge^{\alpha(R)}}\right)^{1/2}\hat{M} \\ &= 2.57\times10^7\ M_\odot\left(\frac{\rm MeV}{mc^2}\right)^2\frac{\hat{M}}{\sqrt{ge^{\alpha(R)}}}. \end{aligned} \tag{H.11}$$

For pure BEC, the effective equation of state, $p_{\rm bec} = (1/3)\,\rho_\lambda c^2\left[(1+\rho_{\rm bec}/\rho_\lambda)^{1/2}-1\right]^2$, where $\rho_\lambda = m/3\lambda\lambda_{\rm C}^3 = \left(8\pi^3/3\lambda\right)\left(c^2/G\zeta^2\right)$ is the fiducial density with $g=1$ and $\alpha(R)=0$. The fiducial length in this situation also depends on the self-coupling strength λ, i.e.,

$$\zeta_\lambda = \sqrt{\frac{c^2}{G\rho_\lambda}} = \sqrt{\frac{3\lambda}{8\pi^3}}\zeta = \lambda_{\rm C}\left(\frac{m_{\rm Pl}}{m}\right)\sqrt{3\lambda}. \tag{H.12}$$

Thus the gravitational mass of the pure condensate

$$\begin{aligned} M &= \frac{c^2\zeta_\lambda}{G}\hat{M} = \sqrt{3\lambda}\ \frac{m_{\rm Pl}^3}{m^2}\hat{M} \\ &= 1.63\times10^6\ M_\odot\left(\frac{\rm MeV}{mc^2}\right)^2\sqrt{3\lambda}\hat{M}, \end{aligned} \tag{H.13}$$

which is valid if $\lambda \gg m^2/m_{\rm Pl}^2$ (Thomas–Fermi regime).

Appendix I

Numerical Results of the Truncated Fermi-Dirac Distribution

In this appendix, we tabulate the numerical results of the truncated Fermi-Dirac (FD) models with and without pair production/annihilation effect, which is significant for $b \gtrsim 0.1$. Generally, given $\alpha(R) < 0$ there is a corresponding (critical) temperature b below which the *degeneracy pressure* is significant such that a marginally stable point exists for FD statistics. In Tables. I.1, I.2, I.3, I.4, I.5, I.6, and I.7, we show marginally stable configurations for $\alpha(R) = -50, -10, -5, -1, 0, 0.5$, and 1, respectively, that satisfy the adiabatic index criterion $\langle\gamma\rangle = \gamma_{\rm cr}$, given different values of the boundary temperature $b = k_B T(R)/mc^2$. From the 2nd to 12th columns, we show their central cutoff function $w(0) = \epsilon_c(0)/k_B T(0)$, gravitational mass $\hat{M}$, system radius $\hat{R}$, compactness $C = GM(R)/c^2 R =$

Table I.1: MB with $\alpha(R) \to -\infty$ (non-degenerate core): Marginally stable points corresponding to different temperature parameters $b = k_B T(R)/mc^2$. For MB distribution, it cannot achieve the GR instability for $b \lesssim 0.1$, as the concentration has to be extremely high (relativistic degenerate gas). More precisely, no unstable configuration exists between $0 \lesssim b \lesssim 0.09$. The results of FD statistics with $\alpha(R) \leq -50$ are indistinguishable from MB statistics for $b \geq 0.09$. The pair production/annihilation effect is significant only if $b \gtrsim 0.1$; while no gravitational bound state exists when $b \gtrsim 0.49$ as $M_{\rm rest} - M \lesssim 0$.

b	$w(0)$	$\hat{M}$	$\hat{R}$	$C = \hat{M}/\hat{R}$	$Z(0)$	$\epsilon_c(0)/mc^2$	$\hat{\rho}(0)$	$\hat{p}(0)$	$v(0)/c$	$v(R)/c$	$\langle\gamma\rangle = \gamma_{\rm cr}$
5.0	6.48150×10^{-2}	2.06015×10^{-1}	2.59700×10^{0}	7.93280×10^{-2}	6.12906×10^{-1}	4.79448×10^{-1}	1.60344×10^{-1}	1.71013×10^{-2}	5.05650×10^{-1}	3.36500×10^{-3}	1.62358
3.0	1.08185×10^{-1}	1.58573×10^{-1}	2.00600×10^{0}	7.90492×10^{-2}	6.13491×10^{-1}	4.80491×10^{-1}	2.71859×10^{-1}	2.89847×10^{-2}	5.65552×10^{-1}	5.01669×10^{-3}	1.62356
2.0	1.62585×10^{-1}	1.28444×10^{-1}	1.63300×10^{0}	7.86552×10^{-2}	6.14252×10^{-1}	4.81854×10^{-1}	4.16754×10^{-1}	4.44142×10^{-2}	5.65434×10^{-1}	8.39347×10^{-4}	1.62354
1.0	3.27070×10^{-1}	8.86277×10^{-2}	1.14300×10^{0}	7.75395×10^{-2}	6.16612×10^{-1}	4.86021×10^{-1}	8.91191×10^{-1}	9.48500×10^{-2}	5.65059×10^{-1}	5.65015×10^{-3}	1.62347
0.5	6.62445×10^{-1}	5.95204×10^{-2}	7.93001×10^{-1}	7.50572×10^{-2}	6.21927×10^{-1}	4.95258×10^{-1}	2.05635×10^{0}	2.18273×10^{-1}	5.64303×10^{-1}	3.66372×10^{-3}	1.62333
0.3	1.12526×10^{0}	4.27849×10^{-2}	5.99001×10^{-1}	7.14271×10^{-2}	6.30406×10^{-1}	5.09562×10^{-1}	4.23693×10^{0}	4.48081×10^{-1}	5.63266×10^{-1}	9.11920×10^{-3}	1.62311
0.2	1.73635×10^{0}	3.14517×10^{-2}	4.77001×10^{-1}	6.59364×10^{-2}	6.44181×10^{-1}	5.21996×10^{-1}	8.65548×10^{0}	9.11403×10^{-1}	5.62044×10^{-1}	7.05363×10^{-2}	1.62278
0.15	2.39865×10^{0}	2.41230×10^{-2}	4.07001×10^{-1}	5.92762×10^{-2}	6.63548×10^{-1}	5.61946×10^{-1}	1.68117×10^{1}	1.76508×10^{0}	5.61211×10^{-1}	9.52828×10^{-3}	1.62239
0.14	2.60081×10^{0}	2.24259×10^{-2}	3.93001×10^{-1}	5.70632×10^{-2}	6.70637×10^{-1}	5.72538×10^{-1}	2.03949×10^{1}	2.14055×10^{0}	5.61128×10^{-1}	1.01614×10^{-2}	1.62225
0.13	2.84350×10^{0}	2.06203×10^{-2}	3.80001×10^{-1}	5.42638×10^{-2}	6.80073×10^{-1}	5.86379×10^{-1}	2.56589×10^{1}	2.69362×10^{0}	5.61190×10^{-1}	8.83738×10^{-3}	1.62209
0.12	3.14240×10^{0}	1.86835×10^{-2}	3.69001×10^{-1}	5.06326×10^{-2}	6.93337×10^{-1}	6.05343×10^{-1}	3.40099×10^{1}	3.57521×10^{0}	5.61577×10^{-1}	5.28167×10^{-3}	1.62188
0.11	3.52490×10^{0}	1.65825×10^{-2}	3.62001×10^{-1}	4.58080×10^{-2}	7.13594×10^{-1}	6.33260×10^{-1}	4.88977×10^{1}	5.16148×10^{0}	5.62734×10^{-1}	6.38807×10^{-3}	1.62159
0.1	4.05150×10^{0}	1.42556×10^{-2}	3.68001×10^{-1}	3.87378×10^{-2}	7.50107×10^{-1}	6.81035×10^{-1}	8.17923×10^{1}	8.74006×10^{0}	5.66189×10^{-1}	8.76561×10^{-3}	1.62117
0.09	5.08620×10^{0}	1.13990×10^{-2}	4.83001×10^{-1}	2.36004×10^{-2}	8.89250×10^{-1}	8.44163×10^{-1}	2.57054×10^{2}	2.96813×10^{1}	5.87872×10^{-1}	5.72277×10^{-3}	1.62023

with pair production/annihilation

b	$w(0)$	$\hat{M}$	$\hat{R}$	$C = \hat{M}/\hat{R}$	$Z(0)$	$\epsilon_c(0)/mc^2$	$\hat{\rho}(0)$	$\hat{p}(0)$	$v(0)/c$	$v(R)$	$\langle\gamma\rangle = \gamma_{\rm cr}$	$\hat{M}_{\rm rest} - \hat{M}$
0.5	5.74700×10^{-1}	6.38546×10^{-2}	9.11001×10^{-1}	7.00928×10^{-2}	5.13186×10^{-1}	4.03186×10^{-1}	1.20516×10^{0}	1.19761×10^{-1}	5.46805×10^{-1}	1.89809×10^{-2}	1.56780	-1.31416×10^{-4}
0.49	5.93850×10^{-1}	6.27608×10^{-2}	8.91001×10^{-1}	7.04386×10^{-2}	5.21631×10^{-1}	4.10402×10^{-1}	1.29191×10^{0}	1.29021×10^{-1}	5.47360×10^{-1}	1.82251×10^{-2}	1.57193	7.73207×10^{-5}
0.48	6.13470×10^{-1}	6.16778×10^{-2}	8.71001×10^{-1}	7.08126×10^{-2}	5.29751×10^{-1}	4.17344×10^{-1}	1.38267×10^{0}	1.38736×10^{-1}	5.48650×10^{-1}	1.74864×10^{-2}	1.57591	2.50896×10^{-4}
0.45	6.75730×10^{-1}	5.84763×10^{-2}	8.16001×10^{-1}	7.16621×10^{-2}	5.52360×10^{-1}	4.36905×10^{-1}	1.68242×10^{0}	1.71017×10^{-1}	5.52220×10^{-1}	1.52699×10^{-2}	1.58697	6.90315×10^{-4}
0.4	7.59200×10^{-1}	5.32861×10^{-2}	7.37001×10^{-1}	7.23013×10^{-2}	5.83600×10^{-1}	4.64700×10^{-1}	2.28321×10^{0}	2.36114×10^{-1}	5.56992×10^{-1}	1.15930×10^{-2}	1.60207	1.17611×10^{-3}
0.3	1.11485×10^{0}	4.30373×10^{-2}	6.04001×10^{-1}	7.12537×10^{-2}	6.22366×10^{-1}	5.02460×10^{-1}	4.07942×10^{0}	4.29395×10^{-1}	5.61940×10^{-1}	5.15468×10^{-3}	1.61903	1.42876×10^{-3}
0.2	1.73380×10^{0}	3.14591×10^{-2}	4.77001×10^{-1}	6.59519×10^{-2}	6.43899×10^{-1}	5.31727×10^{-1}	8.64353×10^{0}	9.10013×10^{-1}	5.62003×10^{-1}	1.25884×10^{-2}	1.62264	1.11842×10^{-3}
0.15	2.39860×10^{0}	2.41235×10^{-2}	4.07001×10^{-1}	5.92713×10^{-2}	6.63529×10^{-1}	5.61927×10^{-1}	1.68101×10^{1}	1.76480×10^{0}	5.61207×10^{-1}	9.73977×10^{-3}	1.62238	8.54384×10^{-4}
0.14	2.60081×10^{0}	2.24259×10^{-2}	3.93001×10^{-1}	5.70631×10^{-2}	6.70637×10^{-1}	5.72538×10^{-1}	2.03949×10^{1}	2.14056×10^{0}	5.61129×10^{-1}	1.02232×10^{-2}	1.62225	7.92345×10^{-4}
0.13	2.84350×10^{0}	2.06203×10^{-2}	3.80001×10^{-1}	5.42638×10^{-2}	6.80073×10^{-1}	5.86379×10^{-1}	2.56589×10^{1}	2.69362×10^{0}	5.61190×10^{-1}	8.86114×10^{-3}	1.62209	7.26980×10^{-4}
0.12	3.14240×10^{0}	1.86835×10^{-2}	3.69001×10^{-1}	5.06326×10^{-2}	6.93337×10^{-1}	6.05343×10^{-1}	3.40099×10^{1}	3.57522×10^{0}	5.61577×10^{-1}	5.29271×10^{-3}	1.62188	6.54548×10^{-4}
0.11	3.52490×10^{0}	1.65825×10^{-2}	3.62001×10^{-1}	4.58080×10^{-2}	7.13594×10^{-1}	6.33260×10^{-1}	4.88977×10^{1}	5.16148×10^{0}	5.62734×10^{-1}	6.39008×10^{-3}	1.62159	5.76084×10^{-4}
0.1	4.05150×10^{0}	1.42556×10^{-2}	3.68001×10^{-1}	3.87378×10^{-2}	7.50107×10^{-1}	6.81035×10^{-1}	8.17923×10^{1}	8.74006×10^{0}	5.66189×10^{-1}	8.76585×10^{-3}	1.62117	4.86859×10^{-4}

$\hat{M}/\hat{R}$, central interior redshift $Z(0) = e^{-\Phi(0)} - 1$, central energy cut off $\epsilon_c(0)$, central energy density $\hat{\rho}(0)$, central pressure $\hat{p}(0)$, central velocity dispersion $v(0)$, boundary velocity dispersion $v(R)$, and $\langle\gamma\rangle = \gamma_{\rm cr}$.

When pair production/annihilation is taken into account, we add the 13th column for the binding energy $\hat{M}_{\rm rest} - \hat{M}$ to examine if the gravitational bound state exists. Although this can still make the system unstable, it becomes gravitationally unbound $\hat{M} - \hat{M}_{\rm rest} \gtrsim 0$ when $b \gtrsim 0.4$–0.5 (depending on $\alpha(R)$). In the classical Maxwell-Boltzmann (MB) limit, the threshold is $b \gtrsim 0.49$, and it decreases as $\alpha(R)$ increases. For completely degenerate case $\alpha(R) = 0, 0.5,$ and 1, the threshold decreases down to $b \gtrsim 0.4, 0.38,$ and 0.36, respectively. This is because the Pauli blocking takes energy to bind fermions together. Thus slightly lower temperature is sufficient to break them apart.

Table I.2: FD with $\alpha(R) = -10$ (partially degenerate core when $b \lesssim 0.014$): Marginally stable points corresponding to different temperature parameters $b = k_B T(R)/mc^2$. No marginal stable point exists between $0.014 \lesssim b \lesssim 0.09$. The pair production/annihilation effect is significant only if $b \gtrsim 0.1$; while no gravitational bound state exists when $b \gtrsim 0.49$ as $M_{\rm rest} - M \lesssim 0$.

b	$w(0)$	$\tilde{M}$	$\tilde{R}$	$C = \tilde{M}/\tilde{R}$	$Z(0)$	$\epsilon_*(0)/mc^2$	$\tilde{p}(0)$	$\tilde{p}(0)$	$v(0)/c$	$v(\tilde{R})$	$\langle\gamma\rangle = \gamma_{\rm cs}$
5.0	6.48150×10^{-2}	2.06020×10^{-1}	2.59700×10^{0}	7.93298×10^{-2}	6.12906×10^{-1}	4.79447×10^{-1}	1.66337×10^{-1}	1.71005×10^{-2}	5.65651×10^{-1}	3.62915×10^{-3}	1.62358
3.0	1.08185×10^{-1}	1.58577×10^{-1}	2.60040×10^{0}	7.90511×10^{-2}	6.13491×10^{-1}	4.80490×10^{-1}	2.71846×10^{-1}	2.89833×10^{-2}	5.65552×10^{-1}	5.19761×10^{-3}	1.62356
2.0	1.62585×10^{-1}	1.28447×10^{-1}	1.63300×10^{0}	7.86571×10^{-2}	6.14253×10^{-1}	4.81853×10^{-1}	4.16733×10^{-1}	4.44120×10^{-2}	5.65434×10^{-1}	1.59714×10^{-3}	1.62354
1.0	3.27070×10^{-1}	8.86301×10^{-2}	1.14300×10^{0}	7.75416×10^{-2}	6.16613×10^{-1}	4.86020×10^{-1}	8.91143×10^{-1}	9.48450×10^{-2}	5.65059×10^{-1}	5.81049×10^{-3}	1.62347
0.5	6.62440×10^{-1}	5.95226×10^{-2}	7.93001×10^{-1}	7.50600×10^{-2}	6.21922×10^{-1}	4.95251×10^{-1}	2.05615×10^{0}	2.18251×10^{-1}	5.64302×10^{-1}	3.96902×10^{-2}	1.62333
0.3	1.12526×10^{0}	4.27867×10^{-2}	5.09001×10^{-1}	7.14300×10^{-2}	6.30409×10^{-1}	5.09561×10^{-1}	4.23656×10^{0}	4.48646×10^{-1}	5.63268×10^{-1}	9.20451×10^{-3}	1.62311
0.2	1.73630×10^{0}	3.14543×10^{-2}	4.77001×10^{-1}	6.59418×10^{-2}	6.44161×10^{-1}	5.31971×10^{-1}	8.65321×10^{0}	9.11156×10^{-1}	5.62042×10^{-1}	7.22504×10^{-3}	1.62278
0.15	2.39855×10^{0}	2.41259×10^{-2}	4.07001×10^{-1}	5.92774×10^{-2}	6.63521×10^{-1}	5.61909×10^{-1}	1.68047×10^{1}	1.76427×10^{0}	5.61213×10^{-1}	9.57081×10^{-3}	1.62239
0.14	2.60070×10^{0}	2.24288×10^{-2}	3.93001×10^{-1}	5.70707×10^{-2}	6.70611×10^{-1}	5.72501×10^{-1}	2.03854×10^{1}	2.13959×10^{0}	5.61133×10^{-1}	1.01503×10^{-2}	1.62226
0.13	2.84330×10^{0}	2.06239×10^{-2}	3.80001×10^{-1}	5.42732×10^{-2}	6.80023×10^{-1}	5.86315×10^{-1}	2.56416×10^{1}	2.69183×10^{0}	5.61193×10^{-1}	8.77667×10^{-3}	1.62209
0.12	3.14215×10^{0}	1.86872×10^{-2}	3.69001×10^{-1}	5.06427×10^{-2}	6.93282×10^{-1}	6.05269×10^{-1}	3.39819×10^{1}	3.57239×10^{0}	5.61586×10^{-1}	4.92349×10^{-3}	1.62188
0.11	3.52430×10^{0}	1.65879×10^{-2}	3.62001×10^{-1}	4.58227×10^{-2}	7.13454×10^{-1}	6.33090×10^{-1}	4.88239×10^{1}	5.15369×10^{0}	5.62735×10^{-1}	5.71357×10^{-3}	1.62159
0.1	4.05000×10^{0}	1.42556×10^{-2}	3.68001×10^{-1}	3.87591×10^{-2}	7.49753×10^{-1}	6.80629×10^{-1}	8.15368×10^{1}	8.71221×10^{0}	5.66172×10^{-1}	7.35478×10^{-3}	1.62117
0.09	5.06130×10^{0}	1.14308×10^{-2}	4.76001×10^{-1}	2.40141×10^{-2}	8.82317×10^{-1}	8.36583×10^{-1}	2.48175×10^{2}	2.84782×10^{1}	5.86729×10^{-1}	4.63031×10^{-3}	1.62027
0.08	—	—	—	—	—	—	—	—	—	—	—
0.05	—	—	—	—	—	—	—	—	—	—	—
0.014	2.60950×10^{3}	2.47115×10^{-3}	5.18000×10^{-2}	4.77055×10^{-3}	5.83182×10^{-1}	5.75618×10^{-1}	8.73487×10^{3}	9.65477×10^{2}	5.75842×10^{-1}	1.94373×10^{-3}	1.62470
0.013	2.75480×10^{3}	2.43927×10^{-3}	1.77000×10^{-2}	1.37812×10^{-2}	5.79839×10^{-1}	5.75927×10^{-1}	8.73394×10^{4}	9.63790×10^{3}	5.75369×10^{-1}	2.85818×10^{-3}	1.62480
0.012	2.92505×10^{3}	2.41484×10^{-3}	1.05000×10^{-2}	2.29984×10^{-2}	5.77219×10^{-1}	5.40731×10^{-1}	8.74315×10^{4}	9.63809×10^{3}	5.75072×10^{-1}	1.34216×10^{-2}	1.62489
0.011	3.12650×10^{3}	2.39448×10^{-3}	7.50001×10^{-3}	3.19264×10^{-2}	5.75073×10^{-1}	5.24112×10^{-1}	8.75621×10^{4}	9.64569×10^{3}	5.74869×10^{-1}	1.14238×10^{-2}	1.62497
10^{-2}	3.36825×10^{3}	2.37725×10^{-3}	5.80001×10^{-3}	4.09870×10^{-2}	5.73283×10^{-1}	5.07737×10^{-1}	8.77049×10^{4}	9.65653×10^{3}	5.74725×10^{-1}	1.63995×10^{-2}	1.62504
10^{-3}	2.72040×10^{2}	2.31026×10^{-4}	1.90001×10^{-3}	1.21592×10^{-1}	5.66625×10^{-1}	3.70760×10^{-1}	8.85156×10^{4}	9.73440×10^{3}	5.74388×10^{-1}	5.49270×10^{-2}	1.62534
10^{-4}	2.65480×10^{3}	2.30790×10^{-4}	1.80001×10^{-3}	1.28216×10^{-1}	5.66484×10^{-1}	3.58606×10^{-1}	8.85619×10^{4}	9.74112×10^{3}	5.74436×10^{-1}	9.06083×10^{-2}	1.62533
10^{-5}	2.64762×10^{4}	2.30707×10^{-4}	1.80001×10^{-3}	1.28170×10^{-1}	5.66413×10^{-1}	3.57643×10^{-1}	8.85773×10^{4}	9.74346×10^{3}	5.74455×10^{-1}	8.99450×10^{-2}	1.62532

with pair production/annihilation

b	$w(0)$	$\tilde{M}$	$\tilde{R}$	$C = \tilde{M}/\tilde{R}$	$Z(0)$	$\epsilon_*(0)/mc^2$	$\tilde{p}(0)$	$\tilde{p}(0)$	$v(0)/c$	$v(\tilde{R})/c$	$\langle\gamma\rangle = \gamma_{\rm cs}$	$\tilde{M}_{\rm rest} - \tilde{M}$
0.5	5.74700×10^{-1}	6.38565×10^{-2}	9.11001×10^{-1}	7.00949×10^{-2}	5.13187×10^{-1}	4.03186×10^{-1}	1.20508×10^{0}	1.19755×10^{-1}	5.46807×10^{-1}	1.89818×10^{-1}	1.56780	-1.10551×10^{-4}
0.49	5.93820×10^{-1}	6.27645×10^{-2}	8.91001×10^{-1}	7.04427×10^{-2}	5.21598×10^{-1}	4.10371×10^{-1}	1.23159×10^{0}	1.26983×10^{-1}	5.47349×10^{-1}	1.82269×10^{-1}	1.57192	7.73989×10^{-5}
0.48	6.13470×10^{-1}	6.16797×10^{-2}	8.71001×10^{-1}	7.08147×10^{-2}	5.29752×10^{-1}	4.17343×10^{-1}	1.38259×10^{0}	1.38728×10^{-1}	5.48652×10^{-1}	1.74873×10^{-1}	1.57591	2.50793×10^{-4}
0.45	6.75730×10^{-1}	5.84782×10^{-2}	8.16001×10^{-1}	7.16643×10^{-2}	5.52361×10^{-1}	4.36904×10^{-1}	1.68231×10^{0}	1.71007×10^{-1}	5.52222×10^{-1}	1.52618×10^{-1}	1.58697	6.90254×10^{-4}
0.4	7.59200×10^{-1}	5.32879×10^{-2}	7.37001×10^{-1}	7.23037×10^{-2}	5.83602×10^{-1}	4.64699×10^{-1}	2.28304×10^{0}	2.36099×10^{-1}	5.56994×10^{-1}	1.15940×10^{-1}	1.60267	1.17611×10^{-3}
0.3	1.11485×10^{0}	4.30390×10^{-2}	6.04001×10^{-1}	7.12566×10^{-2}	6.22369×10^{-1}	5.02459×10^{-1}	4.07906×10^{0}	4.29362×10^{-1}	5.61943×10^{-1}	5.15631×10^{-2}	1.61903	1.42880×10^{-3}
0.2	1.73375×10^{0}	3.14617×10^{-2}	4.77001×10^{-1}	6.59572×10^{-2}	6.43879×10^{-1}	5.31702×10^{-1}	8.64126×10^{0}	9.09766×10^{-1}	5.62001×10^{-1}	1.26956×10^{-2}	1.62264	1.11852×10^{-3}
0.15	2.39850×10^{0}	2.41364×10^{-2}	4.07001×10^{-1}	5.92785×10^{-2}	6.63502×10^{-1}	5.61890×10^{-1}	1.68030×10^{1}	1.76406×10^{0}	5.61209×10^{-1}	9.78142×10^{-3}	1.62238	8.54495×10^{-4}
0.14	2.60060×10^{0}	2.24297×10^{-2}	3.93001×10^{-1}	5.70728×10^{-2}	6.70576×10^{-1}	5.72465×10^{-1}	2.03815×10^{1}	2.13910×10^{0}	5.61544×10^{-1}	1.02744×10^{-2}	1.62225	7.92500×10^{-4}
0.13	2.84330×10^{0}	2.06239×10^{-2}	3.80001×10^{-1}	5.42731×10^{-2}	6.80023×10^{-1}	5.86315×10^{-1}	2.56416×10^{1}	2.69183×10^{0}	5.61193×10^{-1}	8.80059×10^{-3}	1.62209	7.26218×10^{-4}
0.12	3.14210×10^{0}	1.86875×10^{-2}	3.69001×10^{-1}	5.06436×10^{-2}	6.93267×10^{-1}	6.05253×10^{-1}	3.39790×10^{1}	3.57303×10^{0}	5.61582×10^{-1}	4.96071×10^{-3}	1.62188	6.54706×10^{-4}
0.11	3.52430×10^{0}	1.65879×10^{-2}	3.62001×10^{-1}	4.58227×10^{-2}	7.13454×10^{-1}	6.33090×10^{-1}	4.88239×10^{1}	5.15369×10^{0}	5.62735×10^{-1}	5.71582×10^{-3}	1.62159	5.76300×10^{-4}
0.1	4.05005×10^{0}	1.42632×10^{-2}	3.68001×10^{-1}	3.87585×10^{-2}	7.49766×10^{-1}	6.80643×10^{-1}	8.15429×10^{1}	8.71297×10^{0}	5.66175×10^{-1}	7.37119×10^{-3}	1.62117	4.87194×10^{-4}

Table I.3: FD with $\alpha(R) = -5$ (partially degenerate core when $b \lesssim 0.08$): Marginally stable points corresponding to different temperature parameters $b = k_B T(R)/mc^2$. The instability is independent of b. The pair production/annihilation effect is significant only if $b \gtrsim 0.1$; while no gravitational bound state exists when $b \gtrsim 0.49$ as $M_{\rm rest} - M \lesssim 0$.

b	$w(0)$	$\tilde{M}$	$\tilde{R}$	$C = \tilde{M}/\tilde{R}$	$Z(0)$	$\epsilon_*(0)/mc^2$	$\tilde{p}(0)$	$\tilde{p}(0)$	$v(0)/c$	$v(R)/c$	$\langle\gamma\rangle = \gamma_{\rm cs}$
5.0	6.48140×10^{-2}	2.06732×10^{-1}	2.60600×10^{0}	7.93293×10^{-2}	6.12906×10^{-1}	4.79440×10^{-1}	1.59225×10^{-1}	1.69823×10^{-2}	5.65657×10^{-1}	2.49564×10^{-3}	1.62358
3.0	1.08180×10^{-1}	1.59140×10^{-1}	2.01300×10^{0}	7.90562×10^{-2}	6.13475×10^{-1}	4.80460×10^{-1}	2.69885×10^{-1}	2.87747×10^{-2}	5.65557×10^{-1}	4.66725×10^{-3}	1.62356
2.0	1.62570×10^{-1}	1.28920×10^{-1}	1.63800×10^{0}	7.87056×10^{-2}	6.14210×10^{-1}	4.81768×10^{-1}	4.13567×10^{-1}	4.40748×10^{-2}	5.65435×10^{-1}	6.03557×10^{-3}	1.62354
1.0	3.27010×10^{-1}	8.89895×10^{-2}	1.14700×10^{0}	7.75845×10^{-2}	6.16534×10^{-1}	4.85882×10^{-1}	8.83448×10^{-1}	9.40293×10^{-2}	5.65069×10^{-1}	6.55257×10^{-3}	1.62347
0.5	6.62150×10^{-1}	5.98192×10^{-2}	7.96001×10^{-1}	7.51496×10^{-2}	6.21728×10^{-1}	4.94923×10^{-1}	2.03283×10^{0}	2.15800×10^{-1}	5.64334×10^{-1}	4.76202×10^{-3}	1.62333
0.3	1.12412×10^{0}	4.30752×10^{-2}	6.02001×10^{-1}	7.15534×10^{-2}	6.29916×10^{-1}	5.08818×10^{-1}	4.16478×10^{0}	4.40566×10^{-1}	5.63339×10^{-1}	4.99364×10^{-3}	1.62312
0.2	1.73222×10^{0}	3.17787×10^{-2}	4.79001×10^{-1}	6.63436×10^{-2}	6.42888×10^{-1}	5.30065×10^{-1}	8.39869×10^{0}	8.84912×10^{-1}	5.62218×10^{-1}	6.48972×10^{-3}	1.62281
0.15	2.38570×10^{0}	2.45354×10^{-2}	4.08001×10^{-1}	6.01358×10^{-2}	6.60194×10^{-1}	5.57237×10^{-1}	1.58716×10^{1}	1.66837×10^{0}	5.61560×10^{-1}	8.15146×10^{-3}	1.62245
0.14	2.58305×10^{0}	2.28743×10^{-2}	3.93001×10^{-1}	5.82041×10^{-2}	6.66221×10^{-1}	5.66395×10^{-1}	1.90079×10^{1}	1.99796×10^{0}	5.61548×10^{-1}	1.15083×10^{-2}	1.62234
0.13	2.81771×10^{0}	2.11203×10^{-2}	3.79001×10^{-1}	5.57262×10^{-2}	6.73895×10^{-1}	5.77974×10^{-1}	2.34430×10^{1}	2.46531×10^{0}	5.61681×10^{-1}	9.85743×10^{-3}	1.62220
0.12	3.10200×10^{0}	1.92611×10^{-2}	3.66001×10^{-1}	5.26259×10^{-2}	6.83976×10^{-1}	5.62103×10^{-1}	3.00599×10^{1}	3.16591×10^{0}	5.67382×10^{-1}	6.30871×10^{-3}	1.62358
0.11	3.45460×10^{0}	1.72843×10^{-2}	3.54001×10^{-1}	4.88255×10^{-2}	6.97738×10^{-1}	6.12842×10^{-1}	4.06396×10^{1}	4.29571×10^{0}	5.63123×10^{-1}	1.03703×10^{-2}	1.62182
0.1	3.90455×10^{0}	1.51841×10^{-2}	3.47001×10^{-1}	4.37581×10^{-2}	7.17285×10^{-1}	6.40510×10^{-1}	5.91033×10^{1}	6.29776×10^{0}	5.65390×10^{-1}	8.80445×10^{-3}	1.62155
0.09	4.49800×10^{0}	1.29781×10^{-2}	3.50001×10^{-1}	3.70802×10^{-2}	7.46112×10^{-1}	6.80146×10^{-1}	9.49222×10^{1}	1.02939×10^{1}	5.70384×10^{-1}	4.80109×10^{-3}	1.62124
0.08	5.29500×10^{0}	1.07669×10^{-2}	3.74001×10^{-1}	2.87884×10^{-2}	7.87032×10^{-1}	7.34871×10^{-1}	1.69995×10^{2}	1.91071×10^{1}	5.80683×10^{-1}	6.39985×10^{-3}	1.62092
0.05	8.47930×10^{0}	5.68169×10^{-3}	3.95001×10^{-1}	1.43840×10^{-2}	7.61525×10^{-1}	7.36004×10^{-1}	5.22206×10^{2}	6.23475×10^{1}	5.98479×10^{-1}	8.27190×10^{-4}	1.62164
10^{-2}	3.00295×10^{1}	2.87811×10^{-3}	3.3001×10^{-2}	8.72129×10^{-2}	5.71331×10^{-1}	4.28740×10^{-1}	5.90467×10^{2}	6.49386×10^{1}	5.74400×10^{-1}	2.93362×10^{-2}	1.62511
10^{-3}	2.68270×10^{2}	2.81430×10^{-3}	2.3001×10^{-2}	1.22355×10^{-1}	5.66349×10^{-1}	3.65189×10^{-1}	5.95686×10^{2}	6.54783×10^{1}	5.74250×10^{-1}	4.96081×10^{-2}	1.62534
10^{-4}	2.65000×10^{3}	2.81169×10^{-3}	2.2001×10^{-2}	1.27798×10^{-1}	5.66258×10^{-1}	3.58108×10^{-1}	5.96047×10^{2}	6.55313×10^{1}	5.74308×10^{-1}	8.67470×10^{-2}	1.62533
10^{-5}	2.64620×10^{4}	2.81155×10^{-3}	2.2001×10^{-2}	1.27792×10^{-1}	5.66215×10^{-1}	3.57587×10^{-1}	5.95992×10^{2}	6.55228×10^{1}	5.74297×10^{-1}	8.63942×10^{-2}	1.62533

with pair production/annihilation

b	$w(0)$	$\tilde{M}$	$\tilde{R}$	$C = \tilde{M}/\tilde{R}$	$Z(0)$	$\epsilon_*(0)/mc^2$	$\tilde{p}(0)$	$\tilde{p}(0)$	$v(0)/c$	$v(R)/c$	$\langle\gamma\rangle = \gamma_{\rm cs}$	$\tilde{M}_{\rm rest} - \tilde{M}$
0.5	5.73800×10^{-1}	6.41894×10^{-2}	9.16001×10^{-1}	7.00757×10^{-2}	5.12249×10^{-1}	4.02314×10^{-1}	1.18726×10^{0}	1.17952×10^{-1}	5.45934×10^{-1}	1.90355×10^{-1}	1.56739	-1.30531×10^{-4}
0.49	5.92940×10^{-1}	6.30935×10^{-2}	8.95001×10^{-1}	7.04955×10^{-2}	5.20705×10^{-1}	4.09497×10^{-1}	1.27269×10^{0}	1.27066×10^{-1}	5.47284×10^{-1}	1.82949×10^{-1}	1.57154	5.99049×10^{-5}
0.48	6.12610×10^{-1}	6.20047×10^{-2}	8.75001×10^{-1}	7.08625×10^{-2}	5.28904×10^{-1}	4.16504×10^{-1}	1.36257×10^{0}	1.36692×10^{-1}	5.48596×10^{-1}	1.75498×10^{-1}	1.57556	2.36010×10^{-4}
0.45	6.74900×10^{-1}	5.87934×10^{-2}	8.20001×10^{-1}	7.16991×10^{-2}	5.51616×10^{-1}	4.36140×10^{-1}	1.65928×10^{0}	1.69540×10^{-1}	5.52184×10^{-1}	1.53071×10^{-1}	1.58669	6.82149×10^{-4}
0.4	7.59400×10^{-1}	5.35885×10^{-2}	7.40001×10^{-1}	7.24168×10^{-2}	5.83019×10^{-1}	4.63998×10^{-1}	2.25041×10^{0}	2.33727×10^{-1}	5.56998×10^{-1}	1.16435×10^{-1}	1.60190	1.17632×10^{-3}
0.3	1.11365×10^{0}	4.33292×10^{-2}	6.07001×10^{-1}	7.13825×10^{-2}	6.21825×10^{-1}	5.01677×10^{-1}	4.00936×10^{0}	4.22125×10^{-1}	5.62010×10^{-1}	5.12401×10^{-2}	1.61901	1.43750×10^{-3}
0.2	1.73163×10^{0}	3.17866×10^{-2}	4.79001×10^{-1}	6.63603×10^{-2}	6.42586×10^{-1}	5.29776×10^{-1}	8.38628×10^{0}	8.83456×10^{-1}	5.62171×10^{-1}	1.23751×10^{-2}	1.62266	1.13046×10^{-3}
0.15	2.38570×10^{0}	2.45354×10^{-2}	4.08001×10^{-1}	6.01357×10^{-2}	6.60194×10^{-1}	5.57237×10^{-1}	1.58716×10^{1}	1.66838×10^{0}	5.61562×10^{-1}	8.35089×10^{-3}	1.62245	8.69873×10^{-4}
0.14	2.58300×10^{0}	2.28747×10^{-2}	3.93001×10^{-1}	5.82052×10^{-2}	6.66203×10^{-1}	5.66377×10^{-1}	1.90061×10^{1}	1.99773×10^{0}	5.61544×10^{-1}	1.15942×10^{-2}	1.62233	8.09350×10^{-4}
0.13	2.81770×10^{0}	2.11204×10^{-2}	3.79001×10^{-1}	5.57264×10^{-2}	6.73892×10^{-1}	5.77971×10^{-1}	2.34426×10^{1}	2.46526×10^{0}	5.61680×10^{-1}	9.88443×10^{-3}	1.62220	7.45214×10^{-4}
0.12	3.10200×10^{0}	1.92611×10^{-2}	3.66001×10^{-1}	5.26259×10^{-2}	6.83976×10^{-1}	5.92938×10^{-1}	3.00599×10^{1}	3.16591×10^{0}	5.62103×10^{-1}	6.31803×10^{-3}	1.62203	6.77000×10^{-4}
0.11	3.45460×10^{0}	1.72843×10^{-2}	3.54001×10^{-1}	4.88255×10^{-2}	6.97738×10^{-1}	6.12842×10^{-1}	4.06396×10^{1}	4.29571×10^{0}	5.63123×10^{-1}	1.03716×10^{-2}	1.62182	6.04079×10^{-4}
0.1	3.90455×10^{0}	1.51841×10^{-2}	3.47001×10^{-1}	4.37581×10^{-2}	7.17285×10^{-1}	6.40510×10^{-1}	5.91033×10^{1}	6.29776×10^{0}	5.65390×10^{-1}	8.80469×10^{-3}	1.62155	5.25946×10^{-4}

Table I.4: FD with $\alpha(R) = -1$ (partially degenerate core when $b \lesssim 0.3$): Marginally stable points corresponding to different temperature parameters $b = k_B T(R)/mc^2$. The instability is independent of b. The pair production/annihilation effect is significant only if $b \gtrsim 0.1$; while no gravitational bound state exists when $b \gtrsim 0.45$ as $M_{\rm rest} - M \lesssim 0$.

b	$w(0)$	M	R	$C = M/R$	$Z(0)$	$\epsilon_*(0)/mc^2$	$\hat{p}(0)$	$\hat{p}(0)$	$v(0)/c$	$v(R)/c$	$\langle\gamma\rangle = \gamma_{\rm ce}$
5.0	6.47360×10^{-2}	2.42184×10^{-1}	3.04400×10^{0}	7.95612×10^{-2}	6.12415×10^{-1}	4.76585×10^{-1}	1.15599×10^{-1}	1.23323×10^{-2}	5.65724×10^{-1}	3.00356×10^{-3}	1.62359
3.0	1.07963×10^{-1}	1.87069×10^{-1}	2.35500×10^{0}	7.94347×10^{-2}	6.12668×10^{-1}	4.79041×10^{-1}	1.94126×10^{-1}	2.07066×10^{-2}	5.65684×10^{-1}	3.24415×10^{-3}	1.62358
2.0	1.62070×10^{-1}	1.52214×10^{-1}	1.92000×10^{0}	7.92780×10^{-2}	6.12965×10^{-1}	4.79590×10^{-1}	2.93887×10^{-1}	3.13420×10^{-2}	5.65632×10^{-1}	3.37873×10^{-3}	1.62357
1.0	3.24880×10^{-1}	1.06550×10^{-1}	1.35100×10^{0}	7.88676×10^{-2}	6.13870×10^{-1}	4.81189×10^{-1}	6.03788×10^{-1}	6.43667×10^{-2}	5.65521×10^{-1}	7.20175×10^{-3}	1.62355
0.5	6.52250×10^{-1}	7.39634×10^{-2}	9.48801×10^{-1}	7.80204×10^{-2}	6.15322×10^{-1}	4.83954×10^{-1}	1.20653×10^{0}	1.34949×10^{-1}	5.65375×10^{-1}	1.18484×10^{-2}	1.62351
0.3	1.09082×10^{0}	5.61277×10^{-2}	7.26001×10^{-1}	7.73107×10^{-2}	6.16473×10^{-1}	4.86372×10^{-1}	2.21714×10^{0}	2.36252×10^{-1}	5.65395×10^{-1}	9.89832×10^{-3}	1.62347
0.2	1.63855×10^{0}	4.50009×10^{-2}	5.86001×10^{-1}	7.67932×10^{-2}	6.16588×10^{-1}	4.87394×10^{-1}	3.44629×10^{0}	3.67762×10^{-1}	5.65807×10^{-1}	1.01965×10^{-2}	1.62347
0.15	2.18075×10^{0}	3.80021×10^{-2}	5.03001×10^{-1}	7.87436×10^{-2}	6.15194×10^{-1}	4.86114×10^{-1}	4.62583×10^{0}	4.94868×10^{-1}	5.66514×10^{-1}	5.65521×10^{-2}	1.62351
0.14	2.33410×10^{0}	3.72481×10^{-2}	4.84001×10^{-1}	7.69588×10^{-2}	6.14570×10^{-1}	4.85301×10^{-1}	4.94221×10^{0}	5.29158×10^{-1}	5.66751×10^{-1}	1.22325×10^{-2}	1.62353
0.13	2.51005×10^{0}	3.58709×10^{-2}	4.66001×10^{-1}	7.69760×10^{-2}	6.13756×10^{-1}	4.84352×10^{-1}	5.29203×10^{0}	5.67283×10^{-1}	5.67038×10^{-1}	2.12217×10^{-3}	1.62355
0.12	2.71390×10^{0}	3.44727×10^{-2}	4.46001×10^{-1}	7.72929×10^{-2}	6.12694×10^{-1}	4.82905×10^{-1}	5.68106×10^{0}	6.09621×10^{-1}	5.67382×10^{-1}	8.82191×10^{-3}	1.62358
0.11	2.95270×10^{0}	3.30576×10^{-2}	4.26001×10^{-1}	7.75998×10^{-2}	6.11298×10^{-1}	4.81022×10^{-1}	6.10855×10^{0}	6.56424×10^{-1}	5.67785×10^{-1}	5.00084×10^{-3}	1.62362
0.1	3.23630×10^{0}	3.16303×10^{-2}	4.05001×10^{-1}	7.80994×10^{-2}	6.09503×10^{-1}	4.78477×10^{-1}	6.57701×10^{0}	7.07950×10^{-1}	5.68261×10^{-1}	2.73960×10^{-3}	1.62367
0.09	3.57870×10^{0}	3.01981×10^{-2}	3.83001×10^{-1}	7.88460×10^{-2}	6.07229×10^{-1}	4.75096×10^{-1}	7.08595×10^{0}	7.64245×10^{-1}	5.68824×10^{-1}	4.49398×10^{-3}	1.62374
0.08	4.00040×10^{0}	2.87721×10^{-2}	3.60001×10^{-1}	7.99223×10^{-2}	6.04347×10^{-1}	4.70621×10^{-1}	7.63014×10^{0}	8.24800×10^{-1}	5.69467×10^{-1}	8.11910×10^{-3}	1.62383
0.05	6.18610×10^{0}	2.47018×10^{-2}	2.87001×10^{-1}	8.60687×10^{-2}	5.91211×10^{-1}	4.47810×10^{-1}	9.34675×10^{0}	1.01863×10^{0}	5.71791×10^{-1}	3.66863×10^{-3}	1.62427
10^{-2}	2.76760×10^{1}	2.11695×10^{-2}	1.88001×10^{-1}	1.11752×10^{-1}	5.67938×10^{-1}	3.82386×10^{-1}	1.08281×10^{1}	1.18911×10^{0}	5.73978×10^{-1}	2.50725×10^{-2}	1.62524
10^{-3}	2.65650×10^{2}	2.07922×10^{-2}	1.70001×10^{-1}	1.22306×10^{-1}	5.65813×10^{-1}	3.61522×10^{-1}	1.08849×10^{1}	1.19536×10^{0}	5.73982×10^{-1}	2.29994×10^{-2}	1.62534
10^{-4}	2.64470×10^{3}	2.07897×10^{-2}	1.68001×10^{-1}	1.23748×10^{-1}	5.65793×10^{-1}	3.59224×10^{-1}	1.08856×10^{1}	1.19545×10^{0}	5.73984×10^{-1}	3.09253×10^{-2}	1.62534
10^{-5}	2.64340×10^{4}	2.07890×10^{-2}	1.68001×10^{-1}	1.23743×10^{-1}	5.65788×10^{-1}	3.59048×10^{-1}	1.08859×10^{1}	1.19549×10^{0}	5.73986×10^{-1}	2.99647×10^{-2}	1.62534

with pair production/annihilation

b	$w(0)$	M	R	$C = M/R$	$Z(0)$	$\epsilon_*(0)/mc^2$	$\hat{p}(0)$	$\hat{p}(0)$	$v(0)/c$	$v(R)/c$	$\langle\gamma\rangle = \gamma_{\rm ce}$	$M_{\rm rest} - M$
0.5	5.30430×10^{-1}	8.04343×10^{-2}	1.16400×10^{0}	6.91016×10^{-2}	4.05998×10^{-1}	3.60939×10^{-1}	6.06069×10^{-1}	5.9186×10^{-2}	5.41264×10^{-1}	2.20388×10^{-1}	1.54624	-1.44481×10^{-3}
0.49	5.51020×10^{-1}	7.91081×10^{-2}	1.13200×10^{0}	6.98835×10^{-2}	4.76952×10^{-1}	3.69860×10^{-1}	6.58229×10^{-1}	6.4705×10^{-2}	5.43052×10^{-1}	2.11825×10^{-1}	1.55171	-1.09617×10^{-3}
0.48	5.72050×10^{-1}	7.77960×10^{-2}	1.10100×10^{0}	7.06594×10^{-2}	4.87350×10^{-1}	3.78497×10^{-1}	7.12946×10^{-1}	7.00305×10^{-2}	5.44780×10^{-1}	2.03352×10^{-1}	1.55703	-7.70918×10^{-4}
0.45	6.38070×10^{-1}	7.39481×10^{-2}	1.01900×10^{0}	7.25692×10^{-2}	5.17079×10^{-1}	4.02751×10^{-1}	8.92377×10^{-1}	8.98466×10^{-2}	5.49588×10^{-1}	1.77631×10^{-1}	1.57196	6.93902×10^{-5}
0.4	7.59880×10^{-1}	6.78419×10^{-2}	9.07001×10^{-1}	7.47981×10^{-2}	5.57855×10^{-1}	4.36661×10^{-1}	1.23998×10^{0}	1.27851×10^{-1}	5.56190×10^{-1}	1.35135×10^{-1}	1.59285	1.05538×10^{-3}
0.3	1.07621×10^{0}	5.65034×10^{-2}	7.36001×10^{-1}	7.67709×10^{-2}	6.05004×10^{-1}	4.76757×10^{-1}	2.10869×10^{0}	2.23273×10^{-1}	5.63682×10^{-1}	5.96790×10^{-2}	1.61732	1.80370×10^{-3}
0.2	1.63770×10^{0}	4.50126×10^{-2}	5.87001×10^{-1}	7.66823×10^{-2}	6.16139×10^{-1}	4.87070×10^{-1}	3.43962×10^{0}	3.66971×10^{-1}	5.65746×10^{-1}	1.17112×10^{-2}	1.62323	1.60997×10^{-3}
0.15	2.18070×10^{0}	3.80026×10^{-2}	5.03001×10^{-1}	7.67445×10^{-2}	6.15174×10^{-1}	4.86097×10^{-1}	4.62544×10^{0}	4.94821×10^{-1}	5.66511×10^{-1}	6.18798×10^{-2}	1.62350	1.38681×10^{-3}
0.14	2.33408×10^{0}	3.72483×10^{-2}	4.84001×10^{-1}	7.69591×10^{-2}	6.14563×10^{-1}	4.85294×10^{-1}	4.94206×10^{0}	5.29140×10^{-1}	5.66750×10^{-1}	1.23311×10^{-2}	1.62352	1.33847×10^{-3}
0.13	2.51005×10^{0}	3.58709×10^{-2}	4.66001×10^{-1}	7.69760×10^{-2}	6.13756×10^{-1}	4.84352×10^{-1}	5.29294×10^{0}	5.67283×10^{-1}	5.67039×10^{-1}	2.12558×10^{-3}	1.62355	1.28926×10^{-3}
0.12	2.71390×10^{0}	3.44727×10^{-2}	4.46001×10^{-1}	7.72929×10^{-2}	6.12694×10^{-1}	4.82905×10^{-1}	5.68106×10^{0}	6.09621×10^{-1}	5.67383×10^{-1}	8.83112×10^{-3}	1.62358	1.23932×10^{-3}
0.11	2.95270×10^{0}	3.30576×10^{-2}	4.26001×10^{-1}	7.75998×10^{-2}	6.11298×10^{-1}	4.81022×10^{-1}	6.10855×10^{0}	6.56424×10^{-1}	5.67785×10^{-1}	5.00443×10^{-3}	1.62362	1.18884×10^{-3}
0.1	3.23630×10^{0}	3.16303×10^{-2}	4.05001×10^{-1}	7.80994×10^{-2}	6.09503×10^{-1}	4.78477×10^{-1}	6.57701×10^{0}	7.07950×10^{-1}	5.68261×10^{-1}	2.74067×10^{-3}	1.62367	1.13801×10^{-3}

Table I.5: FD with $\alpha(R) = 0$ (completely degenerate core): Marginally stable points corresponding to different temperature parameters $b = k_B T(R)/mc^2$. The instability is independent of b. The pair production/annihilation effect is significant only if $b \gtrsim 0.1$; while no gravitational bound state exists when $b \gtrsim 0.4$ as $M_{\rm rest} - M \lesssim 0$.

b	$w(0)$	M	R	$C = M/R$	$Z(0)$	$\epsilon_*(0)/mc^2$	$\hat{p}(0)$	$\hat{p}(0)$	$v(0)/c$	$v(R)/c$	$\langle\gamma\rangle = \gamma_{\rm ce}$
5.0	6.46710×10^{-2}	2.94115×10^{-1}	3.68700×10^{0}	7.97708×10^{-2}	6.12023×10^{-1}	4.77869×10^{-1}	7.81440×10^{-2}	8.33855×10^{-3}	5.65794×10^{-1}	4.40456×10^{-3}	1.62360
3.0	1.07780×10^{-1}	2.27846×10^{-1}	2.85600×10^{0}	7.97778×10^{-2}	6.11999×10^{-1}	4.77836×10^{-1}	1.30191×10^{-1}	1.38924×10^{-2}	5.65796×10^{-1}	4.49651×10^{-3}	1.62360
2.0	1.61655×10^{-1}	1.86075×10^{-1}	2.33200×10^{0}	7.97921×10^{-2}	6.11951×10^{-1}	4.77769×10^{-1}	1.95139×10^{-1}	2.08233×10^{-2}	5.65810×10^{-1}	4.73996×10^{-3}	1.62360
1.0	3.23190×10^{-1}	1.31718×10^{-1}	1.64900×10^{0}	7.98772×10^{-2}	6.11796×10^{-1}	4.77498×10^{-1}	3.88896×10^{-1}	4.15081×10^{-2}	5.65861×10^{-1}	6.26828×10^{-3}	1.62361
0.5	6.45350×10^{-1}	9.33447×10^{-2}	1.16700×10^{0}	8.01582×10^{-2}	6.11080×10^{-1}	4.76365×10^{-1}	7.66630×10^{-1}	8.18806×10^{-2}	5.66054×10^{-1}	7.43761×10^{-3}	1.62363
0.3	1.07176×10^{0}	7.31815×10^{-2}	9.06001×10^{-1}	8.07742×10^{-2}	6.09507×10^{-1}	4.73861×10^{-1}	1.23686×10^{0}	1.32302×10^{-1}	5.66479×10^{-1}	8.46604×10^{-3}	1.62368
0.2	1.59765×10^{0}	6.08369×10^{-2}	7.43001×10^{-1}	8.18788×10^{-2}	6.06833×10^{-1}	4.69514×10^{-1}	1.75163×10^{0}	1.87835×10^{-1}	5.67189×10^{-1}	1.03413×10^{-2}	1.62376
0.15	2.11415×10^{0}	5.38941×10^{-2}	6.48001×10^{-1}	8.31698×10^{-2}	6.03689×10^{-1}	4.64346×10^{-1}	2.17671×10^{0}	2.34054×10^{-1}	5.67961×10^{-1}	9.15085×10^{-3}	1.62385
0.14	2.26000×10^{0}	5.24381×10^{-2}	6.28001×10^{-1}	8.35000×10^{-2}	6.02774×10^{-1}	4.62840×10^{-1}	2.28244×10^{0}	2.45619×10^{-1}	5.68188×10^{-1}	2.48344×10^{-3}	1.62388
0.13	2.42735×10^{0}	5.09607×10^{-2}	6.06001×10^{-1}	8.40934×10^{-2}	6.01719×10^{-1}	4.60972×10^{-1}	2.39629×10^{0}	2.58106×10^{-1}	5.68448×10^{-1}	1.11196×10^{-2}	1.62392
0.12	2.62130×10^{0}	4.94640×10^{-2}	5.85001×10^{-1}	8.45536×10^{-2}	6.00480×10^{-1}	4.58903×10^{-1}	2.51850×10^{0}	2.71548×10^{-1}	5.68739×10^{-1}	3.2558×10^{-3}	1.62396
0.11	2.84880×10^{0}	4.79502×10^{-2}	5.62001×10^{-1}	8.53205×10^{-2}	5.99026×10^{-1}	4.56333×10^{-1}	2.64931×10^{0}	2.85982×10^{-1}	5.69068×10^{-1}	9.85064×10^{-3}	1.62400
0.1	3.11960×10^{0}	4.64223×10^{-2}	5.39001×10^{-1}	8.61266×10^{-2}	5.97349×10^{-1}	4.53364×10^{-1}	2.78900×10^{0}	3.01466×10^{-1}	5.69450×10^{-1}	8.63863×10^{-3}	1.62406
0.09	3.44745×10^{0}	4.48864×10^{-2}	5.15001×10^{-1}	8.71578×10^{-2}	5.95385×10^{-1}	4.49793×10^{-1}	2.93687×10^{0}	3.17934×10^{-1}	5.69884×10^{-1}	9.79655×10^{-3}	1.62413
0.08	3.85285×10^{0}	4.33505×10^{-2}	4.90001×10^{-1}	8.84703×10^{-2}	5.93079×10^{-1}	4.45477×10^{-1}	3.09161×10^{0}	3.35258×10^{-1}	5.70371×10^{-1}	1.28836×10^{-2}	1.62421
0.05	5.98040×10^{0}	3.88844×10^{-2}	4.12001×10^{-1}	9.43795×10^{-2}	5.83694×10^{-1}	4.26527×10^{-1}	3.56856×10^{0}	3.89383×10^{-1}	5.72141×10^{-1}	9.74573×10^{-3}	1.62455
10^{-2}	2.73890×10^{1}	3.45579×10^{-2}	3.03001×10^{-1}	1.14052×10^{-1}	5.67411×10^{-1}	3.77171×10^{-1}	3.98720×10^{0}	4.37833×10^{-1}	5.73959×10^{-1}	8.36024×10^{-3}	1.62526
10^{-3}	2.65345×10^{2}	3.42798×10^{-2}	2.80001×10^{-1}	1.22427×10^{-1}	5.65797×10^{-1}	3.61045×10^{-1}	4.00419×10^{0}	4.39725×10^{-1}	5.73976×10^{-1}	1.81042×10^{-2}	1.62534
10^{-4}	2.64440×10^{3}	3.42765×10^{-2}	2.78001×10^{-1}	1.23296×10^{-1}	5.65796×10^{-1}	3.59399×10^{-1}	4.00461×10^{0}	4.39783×10^{-1}	5.73984×10^{-1}	1.67281×10^{-2}	1.62535
10^{-5}	2.64330×10^{4}	3.42758×10^{-2}	2.78001×10^{-1}	1.23294×10^{-1}	5.65767×10^{-1}	3.59244×10^{-1}	4.00429×10^{0}	4.39734×10^{-1}	5.73975×10^{-1}	1.37005×10^{-2}	1.62534

with pair production/annihilation

b	$w(0)$	M	R	$C = M/R$	$Z(0)$	$\epsilon_*(0)/mc^2$	$\hat{p}(0)$	$\hat{p}(0)$	$v(0)/c$	$v(R)/c$	$\langle\gamma\rangle = \gamma_{\rm ce}$	$M_{\rm rest} - M$
0.5	4.65550×10^{-1}	1.03921×10^{-1}	1.61200×10^{0}	6.44671×10^{-2}	3.96497×10^{-1}	3.03390×10^{-1}	2.52824×10^{-1}	2.39938×10^{-2}	5.32468×10^{-1}	2.63570×10^{-1}	1.51285	-4.60647×10^{-3}
0.49	4.80090×10^{-1}	1.02217×10^{-1}	1.55200×10^{0}	6.58617×10^{-2}	4.11430×10^{-1}	3.15191×10^{-1}	2.83256×10^{-1}	2.70165×10^{-2}	5.34916×10^{-1}	2.53507×10^{-1}	1.52020	-3.92886×10^{-3}
0.48	5.13020×10^{-1}	1.00523×10^{-1}	1.49600×10^{0}	6.71944×10^{-2}	4.25966×10^{-1}	3.26698×10^{-1}	3.15703×10^{-1}	3.03796×10^{-2}	5.37295×10^{-1}	2.43440×10^{-1}	1.52741	-3.29188×10^{-3}
0.45	5.87300×10^{-1}	9.55365×10^{-2}	1.35100×10^{0}	7.07153×10^{-2}	4.66849×10^{-1}	3.59208×10^{-1}	4.24691×10^{-1}	4.18869×10^{-2}	5.43956×10^{-1}	2.13096×10^{-1}	1.54796	-1.62883×10^{-3}
0.4	7.21030×10^{-1}	8.76858×10^{-2}	1.16800×10^{0}	7.50734×10^{-2}	5.24332×10^{-1}	4.05289×10^{-1}	6.40734×10^{-1}	6.53718×10^{-2}	5.53245×10^{-1}	1.62655×10^{-1}	1.57760	4.10689×10^{-4}
0.3	1.04949×10^{0}	7.38234×10^{-2}	9.26001×10^{-1}	7.97728×10^{-2}	5.91886×10^{-1}	4.59512×10^{-1}	1.14760×10^{0}	1.21704×10^{-1}	5.64050×10^{-1}	7.14177×10^{-2}	1.61403	2.18779×10^{-3}
0.2	1.59635×10^{0}	6.08552×10^{-2}	7.44001×10^{-1}	8.17946×10^{-2}	6.06136×10^{-1}	4.68976×10^{-1}	1.74665×10^{0}	1.8725×10^{-1}	5.67112×10^{-1}	1.57011×10^{-2}	1.62337	2.17615×10^{-3}
0.15	2.11410×10^{0}	5.38945×10^{-2}	6.48001×10^{-1}	8.31704×10^{-2}	6.03669×10^{-1}	4.64329×10^{-1}	2.17654×10^{0}	2.34036×10^{-1}	5.67961×10^{-1}	9.61245×10^{-3}	1.62384	1.94266×10^{-3}
0.14	2.26000×10^{0}	5.24380×10^{-2}	6.28001×10^{-1}	8.34998×10^{-2}	6.02774×10^{-1}	4.62840×10^{-1}	2.28245×10^{0}	2.45623×10^{-1}	5.68191×10^{-1}	2.95561×10^{-3}	1.62388	1.89032×10^{-3}
0.13	2.42730×10^{0}	5.09612×10^{-2}	6.06001×10^{-1}	8.40943×10^{-2}	6.01702×10^{-1}	4.60957×10^{-1}	2.39611×10^{0}	2.58083×10^{-1}	5.68442×10^{-1}	1.12380×10^{-2}	1.62391	1.83772×10^{-3}
0.12	2.62129×10^{0}	4.94640×10^{-2}	5.85001×10^{-1}	8.45538×10^{-2}	6.00477×10^{-1}	4.58900×10^{-1}	2.51846×10^{0}	2.71544×10^{-1}	5.68739×10^{-1}	3.34270×10^{-3}	1.62396	1.78432×10^{-3}
0.11	2.84880×10^{0}	4.79502×10^{-2}	5.62001×10^{-1}	8.53205×10^{-2}	5.99026×10^{-1}	4.56333×10^{-1}	2.64931×10^{0}	2.85982×10^{-1}	5.69068×10^{-1}	9.85333×10^{-3}	1.62400	1.73035×10^{-3}
0.1	3.11965×10^{0}	4.64220×10^{-2}	5.39001×10^{-1}	8.61259×10^{-2}	5.97362×10^{-1}	4.53376×10^{-1}	2.78916×10^{0}	3.01489×10^{-1}	5.69456×10^{-1}	8.55584×10^{-3}	1.62406	1.67588×10^{-3}

Table I.6: FD with $\alpha(R) = 0.5$ (overly degenerate core): Marginally stable points corresponding to different temperature parameters $b = k_B T(R)/mc^2$. The instability is independent of b. The pair production/annihilation effect is significant only if $b \gtrsim 0.1$; while no gravitational bound state exists when $b \gtrsim 0.38$ as $M_{\rm rest} - M \lesssim 0$.

b	$w(0)$	$\bar{M}$	$\bar{R}$	$C = M/R$	$Z(0)$	$\epsilon_*(0)/mc^2$	$\bar{\rho}(0)$	$\bar{p}(0)$	$v(0)/c$	$v(R)/c$	$\langle\gamma\rangle = \gamma_{\rm ss}$
5.0	6.46370×10^{-2}	3.39241×10^{-1}	4.24800×10^{0}	7.98589×10^{-2}	6.11818×10^{-1}	4.77507×10^{-1}	5.86445×10^{-2}	6.25860×10^{-3}	5.65830×10^{-1}	1.67907×10^{-3}	1.62361
3.0	1.07685×10^{-1}	2.63201×10^{-1}	3.29200×10^{0}	7.99518×10^{-2}	6.11652×10^{-1}	4.77213×10^{-1}	9.73051×10^{-2}	1.03853×10^{-2}	5.65853×10^{-1}	4.59333×10^{-3}	1.62361
2.0	1.61447×10^{-1}	2.15349×10^{-1}	2.69000×10^{0}	8.00554×10^{-2}	6.11458×10^{-1}	4.76859×10^{-1}	1.45130×10^{-1}	1.54919×10^{-2}	5.65893×10^{-1}	5.15083×10^{-3}	1.62362
1.0	3.22360×10^{-1}	1.53287×10^{-1}	1.90700×10^{0}	8.03813×10^{-2}	6.10798×10^{-1}	4.75691×10^{-1}	2.84959×10^{-1}	3.04326×10^{-2}	5.66029×10^{-1}	5.86189×10^{-3}	1.62364
0.5	6.42189×10^{-1}	1.10020×10^{-1}	1.35600×10^{0}	8.11353×10^{-2}	6.09199×10^{-1}	4.72927×10^{-1}	5.46316×10^{-1}	5.84123×10^{-2}	5.66357×10^{-1}	7.55503×10^{-3}	1.62368
0.3	1.06375×10^{0}	8.71760×10^{-2}	1.06000×10^{0}	8.22414×10^{-2}	6.06723×10^{-1}	4.68683×10^{-1}	8.53315×10^{-1}	9.14147×10^{-2}	5.66910×10^{-1}	5.22698×10^{-3}	1.62376
0.2	1.58197×10^{0}	7.34611×10^{-2}	8.76001×10^{-1}	8.38596×10^{-2}	6.03347×10^{-1}	4.62797×10^{-1}	1.16992×10^{0}	1.25675×10^{-1}	5.67685×10^{-1}	7.92247×10^{-3}	1.62386
0.15	2.09042×10^{0}	6.57972×10^{-2}	7.69001×10^{-1}	8.55619×10^{-2}	5.99945×10^{-1}	4.56746×10^{-1}	1.41940×10^{0}	1.52895×10^{-1}	5.68467×10^{-1}	9.88243×10^{-3}	1.62397
0.14	2.23398×10^{0}	6.41939×10^{-2}	7.46001×10^{-1}	8.60507×10^{-2}	5.98997×10^{-1}	4.55034×10^{-1}	1.47998×10^{0}	1.59541×10^{-1}	5.68682×10^{-1}	1.02912×10^{-2}	1.62400
0.13	2.39875×10^{0}	6.25678×10^{-2}	7.23001×10^{-1}	8.65390×10^{-2}	5.97929×10^{-1}	4.53125×10^{-1}	1.54469×10^{0}	1.66661×10^{-1}	5.68927×10^{-1}	6.15021×10^{-3}	1.62404
0.12	2.58980×10^{0}	6.09207×10^{-2}	6.99001×10^{-1}	8.71539×10^{-2}	5.96709×10^{-1}	4.50902×10^{-1}	1.61361×10^{0}	1.74264×10^{-1}	5.69199×10^{-1}	3.07272×10^{-3}	1.62408
0.11	2.81410×10^{0}	5.92542×10^{-2}	6.74001×10^{-1}	8.79141×10^{-2}	5.95329×10^{-1}	4.48323×10^{-1}	1.68695×10^{0}	1.82383×10^{-1}	5.69512×10^{-1}	4.28778×10^{-3}	1.62413
0.1	3.08114×10^{0}	5.75729×10^{-2}	6.48001×10^{-1}	8.88469×10^{-2}	5.93727×10^{-1}	4.45289×10^{-1}	1.76439×10^{0}	1.90986×10^{-1}	5.69855×10^{-1}	8.27089×10^{-3}	1.62418
0.09	3.40490×10^{0}	5.58803×10^{-2}	6.22001×10^{-1}	8.98396×10^{-2}	5.91927×10^{-1}	4.41837×10^{-1}	1.84607×10^{0}	2.00109×10^{-1}	5.70256×10^{-1}	1.76092×10^{-2}	1.62425
0.08	3.80560×10^{0}	5.41863×10^{-2}	5.94001×10^{-1}	9.12226×10^{-2}	5.89821×10^{-1}	4.37643×10^{-1}	1.93082×10^{0}	2.09615×10^{-1}	5.70692×10^{-1}	1.12090×10^{-2}	1.62432
0.05	5.91600×10^{0}	4.92322×10^{-2}	5.08001×10^{-1}	9.69136×10^{-2}	5.81521×10^{-1}	4.20037×10^{-1}	2.19034×10^{0}	2.39117×10^{-1}	5.72282×10^{-1}	5.41712×10^{-3}	1.62464
10^{-2}	2.72990×10^{1}	4.43385×10^{-2}	3.85001×10^{-1}	1.15165×10^{-1}	5.67263×10^{-1}	3.75354×10^{-1}	2.41939×10^{0}	2.65677×10^{-1}	5.73964×10^{-1}	1.80675×10^{-2}	1.62527
10^{-3}	2.65250×10^{2}	4.40157×10^{-2}	3.60001×10^{-1}	1.22266×10^{-1}	5.65797×10^{-1}	3.60993×10^{-1}	2.42868×10^{0}	2.66710×10^{-1}	5.73977×10^{-1}	5.72791×10^{-3}	1.62534
10^{-4}	2.64420×10^{3}	4.40119×10^{-2}	3.57001×10^{-1}	1.23282×10^{-1}	5.65794×10^{-1}	3.59392×10^{-1}	2.43112×10^{0}	2.66740×10^{-1}	5.73722×10^{-1}	1.59393×10^{-2}	1.62535
10^{-5}	2.64335×10^{4}	4.40110×10^{-2}	3.57001×10^{-1}	1.23280×10^{-1}	5.65781×10^{-1}	3.59261×10^{-1}	2.42885×10^{0}	2.66731×10^{-1}	5.73980×10^{-1}	1.28157×10^{-2}	1.62534

with pair production/annihilation

b	$w(0)$	$\bar{M}$	$\bar{R}$	$C = M/R$	$Z(0)$	$\epsilon_*(0)/mc^2$	$\bar{\rho}(0)$	$\bar{p}(0)$	$v(0)/c$	$v(R)/c$	$\langle\gamma\rangle = \gamma_{\rm ss}$	$M_{\rm rest} - \bar{M}$
0.5	4.04250×10^{-1}	1.24244×10^{-1}	2.13200×10^{0}	5.82759×10^{-2}	3.33419×10^{-1}	2.53325×10^{-1}	1.19420×10^{-1}	1.09154×10^{-2}	5.23051×10^{-1}	2.99936 × 10^{-3}	1.48259	-8.65551×10^{-3}
0.49	4.30850×10^{-1}	1.22276×10^{-1}	2.02600×10^{0}	6.03535×10^{-2}	3.51807×10^{-1}	2.67611×10^{-1}	1.39199×10^{-1}	1.28713×10^{-2}	5.26689×10^{-1}	2.88762×10^{-4}	1.49144	-7.59957×10^{-3}
0.48	4.57750×10^{-1}	1.20288×10^{-1}	1.93100×10^{0}	6.22931×10^{-2}	3.69752×10^{-1}	2.81591×10^{-1}	1.60739×10^{-1}	1.50295×10^{-2}	5.29630×10^{-1}	2.77493×10^{-4}	1.50016	-6.59957×10^{-3}
0.45	5.40800×10^{-1}	1.14293×10^{-1}	1.69500×10^{0}	6.74294×10^{-2}	4.20900×10^{-1}	3.21630×10^{-1}	2.36281×10^{-1}	2.27964×10^{-2}	5.37097×10^{-1}	2.43372×10^{-4}	1.52541	-3.94246×10^{-3}
0.4	6.87710×10^{-1}	1.04702×10^{-1}	1.41800×10^{0}	7.38374×10^{-2}	4.94179×10^{-1}	3.79464×10^{-1}	3.94455×10^{-1}	3.97448×10^{-2}	5.49797×10^{-1}	1.86288×10^{-4}	1.56278	-6.42921×10^{-4}
0.39	7.19630×10^{-1}	1.02683×10^{-1}	1.37400×10^{0}	7.48781×10^{-2}	5.06769×10^{-1}	3.93378×10^{-1}	4.29963×10^{-1}	4.36374×10^{-2}	5.51791×10^{-1}	1.75134×10^{-4}	1.56503	-1.43421×10^{-4}
0.38	7.50150×10^{-1}	1.01102×10^{-1}	1.33400×10^{0}	7.57885×10^{-2}	5.18450×10^{-1}	3.98693×10^{-1}	4.66390×10^{-1}	4.76541×10^{-2}	5.53651×10^{-1}	1.63954×10^{-4}	1.57552	3.08839×10^{-4}
0.37	7.82330×10^{-1}	9.93597×10^{-2}	1.29700×10^{0}	7.66073×10^{-2}	5.29384×10^{-1}	4.07376×10^{-1}	5.03571×10^{-1}	5.17741×10^{-2}	5.55375×10^{-1}	1.52857×10^{-4}	1.58132	7.12838×10^{-4}
0.36	8.15250×10^{-1}	9.76548×10^{-2}	1.26200×10^{0}	7.73809×10^{-2}	5.39506×10^{-1}	4.15388×10^{-1}	5.41361×10^{-1}	5.59792×10^{-2}	5.56969×10^{-1}	1.42006×10^{-4}	1.58674	1.07165×10^{-3}
0.35	8.48990×10^{-1}	9.59862×10^{-2}	1.22900×10^{0}	7.81010×10^{-2}	5.48897×10^{-1}	4.22753×10^{-1}	5.79595×10^{-1}	6.02478×10^{-2}	5.58430×10^{-1}	1.31402×10^{-4}	1.59175	1.38747×10^{-3}
0.3	1.03363×10^{0}	8.81354×10^{-2}	1.09100×10^{0}	8.07840×10^{-2}	5.82871×10^{-1}	4.49434×10^{-1}	7.71830×10^{-1}	8.17669×10^{-2}	5.63753×10^{-1}	8.22142×10^{-5}	1.61061	2.40460×10^{-3}
0.2	1.58020×10^{0}	7.34895×10^{-2}	8.77001×10^{-1}	8.37964×10^{-2}	6.02392×10^{-1}	4.62039×10^{-1}	1.16546×10^{0}	1.25155×10^{-1}	5.67591×10^{-1}	1.74522×10^{-5}	1.62332	2.62279×10^{-3}
0.15	2.09035×10^{0}	6.57977×10^{-2}	7.69001×10^{-1}	8.55626×10^{-2}	5.99916×10^{-1}	4.56722×10^{-1}	1.41924×10^{0}	1.52879×10^{-1}	5.68468×10^{-1}	1.04596×10^{-5}	1.62395	2.37308×10^{-3}
0.14	2.23397×10^{0}	6.41938×10^{-2}	7.46001×10^{-1}	8.60506×10^{-2}	5.98992×10^{-1}	4.55030×10^{-1}	1.47996×10^{0}	1.59542×10^{-1}	5.68686×10^{-1}	1.04743×10^{-5}	1.62400	2.31635×10^{-3}
0.13	2.39875×10^{0}	6.25677×10^{-2}	7.23001×10^{-1}	8.65389×10^{-2}	5.97929×10^{-1}	4.53125×10^{-1}	1.54469×10^{0}	1.66662×10^{-1}	5.68929×10^{-1}	6.24222×10^{-5}	1.62404	2.25852×10^{-3}
0.12	2.58980×10^{0}	6.09206×10^{-2}	6.99001×10^{-1}	8.71539×10^{-2}	5.96709×10^{-1}	4.50902×10^{-1}	1.61361×10^{0}	1.74264×10^{-1}	5.69200×10^{-1}	3.12404×10^{-5}	1.62408	2.19982×10^{-3}
0.11	2.81410×10^{0}	5.92542×10^{-2}	6.74001×10^{-1}	8.79141×10^{-2}	5.95329×10^{-1}	4.48323×10^{-1}	1.68695×10^{0}	1.82383×10^{-1}	5.69512×10^{-1}	4.29598×10^{-5}	1.62413	2.14041×10^{-3}
0.1	3.08115×10^{0}	5.75728×10^{-2}	6.48001×10^{-1}	8.88468×10^{-2}	5.93730×10^{-1}	4.45292×10^{-1}	1.76441×10^{0}	1.90989×10^{-1}	5.69856×10^{-1}	8.25373×10^{-5}	1.62418	2.08051×10^{-3}

Table I.7: FD with $\alpha(R) = 1$ (overly degenerate core): Marginally stable points corresponding to different temperature parameters $b = k_B T(R)/mc^2$. The instability is independent of b. The pair production/annihilation effect is significant only if $b \gtrsim 0.1$; while no gravitational bound state exists when $b \gtrsim 0.36$ as $M_{\rm rest} - M \lesssim 0$.

b	$w(0)$	$\bar{M}$	$\bar{R}$	$C = M/R$	$Z(0)$	$\epsilon_*(0)/mc^2$	$\bar{\rho}(0)$	$\bar{p}(0)$	$v(0)/c$	$v(R)/c$	$\langle\gamma\rangle = \gamma_{\rm ss}$
5.0	6.46050×10^{-2}	4.02755×10^{-1}	5.03700×10^{0}	7.99592×10^{-2}	6.11611×10^{-1}	4.77152×10^{-1}	4.15454×10^{-2}	4.43410×10^{-3}	5.65850×10^{-1}	3.53112×10^{-3}	1.62361
3.0	1.07604×10^{-1}	3.12882×10^{-1}	3.90600×10^{0}	8.01029×10^{-2}	6.11366×10^{-1}	4.76684×10^{-1}	6.87023×10^{-2}	7.33400×10^{-3}	5.65908×10^{-1}	4.49437×10^{-3}	1.62362
2.0	1.61260×10^{-1}	2.56419×10^{-1}	3.19500×10^{0}	8.02562×10^{-2}	6.10998×10^{-1}	4.76057×10^{-1}	1.02011×10^{-1}	1.08918×10^{-2}	5.65960×10^{-1}	5.65126×10^{-3}	1.62363
1.0	3.21650×10^{-1}	1.83381×10^{-1}	2.27000×10^{0}	8.07845×10^{-2}	6.09944×10^{-1}	4.74163×10^{-1}	1.97820×10^{-1}	2.11365×10^{-2}	5.66163×10^{-1}	1.82056×10^{-3}	1.62366
0.5	6.39610×10^{-1}	1.32760×10^{-1}	1.62100×10^{0}	8.19001×10^{-2}	6.07691×10^{-1}	4.70157×10^{-1}	3.70892×10^{-1}	3.96896×10^{-2}	5.66598×10^{-1}	4.19084×10^{-3}	1.62373
0.3	1.05751×10^{0}	1.06243×10^{-1}	1.27300×10^{0}	8.34589×10^{-2}	6.04620×10^{-1}	4.64647×10^{-1}	5.65332×10^{-1}	6.06340×10^{-2}	5.67240×10^{-1}	6.98121×10^{-3}	1.62382
0.2	1.57027×10^{0}	9.04316×10^{-2}	1.05900×10^{0}	8.53933×10^{-2}	6.00850×10^{-1}	4.57813×10^{-1}	7.57414×10^{-1}	8.14694×10^{-2}	5.68056×10^{-1}	7.20648×10^{-3}	1.62394
0.15	2.07315×10^{0}	8.16331×10^{-2}	9.35001×10^{-1}	8.73080×10^{-2}	5.97334×10^{-1}	4.51280×10^{-1}	9.03894×10^{-1}	9.74910×10^{-2}	5.68832×10^{-1}	8.85254×10^{-3}	1.62406
0.14	2.21515×10^{0}	7.97954×10^{-2}	9.09001×10^{-1}	8.77836×10^{-2}	5.96378×10^{-1}	4.49515×10^{-1}	9.38887×10^{-1}	1.01338×10^{-1}	5.69037×10^{-1}	5.19705×10^{-3}	1.62409
0.13	2.37829×10^{0}	7.79315×10^{-2}	8.82001×10^{-1}	8.83576×10^{-2}	5.95328×10^{-1}	4.47524×10^{-1}	9.76111×10^{-1}	1.05443×10^{-1}	5.69272×10^{-1}	1.66351×10^{-3}	1.62413
0.12	2.56730×10^{0}	7.60441×10^{-2}	8.54001×10^{-1}	8.90445×10^{-2}	5.94136×10^{-1}	4.45242×10^{-1}	1.01552×10^{0}	1.09799×10^{-1}	5.69530×10^{-1}	2.74336×10^{-3}	1.62417
0.11	2.78940×10^{0}	7.41345×10^{-2}	8.25001×10^{-1}	8.98599×10^{-2}	5.92805×10^{-1}	4.42637×10^{-1}	1.05722×10^{0}	1.14426×10^{-1}	5.69823×10^{-1}	6.11333×10^{-3}	1.62422
0.1	3.05400×10^{0}	7.22071×10^{-2}	7.95001×10^{-1}	9.08264×10^{-2}	5.91289×10^{-1}	4.39630×10^{-1}	1.10108×10^{0}	1.19309×10^{-1}	5.70146×10^{-1}	9.65430×10^{-3}	1.62427
0.09	3.37490×10^{0}	7.02665×10^{-2}	7.65001×10^{-1}	9.18516×10^{-2}	5.89579×10^{-1}	4.36224×10^{-1}	1.14701×10^{0}	1.24444×10^{-1}	5.70511×10^{-1}	6.72757×10^{-3}	1.62433
0.08	3.77260×10^{0}	6.83210×10^{-2}	7.34001×10^{-1}	9.30802×10^{-2}	5.87648×10^{-1}	4.32269×10^{-1}	1.19468×10^{0}	1.29804×10^{-1}	5.70925×10^{-1}	1.73542×10^{-3}	1.62440
0.05	5.87160×10^{0}	6.26124×10^{-2}	6.34001×10^{-1}	9.87576×10^{-2}	5.80093×10^{-1}	4.15554×10^{-1}	1.33967×10^{0}	1.46309×10^{-1}	5.72398×10^{-1}	8.43759×10^{-3}	1.62470
10^{-2}	2.72360×10^{1}	5.69005×10^{-2}	4.92001×10^{-1}	1.15651×10^{-1}	5.67146×10^{-1}	3.74223×10^{-1}	1.46781×10^{0}	1.61183×10^{-1}	5.73963×10^{-1}	1.37775×10^{-2}	1.62528
10^{-3}	2.65180×10^{2}	5.65170×10^{-2}	4.62001×10^{-1}	1.22331×10^{-1}	5.65787×10^{-1}	3.60864×10^{-1}	1.47302×10^{0}	1.61760×10^{-1}	5.73973×10^{-1}	5.57449×10^{-3}	1.62534
10^{-4}	2.64430×10^{3}	5.65117×10^{-2}	4.59001×10^{-1}	1.23119×10^{-1}	5.65805×10^{-1}	3.59472×10^{-1}	1.47455×10^{0}	1.61801×10^{-1}	5.73749×10^{-1}	6.52385×10^{-3}	1.62534
10^{-5}	2.64335×10^{4}	5.65113×10^{-2}	4.58001×10^{-1}	1.23387×10^{-1}	5.65782×10^{-1}	3.59210×10^{-1}	1.47317×10^{0}	1.61780×10^{-1}	5.73980×10^{-1}	1.82917×10^{-2}	1.62534

with pair production/annihilation

b	$w(0)$	$\bar{M}$	$\bar{R}$	$C = M/R$	$Z(0)$	$\epsilon_*(0)/mc^2$	$\bar{\rho}(0)$	$\bar{p}(0)$	$v(0)/c$	$v(R)/c$	$\langle\gamma\rangle = \gamma_{\rm ss}$	$M_{\rm rest} - \bar{M}$
0.5	3.08600×10^{-1}	1.51671×10^{-1}	3.24800×10^{0}	4.66966×10^{-2}	2.41847×10^{-1}	1.82450×10^{-1}	3.75023×10^{-2}	3.24992×10^{-3}	5.09880×10^{-1}	3.49075×10^{-3}	1.43970	-1.64021×10^{-2}
0.49	3.40120×10^{-1}	1.48908×10^{-1}	3.00000×10^{0}	4.99361×10^{-2}	2.64792×10^{-1}	1.99986×10^{-1}	4.77962×10^{-2}	4.20552×10^{-3}	5.13776×10^{-1}	3.36509×10^{-3}	1.45034	-1.47114×10^{-2}
0.48	3.71900×10^{-1}	1.47743×10^{-1}	2.78900×10^{0}	5.29735×10^{-2}	2.87386×10^{-1}	2.17299×10^{-1}	5.96323×10^{-2}	5.32493×10^{-3}	5.17579×10^{-1}	3.23806×10^{-3}	1.46093	-1.31151×10^{-2}
0.45	4.69100×10^{-1}	1.40833×10^{-1}	2.31200×10^{0}	6.09138×10^{-2}	3.52640×10^{-1}	2.67578×10^{-1}	1.04894×10^{-1}	9.76385×10^{-3}	5.28440×10^{-1}	2.84958×10^{-3}	1.49214	-8.69390×10^{-3}
0.4	6.37680×10^{-1}	1.28777×10^{-1}	1.82000×10^{0}	7.07563×10^{-2}	4.48833×10^{-1}	3.42411×10^{-1}	2.11826×10^{-1}	2.08073×10^{-2}	5.44021×10^{-1}	2.19147×10^{-3}	1.54006	-3.00119×10^{-3}
0.39	6.72550×10^{-1}	1.26442×10^{-1}	1.74900×10^{0}	7.22938×10^{-2}	4.65631×10^{-1}	3.55551×10^{-1}	2.37261×10^{-1}	2.36364×10^{-2}	5.46686×10^{-1}	2.06076×10^{-3}	1.54869	-2.11911×10^{-3}
0.38	7.07990×10^{-1}	1.24152×10^{-1}	1.68400×10^{0}	7.37246×10^{-2}	4.81540×10^{-1}	3.67977×10^{-1}	2.63764×10^{-1}	2.65184×10^{-2}	5.49195×10^{-1}	1.93156×10^{-3}	1.55692	-1.31877×10^{-3}
0.37	7.4370×10^{-1}	1.21918×10^{-1}	1.62600×10^{0}	7.49802×10^{-2}	4.96360×10^{-1}	3.79625×10^{-1}	2.91066×10^{-1}	2.95111×10^{-2}	5.51515×10^{-1}	1.80230×10^{-3}	1.56470	-5.97478×10^{-4}
0.36	7.80050×10^{-1}	1.19738×10^{-1}	1.57200×10^{0}	7.61692×10^{-2}	5.10186×10^{-1}	3.90451×10^{-1}	3.19034×10^{-1}	3.2599×10^{-2}	5.53662×10^{-1}	1.67601×10^{-3}	1.57302	4.78257×10^{-5}
0.35	8.17020×10^{-1}	1.17614×10^{-1}	1.52300×10^{0}	7.72253×10^{-2}	5.22960×10^{-1}	4.00460×10^{-1}	3.47480×10^{-1}	3.57391×10^{-2}	5.55634×10^{-1}	1.55096×10^{-3}	1.57884	6.20467×10^{-4}
0.3	1.01455×10^{0}	1.07803×10^{-1}	1.32800×10^{0}	8.11766×10^{-2}	5.70643×10^{-1}	4.37525×10^{-1}	4.90296×10^{-1}	5.17848×10^{-2}	5.62901×10^{-1}	9.69969×10^{-4}	1.60501	2.52592×10^{-3}
0.2	1.56771×10^{0}	9.04779×10^{-2}	1.06100×10^{0}	8.52760×10^{-2}	5.99464×10^{-1}	4.56736×10^{-1}	7.53286×10^{-1}	8.09893×10^{-2}	5.67930×10^{-1}	1.92587×10^{-4}	1.62315	3.21586×10^{-3}
0.15	2.07300×10^{0}	8.16347×10^{-2}	9.35001×10^{-1}	8.73098×10^{-2}	5.97273×10^{-1}	4.51229×10^{-1}	9.03681×10^{-1}	9.74663×10^{-2}	5.68827×10^{-1}	9.95822×10^{-5}	1.62403	2.94573×10^{-3}
0.14	2.21510×10^{0}	7.97957×10^{-2}	9.09001×10^{-1}	8.77840×10^{-2}	5.96359×10^{-1}	4.49500×10^{-1}	9.38820×10^{-1}	1.01331×10^{-1}	5.69037×10^{-1}	5.81550×10^{-5}	1.62408	2.88111×10^{-3}
0.13	2.37817×10^{0}	7.79318×10^{-2}	8.82001×10^{-1}	8.83579×10^{-2}	5.95317×10^{-1}	4.47516×10^{-1}	9.76071×10^{-1}	1.05438×10^{-1}	5.69271×10^{-1}	2.34635×10^{-5}	1.62412	2.81500×10^{-3}
0.12	2.56730×10^{0}	7.60441×10^{-2}	8.54001×10^{-1}	8.90445×10^{-2}	5.94136×10^{-1}	4.45242×10^{-1}	1.01552×10^{0}	1.09800×10^{-1}

Appendix J

Numerical Results of the Truncated Bose-Einstein Distribution

In this appendix, we tabulate the numerical results of the truncated Bose-Einstein (BE) models with and without pair production/annihilation effect, which is significant for $b \gtrsim 0.1$. Generally, given $\alpha(R) < 0$ there is a corresponding (critical) temperature b below which the *condensate pressure* has to happen such that a marginally stable point exists for BE statistics. In Tables. J.1, J.2, J.3, J.4, and J.5, we show marginally stable configurations for $\alpha(R) = -50, -10, -5, -1$, and -0.5, respectively, that satisfy the adiabatic index criterion $\langle\gamma\rangle = \gamma_{\rm cr}$, given different values of the boundary temperature $b = k_B T(R)/mc^2$. From the 2nd to 12th columns, we show their central cutoff function $w(0) = \epsilon_c(0)/k_B T(0)$, gravitational mass $\hat{M}$, system radius $\hat{R}$, compactness $C = GM(R)/c^2 R = \hat{M}/\hat{R}$, central

Table J.1: MB with $\alpha(R) \to -\infty$ (non-degenerate core): Marginally stable points corresponding to different temperature parameters $b = k_B T(R)/mc^2$. For MB distribution, it cannot achieve the GR instability for $b \lesssim 10^{-1}$, as the concentration has to be extremely high (relativistic degenerate gas). More precisely, no unstable configuration exists between $0 \lesssim b \lesssim 0.09$. The results of BE statistics with $\alpha(R) \leq -50$ are indistinguishable from MB statistics for $b \geq 0.09$. The pair production/annihilation effect is significant only if $b \gtrsim 0.1$; while no gravitational bound state exists when $b \gtrsim 0.49$ as $M_{\rm rest} - M \lesssim 0$.

b	$w(0)$	$\hat{M}$	$\hat{R}$	$C = \hat{M}/\hat{R}$	$Z(0)$	$\epsilon_c(0)/mc^2$	$\hat{\rho}(0)$	$\hat{p}(0)$	$v(0)/c$	$v(R)/c$	$\langle\gamma\rangle = \gamma_{\rm cr}$
5.0	6.48150×10^{-2}	2.06015×10^{-1}	2.59700×10^{0}	7.93280×10^{-2}	6.12906×10^{-1}	4.79448×10^{-1}	1.60344×10^{-1}	1.71013×10^{-2}	5.05650×10^{-1}	3.36500×10^{-3}	1.62358
3.0	1.08185×10^{-1}	1.58573×10^{-1}	2.00600×10^{0}	7.90492×10^{-2}	6.13491×10^{-1}	4.80491×10^{-1}	2.71859×10^{-1}	2.89847×10^{-2}	5.65552×10^{-1}	5.01669×10^{-3}	1.62356
2.0	1.62585×10^{-1}	1.28444×10^{-1}	1.63300×10^{0}	7.86552×10^{-2}	6.14252×10^{-1}	4.81854×10^{-1}	4.16754×10^{-1}	4.44142×10^{-2}	5.65434×10^{-1}	8.39347×10^{-4}	1.62354
1.0	3.27070×10^{-1}	8.86277×10^{-2}	1.14300×10^{0}	7.75395×10^{-2}	6.16612×10^{-1}	4.86021×10^{-1}	8.91191×10^{-1}	9.48580×10^{-2}	5.65059×10^{-1}	5.65015×10^{-3}	1.62347
0.5	6.62445×10^{-1}	5.95204×10^{-2}	7.93001×10^{-1}	7.50572×10^{-2}	6.21927×10^{-1}	4.95258×10^{-1}	2.05635×10^{0}	2.18273×10^{-1}	5.64303×10^{-1}	3.66372×10^{-3}	1.62333
0.3	1.12526×10^{0}	4.27849×10^{-2}	5.99001×10^{-1}	7.14271×10^{-2}	6.30406×10^{-1}	5.09562×10^{-1}	4.23693×10^{0}	4.48081×10^{-1}	5.63266×10^{-1}	9.11920×10^{-3}	1.62311
0.2	1.73635×10^{0}	3.14517×10^{-2}	4.77001×10^{-1}	6.59364×10^{-2}	6.44181×10^{-1}	5.21996×10^{-1}	8.65548×10^{0}	9.11403×10^{-1}	5.62044×10^{-1}	7.05363×10^{-3}	1.62278
0.15	2.39865×10^{0}	2.41230×10^{-2}	4.07001×10^{-1}	5.92762×10^{-2}	6.63548×10^{-1}	5.61946×10^{-1}	1.68117×10^{1}	1.76508×10^{0}	5.61211×10^{-1}	9.52828×10^{-3}	1.62239
0.14	2.60081×10^{0}	2.24259×10^{-2}	3.93001×10^{-1}	5.70632×10^{-2}	6.70637×10^{-1}	5.72538×10^{-1}	2.03949×10^{1}	2.14055×10^{0}	5.61128×10^{-1}	1.01614×10^{-2}	1.62225
0.13	2.84350×10^{0}	2.06203×10^{-2}	3.80001×10^{-1}	5.42638×10^{-2}	6.80073×10^{-1}	5.86379×10^{-1}	2.56589×10^{1}	2.69362×10^{0}	5.61190×10^{-1}	8.83738×10^{-3}	1.62209
0.12	3.14240×10^{0}	1.86835×10^{-2}	3.69001×10^{-1}	5.06326×10^{-2}	6.93337×10^{-1}	6.05343×10^{-1}	3.40099×10^{1}	3.57521×10^{0}	5.61577×10^{-1}	5.28167×10^{-3}	1.62188
0.11	3.52490×10^{0}	1.65825×10^{-2}	3.62001×10^{-1}	4.58080×10^{-2}	7.13594×10^{-1}	6.33260×10^{-1}	4.88977×10^{1}	5.16148×10^{0}	5.62734×10^{-1}	6.38807×10^{-3}	1.62159
0.1	4.05150×10^{0}	1.42556×10^{-2}	3.68001×10^{-1}	3.87378×10^{-2}	7.50107×10^{-1}	6.81035×10^{-1}	8.17923×10^{1}	8.74006×10^{0}	5.66189×10^{-1}	8.76561×10^{-3}	1.62117
0.09	5.08620×10^{0}	1.13990×10^{-2}	4.83001×10^{-1}	2.36004×10^{-2}	8.89250×10^{-1}	8.44163×10^{-1}	2.57054×10^{2}	2.96813×10^{1}	5.87872×10^{-1}	5.72277×10^{-3}	1.62023

with pair production/annihilation

b	$w(0)$	$\hat{M}$	$\hat{R}$	$C = \hat{M}/\hat{R}$	$Z(0)$	$\epsilon_c(0)/mc^2$	$\hat{\rho}(0)$	$\hat{p}(0)$	$v(0)/c$	$v(R)/c$	$\langle\gamma\rangle = \gamma_{\rm cr}$	$\hat{M}_{\rm rest} - \hat{M}$
0.5	5.74700×10^{-1}	6.38546×10^{-2}	9.11001×10^{-1}	7.00928×10^{-2}	5.13186×10^{-1}	4.03186×10^{-1}	1.20516×10^{0}	1.19761×10^{-1}	5.46805×10^{-1}	1.89809×10^{-3}	1.56780	-1.31416×10^{-4}
0.49	5.93850×10^{-1}	6.27608×10^{-2}	8.91001×10^{-1}	7.04386×10^{-2}	5.21631×10^{-1}	4.10402×10^{-1}	1.29191×10^{0}	1.29021×10^{-1}	5.47360×10^{-1}	1.82251×10^{-3}	1.57193	7.73207×10^{-5}
0.48	6.13470×10^{-1}	6.16778×10^{-2}	8.71001×10^{-1}	7.08126×10^{-2}	5.29751×10^{-1}	4.17344×10^{-1}	1.38267×10^{0}	1.38736×10^{-1}	5.48650×10^{-1}	1.74864×10^{-3}	1.57591	2.50896×10^{-4}
0.45	6.75730×10^{-1}	5.84763×10^{-2}	8.16001×10^{-1}	7.16621×10^{-2}	5.52360×10^{-1}	4.36905×10^{-1}	1.68242×10^{0}	1.71017×10^{-1}	5.52220×10^{-1}	1.52609×10^{-3}	1.58697	6.90315×10^{-4}
0.4	7.59200×10^{-1}	5.32861×10^{-2}	7.57001×10^{-1}	7.23013×10^{-2}	5.83600×10^{-1}	4.64700×10^{-1}	2.28321×10^{0}	2.36114×10^{-1}	5.56992×10^{-1}	1.15930×10^{-3}	1.60207	1.17611×10^{-3}
0.3	1.11485×10^{0}	4.30373×10^{-2}	6.04001×10^{-1}	7.12537×10^{-2}	6.22366×10^{-1}	5.02460×10^{-1}	4.07942×10^{0}	4.29395×10^{-1}	5.61940×10^{-1}	5.15468×10^{-4}	1.61903	1.42876×10^{-3}
0.2	1.73580×10^{0}	3.14591×10^{-2}	4.77001×10^{-1}	6.59519×10^{-2}	6.43899×10^{-1}	5.31727×10^{-1}	8.64353×10^{0}	9.10013×10^{-1}	5.62003×10^{-1}	1.25884×10^{-3}	1.62264	1.11842×10^{-3}
0.15	2.39860×10^{0}	2.41235×10^{-2}	4.07001×10^{-1}	5.92713×10^{-2}	6.63529×10^{-1}	5.61927×10^{-1}	1.68101×10^{1}	1.76401×10^{0}	5.61207×10^{-1}	9.73977×10^{-3}	1.62238	8.54384×10^{-4}
0.14	2.60081×10^{0}	2.24259×10^{-2}	3.93001×10^{-1}	5.70631×10^{-2}	6.70637×10^{-1}	5.72538×10^{-1}	2.03949×10^{1}	2.14056×10^{0}	5.61129×10^{-1}	1.02232×10^{-2}	1.62225	7.92345×10^{-4}
0.13	2.84350×10^{0}	2.06203×10^{-2}	3.80001×10^{-1}	5.42638×10^{-2}	6.80073×10^{-1}	5.86379×10^{-1}	2.56589×10^{1}	2.69362×10^{0}	5.61190×10^{-1}	8.86114×10^{-3}	1.62209	7.26980×10^{-4}
0.12	3.14240×10^{0}	1.86835×10^{-2}	3.69001×10^{-1}	5.06326×10^{-2}	6.93337×10^{-1}	6.05343×10^{-1}	3.40099×10^{1}	3.57522×10^{0}	5.61577×10^{-1}	5.29271×10^{-3}	1.62188	6.54548×10^{-4}
0.11	3.52490×10^{0}	1.65825×10^{-2}	3.62001×10^{-1}	4.58080×10^{-2}	7.13594×10^{-1}	6.33260×10^{-1}	4.88977×10^{1}	5.16148×10^{0}	5.62734×10^{-1}	6.39008×10^{-3}	1.62159	5.76084×10^{-4}
0.1	4.05150×10^{0}	1.42556×10^{-2}	3.68001×10^{-1}	3.87378×10^{-2}	7.50107×10^{-1}	6.81035×10^{-1}	8.17923×10^{1}	8.74006×10^{0}	5.66189×10^{-1}	8.76585×10^{-3}	1.62117	4.86859×10^{-4}

interior redshift $Z(0) = e^{-\Phi(0)} - 1$, central energy cut off $\epsilon_c(0)$, central energy density $\hat{\rho}(0)$, central pressure $\hat{p}(0)$, central velocity dispersion $v(0)$, boundary velocity dispersion $v(R)$, and $\langle\gamma\rangle = \gamma_{\rm cr}$.

When pair production/annihilation is taken into account, we add the 13th column for the binding energy $\hat{M}_{\rm rest} - \hat{M}$ to examine if the gravitational bound state exists. Although this can still make the system unstable, it becomes gravitationally unbound $\hat{M} - \hat{M}_{\rm rest} \gtrsim 0$ when $b \gtrsim 0.5$–0.7 (depending on $\alpha(R)$). In the classical Maxwell-Boltzmann (MB) limit, the threshold is $b \gtrsim 0.49$. As $\alpha(R)$ increases, the threshold increases up to $b \gtrsim 0.7$ in the nearly degenerate limit $\alpha(R) = -0.5$. This is in contrast to the Pauli blocking of fermions, bosons tend to party and are easier to be gravitationally bound. Thus slightly higher temperature is required to break them apart.

Table J.2: BE with $\alpha(R) = -10$ (partially condensate core when $b \lesssim 0.09$): Marginally stable points corresponding to different temperature parameters $b = k_B T(R)/mc^2$. No marginal stable point exists for $0 \leq b \lesssim 0.09$ if the particles are purely thermal. BEC must happen for $w(0 \leq r \leq r_c) = 10$ at $b \lesssim 0.09$ in order to have marginal stable points. The pair production/annihilation effect is significant only if $b \gtrsim 0.1$; while no gravitational bound state exists when $b \gtrsim 0.49$ as $M_{\rm rest} - M \lesssim 0$.

b	$w(0)$	$\bar{M}$	$\bar{R}$	$C = \bar{M}/\bar{R}$	$Z(0)$	$\epsilon_*(0)/mc^2$	$\bar{p}(0)$	$\bar{\rho}(0)$	$v(0)/c$	$v(R)/c$	$\langle\gamma\rangle = \gamma_\infty$
5.0	6.48150×10^{-2}	2.06010×10^{-1}	2.59700×10^{0}	7.93261×10^{-2}	6.12905×10^{-1}	4.79449×10^{-1}	1.60352×10^{-1}	1.71021×10^{-2}	5.65650×10^{-1}	3.07825×10^{-3}	1.62358
3.0	1.08185×10^{-1}	1.58569×10^{-1}	2.00600×10^{0}	7.90474×10^{-2}	6.13491×10^{-1}	4.80492×10^{-1}	2.71872×10^{-1}	2.88960×10^{-2}	5.65552×10^{-1}	4.82900×10^{-3}	1.62356
2.0	1.62585×10^{-1}	1.28441×10^{-1}	1.63200×10^{0}	7.87014×10^{-2}	6.14252×10^{-1}	4.81828×10^{-1}	4.16774×10^{-1}	4.44163×10^{-2}	5.65433×10^{-1}	6.91964×10^{-3}	1.62354
1.0	3.27070×10^{-1}	8.86253×10^{-2}	1.14300×10^{0}	7.75374×10^{-2}	6.16612×10^{-1}	4.86022×10^{-1}	8.91240×10^{-1}	9.48549×10^{-2}	5.65058×10^{-1}	1.48513×10^{-2}	1.62347
0.5	6.62445×10^{-1}	5.95185×10^{-2}	7.93001×10^{-1}	7.50548×10^{-2}	6.21926×10^{-1}	4.95259×10^{-1}	2.05649×10^{0}	2.18287×10^{-1}	5.64302×10^{-1}	3.41271×10^{-2}	1.62333
0.3	1.12528×10^{0}	4.27826×10^{-2}	5.99001×10^{-1}	7.14233×10^{-2}	6.30419×10^{-1}	5.09578×10^{-1}	4.23762×10^{0}	4.48158×10^{-1}	5.63269×10^{-1}	8.96816×10^{-2}	1.62311
0.2	1.73638×10^{0}	3.14495×10^{-2}	4.77001×10^{-1}	6.59317×10^{-2}	6.44190×10^{-1}	5.32011×10^{-1}	8.65730×10^{0}	9.11592×10^{-1}	5.62043×10^{-1}	6.92353×10^{-2}	1.62278
0.15	2.39870×10^{0}	2.41206×10^{-2}	4.07001×10^{-1}	5.92642×10^{-2}	6.63557×10^{-1}	5.61965×10^{-1}	1.68171×10^{1}	1.76553×10^{0}	5.61204×10^{-1}	9.52818×10^{-2}	1.62239
0.14	2.60090×10^{0}	2.24231×10^{-2}	3.93001×10^{-1}	5.70561×10^{-2}	6.70656×10^{-1}	5.72569×10^{-1}	2.04037×10^{1}	2.14141×10^{0}	5.61121×10^{-1}	1.01851×10^{-2}	1.62225
0.13	2.84370×10^{0}	2.06167×10^{-2}	3.80001×10^{-1}	5.42544×10^{-2}	6.80122×10^{-1}	5.86444×10^{-1}	2.56761×10^{1}	2.69541×10^{0}	5.61187×10^{-1}	8.89810×10^{-3}	1.62209
0.12	3.14270×10^{0}	1.86794×10^{-2}	3.69001×10^{-1}	5.06216×10^{-2}	6.93407×10^{-1}	6.05434×10^{-1}	3.40408×10^{1}	3.57841×10^{0}	5.61572×10^{-1}	5.59585×10^{-1}	1.62188
0.11	3.52555×10^{0}	1.65770×10^{-2}	3.62001×10^{-1}	4.57926×10^{-2}	7.13749×10^{-1}	6.33445×10^{-1}	4.89757×10^{1}	5.16977×10^{0}	5.62738×10^{-1}	6.99840×10^{-3}	1.62159
0.1	4.05285×10^{0}	1.42484×10^{-2}	3.69001×10^{-1}	3.86133×10^{-2}	7.50422×10^{-1}	6.81476×10^{-1}	8.20304×10^{1}	8.76572×10^{0}	5.66196×10^{-1}	1.22065×10^{-2}	1.62117
0.09	5.12000×10^{0}	1.13595×10^{-2}	4.93001×10^{-1}	2.30416×10^{-2}	8.98789×10^{-1}	8.54564×10^{-1}	2.70931×10^{2}	3.13829×10^{1}	5.89492×10^{-1}	5.95293×10^{-3}	1.62019

with pair production/annihilation

b	$w(0)$	$\bar{M}$	$\bar{R}$	$C = \bar{M}/\bar{R}$	$Z(0)$	$\epsilon_*(0)/mc^2$	$\bar{p}(0)$	$\bar{\rho}(0)$	$v(0)/c$	$v(R)/c$	$\langle\gamma\rangle = \gamma_\infty$	$\bar{M}_{\rm rest} - \bar{M}$
0.5	5.74700×10^{-1}	6.38527×10^{-2}	9.11001×10^{-1}	7.00907×10^{-2}	5.13186×10^{-1}	4.03187×10^{-1}	1.20523×10^{0}	1.19767×10^{-1}	5.46903×10^{-1}	1.89801×10^{-1}	1.56780	-1.10282×10^{-4}
0.49	5.93850×10^{-1}	6.27590×10^{-2}	8.91001×10^{-1}	7.04365×10^{-2}	5.21630×10^{-1}	4.10403×10^{-1}	1.29199×10^{0}	1.29028×10^{-1}	5.47358×10^{-1}	1.82343×10^{-1}	1.57193	7.74387×10^{-5}
0.48	6.13490×10^{-1}	6.16748×10^{-2}	8.71001×10^{-1}	7.08091×10^{-2}	5.29773×10^{-1}	4.17365×10^{-1}	1.38293×10^{0}	1.38765×10^{-1}	5.48657×10^{-1}	1.74849×10^{-1}	1.57592	2.50989×10^{-4}
0.45	6.75730×10^{-1}	5.84745×10^{-2}	8.16001×10^{-1}	7.16598×10^{-2}	5.52359×10^{-1}	4.36905×10^{-1}	1.68253×10^{0}	1.71027×10^{-1}	5.52218×10^{-1}	1.52601×10^{-1}	1.58697	6.90375×10^{-4}
0.4	7.93200×10^{-1}	5.32843×10^{-2}	7.37001×10^{-1}	7.22988×10^{-2}	5.83599×10^{-1}	4.64701×10^{-1}	2.28337×10^{0}	2.36129×10^{-1}	5.56990×10^{-1}	1.15920×10^{-1}	1.60207	1.17612×10^{-3}
0.3	1.11485×10^{0}	4.30356×10^{-2}	6.04001×10^{-1}	7.12508×10^{-2}	6.22364×10^{-1}	5.02461×10^{-1}	4.07977×10^{0}	4.29428×10^{-1}	5.61937×10^{-1}	5.15305×10^{-2}	1.61903	1.42871×10^{-3}
0.2	1.73580×10^{0}	3.14573×10^{-2}	4.77001×10^{-1}	6.59481×10^{-2}	6.43893×10^{-1}	5.31727×10^{-1}	8.64467×10^{0}	9.10113×10^{-1}	5.61997×10^{-1}	1.25533×10^{-2}	1.62264	1.11836×10^{-3}
0.15	2.39870×10^{0}	2.41206×10^{-2}	4.07001×10^{-1}	5.92642×10^{-2}	6.63556×10^{-1}	5.61965×10^{-1}	1.68171×10^{1}	1.76553×10^{0}	5.61206×10^{-1}	9.69811×10^{-2}	1.62238	8.54273×10^{-5}
0.14	2.60090×10^{0}	2.24231×10^{-2}	3.93001×10^{-1}	5.70561×10^{-2}	6.70656×10^{-1}	5.72569×10^{-1}	2.04037×10^{1}	2.14142×10^{0}	5.61122×10^{-1}	1.02468×10^{-2}	1.62225	7.92244×10^{-4}
0.13	2.84370×10^{0}	2.06167×10^{-2}	3.80001×10^{-1}	5.42544×10^{-2}	6.80122×10^{-1}	5.86444×10^{-1}	2.56761×10^{1}	2.69541×10^{0}	5.61188×10^{-1}	8.92169×10^{-3}	1.62209	7.25942×10^{-4}
0.12	3.14270×10^{0}	1.86794×10^{-2}	3.69001×10^{-1}	5.06216×10^{-2}	6.93407×10^{-1}	6.05434×10^{-1}	3.40408×10^{1}	3.57841×10^{0}	5.61572×10^{-1}	5.60627×10^{-1}	1.62188	6.54390×10^{-4}
0.11	3.52555×10^{0}	1.65772×10^{-2}	3.62001×10^{-1}	4.57934×10^{-2}	7.13735×10^{-1}	6.33430×10^{-1}	4.89718×10^{1}	5.16928×10^{0}	5.62734×10^{-1}	7.00196×10^{-3}	1.62159	5.73868×10^{-4}
0.1	4.05285×10^{0}	1.42484×10^{-2}	3.69001×10^{-1}	3.86133×10^{-2}	7.50422×10^{-1}	6.81476×10^{-1}	8.20304×10^{1}	8.76572×10^{0}	5.66196×10^{-1}	1.22235×10^{-2}	1.62117	4.86545×10^{-4}

Table J.3: BE with $\alpha(R) = -5$ (partially condensate core when $b \lesssim 0.11$): Marginally stable points corresponding to different temperature parameters $b = k_B T(R)/mc^2$. No marginal stable point exists for $0 \leq b \lesssim 0.11$ if the particles are purely thermal. BEC must happen for $w(0 \leq r \leq r_c) = 5$ at $b \lesssim 0.11$ in order to have marginal stable points. The pair production/annihilation effect is significant only if $b \gtrsim 0.1$; while no gravitational bound state exists when $b \gtrsim 0.49$ as $M_{\rm rest} - M \lesssim 0$.

b	$w(0)$	$\bar{M}$	$\bar{R}$	$C = \bar{M}/\bar{R}$	$Z(0)$	$\epsilon_*(0)/mc^2$	$\bar{p}(0)$	$\bar{\rho}(0)$	$v(0)/c$	$v(R)/c$	$\langle\gamma\rangle = \gamma_\infty$
5.0	6.48170×10^{-2}	2.05293×10^{-1}	2.58800×10^{0}	7.93249×10^{-2}	6.12918×10^{-1}	4.79468×10^{-1}	1.61489×10^{-1}	1.72233×10^{-2}	5.65648×10^{-1}	3.78285×10^{-3}	1.62358
3.0	1.08190×10^{-1}	1.58004×10^{-1}	1.99900×10^{0}	7.90413×10^{-2}	6.13507×10^{-1}	4.80523×10^{-1}	2.73861×10^{-1}	2.91975×10^{-2}	5.65547×10^{-1}	5.25971×10^{-3}	1.62356
2.0	1.62600×10^{-1}	1.27966×10^{-1}	1.62700×10^{0}	7.86517×10^{-2}	6.14294×10^{-1}	4.81913×10^{-1}	4.19988×10^{-1}	4.47585×10^{-2}	5.65432×10^{-1}	3.61058×10^{-3}	1.62354
1.0	3.27130×10^{-1}	8.82646×10^{-2}	1.13900×10^{0}	7.74930×10^{-2}	6.16690×10^{-1}	4.86160×10^{-1}	8.99061×10^{-1}	9.56836×10^{-2}	5.65047×10^{-1}	4.47708×10^{-3}	1.62347
0.5	6.62740×10^{-1}	5.92204×10^{-2}	7.90001×10^{-1}	7.49625×10^{-2}	6.22122×10^{-1}	4.95593×10^{-1}	2.08035×10^{0}	2.20794×10^{-1}	5.64269×10^{-1}	1.93680×10^{-2}	1.62332
0.3	1.12642×10^{0}	4.24925×10^{-2}	5.97001×10^{-1}	7.11766×10^{-2}	6.30902×10^{-1}	5.10392×10^{-1}	4.31154×10^{0}	4.55841×10^{-1}	5.63185×10^{-1}	4.75599×10^{-3}	1.62309
0.2	1.74070×10^{0}	3.11191×10^{-2}	4.75001×10^{-1}	6.55138×10^{-2}	6.45551×10^{-1}	5.34033×10^{-1}	8.93060×10^{0}	9.39739×10^{-1}	5.61854×10^{-1}	7.86951×10^{-3}	1.62275
0.15	2.41305×10^{0}	2.36937×10^{-2}	4.07001×10^{-1}	5.82154×10^{-2}	6.67340×10^{-1}	5.67286×10^{-1}	1.78990×10^{1}	1.87641×10^{0}	5.60802×10^{-1}	3.41279×10^{-3}	1.62231
0.14	2.62130×10^{0}	2.19518×10^{-2}	3.94001×10^{-1}	5.57150×10^{-2}	6.75861×10^{-1}	5.79734×10^{-1}	2.20708×10^{1}	2.31239×10^{0}	5.60637×10^{-1}	4.67995×10^{-4}	1.62216
0.13	2.87470×10^{0}	2.00797×10^{-2}	3.82001×10^{-1}	5.25646×10^{-2}	6.87796×10^{-1}	5.96673×10^{-1}	2.85165×10^{1}	2.98724×10^{0}	5.60594×10^{-1}	7.02963×10^{-3}	1.62196
0.12	3.19540×10^{0}	1.80339×10^{-2}	3.74001×10^{-1}	4.82189×10^{-2}	7.06181×10^{-1}	6.21886×10^{-1}	3.97295×10^{1}	4.16615×10^{0}	5.60882×10^{-1}	7.19578×10^{-3}	1.62169
0.11	3.63692×10^{0}	1.57129×10^{-2}	3.77001×10^{-1}	4.16787×10^{-2}	7.40772×10^{-1}	6.66758×10^{-1}	6.45488×10^{1}	6.80229×10^{0}	5.62269×10^{-1}	1.00370×10^{-2}	1.62125

with pair production/annihilation

b	$w(0)$	$\bar{M}$	$\bar{R}$	$C = \bar{M}/\bar{R}$	$Z(0)$	$\epsilon_*(0)/mc^2$	$\bar{p}(0)$	$\bar{\rho}(0)$	$v(0)/c$	$v(R)/c$	$\langle\gamma\rangle = \gamma_\infty$	$\bar{M}_{\rm rest} - \bar{M}$
0.5	5.75630×10^{-1}	6.35168×10^{-2}	9.07001×10^{-1}	7.00294×10^{-2}	5.14156×10^{-1}	4.04127×10^{-1}	1.22368×10^{0}	1.21638×10^{-1}	5.46987×10^{-1}	1.89058×10^{-1}	1.56821	-9.04833×10^{-5}
0.49	5.94730×10^{-1}	6.24288×10^{-2}	8.86001×10^{-1}	7.04613×10^{-2}	5.22521×10^{-1}	4.11240×10^{-1}	1.31130×10^{0}	1.30985×10^{-1}	5.47420×10^{-1}	1.81771×10^{-1}	1.57231	9.45706×10^{-5}
0.48	6.14350×10^{-1}	6.13486×10^{-2}	8.67001×10^{-1}	7.07595×10^{-2}	5.30619×10^{-1}	4.18205×10^{-1}	1.40339×10^{0}	1.40845×10^{-1}	5.48709×10^{-1}	1.74222×10^{-1}	1.57627	2.65611×10^{-4}
0.45	6.76550×10^{-1}	5.81586×10^{-2}	8.13001×10^{-1}	7.15357×10^{-2}	5.53091×10^{-1}	4.37705×10^{-1}	1.70701×10^{0}	1.73533×10^{-1}	5.52247×10^{-1}	1.51867×10^{-1}	1.58725	6.98360×10^{-4}
0.4	7.94020×10^{-1}	5.29816×10^{-2}	7.34001×10^{-1}	7.21819×10^{-2}	5.84197×10^{-1}	4.65420×10^{-1}	2.31701×10^{0}	2.39606×10^{-1}	5.56988×10^{-1}	1.15416×10^{-1}	1.60224	1.17578×10^{-3}
0.3	1.11610×10^{0}	4.27424×10^{-2}	6.02001×10^{-1}	7.10006×10^{-2}	6.22936×10^{-1}	5.03349×10^{-1}	4.15233×10^{0}	4.36963×10^{-1}	5.61871×10^{-1}	5.06917×10^{-2}	1.61906	1.41989×10^{-3}
0.2	1.74010×10^{0}	3.11273×10^{-2}	4.75001×10^{-1}	6.55310×10^{-2}	6.45244×10^{-1}	5.33739×10^{-1}	8.91704×10^{0}	9.38146×10^{-1}	5.61805×10^{-1}	1.39815×10^{-2}	1.62261	1.10924×10^{-3}
0.15	2.41305×10^{0}	2.36937×10^{-2}	4.07001×10^{-1}	5.82154×10^{-2}	6.67340×10^{-1}	5.67286×10^{-1}	1.78991×10^{1}	1.87642×10^{0}	5.60804×10^{-1}	3.85887×10^{-3}	1.62231	8.38163×10^{-5}
0.14	2.62130×10^{0}	2.19518×10^{-2}	3.94001×10^{-1}	5.57150×10^{-2}	6.75861×10^{-1}	5.79734×10^{-1}	2.20708×10^{1}	2.31240×10^{0}	5.60638×10^{-1}	1.21278×10^{-3}	1.62216	7.74288×10^{-4}
0.13	2.87470×10^{0}	2.00797×10^{-2}	3.82001×10^{-1}	5.25646×10^{-2}	6.87796×10^{-1}	5.96673×10^{-1}	2.85165×10^{1}	2.98725×10^{0}	5.60594×10^{-1}	7.05825×10^{-3}	1.62196	7.05209×10^{-4}
0.12	3.19540×10^{0}	1.80339×10^{-2}	3.74001×10^{-1}	4.82189×10^{-2}	7.06181×10^{-1}	6.21886×10^{-1}	3.97295×10^{1}	4.16615×10^{0}	5.60882×10^{-1}	7.20382×10^{-3}	1.62169	6.28892×10^{-4}
0.11	3.63692×10^{0}	1.57129×10^{-2}	3.77001×10^{-1}	4.16787×10^{-2}	7.40772×10^{-1}	6.66758×10^{-1}	6.45488×10^{1}	6.80229×10^{0}	5.62269×10^{-1}	1.00383×10^{-2}	1.62125	5.40928×10^{-4}

Table J.4: BE with $\alpha(R) = -1$ (partially condensate core when $b \lesssim 0.4$): Marginally stable points corresponding to different temperature parameters $b = k_B T(R)/mc^2$. No marginal stable point exists for $0 \leq b \lesssim 0.4$ if the particles are purely thermal. BEC must happen for $w(0 \leq r \leq r_c) = 1$ at $b \lesssim 0.4$ in order to have marginal stable points. The pair production/annihilation effect is significant only if $b \gtrsim 0.1$; while no gravitational bound state exists when $b \gtrsim 0.57$ as $M_{\rm rest} - M \lesssim 0$.

b	$w(0)$	M	R	$C = M/R$	$Z(0)$	$\epsilon_*(0)/mc^2$	$\tilde{\mu}(0)$	$\tilde{\mu}(0)$	$v(0)/c$	$v(R)/c$	$\langle\gamma\rangle = \gamma_{\rm ex}$
5.0	6.49895×10^{-2}	1.61952×10^{-1}	2.05500×10^{0}	7.88089×10^{-2}	6.13979×10^{-1}	4.81355×10^{-1}	2.61607×10^{-1}	2.78834×10^{-2}	5.65469×10^{-1}	4.41211×10^{-3}	1.62355
3.0	1.08694×10^{-1}	1.23652×10^{-1}	1.58300×10^{0}	7.81126×10^{-2}	6.15396×10^{-1}	4.83859×10^{-1}	4.53639×10^{-1}	4.83113×10^{-2}	5.65236×10^{-1}	1.24702×10^{-3}	1.62350
2.0	1.63800×10^{-1}	9.96824×10^{-2}	1.28300×10^{0}	7.77271×10^{-2}	6.17320×10^{-1}	4.87201×10^{-1}	7.16945×10^{-1}	7.62675×10^{-2}	5.64921×10^{-1}	3.89377×10^{-3}	1.62345
1.0	3.33030×10^{-1}	6.58069×10^{-2}	8.88001×10^{-1}	7.41068×10^{-2}	6.24505×10^{-1}	4.99309×10^{-1}	1.71610×10^{0}	1.81808×10^{-1}	5.63762×10^{-1}	3.79838×10^{-3}	1.62326
0.5	7.05170×10^{-1}	3.90184×10^{-2}	6.08001×10^{-1}	6.41748×10^{-2}	6.54289×10^{-1}	5.44561×10^{-1}	6.09851×10^{0}	6.34601×10^{-1}	5.58726×10^{-1}	8.27840×10^{-3}	1.62257
0.40208	1.00000×10^{0}	2.84108×10^{-2}	5.89001×10^{-1}	4.82357×10^{-2}	7.59446×10^{-1}	6.72449×10^{-1}	2.99265×10^{1}	2.37776×10^{0}	4.88222×10^{-1}	4.44351×10^{-3}	1.62105

with pair production/annihilation

b	$w(0)$	M	R	$C = M/R$	$Z(0)$	$\epsilon_*(0)/mc^2$	$\tilde{\mu}(0)$	$\tilde{\mu}(0)$	$v(0)/c$	$v(R)/c$	$\langle\gamma\rangle = \gamma_{\rm ex}$	$M_{\rm rest} - M$
0.6	4.82330×10^{-1}	5.10951×10^{-2}	7.84001×10^{-1}	6.51722×10^{-2}	5.09036×10^{-1}	4.07257×10^{-1}	1.99507×10^{0}	1.88312×10^{-1}	5.38263×10^{-1}	2.11376×10^{-1}	1.56967	-3.14878×10^{-4}
0.59	4.96570×10^{-1}	5.01640×10^{-2}	7.68001×10^{-1}	6.53176×10^{-2}	5.16850×10^{-1}	4.14358×10^{-1}	2.10520×10^{0}	2.03818×10^{-1}	5.39318×10^{-1}	2.05641×10^{-1}	1.56410	-1.83122×10^{-4}
0.58	5.11230×10^{-1}	4.92315×10^{-2}	7.53001×10^{-1}	6.53804×10^{-2}	5.24581×10^{-1}	4.21468×10^{-1}	2.26070×10^{0}	2.20019×10^{-1}	5.40342×10^{-1}	1.99782×10^{-1}	1.56746	-5.96554×10^{-5}
0.57	5.26320×10^{-1}	4.82983×10^{-2}	7.39001×10^{-1}	6.53562×10^{-2}	5.32308×10^{-1}	4.28573×10^{-1}	2.43145×10^{0}	2.37499×10^{-1}	5.41325×10^{-1}	1.93787×10^{-1}	1.57074	5.56315×10^{-5}
0.56	5.41880×10^{-1}	4.73632×10^{-2}	7.25001×10^{-1}	6.53285×10^{-2}	5.39749×10^{-1}	4.35649×10^{-1}	2.61599×10^{0}	2.56415×10^{-1}	5.42268×10^{-1}	1.87857×10^{-1}	1.57394	1.62873×10^{-4}
0.55	5.57950×10^{-1}	4.64252×10^{-2}	7.11001×10^{-1}	6.52956×10^{-2}	5.47214×10^{-1}	4.42711×10^{-1}	2.81609×10^{0}	2.76948×10^{-1}	5.43171×10^{-1}	1.82003×10^{-1}	1.57705	2.62196×10^{-4}
0.5	6.47400×10^{-1}	4.16647×10^{-2}	6.56001×10^{-1}	6.40995×10^{-2}	5.83606×10^{-1}	4.78629×10^{-1}	4.13293×10^{0}	4.11996×10^{-1}	5.46862×10^{-1}	1.51831×10^{-1}	1.59116	6.44714×10^{-4}
0.49	6.67550×10^{-1}	4.06879×10^{-2}	6.39001×10^{-1}	6.36742×10^{-2}	5.90845×10^{-1}	4.86103×10^{-1}	4.48658×10^{0}	4.48121×10^{-1}	5.47395×10^{-1}	1.45764×10^{-1}	1.59367	6.99305×10^{-4}
0.48	6.88650×10^{-1}	3.96982×10^{-2}	6.28001×10^{-1}	6.32135×10^{-2}	5.98144×10^{-1}	4.93748×10^{-1}	4.88463×10^{0}	4.88659×10^{-1}	5.47833×10^{-1}	1.39837×10^{-1}	1.59606	7.46874×10^{-4}
0.45	7.59180×10^{-1}	3.66118×10^{-2}	5.99001×10^{-1}	6.11214×10^{-2}	6.21204×10^{-1}	5.18898×10^{-1}	6.47621×10^{0}	6.49183×10^{-1}	5.48382×10^{-1}	1.21704×10^{-1}	1.60254	8.48139×10^{-4}
0.4	9.29193×10^{-1}	3.03549×10^{-2}	5.70001×10^{-1}	5.32541×10^{-2}	6.83616×10^{-1}	5.91499×10^{-1}	1.41131×10^{1}	1.36907×10^{0}	5.39465×10^{-1}	9.25160×10^{-2}	1.61057	8.65748×10^{-4}
0.39327	1.00000×10^{0}	2.84061×10^{-2}	5.88001×10^{-1}	4.83096×10^{-2}	7.33929×10^{-1}	6.48123×10^{-1}	2.80443×10^{1}	2.17340×10^{0}	4.82179×10^{-1}	8.87732×10^{-3}	1.61089	8.19088×10^{-4}

Table J.5: BE with $\alpha(R) = -0.5$ (partially condensate core when $b \lesssim 0.7$ or 0.8): Marginally stable points corresponding to different temperature parameters $b = k_B T(R)/mc^2$. No marginal stable point exists for $0 \leq b \lesssim 0.4$ if the particles are purely thermal. BEC must happen for $w(0 \leq r \leq r_c) = 1$ at $b \lesssim 0.7$ or 0.8 (with or without pair production/annihilation) in order to have marginal stable points. The pair production/annihilation effect is significant only if $b \gtrsim 0.1$; while no gravitational bound state exists when $b \gtrsim 0.7$ as $M_{\rm rest} - M \lesssim 0$.

b	$w(0)$	M	R	$C = M/R$	$Z(0)$	$\epsilon_*(0)/mc^2$	$\tilde{\mu}(0)$	$\tilde{\mu}(0)$	$v(0)/c$	$v(R)/c$	$\langle\gamma\rangle = \gamma_{\rm ex}$
5.0	6.52990×10^{-2}	1.25310×10^{-1}	1.60900×10^{0}	7.78809×10^{-2}	6.15922×10^{-1}	4.84763×10^{-1}	4.43484×10^{-1}	4.72153×10^{-2}	5.65149×10^{-1}	3.53529×10^{-3}	1.62349
3.0	1.09642×10^{-1}	9.42484×10^{-2}	1.23200×10^{0}	7.65003×10^{-2}	6.19037×10^{-1}	4.90113×10^{-1}	8.02845×10^{-1}	8.53158×10^{-2}	5.64624×10^{-1}	7.86822×10^{-3}	1.62340
2.0	1.66259×10^{-1}	7.38859×10^{-2}	9.93001×10^{-1}	7.44066×10^{-2}	6.23831×10^{-1}	4.98159×10^{-1}	1.35464×10^{0}	1.43552×10^{-1}	5.63836×10^{-1}	3.77594×10^{-3}	1.62327
1.0	3.51100×10^{-1}	4.41888×10^{-2}	6.80001×10^{-1}	6.49834×10^{-2}	6.52009×10^{-1}	5.41017×10^{-1}	4.67989×10^{0}	4.87236×10^{-1}	5.58872×10^{-1}	9.09096×10^{-3}	1.62262
0.79835	5.00000×10^{-1}	3.21537×10^{-2}	6.51001×10^{-1}	4.93912×10^{-2}	7.53085×10^{-1}	6.64326×10^{-1}	2.24706×10^{1}	1.78692×10^{0}	4.88434×10^{-1}	8.22334×10^{-3}	1.62112

with pair production/annihilation

b	$w(0)$	M	R	$C = M/R$	$Z(0)$	$\epsilon_*(0)/mc^2$	$\tilde{\mu}(0)$	$\tilde{\mu}(0)$	$v(0)/c$	$v(R)/c$	$\langle\gamma\rangle = \gamma_{\rm ex}$	$M_{\rm rest} - M$
0.8	3.51600×10^{-1}	4.31632×10^{-2}	7.39001×10^{-1}	5.84076×10^{-2}	4.80415×10^{-1}	3.91334×10^{-1}	2.63651×10^{0}	2.38916×10^{-1}	5.21397×10^{-1}	2.56511×10^{-1}	1.54028	-8.71148×10^{-4}
0.71	4.62120×10^{-1}	3.42885×10^{-2}	6.56001×10^{-1}	5.27514×10^{-2}	5.73545×10^{-1}	4.88294×10^{-1}	7.59216×10^{0}	6.70590×10^{-1}	5.14762×10^{-1}	2.18430×10^{-1}	1.56509	-2.32943×10^{-5}
0.7	4.90300×10^{-1}	3.24569×10^{-2}	6.53001×10^{-1}	4.97042×10^{-2}	6.04345×10^{-1}	5.22542×10^{-1}	1.13357×10^{1}	9.31147×10^{-1}	4.96416×10^{-1}	2.13955×10^{-1}	1.56744	4.94255×10^{-5}
0.69958	5.00000×10^{-1}	3.19603×10^{-2}	6.59001×10^{-1}	4.84981×10^{-2}	6.18445×10^{-1}	5.37960×10^{-1}	1.55491×10^{1}	1.07425×10^{0}	4.55261×10^{-1}	2.13735×10^{-1}	1.56742	5.57749×10^{-5}

Appendix K

Formulation of the Relativistic Bondi Accretion

K.1 Inconsistency of non-relativistic Bondi accretion for the SIDM

In this appendix, we show that the non-relativistic Bondi accretion of SIDM obeying Eq. 6.6 is not consistent because it yields relativistic sound speed and fluid speed.

We start with the non-relativistic continuity equation and Euler equation

$$\frac{1}{r^2}\frac{\mathrm{d}}{\mathrm{d}r}(r^2\rho v) = 0 \,, \tag{K.1}$$

$$v\frac{\mathrm{d}v}{\mathrm{d}r} + \frac{1}{\rho}\frac{\mathrm{d}p}{\mathrm{d}r} + \frac{M}{r^2} = 0 \,. \tag{K.2}$$

Note that in the non-relativistic limit, the rest mass density ρ_0 and the total energy density

ρ are approximately equal, thus we do not distinguish them here. The continuity equation Eq. K.1 implies a constant accretion rate,

$$\dot{M} = 4\pi r^2 \rho v. \tag{K.3}$$

Instead of directly solving the Euler equation Eq. K.2, we rewrite it into the following "Bondi equation" [246, 247]:

$$\frac{1}{2}\left(1 - \frac{a^2}{v^2}\right)\frac{\mathrm{d}v^2}{\mathrm{d}r} = -\frac{M}{r^2}\left[1 - \left(\frac{2a^2 r}{M}\right)\right] . \tag{K.4}$$

Assuming $a^2(r)$ does not increase too rapidly as r increases, we can see that the RHS will change from positive value to the negative one at the sonic horizon $r = r_s$ with

$$r_s = \frac{M}{2a^2(r_s)}. \tag{K.5}$$

This implies that the LHS shall also change the sign accordingly. Since $\mathrm{d}v^2/\mathrm{d}r < 0$, a physically reasonable initial condition [246, 247] is as follows:

$$v^2 \to 0 \quad \text{as} \quad r \to \infty \qquad \text{and} \qquad v^2(r_s) = a_s^2 := a^2(r_s). \tag{K.6}$$

This condition implies that the fluid starts as subsonic fluid at large r and then turns into the supersonic one after crossing the sonic horizon as r decreases. Subject to the above initial condition, we will now solve the Euler equation Eq. K.2 based on the EoS Eq. 6.6.

By the definition of sound speed $a^2 = (\partial p/\partial\rho)_{\mathrm{ad}}$, the EoS Eq. 6.6 can be put into

the following form:

$$\frac{\rho}{\rho_B} = \frac{4a^2(2-3a^2)}{(1-3a^2)^2} \qquad \text{or} \qquad \sqrt{\frac{p}{\rho_B}} = \frac{2a^2}{1-3a^2} \ . \tag{K.7}$$

The second expression implies $a^2 \leq 1/3$ which is the so-called sound barrier. Integrating Eq. K.2 and using Eq. K.7 we obtain

$$\frac{v^2}{2} + \frac{2}{3}\ln\left(\frac{2-3a^2}{1-3a^2}\right) - \frac{M}{r} = \frac{2}{3}\ln\left(\frac{2-3a_\infty^2}{1-3a_\infty^2}\right) \ . \tag{K.8}$$

where $a_\infty = a(\infty)$. At the sonic horizon $r = r_s$, *i.e.*, Eq. K.5, $v^2(r_s) = a_s^2$. We can then use this equation to relate the sound speed at sound horizon to the asymptotic sound speed $0 \leq a_\infty \leq 1/\sqrt{3}$, and find that

$$0.38c \lesssim a_s \leq 0.58c \tag{K.9}$$

where we have recovered the speed of light c. We see that the sound speed at the sound horizon is of the order of c, which implies that the non-relativistic formulation of Bondi accretion is not consistent, at least near the sound horizon region. Therefore, a relativistic formulation of Bondi accretion is needed for the SIDM with EoS given by Eq. 6.6.

K.2 Relativistic Euler equation in Schwarzschild spacetime

By the conservation law of spherically symmetric stationary inflow in Schwarzschild background, one obtains the relativistic Euler equation [57]:

$$\begin{aligned} &\frac{u'}{u}+\frac{\rho_0'}{\rho_0}=-\frac{2}{r}\ , \\ &uu'+\left(1-\frac{2M}{r}+u^2\right)\frac{a^2}{\rho_0}\rho_0'=-\frac{M}{r^2}, \end{aligned} \tag{K.10}$$

where "prime" denotes the derivative with respect to the radial coordinate. The solution is

$$u'=\frac{\Delta_1}{\Delta}\quad\text{and}\quad\rho_0'=\frac{\Delta_2}{\Delta}, \tag{K.11}$$

where

$$\begin{aligned} &\Delta\equiv\frac{1}{\rho_0 u}\left[\left(1-\frac{2M}{r}+u^2\right)a^2-u^2\right], \\ &\Delta_1\equiv\frac{1}{\rho_0}\left[\frac{M}{r^2}-\frac{2a^2}{r}\left(1-\frac{2M}{r}+u^2\right)\right]\quad\text{and}\quad\Delta_2\equiv\frac{1}{u}\left(\frac{2u^2}{r}-\frac{M}{r^2}\right). \end{aligned} \tag{K.12}$$

Remark (i) $\Delta>0$ as $r\to\infty$, $u\to 0$ and $a\to a_\infty$ (subsonic $u^2<a^2$) (ii) $\Delta=(u/\rho_0)(a^2-1)<0$ at $r=2M$ as $a<1$. (iii) Δ must pass through zero at *some critical point* $r=r_s$ outside $r=2M$. To avoid the singularities in the stationary flow, one demands $\Delta=\Delta_1=\Delta_2=0$ at $r=r_s$. Thus, at this *critical point* (sound horizon), one derives Eq. 6.16.

K.3 Deriving profile equation for sound speed

We determine the spatial profile of the Bondi accretion from the relativistic Bernoulli equation Eq. 6.13 given the boundary condition to fix

$$c_B \equiv \left(\frac{p_\infty + \rho_\infty}{\rho_{0,\infty}} \right)^2 . \tag{K.13}$$

We aim to solve Eq. 6.13 for the sound speed profile. However, there is still u in the LHS of Eq. 6.13. We can use Eqs. 6.8 and 6.10 to express $u = u(a, \bar{r})$ and the result is

$$u = \frac{c_A (1 - 3a^2)^{3/2}}{a^2 \bar{r}^2 \sqrt{1 - a^2}} \tag{K.14}$$

where

$$c_A \equiv \frac{\dot{M}}{128\pi M^2 \rho_B} , \tag{K.15}$$

and we have introduced the radius coordinate $\bar{r} = r/2M$ in the unit of Schwarzschild radius.

With Eq. K.14, we can turn Eq. 6.13 into the following to solve for $x \equiv a^2$:

$$(27c_A^2 - \bar{r}^3 + \bar{r}^4 - 3c_B \bar{r}^4)x^3 - (27c_A^2 - \bar{r}^3 + \bar{r}^4 - c_B \bar{r}^4)x^2 + 9c_A^2 x - c_A^2 = 0 . \tag{K.16}$$

Once the boundary condition is specified, the profile of sound speed can be obtained and, in turn, the density profile around the central hole. We need to specify the physical boundary conditions, such as a_∞, of the dark halo to fix c_A, c_B and select the right and physical profile. As for the dark halo, the typical value for the fluid velocity dispersion is about 100 km s^{-1}, which is roughly also the value of $a_\infty \approx 10^{-3.5}$ in unit of light speed. Thus, we

solve $x = x(\bar{r})$, or equivalently $\bar{r} = \bar{r}(x)$, from Eq. K.16, and only real solution can satisfy the boundary conditions. Given the sound speed profile, we can in turn obtain the mass density profile $\rho_0(\bar{r})$.

K.4 Local Mach number

The proper speed of the fluid $v \equiv |v^r| = |\mathrm{d}r_{\rm obs}/\mathrm{d}t_{\rm obs}|$ measured by a "local" and "stationary" observer at r with the observer's proper length $\mathrm{d}r_{\rm obs}(r) = \mathrm{d}r/\sqrt{1-2M/r}$ and proper time $\mathrm{d}t_{\rm obs}(r) = \sqrt{1-2M/r}\mathrm{d}t$, thus

$$v^r = \frac{\mathrm{d}r_{\rm obs}}{\mathrm{d}t_{\rm obs}} = \frac{\mathrm{d}r/\mathrm{d}t}{1-2M/r} = \frac{u^r/u^t}{1-2M/r}$$

and with the normalization

$$-1 = -\left(u^t\right)^2\left(1-\frac{2M}{r}\right) + (u^r)^2\left(1-\frac{2M}{r}\right)^{-1},$$

one can readily solve for

$$v = \frac{u}{\sqrt{1-2M/r+u^2}}. \tag{K.17}$$

Hence at $r \gg 2M$, $v \simeq u \ll 1$ and is subsonic; while at $r = 2M$, $v \equiv 1 > a$, *independent* of u, supersonic. Then we define the "local" Mach number

$$\mathcal{M} \equiv \frac{v}{a} = \frac{u/a}{\sqrt{1-2M/r+u^2}}. \tag{K.18}$$

Note that at the sound horizon ($v_s = a_s$), $\mathcal{M}_s = v_s/a_s = 1$; at the event horizon ($v_h = 1$), $\mathcal{M}_h = v_h/a_h = 1/a_h$.